ISBN 978-82-326-6674-4 (printed ver.)
ISBN 978-82-326-6738-3 (electronic ver.)
ISSN 1503-8181 (printed ver.)
ISSN 2703-8084 (electronic ver.)

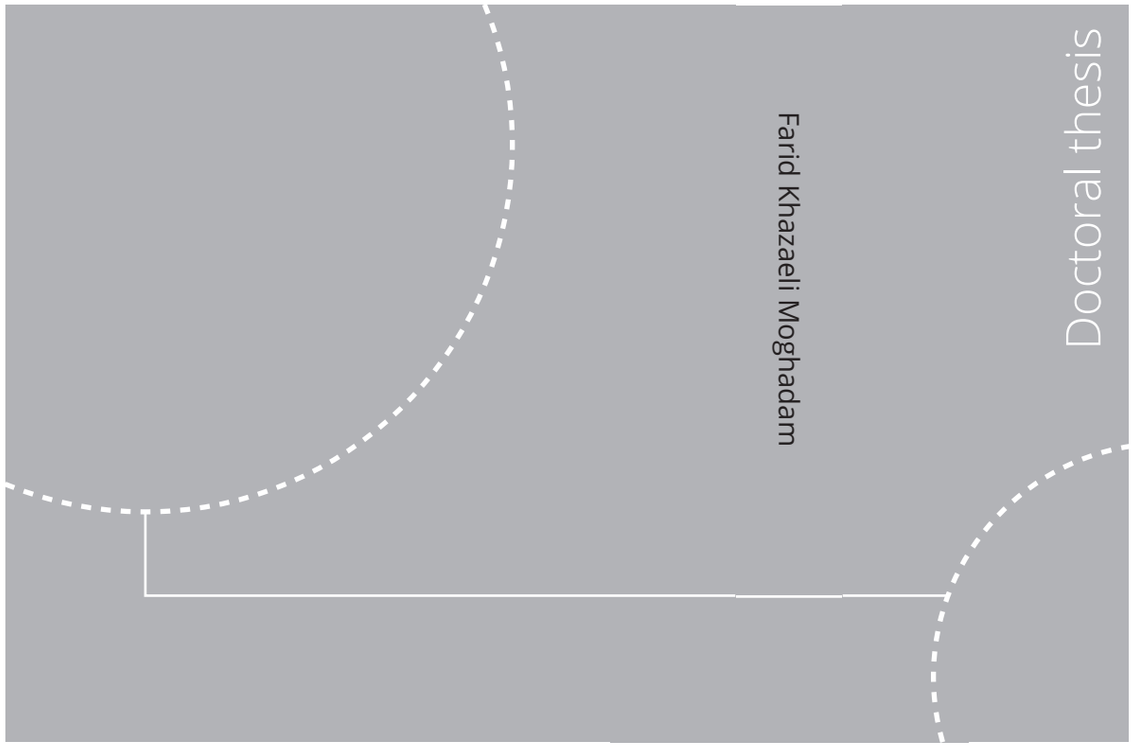

Doctoral theses at NTNU, 2021:109

Farid Khazaeli Moghadam

Vibration-Based Condition Monitoring of Drivetrains in Large Offshore Wind Turbines in a Digital Twin Perspective

NTNU
Norwegian University of
Science and Technology

Doctoral theses at NTNU, 2021:109

NTNU
Norwegian University of
Science and Technology
Thesis for the degree of
Philosophiae Doctor
Faculty of Engineering
Department of Marine Technology

NTNU
Norwegian University of
Science and Technology

Farid Khazaeli Moghadam

Vibration-Based Condition Monitoring of Drivetrains in Large Offshore Wind Turbines in a Digital Twin Perspective

Thesis for the degree of Philosophiae Doctor

Trondheim, March 2021

Norwegian University of Science and Technology
Faculty of Engineering
Department of Marine Technology

NTNU
Norwegian University of
Science and Technology

NTNU
Norwegian University of Science and Technology

Thesis for the degree of Philosophiae Doctor

Faculty of Engineering
Department of Marine Technology

ISBN 978-82-326-6674-4 (printed ver.)
ISBN 978-82-326-6738-3 (electronic ver.)
ISSN 1503-8181 (printed ver.)
ISSN 2703-8084 (electronic ver.)

Doctoral theses at NTNU, 2021:109

Printed by Skipnes Kommunikasjon AS

Engineering problems are under-defined, there are many solutions, good, bad and indifferent. The art is to arrive at a good solution. This is a creative activity, involving imagination, intuition and deliberate choice."

Ove Nyquist Arup (1895-1988), Engineer and philosopher, author of Philosophy of Design book and founder of Arup firm.

The problem in this business isn't to keep people from stealing your ideas; it's making them steal your ideas!"

Howard Hathaway Aiken (1900-1973), Engineer, physicist and a pioneer in computing, recipient of IEEE's Edison Medal in 1970 for his contribution to the development of digital computers.

Abstract

According to EU 2050 plan, offshore wind farms based on large floating wind turbines are considered as a main source of power supply in the coming future. Among the turbine systems, drivetrain contributes significantly in levelized cost of energy (LCOE). In other words, the careful selection of the drivetrain configuration and the employment of properly designed condition monitoring systems can help to considerably reduce the cost of energy in floating offshore wind turbines.

As the first study in this thesis, an analytical system-level drivetrain design approach supported by numerical simulations is employed to identify the most economical drivetrain configuration of large floating offshore wind turbines in a life cycle perspective.

The medium-speed PMSG drivetrain technology is selected as a compromise between design, manufacturing and installation, and operation and maintenance costs, and in the next steps of this research, the drivetrain vibration-based condition monitoring tools are designed or developed to realize the improved availability of future offshore wind turbines by following the sequence described underneath:

In the first step, the classical vibration-based condition monitoring based on the time and frequency domain analytical tools based on the translational vibration measurements captured by accelerometers which are placed on the different parts of drivetrain are reviewed as the wind turbine standard condition monitoring solution. As the research contribution in time domain analysis of translational vibration measurements for condition monitoring of the drivetrain components, a data-driven statistical learning-based condition monitoring approach grounded on monitoring the unusual variations of the parameters of the multi-variate distribution which fits the combined measurements of the drivetrain accelerometers is studied. The potentials of this approach in early-stage fault detection compared to the classical time-domain fault detection approach based on monitoring the exceedance of the root mean square (RMS) of the axial and lateral acceleration and velocity is demonstrated. To take the vibration-based condition monitoring of the drivetrain further, the topic of innovative condition monitoring of the drivetrain based on the torsional vibration measurements captured by the drivetrain encoders is introduced and discussed, and the possibility of observing the different classes of drivetrain faults by using the torsional instead of translational vibration measurements is studied. The possibility of using the torsional response to provide better insights into the drivetrain internal and external excitation sources is discussed, which can be used to improve the

available condition monitoring systems for realizing an earlier stage fault detection.

As the second step, the drivetrain condition monitoring by using the torsional measurements is investigated in more detail. In this study, the possibility of performing drivetrain modal analysis by using the torsional response is discussed. Then an analytical approach is proposed to diagnose the drivetrain faults at system-level by monitoring the variations of the drivetrain dynamic properties (*i.e.* natural frequencies, mode shapes and damping coefficients) which can be estimated from the torsional measurements.

In the third step, the drivetrain online fault prognosis by monitoring the residual life of the components is emphasized. For this purpose, the multi-degree of freedom (DOF) linear torsional models of the drivetrain are proposed to be used as the digital twin of drivetrain, and their capabilities in prediction of the remaining useful lifetime (RUL) of the different drivetrain components is discussed. Digital twin in this thesis context is defined as the combination of equivalent model, online measurements and RUL model. The algorithm for the near real-time estimation of the parameters of drivetrain equivalent reduced order model (ROM) in the cases of different degrees of model complexity by using the drivetrain torsional measurements is presented, and the application of proposed digital twin model for estimating the degradation of the drivetrain gears and shafts is demonstrated. Load observers are designed for the different components of the drivetrain, which receive the parameters of the updated drivetrain equivalent model and the online torsional response to estimate loads in the different components of the drivetrain. The employed stochastic physics-based degradation model works based on the real-time cycle counting of the equivalent stress, and is able to provide confidence interval for the estimated damage.

The integration of the model with the real-time operational data in a digital twin platform, which provides the drivetrain updated ROM parameters and dynamic properties, can also support fault diagnosis algorithms which are discussed in this PhD thesis: In a direct way, by having access to the real-time values of system parameters, it is possible to define different fault states of the different classes of progressive faults in the drivetrain components in terms of the variation of the ROM parameters. Seeing that the ROM parameters are directly connected to the physics of the system and the components, defining thresholds for the different states of progressive faults is straightforward. In an indirect approach, the proposed algorithm provides the real-time values of drivetrain dynamic properties, which can support the proposed fault diagnosis approach based on monitoring the variations of dynamic properties to estimate the state of the faults.

Preface

This thesis is submitted to the Norwegian University of Science and Technology (NTNU) in partial fulfilment of the requirements for the degree of philosophiae doctor.

This doctoral work has been performed at the Department of Marine Technology, NTNU, Trondheim, with Professor Amir Rasekhi Nejad as the main supervisor, with co-supervisors Professor Eilif Pedersen at the Department of Marine Technology, NTNU, and Professor Kourosh Koushan at SINTEF Ocean AS.

The work has been financially supported by the Department of Marine Technology, NTNU, from 2018 to 2021, through the project number 70441829.

Acknowledgement

Firstly I would like to express my deepest gratitude to my supervisor, Professor Amir Rasekhi Nejad for his trust, patience, encouragement, positive attitude and consistent support. In the previous research and professional experiences, I had the chance to work with the electrical generator, power converter system and the turbine control systems design of the wind turbines. Joining Amir's research group was a great opportunity for me to obtain a deeper understanding about wind turbine machinery design in a mechanical engineering perspective, so that by the end of this milestone I would say that I could obtain a good understanding about the wind turbine power train as a complex electromechanical system. In the most difficult parts of my PhD research, Amir was my best teacher. When life was getting complicated and I was in need of someone to rely on, he was like the best friend. His door was always open for me for discussions and advice, and the words are not enough to express my gratitude to him.

I extend my gratitude to my co-supervisors Professor Eilif Pedersen and Professor Kourosh Koushan for their ideas and constructive feedbacks throughout this PhD project.

I was also fortunate for the excellent collaboration with Kongsberg Digital for the drivetrain condition monitoring during this project. This collaboration provided me access to the operational measurements which are used for the validation of a part of studies in this research.

I would like to thank Dr. John Marius Hegseth for providing the DTU 10 MW spar floating wind turbine global analysis simulation data.

I very much appreciate the time and effort of Kjell Olav Skjølsvik for helping me to gain insight on the business-oriented engineering design, and his support to patent a part of the outputs of my PhD project.

I have enjoyed very interesting discussions with my colleagues Dr. Geraldo Francisco Rebouças and Shuaishuai Wang during my PhD studies about the different aspects of analytical modelling and numerical analysis of the drivetrain system components.

I am very grateful for the support received from the lab technicians at NTNU Department of Marine Technology to equip the Marine Dynamics and Vibration Lab (MD Lab) with a scaled 15 kw offgrid wind turbine drivetrain test rig, in particular Frode Gran and Øystein Kristiansen.

I am also grateful for the help and support received from NTNU Department of Marine Technology administration staff, to name a few Astrid Elisabeth Hansen, Dorota Wesoly and Bjørn Tore Bach.

Most fundamentally, I deeply thank my wife, Farzaneh who supported

me in this journey, with many challenges of living in a new country and far from our families, with her endless love and support. I would like to thank my mother Nasrin and my brother Vahid for encouraging me to keep going and remaining strong when life was challenging me.

List of Appended Papers

This thesis consists of an introductory part and seven papers which form the basis of the thesis. From these seven papers, six papers are appended. One paper is under development and thus has not been included in this thesis. The list of papers, as well as a declaration of authorship, is presented in the following:

Paper 1:
Evaluation of PMSG-based drivetrain technologies for 10-MW floating offshore wind turbines: Pros and cons in a life cycle perspective.
Authors: Farid Khazaeli Moghadam, Amir Rasekhi Nejad
Published in *Wind Energy*, 2020, DOI: 10.1002/we.2499.

Paper 2:
Experimental validation of angular velocity measurements for wind turbines drivetrain condition monitoring.
Authors: Farid Khazaeli Moghadam, Amir Rasekhi Nejad
Published in *Proceedings of the ASME 2019 2nd International Offshore Wind Technical Conference IOWTC2019, November 3-6, St. Julian's, Malta*, 2019, IOWTC2019-7620, V001T01A035; 9 pages.

Paper 3:
Natural frequency estimation by using torsional response, and applications for wind turbine drivetrain fault diagnosis.
Authors: Farid Khazaeli Moghadam, Amir Rasekhi Nejad
Published in *In Journal of Physics: Conference Series*, September 2020, Vol. 1618, No. 2, p. 022019. IOP Publishing.

Paper 4:
Theoretical and experimental study of wind turbine drivetrain fault diagnosis by using torsional vibrations and modal estimation.
Authors: Farid Khazaeli Moghadam, Amir Rasekhi Nejad
Under review at Elsevier Journal of Sound and Vibration.

Paper 5:
Digital twin modeling for predictive maintenance of floating offshore wind turbine drivetrains.
Authors: Farid Khazaeli Moghadam, Geraldo Francisco de Souza Rebouças, Amir Rasekhi Nejad

Accepted to Springer Journal of Forschung im Ingenieurwesen.

Paper 6:
Online condition monitoring of floating wind turbines drivetrain by using digital twin modeling approach.
Authors: Farid Khazaeli Moghadam, Amir Rasekhi Nejad
Under review at Elsevier Journal of Mechanical Systems and Signal Processing.

The following work has been prepared during the PhD period, but has not yet been submitted, thus is not included in the thesis:

Paper 7:
Drivetrain fault detection of multi-megawatt offshore wind turbines by statistical learning.
Authors: Farid Khazaeli Moghadam, Amir Rasekhi Nejad

Declaration of Authorship

All the six papers that serve as the core content of this thesis are co-authored. In all these papers, I was the first author and responsible for initiating ideas, performing the analysis and calculations, providing the results and writing the papers. Professor Amir Rasekhi Nejad contributed to the idea, scientific support, corrections and constructive comments to increase the scientific quality of the publication. In Paper 5, Dr. Geraldo Francisco de Souza Rebouças has contributed to the lumped parameter model of the drivetrain, estimation of loads and stresses, analysis of the related results and writing of the paper in general.

Abbreviations

BEM	Blade Element Momentum
CLT	Central Limit Theorem
CM	Condition Monitoring
DDPMSG	Direct-Drive Permanent Magnet Synchronous Generator
DOF	Degree of Freedom
DT	Digital Twin
DTU	Technical University of Denmark
EU	European Union
FEM	Finite Element Method
FFT	Fast Fourier Transform
FRF	Frequency Response Function
FWT	Floating Wind Turbine
GMRF	Gaussian Markov Random Field
HSPMSG	High-Speed Permanent Magnet Synchronous Generator
IID	Independent Identically Distributed
ISO	International Organization for Standardization
LCOE	Levelized Cost of Energy
LSE	Least Square Error
MBS	Multi-body Simulation

ML	Maximum Likelihood
MSPMSG	Medium-Speed Permanent Magnet Synchronous Generator
NREL	National Renewable Energy Laboratory
O&M	Operation and Maintenance
OMA	Operational Modal Analysis
OPEX	Operational Expenditure
PMSG	Permanent Magnet Synchronous Generator
POF	Probability of Failure
PSD	Power Spectral Density
RMS	Root Mean Square
ROM	Reduced-Order Model
RUL	Remaining Useful Lifetime
SCADA	Supervisory Control and Data Acquisition

Contents

List of Tables **xvii**

List of Figures **xix**

1 Introduction **1**
1.1 Background & motivation 1
1.2 Drivetrain basics and available technologies 2
1.3 Drivetrain failures 4
1.4 Available drivetrain performance and condition monitoring techniques 5
1.5 Aims and scope 6
1.6 Thesis outline 8

2 Global dynamic response analysis **11**
2.1 General 11
2.2 Decoupled analysis approach 12
2.3 Test cases 13

3 Optimal drivetrain configuration for large turbines **17**
3.1 General 17
3.2 Life cycle optimization 18
3.3 Drivetrain optimization approach 20
3.3.1 Algorithm 21
3.3.2 Generator optimization 21
3.3.3 Gearbox optimization 23
3.4 Comparison of different configurations 25

4 Physics-based and data-driven vibration-based condition monitoring **27**
4.1 Literature review on vibration-based condition monitoring methods 27

4.2 Data-driven condition monitoring based on translational vibrations . . . 31
4.3 Innovative condition monitoring by means of torsional vibrations 36
4.3.1 Torsional responses error function . . . 37
4.3.2 Comparison of translational and torsional vibrations-based condition monitoring . . . 38

5 Fault diagnosis and modal analysis by using torsional vibrations 45
5.1 General . . . 45
5.2 Drivetrain modal analysis by torsional measurements . . . 48
5.2.1 Construction of the input function for the modal analysis approach . . . 48
5.2.2 Analytical proof . . . 50
5.2.3 Results of modal analysis approach validation . . . 51
5.3 Proposed drivetrain system-level fault diagnosis approach . . . 54
5.3.1 3-DOF equivalent model dynamic properties as a function of model parameters . . . 55
5.3.2 Sensitivity analysis . . . 57
5.3.3 Results of proposed fault diagnosis approach validation 58

6 Digital twin-based fault prognosis by torsional measurements 65
6.1 General . . . 65
6.2 Estimation of drivetrain equivalent model by using the torsional measurements . . . 67
6.2.1 Estimation of moment of inertia matrix . . . 67
6.2.2 Estimation of stiffness matrix . . . 70
6.2.3 Results of ROM model estimation . . . 73
6.3 Estimation of load and stress in the drivetrain components . . 77
6.3.1 Estimation of load and stress in main and high-speed shafts . . . 77
6.3.2 Estimation of contact load and stress at each gear stage 81
6.4 Degradation model . . . 87
6.4.1 Degradation model for residual life estimation . . . 87
6.4.2 Degradation of main and high-speed shafts . . . 90
6.4.3 Degradation of gears in the gearbox . . . 90

7 Conclusions 93
7.1 Conclusions . . . 93
7.2 Original contributions . . . 96
7.3 Recommendations for future works . . . 99

References **101**

A Appended papers **109**
A.1 Paper 1 109
A.2 Paper 2 133
A.3 Paper 3 145
A.4 Paper 4 161
A.5 Paper 5 201
A.6 Paper 6 225

B List of previous PhD theses at Dept. of Marine Tech. **253**

List of Tables

1.1 Drivetrain most conventional technologies 3
1.2 Basic failure modes study of PMSG drivetrain components . . 4

3.1 Case study technologies 21

4.1 Energy indices for the suspicious frequency $\omega^* = 529$ Hz. 43
4.2 Energy indices for the suspicious frequency $\omega^* = 170$ Hz. 43
4.3 Energy indices for the suspicious frequency $\omega^* = 0.05$ Hz. . . . 43

5.1 Estimation of damping coefficient for DTU 10 MW model . . . 52
5.2 14-DOF drivetrain model natural frequencies of NREL 5 MW . 54
5.3 Main shaft fault cases 59
5.4 High-speed shaft fault cases 59
5.5 Inertia-related fault cases (rotor). 60
5.6 Inertia-related fault cases (gearbox). 61
5.7 Inertia-related fault cases (generator). 61

6.1 Estimation of NREL 5 MW drivetrain 14-DOF model. 80
6.2 Main shaft accumulated damage in DTU 10 MW drivetrain. . . 90
6.3 Gears accumulated damage in NREL 5 MW drivetrain. 92

List of Figures

1.1 Relations between the appended papers and the thesis chapters. 6

2.1 Decoupled simulation approach for drivetrain analysis 12
2.2 Rotor torque obtained from global simulation models 15

3.1 Drivetrain life cycle assessment approach 19
3.2 Proposed drivetrain optimization approach 22
3.3 Comparison between different drivetrain topologies. 26

4.1 Graphical model of gearbox for NREL 5 MW drivetrain. 34
4.2 SIMPACK model and the fault case. 35
4.3 Detection of bearing fault by proposed data-driven approach. . 35
4.4 Experimental validation on Vestas 1.75 MW turbine. 36
4.5 Vestas 1.75 MW drivetrain accelerometers and encoders placement 40
4.6 First test scenario. 41
4.7 Second test scenario. 41
4.8 Third Test scenario. 42

5.1 Proposed drivetrain fault diagnosis algorithm by using torsional measurements and estimated modes. 48
5.2 Simulation results of estimating drivetrain torsional natural frequencies based on DTU 10 MW model 53
5.3 Estimation of natural frequencies by using gearbox 2^{nd} stage error function. 53
5.4 Modal analysis based on Vestas 1.75 MW drivetrain torsional response. 55
5.5 Simulation results of stiffness-related faults based on DTU 10 MW model. 60
5.6 Simulation results of inertia-related faults based on DTU 10 MW model. 62

5.7 Experimental results of stiffness-related faults based on Vestas 1.75 MW drivetrain operational data. 64

6.1 Proposed algorithm for estimation of drivetrain ROM model . . 72
6.2 Estimated ROM model parameters of DTU 10 MW drivetrain, by using the actual aerodynamic torque. 75
6.3 Estimated ROM parameters of DTU 10 MW drivetrain, by using the estimated aerodynamic torque. 77
6.4 Estimated ROM model parameters of DTU 10 MW drivetrain in different fault scenarios. 79
6.5 Real-time torque on the main shaft of DTU 10 MW drivetrain model. 83
6.6 Real-time equivalent von Mises stress on the main shaft of DTU 10 MW drivetrain model. 85
6.7 Estimated input and output torques at NREL 5 MW gearbox stages. 87
6.8 Validation of estimated sun-planet contact stress of the 2^{nd} stage of gearbox in NREL 5 MW drivetrain. 88
6.9 Algorithm for estimation of main and high-speed shafts RUL. . 91

Chapter 1

Introduction

1.1 Background & motivation

The increase of Europe's offshore wind capacity from its current level of 12 GW to 60 GW (5 fold) by 2030 and 300 GW (25 fold) by 2050 is presented by the European Commission as a part of the European Union's (EU) planned strategy to meet the EU's goal of climate neutrality by 2050 [1]. There have been about 84 MW of floating wind turbines (FWT) installed worldwide at the end of 2019. Globally there are over 7000 MW of FWT in planning and permitting phases of development, with the first commercial-scale project expected to be operational in 2024 [2]. However, there are yet very limited experiences with floating wind turbines to estimate the actual operational expenditure (OPEX). The overall risk of loss of turbine is expected to be higher in FWT mainly because of higher power ranges, larger components and being exposed to wider range of excitation frequencies. Based on a report published by the National Renewable Energy Laboratory (NREL), the levelized cost of energy (LCOE) of FWT will reach the same level with land-based turbines, and technological innovations in maintenance strategies based on condition-based maintenance is emphasized as a significant contributor [2]. According to the study performed by Ioannou *et al.* [3], the proportion of OPEX expenses to the total costs in offshore wind turbines are in average twice more than the land-based wind turbines. In this between, the reduced availability of offshore turbines due to longer downtime caused by first more difficulty in access to offshore assets and second the utilization of larger components to realize the higher power ranges play a significant role. Dynamic asset management by using preventive condition-based maintenance techniques to optimize the scheduled maintenance intervals based on monitoring the operating states of the critical components is considered as an effective solution

to flatten the gap between OPEX in offshore and land-based wind turbines.

The drivetrain system including rotor, shafts, main bearings, gearbox, generator and power converter accounts for 57% of turbine total failures and 65% of turbine total downtime [4], which shows a high potential in reduction of OPEX by applying innovative condition monitoring strategies to the drivetrain system.

The motivation of this research is improving the availability of drivetrain system of future large FWTs by applying innovative condition-based maintenance approaches which are computationally inexpensive, are able to detect the drivetrain system faults in early stages, and can estimate the residual life of the drivetrain components near real-time.

Condition-based and predictive maintenance types are the subcategories of preventive maintenance strategies, aimed at reducing downtime and optimizing resources by performing maintenance when it is needed [5]. In condition-based approaches, maintenance is initiated when a condition variable approaches or passes a threshold value. Predictive maintenance offers a higher level functionality by combining the fault detection algorithm with precise algorithmic formulas to predict the exact moment when a maintenance action should be taken.

Condition monitoring in this thesis context means fault diagnosis and prognosis activities including the estimation of remaining useful lifetime (RUL).

1.2 Drivetrain basics and available technologies

In the definition of drivetrain in this thesis, this system consists of all the components of the wind turbine rotary system and the related controller. On this basis, the drivetrain system consists of prime mover/rotor, main bearing/bearings, main shaft, gearbox, high-speed shaft, generator and power converter system.

A review of the different drivetrain technologies for different ranges of power and application (onshore/offshore) is performed by Moghadam and Nejad [6] in paper 1. A brief overview of the commercialized wind turbines (see Table 1.1) and the reference turbines developed by research institutions and universities [7, 8] shows a unanimous interest in PMSG for high-power offshore wind turbine drivetrain systems. According to [9], a higher efficiency due to external excitation circuit removal; higher reliability and availability, and less maintenance costs due to the compactness and lightweight design and brushes elimination are the motivations for choosing permanent magnet synchronous generator (PMSG) drivetrain technology in high-power offshore

wind turbine applications with the nominal power higher than 8 MW. For this reason, PMSG drivetrain technology is selected as the main case study of the drivetrain analyses in this research. However, the methods developed in this research for the drivetrain condition monitoring are not restricted by the drivetrain technology and configuration, so that they can be adjusted according to the drivetrain design for various applications.

PMSG-based drivetrain technology can be realized based on two different configurations, namely with and without gearbox. The gearbox in the wind turbine drivetrain can be based on different combinations of planetary and parallel gear stages aimed to realize different gear ratios. The frequency of the rotation of prime mover/rotor is far less than the frequency of the generated electrical power, and the gearbox is responsible to adjust/convert the lower speed of the prime mover to the proper speed level for the generator operation. In fact, in order to convert the variable frequency of the rotor to a regulated frequency of the generator output electrical power which is necessary for the synchronization of the wind farm with the power grid, three strategies are simultaneously used, which are the use of gearbox, the use of generator with a proper number of poles and the active control implemented by the power converter system. A tailored combination of these strategies can significantly influence the efficiency, weight and dimension of drivetrain, and subsequently the manufacturing and O&M costs. A comparison between different PMSG-based drivetrain configurations by taking into account the costs over the drivetrain life cycle is presented in Chapter 3. The drivetrain configuration which offers a better compromise between the criteria obliged by the life cycle assessment approach is selected as the main case study for the condition monitoring studies in this PhD thesis.

Table 1.1: Drivetrain most conventional technologies

HSSCIG	**HSDFIG**	**DDWRSG**	**MSWRSG**	**DDPMSG**	**MSPMSG**
SWT-4.0-130	GE 5.3-153	EN136-4.2	SCD 8.0/168	SG 14-222	V164-10
Siemens	General Electric	Envision	Aerodyn	Siemens	Vestas
4 MW	5.3 MW	4.2 MW	8 MW	14 MW	10 MW
Off-/onshore	Onshore	Off-/onshore	Offshore	Offshore	Offshore
Geared (1:119)	Geared (NA)	Direct-drive	Geared (1:27)	Direct-drive	Geared (1:38)
V136-4.2 MW	6.2M126	E-126 7.580	NA	GE Haliade-X 12	BW 14.xM225
Vestas	Senvion	Enercon	NA	General Electric	Bewind
4 MW	6.2 MW	7.6 MW	NA	12 MW	14 MW
Onshore	Offshore	Onshore	NA	Offshore	Offshore
Geared (NA)	Geared (1:97)	Direct-drive	NA	Direct-drive	Geared (NA)

1.3 Drivetrain failures

Functional failures and failure modes in the horizontal axis wind turbines including the drivetrain faults are summarized in [10] and [6] (paper 1). A basic failure modes study about the generator and gearbox in PMSG drivetrain systems is presented in Table 1.2.

Table 1.2: Basic failure modes study of PMSG drivetrain components [6] (paper 1)

PMSG ([11, 12, 13, 14])	**Gearbox ([15, 16])**
Possible faults	**Possible faults**
Mechanical faults	**Gear fault**
Blocking bearings	**Shaft fault**
Stucking filings in the air-gap	**Bearing fault**
Electrical faults	Shaft misalignment
Short circuit faults	Shaft bending
Finite resistance circuit faults	Shaft loose
Open circuit faults	**Housing fault**
Magnetic faults	**Fastener fault**
Demagnetization of rotor magnets	**Seal fault**
Detachment of rotor magnets	**Root causes**
Root causes	Underestimated design loads
Over current	Torque overloads
Voltage sags, swells and harmonics	Material defects
Cooling and lubrication system dysfunction	Manufacturing errors
Sensors and communication network dysfunction	Dirt in the lubricant or poor lubrication
Rotor torque oscillation by wave/wind induced moments	Damage during transportation and assembly
Electromagnetic torque oscillations	Misalignment of components in the shaft
Poor or contaminated bearing lubrication	**Failure modes**
Bearing installation problems	Gear wear, scuffing and contact fatigue (fatigue)
Failure modes	Gear plastic deform, crack, fracture, bending (ultimate/fatigue)
Stator winding insulation fail (fatigue, ultimate)	Bearing spalling: excessive load/poor lubrication (fatigue)
Demagnetization: magnet heating (ultimate)	Bear. smearing: foreign objects trapped within (fatigue)
Demagnetization: increased flux density (ultimate)	Bear. worn surface: skewed roller/lubrication (fatigue)
Phase/path cut-off (fatigue, ultimate)	Bear. partial chipping of rings/roller:excessive load (fatigue)
Stator tooth fretting damage/crack (fatigue/ultimate)	Bear. ring split/crack:excessive load/loose fit (fatigue)
Detached magnet:raised centrifugal forces (fatigue)	Bear. fretting corrosion:fluctuating load/lubrication (fatigue)
Bearing pitting and sanding (fatigue)	Bear. electrical pitting:sparks by electric current (fatigue)
Bearing brinelling/false brinelling (fatigue)	Bear. damaged retainer:heavy vibration/speed change (fatigue)

Drivetrain faults can be classified into two main categories of the faults in the electrical and mechanical components. Based on this classification, the faults in the permanent magnets and winding of the generator, and the faults in the power converter system (*e.g.* faulty power electronic switches, the capacitors of DC-link and grid filter) are considered as electric faults. However, the faults in the rotor blades and bearings, gearbox gears and bearings, generator bearings, shafts and couplings are considered as mechanical faults.

In this PhD thesis, the mechanical faults of the drivetrain system are focused. Drivetrain mechanical faults can also be classified into two categories of system- and component-level faults:

System-level faults are categorized into the faults which change the tor-

sional stiffness the most (*e.g.* crack in the shafts and bearing wear specially in gearbox), and faults which influence mostly the inertia of the drivetrain components (changes in mass balance/distribution which can be due to *e.g.* loss of mass, wear and unbalance; and also change in the axis of rotation which can be due to *e.g.* misalignment and looseness).

Component-level faults consist of faults in the subcomponents of the main drivetrain components. For example, faults in each bearing or gear of the gearbox, each bearing of the generator, each blade of the rotor or each of the main bearings are considered in this category.

The possibility of detecting the different classes of drivetrain mechanical faults, namely system- and component-level faults, by using different techniques which are based on vibration measurements are investigated in this thesis.

1.4 Available drivetrain performance and condition monitoring techniques

The fault diagnosis of the drivetrain components of the available wind turbines is mostly reliant on monitoring the performance of the individual components by using the variations in physical parameters *e.g.* temperature and pressure. The latter is supported by condition monitoring systems based on three-axial measurements of translational vibrations in the different places of the drivetrain to support an earlier stage component-level fault detection in the drivetrain.

The classical performance and condition monitoring of the drivetrain is performed by analyzing one or a combination of different types of measurements by using several techniques to create a feature space for fault diagnosis and prognosis purposes [17], namely vibration analysis [18, 19], electrical signature (currents, voltages and power signals) [20], acoustic emissions analysis [21], thermography [22] and temperature analysis [23], oil pressure and analysis of oil particles [24].

The focus of this PhD research is the drivetrain condition monitoring by using the vibration measurements including both torsional and translational vibrations, by leveraging the combination of physical models and data-driven approaches.

1.5 Aims and scope

This thesis is written as the summary of papers, including two published journal articles, a published conference article, and three submitted journal articles, as attached in the Appendix. One paper is under preparation and thus has not been included in this thesis. The scope of the thesis is shown in Figure 1.1 where the main topics and the interconnections between the appended papers and chapters are demonstrated.

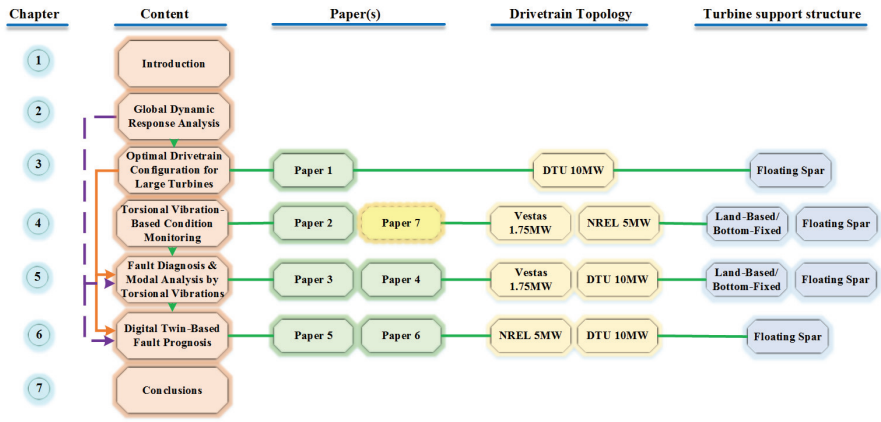

Figure 1.1: Relations between the appended papers and the thesis chapters.

As discussed earlier, available drivetrain health monitoring solutions do not sufficiently address the needs of future FWT. We need approaches which can more efficiently capture the internal dynamics of the drivetrain system and the interactions with the loads and the rest of turbine and power grid, which calls for the employment of innovations in the drivetrain condition monitoring solutions. Therefore, the main purpose of this thesis is proposing innovative and cost effective condition monitoring approaches mainly based on the drivetrain torsional vibrations for improving the availability of future FWT. The proposed methods are computationally fast, simple to implement, and can be integrated into the available control and monitoring system of both turbine and farm levels. This goal is achieved by the realization of the following procedure:

The evaluation of different available drivetrain topologies for high power FWT applications over the drivetrain life cycle by considering simultaneously the design, manufacturing, installation and operation & maintenance costs is investigated in *paper1*. The outcome determines the drivetrain configuration

and dimensions for further studies which are focused on fault diagnosis and prognosis of the drivetrain system and components.

A data-driven drivetrain condition monitoring approach based on translational vibrations by assuming the drivetrain vibration measurement set as a Gaussian Markov random field (GMRF) is discussed in *paper 7*. The drivetrain condition monitoring by time and frequency domain analyses of angular velocity residual function as the drivetrain torsional response, and its performance compared to the conventional approaches based on analysis of lateral and axial vibrations are discussed in *paper 2*. The possibility of using torsional response for estimation of the drivetrain torsional modes is explained in *paper 3*. The analytical proof of the drivetrain modal estimation by using the torsional response, and the design of an analytical approach to detect the drivetrain system-level faults by monitoring the variations in the dynamic properties of the drivetrain over the time are presented in *paper 4*. The fault detection approach combines a data-driven approach to estimate the dynamic properties from operational torsional measurements, and a physics-based approach for extracting fault detection features and defining thresholds based on analysing the analytical relationship between the variations of the physical system and the variations of the system dynamics, so that the result can be quantified into different states of a progressive faults to determine the state/condition of the system.

The other perspective of condition-based maintenance is predicting the system faults by estimating the residual life of the system components. In order to achieve this purpose as the main goal of this PhD project, a digital twin modelling approach for estimating the near real-time value of load in the different components of the drivetrain by using the drivetrain torsional measurements, and the subsequent use of estimated loads for estimating the equivalent stress and then the fatigue damage in the drivetrain components are discussed. The application of proposed digital twin model as the combination of the drivetrain near real-time estimated equivalent model, online measurements and the degradation model, for monitoring the RUL of the gears is discussed in *paper 5*. The application of the digital twin model for estimating the residual life of the main shaft while addressing the different sources of uncertainty by using statistical approaches and stochastic models is studied in *paper 6*. The proposed digital twin model is presented in the general form, so that it can be adjusted and used for the residual life monitoring of different drivetrain components.

1.6 Thesis outline

The chapters are structured in the same sequence as one carries out the wind turbine drivetrain condition monitoring analysis. A brief description of each chapter is provided as follows:

Chapter 1:
This chapter includes introduction, background, motivations, aim and scope and outline of the thesis. The brief review of the common drivetrain technologies of large FWT, the different categories of drivetrain failures, and the available solutions of drivetrain performance and condition monitoring is performed.

Chapter 2:

Wind turbine global analysis and drivetrain decoupled simulation approach are discussed in this chapter. The drivetrain loads which are estimated from the global simulations play the role as inputs applied to the drivetrain model used for the drivetrain studies of *papers 1, 3, 4, 5, 6 and 7*.

Chapter 3:

In this chapter, different PMSG-based drivetrain configurations are described, and the pros and cons of each configuration over the drivetrain life cycle are discussed. This chapter covers the main results of *paper 1* with the main focus on the optimization of drivetrain in a life cycle perspective in both system and component levels to obtain the most promising PMSG-based drivetrain configuration for future high-power FWT by considering simultaneously the design, manufacturing, installation and operation and maintenance (O&M). The design specifications of the different PMSG-based drivetrain configurations are presented. The medium-speed PMSG drivetrain topology selected in this study is considered as the main simulation case used throughout this thesis, and used as the drivetrain model in *papers 3, 4 and 6*. *The main contribution* of this chapter is establishing a drivetrain system optimization approach which ensures an optimized overall cost, weight, size, and improved efficiency and reliability.

Chapter 4:

The classification of different vibration-based condition monitoring ap-

proaches is presented in this chapter. The literature of vibration-based condition monitoring grounded on translational vibrations obtained by accelerometers by using both physics-based and data-driven approaches is reviewed. The condition monitoring based on translational vibrations is used as a baseline to validate the condition monitoring methods developed in *papers 2, 3, 4, 5, 6 and 7*. The performance of a novel data-driven statistical learning-based condition monitoring approach grounded on translational vibrations compared to the conventional time-domain approaches is evaluated. Then as a separate part in this chapter, drivetrain innovative condition monitoring techniques based on monitoring the torsional vibrations are introduced. The performance of condition monitoring by the time and frequency domains analysis of torsional vibrations and their residual functions is demonstrated and compared to the case of using lateral and axial vibrations, so that the complementary role of torsional vibrations to the available approaches is demonstrated. It is shown that how torsional measurements can provide better understanding about the excitation sources, which can be used for finding the root cause of different drivetrain failures and also to support the detection of faults in an earlier stage. The test case used for the experimental studies is Vestas V66-1.750MW high-speed drivetrain technology. This chapter covers the main results of *papers 2 and 7*. The torsional vibrations are then investigated in more detail in *papers 3, 4, 5 and 6*. *The main contributions* of this chapter are: *first* developing a drivetrain fault diagnosis method at component level based on the translational vibrations by using the combination of physics-based and data-driven approaches, and monitoring the variations of drivetrain statistical properties; and *second* classifying the different sources of excitation in drivetrain condition monitoring analyses and proposing the efficient vibration-based diagnosis solutions based on the source of excitation

Chapter 5:

This chapter performs a more detailed investigation of the drivetrain torsional vibration response. A drivetrain fault diagnosis algorithm by using the torsional vibrations based on the estimation of drivetrain dynamical properties from the preprocessed torsional measurements is discussed. An analytical model which defines the logical relationship between the drivetrain faults at system level and the variations of drivetrain dynamic properties is presented. The test case used for the simulation studies of this chapter is DTU 10 MW medium-speed drivetrain. The test case for the experimental studies is Vestas V66-1.750MW high-speed drivetrain technology. This

chapter covers the main results of *papers 3 and 4*. *The main contributions* of this chapter are: *first* designing methods for drivetrain modal analysis by means of torsional vibrations; and *second* designing methods for drivetrain fault diagnosis at both system and component levels based on monitoring the variations of the drivetrain dynamic properties.

Chapter 6:

This chapter investigates in more detail the innovative drivetrain condition monitoring based on the torsional measurements but for a higher level purpose which is the online estimation of the RUL of the drivetrain components. The application of digital twin as the combination of equivalent reduced-order model, online measurements and RUL model to support the predictive maintenance of the drivetrain system is discussed, and the proposed algorithm for the near real-time estimation of drivetrain equivalent model parameters by using the torsional measurements is explained. The test cases for simulation studies of this chapter are DTU 10 MW medium-speed and NREL 5 MW high-speed PMSG-based drivetrain technologies. This chapter covers the main results of *papers 5 and 6*. *The main contributions* of this chapter are: *first* establishing the digital twin approach for fault prognosis of the drivetrain components by using the drivetrain torsional measurements; and *second* designing a robust and computationally fast method for estimating the parameters of drivetrain equivalent models of different degrees of complexity by using the torsional measurements, for fault diagnosis and prognosis applications.

Chapter 7:
This chapter includes the conclusions made by this PhD project, the original contributions of the work and the recommendations for future researches.

Chapter 2

Global dynamic response analysis

2.1 General

Accurate and computationally inexpensive models for modelling faults and analyzing the system behavior under fault conditions are highly demanded by offshore wind industry where faults can be extremely costly [25]. The simulation-based condition monitoring study of the drivetrain system of a spar floating wind turbine concerns modelling of turbine including drivetrain, tower, support substructure and environmental loads. This model should be able to capture the global dynamics of spar FWT from the interactions with the environmental loads and determine the influences on the drivetrain loads and motions. To this target, there are some challenges of using the coupled models for two main reasons: *First*, the weakness of simulation tools in modelling such a complex dynamical system with various loads, components dynamics and uncertainties; *Second*, the high computational complexity of such huge dynamical model in which the simulation time step should be small enough to capture the very fast dynamics of the drivetrain components (*e.g.* those related to the gears and bearings of the high-speed side) with the defect frequencies pretty higher than the frequencies of the other turbine components. The decoupled simulation-based analysis of the turbine and drivetrain is an alternative to coupled simulations, which is proposed in literature to cope with the aforedescribed challenges. Nejad *et al.* [26] reports the successful use of a decoupled simulation approach for estimating load effects and subsequently the fatigue damage of the drivetrain components. The procedure for estimating the drivetrain loads from the global simulations and then applying them to a decoupled drivetrain model

to estimate the load effects and responses of the gears of the drivetrain gearbox is summarized in Figure 2.1.

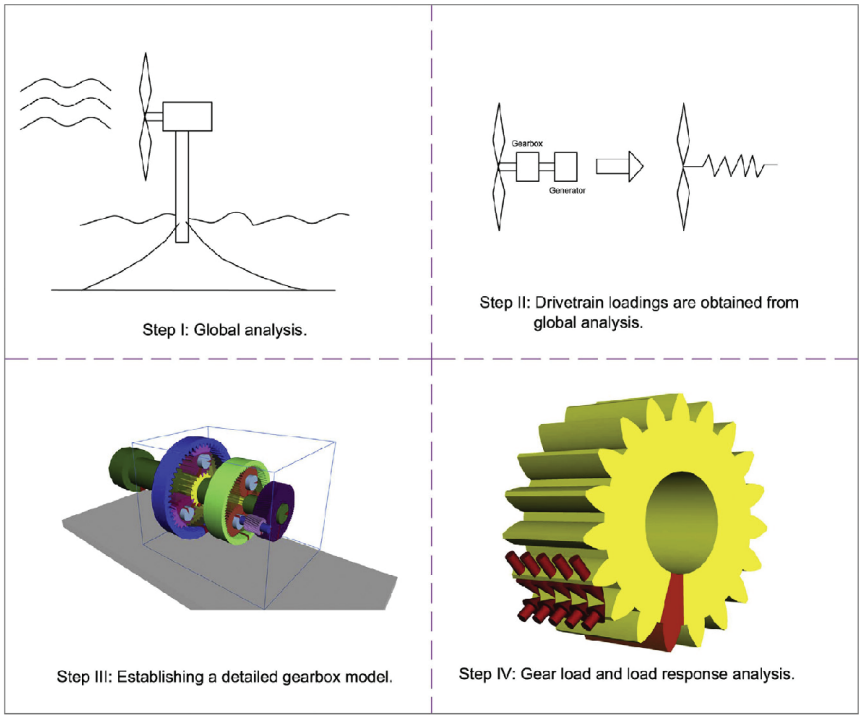

Figure 2.1: Decoupled simulation approach for wind turbine drivetrain analysis [26].

2.2 Decoupled analysis approach

The decoupled analysis approach is used for the drivetrain studies in this work. The latter means that the rotor aerodynamic loads and the bed-plate motions obtained from turbine global simulation study are applied to a decoupled detailed model of drivetrain in a secondary software. Then the drivetrain components load effects and responses are calculated for post processing analysis aimed at condition monitoring of the drivetrain system components. The implementation of decoupled simulation approach consists of two steps:

In the first step, global simulation analysis in different environmental

conditions is performed. In the global simulation, the blades and hub assembly, the structural module including the flexible multi-body systems for tower and platform including the floating support substructure and the nacelle are modelled. This model is coping with combined aerodynamic and hydrodynamic loads by using probabilistic numerical models of wind, waves and current in the global simulation software to capture the integrated and synergistic effects of the environmental loads and the wind turbine control system on the turbine components. The results of the global simulation are the load effects in the different parts of turbine, which contain the information about the interactions between the turbine subsystems. The latter includes the loads and motions transferred from the rotor and structure to the drivetrain described by the time series of the resultant moments and forces on the rotor, tower top accelerations, bed-plate motions and other responses of interest.

In the second step of the decoupled analysis, the calculated rotor aerodynamic torque and the responses of interest estimated from the global simulation are applied as the input to a decoupled offline drivetrain model in another simulation software suitable for multiple physics modelling and analysis of rotating machinery to calculate and analyse the drivetrain components load effects and responses. Then the results are used for post processing analyses aimed at health monitoring the drivetrain at component and system levels.

Decoupled simulation models are computationally faster than coupled/co-simulation models, where the sampling frequency for each decoupled simulation model can be decided based on the type of analysis and the physical properties of system. Decoupled analysis approach is employed for all the drivetrain studies in this thesis. The decoupled approach is used by Moghadam and Nejad in paper 1 [6] aimed at optimizing the drivetrain system by the analysis of torsional dynamics in the different drivetrain topologies, in papers 3 and 4 [27, 28] focused on modal analysis and fault diagnosis in the drivetrain system, and the researches conducted in papers 5 and 6 [29, 30] on the estimation of the remaining useful lifetime of the drivetrain system components.

2.3 Test cases

Two different wind turbine models are applied to the drivetrain simulation-based studies of this thesis, namely DTU 10 MW and NREL 5 MW turbine models, which are equipped with spar floating support substructures.

DTU 10 MW reference wind turbine [7] with a spar floating support sub-

structure is the main test case. The wind turbine specification and the overall characteristics of the floating platform is obtained from [7] and [31]. The drivetrain system is a medium-speed permanent magnet synchronous generator technology based on the gearbox and generator design specifications reported by Moghadam and Nejad (paper 1) [6]. DTU 10 MW global simulation model is simulated in SIMA global simulation software, a simulation and analysis tool developed by SINTEF Ocean [32]. SIMA is the updated version of SIMO-RIFLEX-AeroDyn global simulation software [33], which includes SIMO-RIFLEX, and an updated aerodynamics module which is not the same as AeroDyn. The global simulation results are applied as input to the drivetrain model for the condition monitoring studies as reported in papers 3, 4 and 6 [27, 28, 30].

NREL 5 MW reference wind turbine [34] with a spar floating support substructure is selected as the second case study. The wind turbine specification and the overall characteristics of the floating platform is obtained from [35]. This model is able to capture the global dynamics of spar FWT from the interactions with the environmental loads and turbine control. NREL 5 MW global simulation is performed by SIMO-RIFLEX-AeroDyn [33]. The 5 MW reference drivetrain [36] is employed as the drivetrain configuration in this test case. The results are applied as input to the drivetrain condition monitoring studies performed by Moghadam *et al.* [29] in paper 5, and Moghadam and Nejad in paper 7 [37], respectively aimed at the real-time estimation of the residual life of the gears in 5 MW drivetrain system gearbox, and the data-driven diagnosis of faults in the drivetrain components including the bearings, gears and shafts.

For all these test cases, the wind flow in the global simulations is assumed turbulent, assuming a Kaimal spectrum for IEC61400-1 class B turbines [38] and a normal turbulence model. The turbulence intensity at hub height $I\,(-)$ depending on the average wind speed at hub height, is obtained according to IEC 61400-1 class B turbines [38]. The wave is also modelled stochastic by two parameters, namely significant wave height $H_s\,(m)$ and peak period $T_p\,(s)$. For 10 MW simulations, four different environmental conditions are simulated to realize the drivetrain different operating conditions including near rated, over rated and under rated operations, as it can be found in papers 1, 3, 4 and 6 [6, 27, 28, 30]. For 5 MW simulations, one environmental condition to realize the drivetrain near rated operation is considered [29].

The rotor torques obtained from global simulation models of both 10 MW and 5 MW, which are related to the operation of turbines near the rated condition, are shown in Figure 2.2.

In the DTU 10 MW rotor torque shown in Figure 2.2a the average wind

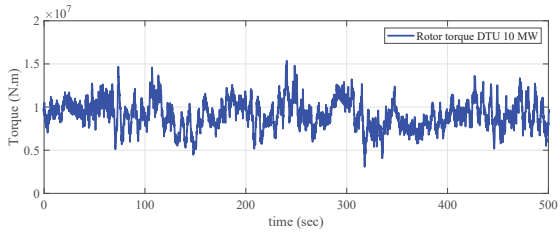

(a) DTU 10 MW

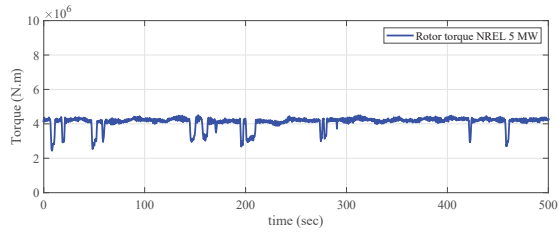

(b) NREL 5 MW

Figure 2.2: Rotor torque obtained from global simulation models, near the rated wind speed (a) DTU 10 MW equipped with spar floating substructure, (b) NREL 5 MW equipped with spar floating substructure.

speed is 11 m/s which is a little lower than the nominal speed (11.6 m/s). In the below rated wind speed, there is only torque control and not any blade pitch, but since the mean wind speed is very close to rated, it will also use pitch control sometimes during the simulation (when the turbulent wind speed comes over rated). The case is similar for the 5 MW model (as shown in Figure 2.2b), where the rotor torque is similarly obtained from the turbine operation near the rated condition. One reason for that the torques obtained from these two models look qualitatively different for these two spar floaters could be the chosen control strategy above rated for the torque controller. In practice, there are two choices, either "constant torque" control strategy (always keep the torque equal to the rated torque for above the rated wind) or "constant power" control strategy (it varies the torque such that the power is always equal to the rated power for above the rated wind, which can cause higher oscillations of the torque). The 10 MW model uses constant power control strategy (which leads to higher torque oscillations), while the 5 MW model uses constant torque strategy. In this case, the dips in the 5 MW model torque curve would then occur when the wind speed drops below rated, and it can no longer keep rated torque, but will change it according to the torque

versus speed control region.

There is another difference between 5 and 10 MW models, which could contribute to the difference between the calculated torques. The demonstrated 10 MW torque shows the pure aerodynamic torque. There is the aerodynamic inertia in the model, but it does not include the rotor inertia. For the 5 MW model, the rotor inertia is included in the model. Modeling the rotor inertia in 5 MW model is the other factor which contributes to the smoother torque observed in this model compared to 10 MW model.

Chapter 3

Optimal drivetrain configuration for large turbines

3.1 General

This chapter compares different drivetrain configurations based on permanent magnet synchronous generator technology to realize the drivetrain system of 10 MW FWT. The advantages and drawbacks of each configuration are discussed. The drivetrain optimization is mostly studied in literature in a component level [39, 40] perspective. The drivetrain optimization in system level for lower power ranges (upto 5 MW) is studied by considering the cost of raw material of both the generator and gearbox as the objective function by [41]. Moghadam and Nejad [6] (paper 1) study the drivetrain optimization for DTU 10 MW turbine with a spar floating support substructure in a life cycle perspective in the system level by simultaneously taking into consideration multiple costs, namely the design and manufacturing, installations process and O&M costs, so that the different drivetrain system configurations based on PMSG, namely direct-drive (DDPMSG), medium-speed (MSPMSG) and high-speed (HSPMSG) drivetrains are studied by taking into account the aforementioned factors participating in the drivetrain costs.

The objective of this chapter is presenting the summary of the work in [6] (paper 1). In other words, the pros and cons of the different 10 MW PMSG drivetrain system configurations over the drivetrain life cycle are studied in this chapter, which is holistic and valuable. In this perspective, the optimal drivetrain system topology is the one which offers a better compromise be-

tween the raw material costs, construction efforts, installation costs, overall rated efficiency, power quality and system availability. The selected configuration should also make sure about the safe operation over the turbine speed range and leaving a safe margin between the system natural frequencies and the external/internal excitation frequencies with a significant energy to prevent resonances in the system.

The research contributions of this PhD work which are covered by this chapter are:

- The drivetrain cost optimization by using a life cycle assessment approach is introduced. Many researchers have done optimization, but we do in a life cycle perspective which is more holistic and valuable. A new analytical design approach is proposed for the optimized design of PMSG based on the optimization of the active material cost. An analytical design model of the gearbox is presented, and a new optimization approach is proposed to optimize the gearbox weight. A comprehensive comparison between the design, raw material cost, weight, size, efficiency and reliability of DDPMSG, MSPMSG and HSPMSG drivetrain technologies is presented. The first torsional natural frequency of the three under consideration PMSG-based drivetrain configurations is calculated, and the feasibility of application in floating offshore wind turbines is investigated.

3.2 Life cycle optimization

The drivetrain life cycle assessment approach and the part of cycle which is emphasized for the optimized drivetrain design in this thesis is demonstrated in Figure 3.1.

Design concerns the complexities of design, maximal design utilization and higher degree of adaptation to site-specific conditions, reliability and controllability. It is important to know that the most of failure modes can be rooted back to design stage. Reliability-based design is concerned with drivetrain design considering failure modes to ensure a safe and reliable operation over the operating speed and torque range [42], while the failure modes depend on the drivetrain technology [6] (paper 1). As a design study in the drivetrain life cycle-based analysis, the first torsional natural frequency of the three different under consideration PMSG-based drivetrain systems is studied, and the feasibility of using these configurations in floating platforms is investigated by performing a study about the possibility of resonance due to the coincidence of the drivetrain natural frequency with the excitation frequencies.

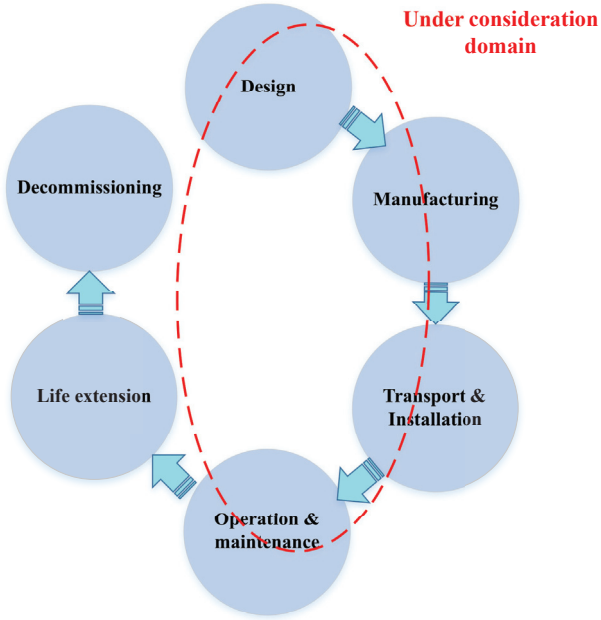

Figure 3.1: Drivetrain life cycle assessment approach [6].

In *manufacturing and installation*, weight, compactness, and special manufacturing and installation requirements are emphasized. An example of more manufacturing efforts is the construction process of DDPMSG, where the high pole count causes small rotor poles with fine stator slotting which makes manufacturing more expensive. In installation efforts, for instance, a less weight drivetrain configuration and the resultant reduced weight nacelle and tower could help to reduce the transportation and craning requirements. The minimization of weight, raw material cost and size of the under consideration drivetrain configurations are among the main objectives addressed in the drivetrain system optimization problem in this thesis, which provides the necessary inputs for further studies about the manufacturing and installation costs.

Operation and maintenance (O&M) is concerned with performance, efficiency, reliability, availability and maintenance costs. In *performance*, the output power quality of the generator is concentrated, where the generator technology and the power frequency converter play a significant role. In *efficiency*, improving the efficiency of drivetrain system is emphasized to specify

which technology and configuration can offer a greater efficiency, which can contribute in the reduction of the cost of energy. For this purpose, the efficiency of all the individual components of the drivetrain system should be taken into consideration. Then the overall efficiency of the different drivetrain systems in the rated power is calculated and compared. In reliability, the failure rates of different drivetrain components and the critical failure modes of the different configurations should be analyzed. Therefore, the failure modes of the subcomponents must be listed, so that the components and subsequently the drivetrain systems could be ranked from the highest to the lowest probability of failure (POF) regarding the most critical failure modes. In availability, the downtime of the unit consisting of the downtime of both scheduled and unscheduled maintenance operations, due to the different failure modes of the drivetrain components are studied. In order to maintain the tip speed ratio (TSR) of larger rotors in higher powers to achieve the highest value of power coefficient, the nominal rotational speed of rotor is reduced. The latter causes different drivetrain dynamic behaviors in the wind turbines of the same technology but different rated powers. Moreover, floating support substructures encounter turbines into different motions induced by the synergistic impacts of wind, wave, and the gravity of turbine on the floater. The lower rotor speed, more diverse excitation frequencies and higher amplitude excitations necessitate a special O&M study for the drivetrain in high-power floating applications. For the under consideration PMSG-based drivetrain topologies, the overall efficiency is calculated and compared considering the efficiency of the individual components, where the efficiency of individual components are seen in the local component-level optimization problems. As a reliability analysis, the failure modes, the defect frequencies and the possibility of coincidence of these frequencies with the excitation frequencies and the system natural frequencies are investigated, while the component level constraints are also imposed to the local problems to mitigate loads and improve the operation. The failure modes affected by the rotor torque and generator electromagnetic torque oscillations in the three under consideration configurations are also discussed and compared. Unequal values of generator cogging torque and frequencies of occurrence in the under consideration drivetrain configurations also influences the different torsional vibration behaviors.

3.3 Drivetrain optimization approach

The three under consideration configurations are listed in Table 3.1. These topologies are selected by taking into consideration the available drivetrain

configurations close to the turbine rated power selected in this research.

Table 3.1: Case study technologies

Topology	Rated power (MW)	Application	Generator	Gearbox
Type 1 (DDPMSG)	10	floating	PMSG	direct-drive
Type 2 (MSPMSG)	10	floating	PMSG	planetary-planetary-parallel (1:50)
Type 3 (MSPMSG)	10	floating	PMSG	three-planetaries (1:50)
Type 4 (HSPMSG)	10	floating	PMSG	three-planetaries (1:156)

3.3.1 Algorithm

The proposed drivetrain optimized design algorithm is summarized in the flowchart in Figure 3.2.

The gearbox affects both the input torque and speed of the generator, which are among the crucial parameters of the design of generator. The weight and size of generator is directly proportional to these two parameters. In each iteration of the proposed drivetrain system optimization approach, the gear-ratio is fixed by the outer loop. Therefore, the optimization problem of each drivetrain configuration is broken into two decoupled problems of optimized gearbox and generator designs. As a result, for each drivetrain topology (or, interchangeably, for each gear ratio), two internal component-level optimization problems are solved.

3.3.2 Generator optimization

Different objective functions with different sets of optimization variables are proposed in literature for the design of PMSG. Li *et al.* [41] tried to minimize the cost of active material, Dubois *et al.* [43] recommended the ratio of the cost of active material to the torque density, and Røkke *et al.* [14] proposed the minimization of the combination of the cost of the active materials (including the housing) and the cost of the lost energy in the machine over the PMSG lifetime. In this thesis, an analytical design based on the minimization of the ratio of the cost of active material to the torque density is employed to find the optimized design of the generator in each of the DDPMSG, MSPMSG and HSPMSG drivetrain configurations. The latter ensures the minimized cost while the electromagnetic (developed) torque density and utilization of the generator weight is maximized. The proposed analytical model represents the cost function and the design constraints as a function of five geometrical variables.

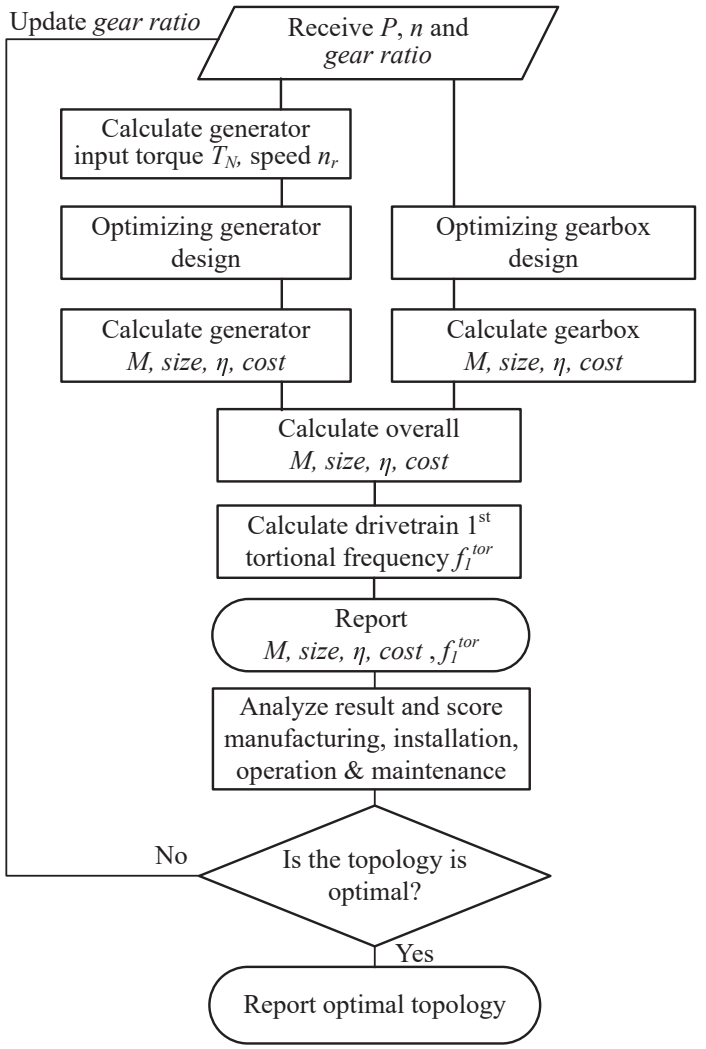

Figure 3.2: Proposed drivetrain optimization approach [6].

The generator optimization problem is defined by

$$\boldsymbol{x}^* = \arg\min_{\boldsymbol{x}} \left(\frac{cost_{active}(\boldsymbol{x})}{T_d(\boldsymbol{x})} \right), \tag{3.1a}$$

$$cost_{active}(\boldsymbol{x}) = cost_{fe}(\boldsymbol{x}) + cost_{cu}(\boldsymbol{x}) + cost_{pm}(\boldsymbol{x}), \tag{3.1b}$$

$$T_d(\boldsymbol{x}) = \frac{T_N}{V(\boldsymbol{x})}, \tag{3.1c}$$

where $\boldsymbol{x}$ is a vector which represents the optimization variables. $\boldsymbol{x}^*$ is called optimal, or a solution of the problem. $cost_{active}$ is the cost of active materials in generator construction in $Euro$. The cost of active materials consists of the cost of the iron used in rotor and stator yokes and stator teeth, the copper used in stator windings, and the surface mounted permanent magnets. $cost_{fe}$ is the total cost of iron, $cost_{cu}$ is the cost of copper, and $cost_{magnet}$ represents the cost of magnet material. T_N is the nominal torque in $kN.m$ and V is the generator active volume in m^3. T_d is the generator torque density in $kN.m/m^3$. The variables in equation 3.1 are defined by

$$\boldsymbol{x} = [x_1, x_2, x_3, x_4, x_5]^T = [D_s, L_s, b_s, h_s, h_m]^T, \tag{3.2a}$$

$$cost_{cu} = c_{cu} m_{cu}, \tag{3.2b}$$

$$cost_{pm} = c_{pm} m_{pm}, \tag{3.2c}$$

$$cost_{fe} = c_{fe} m_{fe}, \tag{3.2d}$$

$$V = \pi \frac{D_{so}^2}{4} L_e, \tag{3.2e}$$

The optimization problem variables D_s, L_s, b_s, h_s and h_m are respectively the air-gap diameter, active length of generator, slot width, slot height and magnet height. c_{fe}, m_{fe}, c_{cu}, m_{cu}, c_{pm} and m_{pm} are respectively the specific costs and total weights of core, copper and magnet. The design of surface mounted PMSG deals with the determination of a high number of variables related to the generator geometry and operation. In the proposed optimized design approach, it was observed that all the generator design variables can be either defined as a function of the five aforementioned geometrical optimization variables, or considered constant, or changed in optimization problem outer loops. The latter helps to turn the generally nonlinear and strongly nonconvex problem of PMSG optimized design to a convex problem to be able to find the global optimizer.

Equation 3.2 is used as the base model in the proposed PMSG analytical design approach by [6] aimed at optimizing PMSG design as discussed in more detail in paper 1.

3.3.3 Gearbox optimization

The gearbox design optimization objective function concerns the minimization of the cost of active material in gearbox by optimizing the stage gear ratios. The optimization problem to optimize a three-stages configuration of

the gearbox is defined by

$$\boldsymbol{u}^* = \arg\min_{\boldsymbol{u}} \Big(cost_{gear}(\boldsymbol{u}) \Big), \tag{3.3a}$$

$$cost_{gear}(\boldsymbol{u}) = cost_{stage1}(\boldsymbol{u}) + cost_{stage2}(\boldsymbol{u}) + cost_{stage3}(\boldsymbol{u}), \tag{3.3b}$$

where $\boldsymbol{u}$ is the vector of optimization variables. $\boldsymbol{u}^*$ is called optimal, or a solution of the problem. $cost_{gear}$ is the total raw material cost of the gears of gearbox stages in $Euro$. The variables of equation (3.3) are described as

$$\boldsymbol{u} = [u_1, u_2, u_3]^T, \tag{3.4a}$$

$$cost_{stage}^{planetary} = c_{gear} m_{gear}^{planetary}, \tag{3.4b}$$

$$cost_{stage}^{parallel} = c_{gear} m_{gear}^{parallel}, \tag{3.4c}$$

In the above equation, c_{gear} is the unit cost of the gears material, and $m_{gear}^{planetary}$ and $m_{gear}^{parallel}$ represent the weights of planetary and parallel stages, respectively, which are defined as the function of gearbox design optimization variables by using the model described in [36] as

$$m_{gear}^{planetary}(u) = \frac{2\rho_{fe} Q_S}{k} \Big(\frac{1}{B} + \frac{1}{B(\frac{u}{2} - 1)} + (\frac{u}{2} - 1) + (\frac{u}{2} - 1)^2 + k_r \frac{(u-1)^2}{B} + k_r \frac{(u-1)^2}{B(\frac{u}{2} - 1)} \Big), \tag{3.5a}$$

$$m_{gear}^{parallel}(u) = \frac{2\rho_{fe} Q_P}{k} (1 + \frac{1}{u} + u + u^2), \tag{3.5b}$$

In the above equation, Q_S and Q_P are the input torques applied to the sun and pinion of planetary and parallel stages, respectively. u is the gear-ratio, B is number of planets of the planetary stage, and k_r is ring scaling factor of the planetary stage. k is the intensity of tooth loads factor.

Equation 3.4 is used as the basis for the optimization of gearbox design studied in paper 1 [6], where a new method is proposed to solve the gearbox weight optimization problem. Even though the optimization problem shows a disciplined nonconvex problem, it demonstrates a convex behavior in the multi-dimensional graphical representation of the objective function and constraints in the defined range of variation of the optimization variables. Therefore, it is possible to find the global optimizer.

3.4 Comparison of different configurations

Drivetrain performance-based and reliability-oriented constraints are imposed to the generator and gearbox component-level optimization problems to ensure the feasibility of the generator and gearbox designs and a fair comparison between the under investigation drivetrain configurations. Finally, the designed drivetrain systems are compared concerning the total weight, cost, size, efficiency and dynamic behaviors.

The results of overall drivetrain weight, cost, efficiency and the first natural frequency for DDPMSG, MSPMSG and HSPMSG drivetrain configurations are summarized in Figures 3.3a-3.3c. The MSPMSG results are related to the MSMPSG configuration of type 2, which is realized based on planetary-planetary-parallel gear stages. As it can be seen, by moving from the direct-drive technology to the medium-speed, the drivetrain weight, raw material cost, efficiency and electromagnetic torque oscillations are significantly improved. A transition from the medium-speed to the high-speed generator still helps to slightly improve all the aforementioned properties.

A larger distance between the drivetrain natural frequency and the rotor torque oscillation frequencies which have a significant energy in the frequencies lower than 1 Hz is an advantage of lower speed generator technologies, where DDPMSG outperforms but HSPMSG falls behind the other configurations. However, the DDPMSG drivetrain with the higher value of first torsional frequency is more susceptible to the torsional vibration frequencies induced by the PMSG, especially seeing that there is no coupling between the generator and rotor to suppress the generator electromagnetic torque vibrations.

As it is discussed in more detail in paper 1 [6], the utilization of gearbox can result in a better dynamic performance and can reduce the possibility of resonance in the drivetrain due to the coincidence of the excitation frequencies which are induced by aerodynamic torque and electromagnetic torque, with the first drivetrain torsional frequency and the individual components defect frequencies, though new failure modes due to the presence of gearbox also appear in the geared drivetrain systems. It is shown that by considering the interactions between the drivetrain components, MSPMSG drievtrain topology can mitigate the influence of excitation sources on some failure modes of the generator and the main bearings while keeping a safe distance between the excitation frequencies and the drivetrain torsional frequency.

Therefore, the selection of drivetrain technology is a multidisciplinary task which needs to compromise between the criteria obliged by the life cycle assessment approach. With respect to weight, material cost, size, efficiency,

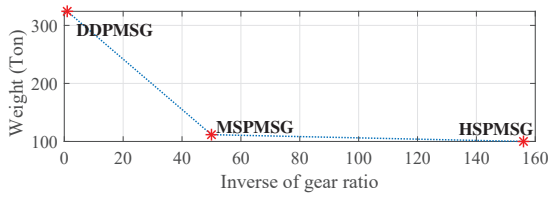

(a) Weight vs. α

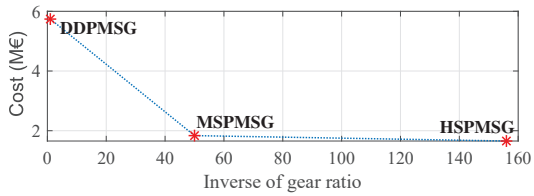

(b) Cost vs. α

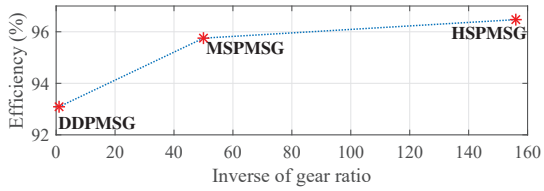

(c) Efficiency vs. α

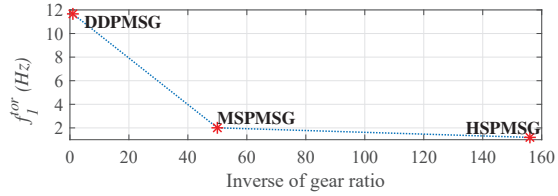

(d) Natural frequency vs. α

Figure 3.3: Comparison between different drivetrain topologies: DDPMSG, MSPMSG and HSPMSG [6] (paper 1)

possibility of resonances and failure modes analysis, MSPMSG can demonstrate a better compromise so that is selected as the main case study of the drivetrain condition monitoring studies in the rest of this PhD thesis.

Chapter 4

Physics-based and data-driven vibration-based condition monitoring

4.1 Literature review on vibration-based condition monitoring methods

The main condition monitoring technique used for fault diagnosis in gears and bearings of the wind turbine drivetrain is vibration analysis. The idea behind the vibration-based condition monitoring of drivetrain as a rotational system is that, generally speaking, the faults in rotational systems in later stages show themselves by increased vibration levels in the drivetrain components represented by the drivetrain vibrational responses, namely translational/torsional acceleration, velocity and displacement, though it may also depend on the location of fault and where the response is measured. Therefore, the act of exceeding the predefined limits of prespecified vibration signal features can be used as criterion to detect abnormalities in the system. Thanks to this general rule, there are guidelines presented in standards, *e.g.* ISO10816-21 [44], ISO 13379, ISO 13374 and ISO 13373-1 [45], for condition monitoring of rotating systems. Classical model-based feature extraction techniques as reviewed by [46] include classical time-domain analysis of the vibrations signals (*e.g.* RMS, energy, peak, average, kurtosis, skewness) [47, 48, 49], frequency-domain analysis (*e.g.* fast Fourier transform (FFT), auto- and cross power spectral density (PSD)) [50] and time-frequency-domain analysis (*e.g.* short-time Fourier transform (STFT), discrete wavelet transform, wavelet packet transform) [51, 52]. Those conven-

tional time and frequency domains methods are followed by more advanced data-driven time-domain approaches such as statistical learning- and artificial neural networks-based approaches, which are considered as the subcategories of artificial intelligence approaches. Statistical learning condition monitoring approaches are based on statistical interpretations obtained from the statistical analysis of the unexpected variations of the distribution fitting the measurements which can be supported by the graphical models of the sensors network data, so that abnormal variations from the multivariate distribution describing the correlations related to normal operations can represent defects in system. One common category of statistical learning approaches track the variations in the correlation of the data (*e.g.* the developed methods proposed by Moghadam and Nejad [37] in paper 7, and Zhang *et al.* in [53]) (including autocorrelation of each sensor data and cross correlation between the measurements of different sensors). The other category of artificial intelligence-based condition monitoring approaches are related to classification tools and feature extraction based on regression analysis, by using support vector machine and neural network techniques [54]. The combination of the different artificial intelligence techniques [55], and the combination of an artificial intelligence technique with classical time and frequency domain approaches [53, 51] are also reported in literature for condition monitoring of the drivetrain components of wind turbines.

There are controversies in applying the different categories of vibration-based condition monitoring approaches to wind turbine drivetrain systems. Standard time-domain approaches are commonly used by the industry for condition monitoring of the drivetrain components based on online/offline analysis of vibration data. They are mainly based on the RMS and peak values of acceleration, velocity and displacement. The applicability of these approaches is when the fault is in a severe condition so that it can result in a considerable amount of energy in different frequency components. In complex systems, it is a bit difficult to rely on this method as literature reports the insufficiency of classical time-domain solutions based on the wind turbine standard ISO10816-21 [44] and other generalized condition monitoring guidelines such as ISO 13379, ISO 13374, ISO 13373-1 [45], in the detection of drivetrain faults of the gears and bearings [25]. The other relevant challenges are in localizing and measuring the state of faults. The frequency-domain approaches based on monitoring the amplitude of response around the characteristic frequencies of the system including the resonance frequencies and the defect frequencies of the components associated to the different failure modes have been suggested in literature to support/improve the time-domain fault detection. The latter could support the fault diagnosis,

but there are still challenges. More specifically, some defects demonstrate nonlinear and complex frequency patterns which may not be possible to observe specially in complex systems like wind turbine drivetrain which includes many components with different dynamic behaviors. In other words, each component has different failure modes and defect frequencies, and fault in different stages of progress represent various frequency patterns in frequency spectrum of response with some similarities between the patterns of the different types of faults. External excitations induced by environmental loads, structural motions, generator and power grid cause also additional harmonics in the response which may not necessarily represent faults in the drivetrain system. The variable wind conditions and turbine operational speed change the characteristic frequencies of the drivetrain components, which can also make the frequency-based fault detection more challenging. Statistical approaches also rely on the assumption that the distribution and covariance matrix of the sensors network data are stationary which may not be realistic due to consistent variations in turbine operating conditions and loads. Then the variations of the parameters of the fitting multivariate distribution are monitored, and the role of each sensor measurements in the variations is measured. Some authors have suggested cyclostationary analysis methods to improve the accuracy of statistical approaches [56], whereas others have been investigating into different types of probability distributions to find the one which better describes the trend of data indicating the normal operations. Multi-sensor data fusion method based on deep convolutional neural networks is also proposed as another category of condition monitoring approaches based on the classification of data and the extract of features out of data. The latter is widely used in other areas such as in image processing applications, but is recently proposed for the detection and prediction of faults in the bearings and gears of the wind turbine drivetrain. In general, the lack of complete verification under complex operation scenarios and difficulty in generalizing the results for different sites and operating conditions are barriers for broad application of these techniques in industry.

There are also different attitudes in both preprocessing and post-processing of the data. Some researchers reported using frequency-domain filtering to cope with background noises, the revolution frequencies and some external excitation frequencies to increase the observability of the defect frequencies of the bearings and gears. Some others have proposed windowing [57] and time synchronous averaging [58] approaches in the time domain, which can improve the effectivity of frequency-domain tools to investigate into a specific failure mode of a subcomponent *e.g.* wear in a tooth of a gear or a rolling element of a roller bearing to support more detailed frequency domain studies.

Preprocessing of the measurements includes the algorithms to neutralize the influences of operational conditions due to the time-varying rotational speed and fluctuating loads. The procedure to compensate the time-varying rotational speed impacts on the measured data can be based on two different strategies, *i.e.* eliminating the corresponding side effect by using the order tracking algorithms and identifying the time-varying spectral components by time-frequency domain analysis [59], even though some negligence in compensating fast and large speed oscillations has been reported in literature. For example, in order to compensate load fluctuation effects on the planetary gear stages of wind turbine drivetrain, there are challenges to realize an efficient algorithm to eliminate the corresponding side effects. The available algorithms are usually designed for other applications than wind turbines (*e.g.* excavator and helicopter planetary gearbox fault diagnosis) with different system dynamics and loading conditions, which need to be developed and adjusted for the different wind turbines applications. The envelope technique of amplitude demodulation is also another preprocessing tool which is employed in some researches to reveal the defect frequencies in some defects which can appear in the amplitude of the vibration signal, [60] and [61] (paper 2). There are also different post-processing approaches to render the features obtained by analyzing data into meaningful conclusions about defects in the system. Post-processing involves the determination of fault sensitive and easy to implement features as the combination of extracted features in data processing step and setting suitable thresholds for the fused features. An effective approach is determining thresholds for the selected features by using the system analytical models supported by extensive simulations and observations. To this purpose, vibration-based condition monitoring of the drivetrain components (*e.g.* gears and bearings of the gearbox) can start from the specification of permissible stress and load due to the specific failure mode of the component, and then estimating the response as a result of applied permissible stress. Some challenges in the realization of this approach are the influences of different failure modes together on the measurements of a sensor in reality. The other threshold specification approach relies on statistical analyses mainly based on extensive observations of various fault cases, which calls for a large amount of data including different turbines and the drivetrain systems of the same type but in different operating conditions.

In the following two sections, drivetrain condition monitoring based on vibration measurements is investigated in more detail. *First*, a novel computationally-fast data-driven condition monitoring technique based on drivetrain translational vibrations is discussed, and the performance of this method in comparison with standard solutions is demonstrated. *Second*, innovative con-

dition monitoring solutions based on analyzing the drivetrain torsional vibration measurements are introduced and then compared with translation vibrations regarding the possibilities of detecting different types of faults by using those measurements.

The research contributions of this PhD work which are covered by this chapter are:

- A statistical learning approach based on the graphical model of drivetrain obtained from Lagrangian approach is proposed for fault detection in the wind turbine drivetrain components. Fulfilling Gaussian Markov Random Field (GMRF) properties in the drivetrain vibration measurements motivated using the features any graph in this field obeys, namely the stationarity of the inverse of covariance matrix in a GMRF and its conditional dependence properties are used to achieve a drivetrain computationally fast abnormality detection approach. The method is able to diagnose the faults that are not detectable by standard condition monitoring approaches. The latter is shown by both experimental and simulation studies.

- An experimental comparison between different available solutions for detecting drivetrain bearings and gears defects initiated by different sources of excitation is performed. Torsional vibrations residual function which is recently proposed in literature of vibration-based condition monitoring of wind turbine drivetrain is experimentally validated by time and frequency domain analysis of torsional versus translational vibrations. To this purpose, Different frequency-domain tools for detecting abnormalities in the drivetrain system, namely FFT, PSD and envelope PSD spectrums and analysis of the energy of the signal at the defect frequencies are employed experimentally by using operational measurements.

4.2 Data-driven condition monitoring based on translational vibrations

As an example of data-driven approaches based on artificial intelligence, the performance of an statistical learning-based approach developed grounded on the drivetrain physical model is discussed in the following. This approach is based on the correlation analysis of time-domain translational vibration measurements. Our extensive observations of both simulation and experimental data captured by translational accelerometers show that the vibration measurements of a rotating system follow a Gaussian distribution for

each turbine operational speed, [62] and [30] (paper 6). Therefore, the set of vibration measurements placed on the different locations of the drivetrain can model a multivariate Gaussian distribution. The other property of the set of vibration sensors in this system is that the measured response at each time step only depends on one previous step (characterized by the memoryless property of Markov processes), which supports the possibility to model the drivetrain vibration measurements network data as a Gaussian Markov random field (GMRF). Therefore, it is possible to take advantage of the rules that each data set in this field follows. One of these rules is that the covariance matrix of the measurements set stays uniform. By GMRF assumption, the centralized/global estimation of information matrix **J** - defined as the inverse of covariance matrix- of the drivetrain graphycal model represented by $\mathcal{G}(\mathcal{V},\mathcal{E})$ (where $\mathcal{V}$ models the node set ($\mathcal{V} = 1,2,...,v$) and $\mathcal{E}$ models the edge set ($\mathcal{E} = 1,2,...,e$)) turns to the simplified convex form as [63]

$$\hat{\mathrm{J}}^{Global}_{centralized} = \arg\min_{\mathrm{J}} tr(\mathrm{SJ}) - log(det(\mathrm{J})), \quad \text{subject to: } \mathrm{J}(i,j) = 0,\ \forall (i,j) \notin \mathcal{E},\ \mathrm{J} \geq \mathbf{0}, \tag{4.1}$$

which is based on the maximum likelihood (ML) principle. The estimate is chosen as the parameter that maximizes the log-likelihood function, which turns to the above minimization problem in terms of **J** as the optimization variable. **S** is the covariance matrix of the nodes data in the system graph. This optimization problem is solved iteratively subject to the equality constraints related to zero elements of the matrix which refer to the unconnected nodes specified by the drivetrain graphical model, which imposes sparsity on the inverse covariance. The inequality constraint is to force the positive definiteness to the optimization matrix variable to ensure the convexity of the problem to attain the global optimizer. Since the variations of drivetrain as a physical system can be monitored by tracking the deviations of autocorrelation and cross correlation of the vibration data time series, any variation in the covariance matrix and the role of each sensor can provide useful information about the variations of this system's physical properties which can represent faults. The inverse covariance, named information matrix can provide the conditional dependencies between the different nodes of the graphical model of drivetrain system. In other words, the zero non-diagonal elements of the adjacent information matrix of the drivetrain system graphical model represent the conditional independence of the data of the associated sensors. Therefore, since the graph of drivetrain is sparse, this sparsity can be imposed to the information matrix estimation problem to reduce the com-

putational complexity. The problem of inverse covariance estimation with a known graphical model is known a priori [63]. The sample covariance matrix of the vibration measurements is near singular (non–invertible); therefore, the ML estimation is used to obtain the information matrix. The graphical demonstration of the drivetrain is a physics-based model obtained from Lagrangian approach. By applying the Lagrange's equation to drive the equations of motion, the lumped model and then the equivalent graphical model of the drivetrain system is obtained. Figure 4.1 shows the graphical model of gearbox of NREL 5 MW drivetrain. In this physics-based graph, each node represents the moment of inertia of a drivetrain subsystem and the associated vibration sensor, and the edges model the stiffness between the subsystems. S_i, $i = (1,...,24)$ in Figure 4.1 represents the sensor which measures the acceleration on i^{th} inertia. The sparsity of the graph is imposed to the optimization problem defined by the equation 4.1 to reduce the computational complexity and improve accuracy of the ML estimation problem. The physical properties of the system inherited in the described graphical model help to derive a physics-based statistical learning approach to obtain a both simple and accurate drivetrain condition monitoring tool. In order to determine the role of each node/sensor in the discrepancy between the estimated information matrices of the normal and faulty operating cases, an anomaly score metric based on the relative entropy calculated by expected Kullback-Leibler (KL) divergence equation is employed [64], which uses a matrix partitioning to quantify the contribution of each node in discrepancy between the two different sets of information matrices. Anomaly score of the node i by using the information matrix $\mathbf{J}$ and the inverse of information matrix $\mathbf{J}^{-1}$ is calculated as

$$
\begin{aligned}
\mathbf{J}_1(i) &= \begin{bmatrix} L_{1[N_i\,N_i]} & l_{1[N_i\,i]} \\ l_{1\,[i\,N_i]}^T & \lambda_{1[i\,i]} \end{bmatrix}, \quad \mathbf{J}_1^{-1}(i) = \begin{bmatrix} W_{1[N_i\,N_i]} & w_{1[N_i\,i]} \\ w_{1\,[i\,N_i]}^T & \sigma_{1[i\,i]} \end{bmatrix}, \\
\mathbf{J}_2(i) &= \begin{bmatrix} L_{2[N_i\,N_i]} & l_{2[N_i\,i]} \\ l_{2\,[i\,N_i]}^T & \lambda_{2[i\,i]} \end{bmatrix}, \quad \mathbf{J}_2^{-1}(i) = \begin{bmatrix} W_{2[N_i\,N_i]} & w_{2[N_i\,i]} \\ w_{2\,[i\,N_i]}^T & \sigma_{2[i\,i]} \end{bmatrix}, \\
AS^1(i) &= w_1^T(l_2 - l_1) + \frac{1}{2}\{\frac{l_2^T W_1 l_2}{\lambda_2} - \frac{l_1^T W_1 l_1}{\lambda_1}\} + \frac{1}{2}\{\ln\frac{\lambda_1}{\lambda_2} - \sigma_1(\lambda_2 - \lambda_1)\}, \\
AS^2(i) &= w_2^T(l_1 - l_2) + \frac{1}{2}\{\frac{l_1^T W_2 l_1}{\lambda_1} - \frac{l_2^T W_2 l_2}{\lambda_2}\} + \frac{1}{2}\{\ln\frac{\lambda_2}{\lambda_1} - \sigma_2(\lambda_1 - \lambda_2)\}, \\
AS(i) &= max\{AS^1(i), AS^2(i)\} \quad ,
\end{aligned}
\tag{4.2}
$$

In the above equation, $\mathbf{J}_1$ and $\mathbf{J}_2$ are respectively the information matrices of normal and abnormal cases. N_i is defined as the set of neighbors of i^{th}

node, L, l, l^T and λ are the partitions of information matrix $\mathbf{J}$, and W, w, w^T and σ are the partitions of the inverse information matrix $\mathbf{J}^{-1}$.

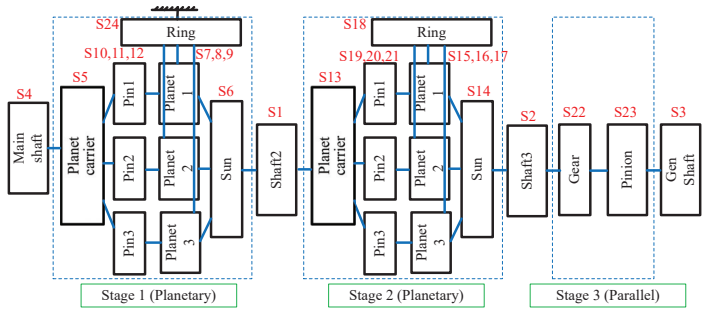

Figure 4.1: Graphical model of gearbox for NREL 5 MW drivetrain.

The described algorithm can be used for offline processing of the drivetrain logged data. It is also possible to implement the algorithm for real-time condition monitoring. In other words, it is possible to classify the operational rotor speeds and the average wind into different intervals, and then obtaining the information matrix of the normal operation for each interval of rotor speed and average wind variations. If the variations of information matrix of each interval is more than a prespecified threshold, an alarm is triggered. The threshold can be set empirically by looking into various sets of data associated with normal operations. In contrast to the other machine learning approaches, the proposed algorithm does not need a large volume of data so that by using few data samples with a moderate sampling frequency, it is possible to have a good estimation of information matrix to be used for monitoring the variations of system. This algorithm can be integrated with the turbine main control system where we can access both the rotor speed and the sufficient processing power to implement the method.

NREL 5 MW drivetrain is simulated in SIMPACK [36] to study the drivetrain dynamic response based on the model and the fault case shown in Figure 4.2. Damage in the radial direction of the high-speed shaft bearing (HS-A) is applied by changing the bearing stiffness in different directions in the model, as explained in [25]. The model is free to vibrate in translational and rotational directions, which can capture the vibrations of the bodies in XYZ directions. The observability of the under consideration fault by using the acceleration measurements of the different directions is shown in Figure 4.3. The fault is observable in all the three directions. By imposing the sparsity, computational complexity reduces to less than half while accuracy is maintained.

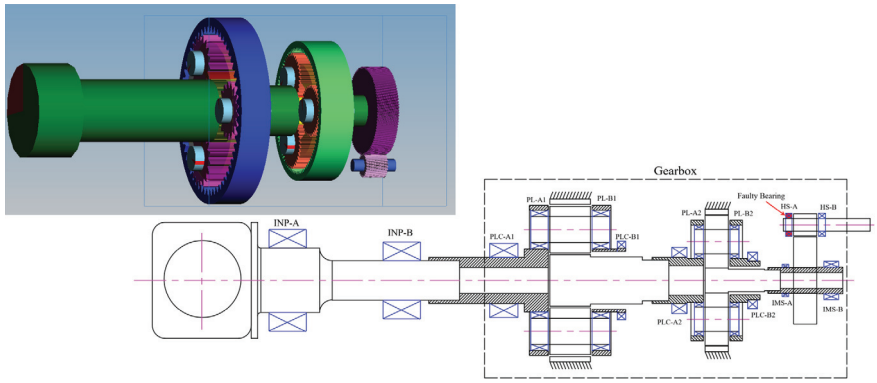

Figure 4.2: SIMPACK model and the fault case.

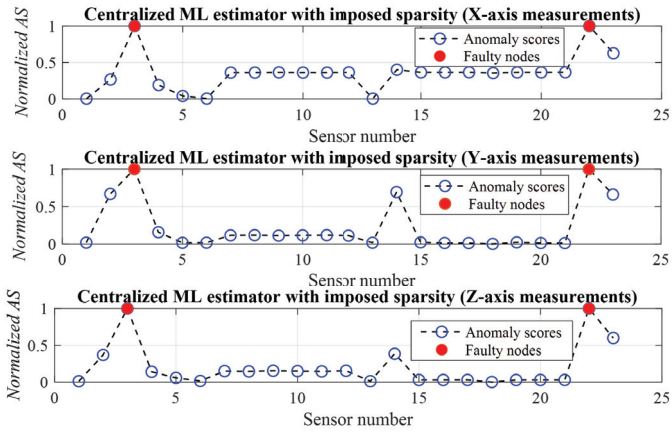

Figure 4.3: Observability of the bearing fault by using the acceleration measurements of different XYZ directions and the proposed data-driven approach.

In order to experimentally validate the proposed approach, the acceleration measurements of an operational Vestas V66-1.750MW turbine drivetrain are employed. The results of applying the algorithm to the lateral acceleration measurements of the Vestas turbine drivetrain to detect a fault in the main bearing (AC2) is shown in Figure 4.4, which shows the success of proposed approach in the diagnosis of the fault. The anomaly scores calculated for the other sensor nodes are also nonzero, because the data associated with those nodes are correlated with the data obtained from the faulty node.

In both the simulation study performed by NREL 5 MW drivetrain model

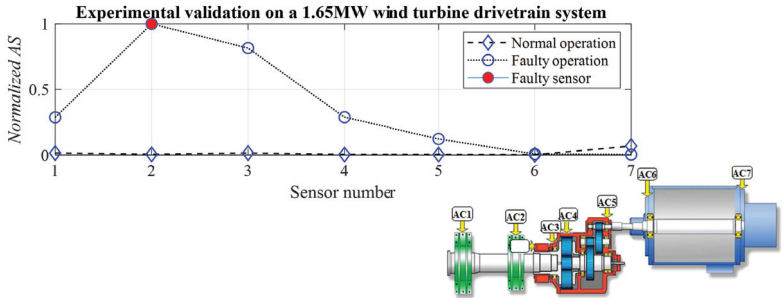

Figure 4.4: Experimental validation on Vestas 1.75 MW turbine.

in SIMPACK and the experimental study based on Vestas 1.750 MW operational turbine, the faults cannot be detected by the analysis of the RMS of the time series of translational acceleration based on the guideline presented in the standard ISO 10816-21 according to the operating speed.

4.3 Innovative condition monitoring by means of torsional vibrations

The rotational motion of the drivetrain system and the torsional nature of most drivetrain loads motivate the application of torsional vibrations for the condition monitoring of the drivetrain components. The latter can provide insight regarding the excitation sources, components defect frequencies and drivetrain system properties as the information which can support both design and condition monitoring of the drivetrain system. The frequency domain torsional vibration response of the equivalent 1-DOF damped rotational model of drivetrain influenced by the excitation source $\tau(t)$ in non-dimensional form can be described by

$$|\theta(\Omega)| = \frac{\frac{|\tau(\Omega)|}{k_t}}{\sqrt{(1-(\frac{\Omega}{\Omega_n})^2)^2 + (2\zeta_t^{\omega}(\frac{\Omega}{\Omega_n}))^2}}, \tag{4.3}$$

where $\theta(\Omega)$ and $\tau(\Omega)$ are the Fourier transforms of angular position and the excitation torque, respectively. Ω_n is the undamped torsional natural frequency of the system, k_t is the torsional stiffness of the shaft, and ζ_t is the torsional damping coefficient of the mode Ω_n at the operating speed ω.

Therefore, by the evaluation of the torsional response, it could be possible to find the response amplified harmonics excited by torsional excitation

frequencies, which can include the components defect frequencies and the system torsional natural frequencies.

4.3.1 Torsional responses error function

In the recent literature of vibration-based condition monitoring, the application of angular velocity measurements for condition monitoring of gearbox is proposed (*e.g.* by Nejad *et al.* in [25] and Sankar *et al.* in [65]). In [65], the power spectral density (PSD) of angular velocity measurements is used for the fault detection in a gearbox. In [25], the energy of the residuals of angular velocity measurements obtained from different places of a 5 MW high fidelity wind turbine drivetrain model is used for the gearbox fault detection.

The angular velocity residual function e^{ω}_{tot} between rotor and generator from the high-speed side is defined by [61] (paper 2)

$$e^{\omega}_{tot} = \omega_{HS} - a_1 a_2 a_3 \omega_{LS}, \tag{4.4}$$

where ω_{HS} and ω_{LS} are the rotational speed in $\frac{rad}{s}$ obtained from the high- and low-speed shafts encoders, respectively. a_1, a_2 and a_3 are the inverse of gear ratios of the gearbox stages. Gear ratio as per definition is $\frac{n_i}{n_o}$, where n_i and n_o are the speeds of input and output shafts, respectively. The error function main feature is removing the excitation frequencies which are transmitted to the drivetrain through the housing, from the resultant torsional response. Angular displacement and acceleration are the other torsional responses of the drivetrain system which could theoretically be used instead of angular velocity for condition monitoring purposes. To this purpose, similar to e^{ω}_{tot}, the angular position error function e^{θ}_{tot} and the angular acceleration error function e^{α}_{tot} are defined by the following equations obtained from paper 3 [28]

$$e^{\theta}_{tot} = \theta_{HS} - a_1 a_2 a_3 \theta_{LS}, \;\; e^{\alpha}_{tot} = \alpha_{HS} - a_1 a_2 a_3 \alpha_{LS}. \tag{4.5}$$

Faults in the drivetrain components may cause a torsional oscillation component which can be observed in the torsional response [17]. In particular, angular acceleration is the torsional response which has a direct relation with the applied load, and contains useful information about how the applied torque interacts with the system. If acceleration or displacement is used for the drivetrain fault studies, the frequency-domain fault criteria obtained by the analysis of angular velocity tend to change, because the relation between acceleration and displacement with velocity in frequency-domain is the function of frequency. The Fourier series of e^{ω}_{tot}, e^{α}_{tot} and

e^{θ}_{tot} are defined by $e^{\omega}_{tot}(\Omega) = \sum_{n=-\infty}^{\infty} C_n e^{ik_n\Omega}$, $e^{\alpha}_{tot}(\Omega) = \sum_{n=-\infty}^{\infty} C_n(ik_n)e^{ik_n\Omega}$, $e^{\theta}_{tot}(\Omega) = \sum_{n=-\infty}^{\infty} C_n(ik_n)^{-1}e^{ik_n\Omega}$.

Differentiation and integration are linear operations that are distributive over addition. As it can be seen, in e^{α}_{tot} compared to e^{ω}_{tot}, the amplitudes of the frequency components higher than 1 Hz are magnified with the gain k_n, and the frequencies lower than 1 Hz are weakened with the same proportion. In e^{θ}_{tot} compared to e^{ω}_{tot}, the amplitudes of the frequency components lower than 1 Hz are magnified with the gain k_n^{-1}, and the frequencies higher than 1 Hz are weakened with the same proportion.

In the next section, the FFT, PSD and energy of the angular velocity residual signal e_{total} and also the angular velocity measurements of individual encoders are studied and compared to the conventional method based on analysis of translational vibrations for the detection of different types of drivetrain abnormalities. The results of the following section are extracted from the experimental studies performed by Moghadam and Nejad [61] in paper 2.

4.3.2 Comparison of translational and torsional vibrations-based condition monitoring

The normalized Cooley–Tukey FFT algorithm is used as the basis to investigate into the capability of torsional vibration response compared to translational acceleration measurements in distinguishing abnormalities, which is defined by $\Theta(j\Omega) = \int_{-\infty}^{+\infty} \theta(t)e^{-i\Omega t}dt$, where $\Theta(j\Omega)$ is the spectrum of the response $\theta(t)$.

Afterwards, the PSD and energy of the signal around the suspicious frequency is used as the abnormality detection tool. The PSD of θ is defined by

$$S_{\Theta\Theta}(\Omega) = \frac{|\,\Theta(j\Omega)\,|^2}{n}, \tag{4.6}$$

where $S_{\theta\theta}$ is the PSD spectrum of $\theta(t)$. The energy of the frequency domain signal Θ in the frequency range $[\Omega_1\ \Omega_2]$ is then calculated by

$$E = \frac{1}{\pi}\int_{\Omega_1}^{\Omega_2} |\,\Theta(j\Omega)^2\,|\,d\Omega. \tag{4.7}$$

The PSD of the envelope of the signal θ obtained by using Hilbert transform is used as the other abnormality detection tool. The Hilbert envelope of θ and the PSD of the envelope signal are defined by

$$\widetilde{\Theta}(j\Omega) = \Theta(j\Omega)(-j.sgn(\Omega)),\ \ S_{\widetilde{\Theta}\widetilde{\Theta}}(j\Omega) = \frac{|\,\widetilde{\Theta}(\Omega)\,|^2}{n}, \tag{4.8}$$

where $\widetilde{\Theta}$ and $S_{\widetilde{\Theta}\widetilde{\Theta}}$ are the envelope and envelope PSD spectrums of θ, and sgn is the signum function. The energy of $\widetilde{\Theta}$ can be used for the fault detection purpose. Since the measurements are discretized in time, the normalized energy based on the normalized length-n discrete Fourier transform is used, where n is the spectrum frequency resolution. The normalization in this context means a division by $\sqrt{n}$ for FFT which is equivalent to a division by n for the PSD of the signal. Two different energy indices EI^1 and EI^2 are then calculated as [61]

$$EI^1 = \frac{E^*}{E},\ EI^2 = \frac{E^*_{\Omega_s}}{E_{\Omega_s}}. \tag{4.9}$$

where * is used as the indicator of the suspicious data set. E and E^* are the energy over all the frequency horizon of normal and suspicious cases, respectively. Ω_s is the frequency horizon which covers the suspicious frequency ${\Omega_s}^*$ and 10% below and above it. E_{Ω_s} is the energy of the acceleration signal in the frequency range Ω_s filtered by the band-pass filter $H(\Omega_s)$, $\Theta(\Omega_s) = \Theta(\Omega)H(\Omega_s)$, and $E^*_{\Omega_s}$ is the same parameter for the suspicious case.

With respect to the different types of excitation sources, three different test scenarios are designed to compare the torsional to the translational vibrations for drivetrain condition monitoring purposes. In *scenario one*, the system responses including axial/radial accelerations, angular velocity measurements and angular velocities residual signal are studied to investigate the influence of internal and non-torsional drivetrain excitations on response. In *scenario two*, the influence of internal and torsional excitations on the different drivetrain responses is studied, while in *scenario three*, the influence of external and torsional excitation sources is investigated. For all these three test scenarios, the accelerometers and the angular velocity measurements of the drivetrain of Vestas V66 1.75 MW wind turbine are used as the input measurements for the proposed frequency-domain energy-based condition monitoring approach. The drivetrain topology and the placement of accelerometers and encoders are specified in Figure 4.5.

In the first scenario, the frequency $f_m = 529$ Hz which is the mesh frequency of the helical gears of the third stage of gearbox, which is a parallel stage, is studied. The frequency spectrum of drivetrain different responses in observing this frequency component is shown in Figure 4.6. The amplified response at this frequency can be due to the defective gear teeth (*e.g.* due to pitting or root bending faults), which causes axial/radial vibrations in the system. The latter can be observed in the frequency spectrum of the radial and axial acceleration sensors installed in different locations of the gearbox at the mesh frequency of the gears, $f_m = 529$ Hz. The mentioned abnormality

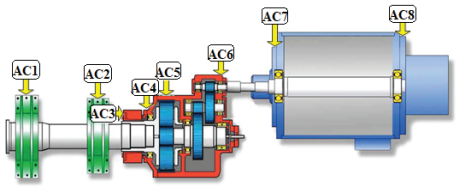

Code	Position
AC1	Main bearing front, clock 3
AC2	Main bearing rear, clock 3
AC3	Gearbox input shaft axial direction (Top)
AC4	Gearbox input shaft bearing radial direction, clock 3
AC5	Gearbox medium speed bearing radial direction, as close as possible (clock 3)
AC6	Gearbox high speed shaft bearing, clock 3
AC7	Generator bearing front, clock 3
AC8	Generator bearing rear, clock 3

(a) Acceleration sensors placement

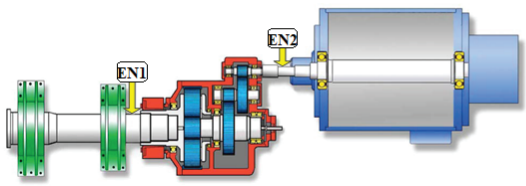

Code	Position
Encoder 1	Low speed shaft
Encoder 2	High speed shaft

(b) Angular velocity sensors placement

Figure 4.5: Drivetrain topology, accelerometers and encoders placement [61] (paper 2).

does not reveal a significant sign in the angular velocity measurements and the angular velocity residual signal, because it does not produce a significant vibration frequency component in an early stage in the rotational rotational degrees of freedom. Data filtering and using higher sampling frequency rates are suggested for improving the performance of torsional vibrations in observing those excitation frequencies.

In the second scenario, the frequency 50 Hz and its harmonics are studied. The frequency spectrum of drivetrain different vibration responses and the possibility of observing these frequency components is shown in Figure 4.7. These frequency components appear in response due to electromagnetic torque oscillations which happen significantly with the voltage frequency 50 Hz and the third order harmonics which happen due to the generator electrical current and back emf harmonics influenced by power electronic converter and the grid low power quality. These abnormalities which can represent excessive vibrations in drivetrain due to generator electromagnetic torque oscillations are observable in angular velocity error function but not observable in acceleration measurements.

In the third scenario, the frequencies 0.05 Hz and 0.97 Hz as the result of structural motions-induced vibrations, respectively due to the excited first tower side-side natural frequency and the tower shadow effect. The frequency spectrum of drivetrain different responses in observing frequency

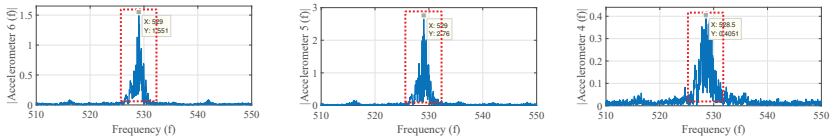

(a) AC6 spectrum vs. Frequency *(b) AC5 spectrum vs. Frequency* *(c) AC4 spectrum vs. Frequency*

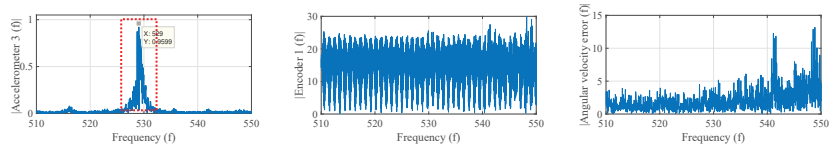

(d) AC3 spectrum vs. Frequency *(e) EN1 spectrum vs. Frequency* *(f) e_{total} spectrum vs. Frequency*

Figure 4.6: First test scenario [61] (paper 2).

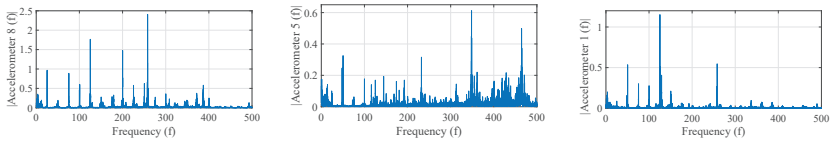

(a) AC8 spectrum vs. Frequency *(b) AC5 spectrum vs. Frequency* *(c) AC1 spectrum vs. Frequency*

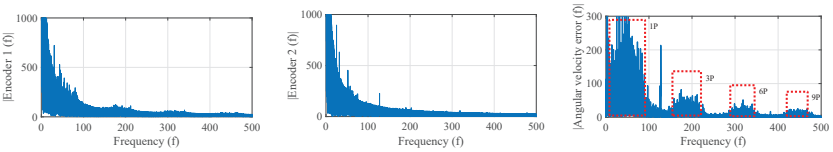

(d) EN1 spectrum vs. Frequency *(e) EN2 spectrum vs. Frequency* *(f) e_{total} spectrum vs. Frequency*

Figure 4.7: Second test scenario [61] (paper 2).

components is shown in Figure 4.8. These excitation frequencies are observable in angular velocity measurements but not observable in acceleration data. The external excitation frequencies are not observable in the angular velocity error function due to the intrinsic filtering properties.

The performance of energy-based abnormality detection which measures the energy of signal around the suspicious frequency, by using the different vibration responses as the input of the energy-based fault detection approach is reported in Tables 4.1, 4.2 and 4.3. Our extensive observations showed that

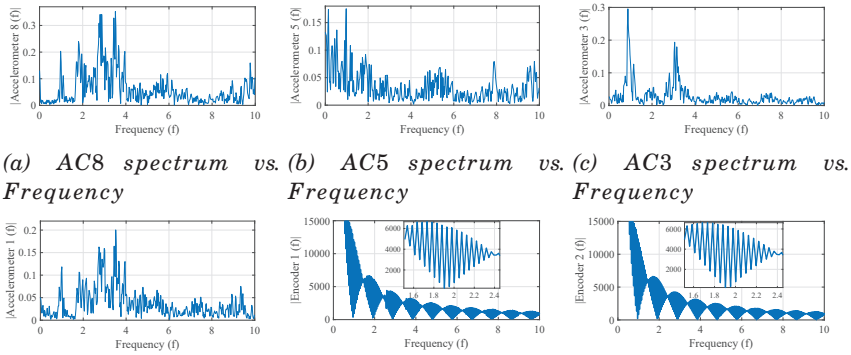

(a) AC8 spectrum vs. Frequency *(b) AC5 spectrum vs. Frequency* *(c) AC3 spectrum vs. Frequency*

(d) AC1 spectrum vs. Frequency *(e) EN1 spectrum vs. Frequency* *(f) EN2 spectrum vs. Frequency*

Figure 4.8: Third Test scenario [61] (paper 2).

for different sets of operational data, the threshold 3 can provide a criterion for the energy indices EI^1 and EI^2 of all the acceleration and angular velocity signals to evaluate if the abnormality can be detected by the energy method applied on the associated sensor. Based on this explanation, the energy index EI^1 is not performing well in detection of the abnormalities, and the energy index EI^2 is preferred based on the simulation study. The higher values of this index can represent both the severity of the abnormality and the higher capability of the sensor in observing it.

The frequency components appeared in the torsional response does not necessarily represent a defect in the system, but provide valuable insights about the torsional loads which can influence the drivetrain components, which may not be considered in the design step. An amplified frequency in angular velocity spectrum can represent either a high-amplitude internal/external torsional excitation source, an amplified component defect frequency or an amplified system torsional natural frequency. The latter is discussed in detail in Chapter 5. In any case, it can considerably affect the fatigue life of the components.

As reported in paper 2 [61], none of the three under consideration cases can be observed by using the time-domain approach based on the RMS value of the translational vibrations obtained from the accelerometers time series data, where these values should not exceed the predefined limits suggested by the standards ISO 10816-21 and ISO 13373-1 by taking into account the rotational frequency and type of application.

The possibility of using the torsional responses residual functions and

Table 4.1: Calculated energy indices for the suspicious frequency $\omega^* = 529\ Hz$.

Criterion \ Sensor	$AC1$	$AC2$	$AC3$	$AC4$	$AC5$	$AC6$	$AC7$	$AC8$	$EN1$	$EN2$	e_{total}
EI^1	1.64	2.41	2.19	2.25	1.66	1.38	0.92	0.96	1.01	1.01	1.06
EI^2	4.71	17.17	25.14	3.19	25.30	7.00	1.11	1.00	1.01	1.00	0.87

Table 4.2: Calculated energy indices for the suspicious frequency $\omega^* = 170\ Hz$.

Criterion \ Sensor	$EN1$	$EN2$	e_{total}
EI^1	1.01	1.01	1.06
EI^2	2.21	1.97	26.47

Table 4.3: Calculated energy indices for the frequency $\omega^* = 0.05\ Hz$.

Criterion \ Sensor	$EN1$	$EN2$	e_{total}
EI^1	1.01	1.01	1.06
EI^2	7.97	7.96	0.64

the low-pass filtered torsional response of individual encoders in estimating drivetrain dynamic properties, and the applications for detecting drivetrain faults by monitoring the variations of drivetrain dynamic properties is the other proposed innovative drivetrain condition monitoring approach based on torsional vibrations in this thesis, which is discussed in the next chapter.

Chapter 5

Fault diagnosis and modal analysis by using torsional vibrations

5.1 General

This chapter discusses about the methodology and a part of results presented by Moghadam and Nejad [27, 28] in papers 3 and 4, and Moghadam *et al.* [29] in paper 5, related to the drivetrain system modal estimation and fault diagnosis by monitoring the variations of drivetrain dynamic properties.

As the first step, the proposed modal estimation approach by using the torsional measurements is presented and proved in the general case for a multi degree-of-freedom (DOF) torsional model of drivetrain. A detailed parametric proof based on 3-DOF model is presented in paper 4 [28]. The method is tested by using DTU 10 MW and NREL 5 MW simulation models, and Vestas 1.75 MW operational data.

As the second step, the analytical relationship between the 3-DOF equivalent model parameters and drivetrain dynamic properties is established, which helps to identify the drivetrain system condition/state-of-operation by monitoring the variations of drivetrain dynamic properties (undamped natural frequencies and normal mode shapes) which can be estimated from the operational measurements by using the proposed modal estimation approach or any other approach in the literature.

The main emphasis of this chapter is on geared drivetrains of wind turbines. Based on the theoretical studies presented in papers 3 and 4 [27, 28], a 3-DOF equivalent torsional model of the geared drivetrain is sufficient for

detecting drivetrain faults at a system-level, because system-level faults represent themselves mainly by changing the torsional stiffness and the moment of inertia parameters of the 3-DOF equivalent model. System-level faults are categorized into the faults which change the torsional stiffness the most (*e.g.* crack in the shafts and bearing wear specially in gearbox), and faults which influence mostly the inertia of the drivetrain bodies (changes in mass balance/distribution which can be due to *e.g.* loss of mass, wear and unbalance; and also changes in the axis of rotation which can be due to *e.g.* misalignment and looseness), which all can be observed by using 3-DOF reduced order model (ROM). The other reason for sticking to 3-DOF model for the proposed drivetain system-level fault diagnosis algorithm, is that the closed form parametric expressions of the drivetrain dynamic properties as a function of equivalent model parameters can be obtained for this simplified model. Those expressions are the required inputs for the proposed fault detection approach based on monitoring the variations of the drivetrain dynamic properties.

The method based on 3-DOF model can be implemented by using only the filtered measurement obtained from one encoder (this method is explained in the next section), which is sufficient for estimating the first and second drivetrain non-rigid natural frequencies. The experimental results presented in paper 4 [28] demonstrate the possibility of observing the natural frequencies by using the angular velocity residual function (constructed by using two encoders measurements) and the filtered angular velocity measurement of one encoder. One of the reasons that the 3-DOF model based fault detection method is selected and developed in this work is that this approach can be implemented only by using one encoder. However, the implementation of method with two encoders renders the easier visibility of torsional modes but may cause additional costs of implementation if the drivetrain is equipped with only one encoder. In the SCADA data, it is a common practice to consider two measurements for the drivetrain speed. Therefore, the cost of implementation of the approach based on two encoders may only be the cost of an additional encoder by using the available data logging and communication infrastructure.

The proposed algorithm for modal analysis and fault diagnosis of the drivetrain system by using the torsional response, developed for 3-DOF model is summarized in the flowchart in Figure 5.1. The different parts of algorithm are explained in the next two sections. The details about the 3-DOF model and the definition of parameters are provided in paper 3 [27].

The research contributions of this PhD work which are covered by this chapter are:

- Drivetrain modal analysis by using the different types of torsional measurements is introduced. The proposed modal analysis approach is analytically proved. The performance of the proposed modal analysis approaches is demonstrated by using both experimental studies based on the operational data and simulation studies. Two different simulation studies based on two different drivetrain systems and two different equivalent models (a simplified 3-DOF and a more complex 14-DOF models) of drivetrain are carried out, and the possibility of observing the system natural frequencies by using different functions of torsional measurements is investigated. An analytical approach for estimating the damping coefficients associated with the different natural frequencies and operating speeds by analyzing the variations of amplitude of torsional response residual function at the natural frequencies and variations of damped natural frequencies in different operating speeds is proposed.

- A drivetrain condition monitoring approach is proposed which works based on monitoring the variations of the system dynamic properties and the amplitude of response at the natural frequencies. The drivetrain system fault detection features are extracted by leveraging sensitivity analysis. The method is tested by using both operational and simulation data obtained respectively from Vestas 1.75 MW and DTU 10 MW wind turbine drivetrains. The results are showing that the state of progression of different categories of drivetrain faults at system-level are observable in an early stage by the fault diagnosis method developed based on 3-DOF equivalent torsional model of the drivetrain, only by tracking the faults consequent variations in the drivetrain dynamic properties. The analytical equations of 3-DOF drivetrain model supported by sensitivity analysis are used to extract the fault detection features which are shown to be sufficient to detect the drivetrain faults at a system level. Then the possibility of extending this work to the drivetrain fault diagnosis at component-level by using higher DOF models of the drivetrain is demonstrated by the simulation studies.

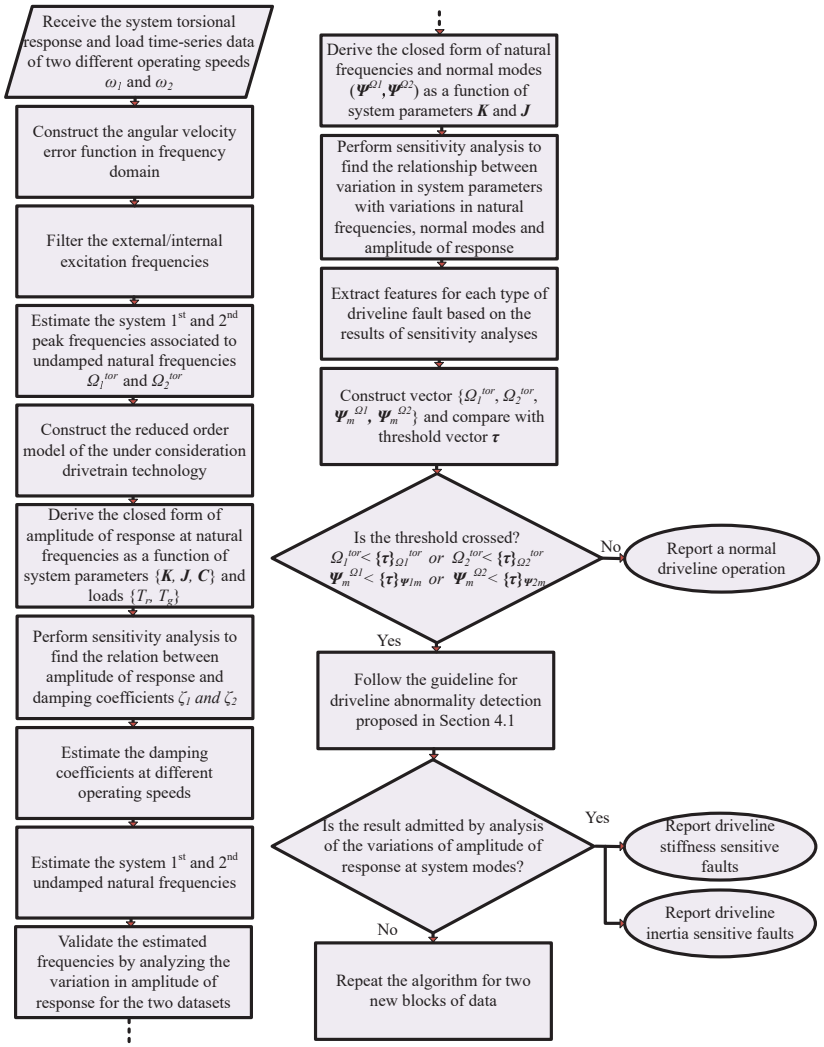

Figure 5.1: Proposed drivetrain fault diagnosis algorithm by using torsional measurements and estimated modes [28].

5.2 Drivetrain modal analysis by torsional measurements

5.2.1 Construction of the input function for the modal analysis approach

in order to realize the drivetrain modal analysis by means of torsional measurements, two methods based on the torsional vibration measurements are

employed:

1- *Torsional vibration residual function:*

The torsional response residual function between l^{th} and m^{th} inertias from the point l based on a multi-DOF lumped parameter model of order n is defined as [30]

$$\boldsymbol{e}^{\boldsymbol{\omega}}_{\boldsymbol{l,m}}(t) \triangleq \boldsymbol{\omega_l}(t) - u_{l,m}\boldsymbol{\omega_m}(t),\ for\ l\ and\ m\ \in \{1,\ldots,n\}, \tag{5.1}$$

with $\boldsymbol{\omega}$ as the time series of angular velocity, and $u_{l,m}$ as the relative gear-ratio between j_l and j_m to make them in the same coordinate. Gear-ratio $u_{l,m}$ as per definition is $\frac{N_l}{N_m}$, where N_l and N_m are the speeds at l^{th} and m^{th} inertias. Both the angular velocity and angular acceleration can be used as the inputs of the residual function. The torsional response can be provided by encoders or strain gauges. It is assumed that the different types of torsional response can be interchangeably used by performing derivation and integration operations. In case of 3-DOF model, the residual function can be constructed by the two encoders located on high- and low-speed shafts of drivetrain. Since most of the wind turbines are equipped with only one angular velocity measurement, the implementation of this method may require an additional moderate resolution encoder. One of the significant features of the error/residual function is the cancellation of the influences of structural motions which are transferred from the bed plate to the drivetrain, from the torsional response. The latter leads to a clean signal with the capability of highlighting the system characteristic frequencies. The transmitted motions to the drivetrain are mainly influenced by wind, wave, structural resonances, natural periods of structural motions and interactions between rotor, tower and support structure, which have a low frequency content. Therefore, the filtered angular velocity of low-speed shaft, which can be implemented with one encoder, has also a potential in highlighting the drivetrain torsional frequencies, which makes the basis for the second method as discussed in the continued part.

2- *Low-pass filtered angular velocity function:*

The filtered signal $X(\Omega_{HP})$ is defined by

$$X(\Omega) = \omega_i(\Omega),\ i\ \in \{1,\ldots,n\},\ X(\Omega_{HP}) = X(\Omega)H(\Omega_{HP}), \tag{5.2}$$

where $H(\Omega_{HP})$ is the transfer function of the high-pass filter applied to the encoder signal to attenuate the low-frequency noises induced by structural motions. The performance of filtered angular velocity of low-speed shaft in highlighting the torsional frequencies compared to the different torsional response error/residual functions is tested with both simulation-based and operational measurements as reported in papers 3, 4 and 5 [27, 28, 29].

The following steps explain the modal estimation approach which are also summarized in Figure 5.1:

1. The torsional response error function (or interchangeably the low-pass filtered signal of the main shaft) is generated. The response can be angular velocity or acceleration.

2. The signal is preprocessed so that the defect frequencies of the components structural motions-induced harmonics are filtered. The result gives the damped torsional natural frequencies of the drivetrain system.

3. The natural frequency is validated by the analysis of the variations of amplitude of response in the suspicious frequencies at different operating speeds. The variation of the amplitude of response in the system damped natural frequency due to the variation of damping coefficient shows a more significant change compared to the variation of the amplitude of response in the harmonics. The variation of damping coefficient is due to the continuous variations in the operating speed.

4. Damping at the natural frequency depends on the operating speed. The damping coefficient at two ensuing operations in two different speeds can be estimated by applying the theory developed by Moghadam and Nejad [27, 28] in papers 3 and 4, based on monitoring the variations of the natural frequency and amplitude of response between the two operations.

5. By using the estimated damped natural frequency from torsional response and the estimated damping coefficient from the analysis of amplitude of response, the undamped natural frequencies are estimated, which provide inputs for the fault detection approach based on monitoring the variations of system dynamic properties.

5.2.2 Analytical proof

The possibility of observing the natural frequencies from the torsional response is explained by the following theorem.

Theorem 1. *Torsional natural frequencies belong to the set of extreme points of the torsional response in the frequency domain.*

Proof. The general form of the discrete multi-DOF torsional model of drivetrain with n degrees of freedom in the time domain is defined by

$$\mathbf{J}\ddot{\theta} + \mathbf{C}\dot{\theta} + \mathbf{K}\theta = T(t), \tag{5.3}$$

where **J**, **C** and **K** are the moment of inertia, damping and stiffness matrices with the size $n \times n$. θ and T are the response and load vectors with the size $n \times 1$, where each element of these two vectors represent a time series data. The representation in frequency domain by using the frequency variable S and Laplace transform is

$$[\mathbf{J}S^2 + \mathbf{C}S + \mathbf{K}]_{n\times n}[\Theta(S)]_{n\times 1} = T(S)_{n\times 1}. \tag{5.4}$$

By replacing the characteristic equation $\mathbf{J}S^2 + \mathbf{C}S + \mathbf{K}$ with **M**, the frequency domain response $\Theta(S)$ is calculated by

$$\Theta(S) = \frac{adj(\mathbf{M})}{det(\mathbf{M})}T(S), \tag{5.5}$$

where $adj(\mathbf{M})$ is the adjugate of **M**, which is a polynomial function with the matrix variable **M**. $det(\mathbf{M})$ is the determinant of system characteristic equation. As it can be seen, the roots of $det(\mathbf{M})$ are the extreme points of response $\Theta(S)$. However, the roots of the determinant of characteristic equation of a system are the system's eigenfrequencies. Therefore, the torsional natural frequencies of the system belong to the set of extreme points of the response. In the undamped system ($\mathbf{C} = \mathbf{0}$), the roots are pure imaginary which represent the undamped natural frequencies Ω_n^i. In the general damped system, the roots are the damped natural frequencies Ω_d^i with the relationship with the undamped frequencies as

$$\Omega_d^i = \zeta^i \Omega_n^i + j\Omega_n^i \sqrt{1-(\zeta^i)^2} \quad i \in 1,..,n. \tag{5.6}$$

The torsional natural frequencies in both cases of damped or undamped system based on the provided proof which refers to the general form of damped system are the extreme points of the frequency-domain response.

Thus, we complete the proof of Theorem 1.

The signal generally used for frequency-domain fault detection studies is the single-sided amplitude spectrum of response. The possibility of extending the results of Theorem 1 to the amplitude of torsional response and more specifically the amplitude of angular velocity error function based on an equivalent 3-DOF model is explained by Moghadam and Nejad [28] in paper 4. The 3-DOF model is applied as the base model for the drivetrain system-level fault diagnosis in Section 5.3.

5.2.3 Results of modal analysis approach validation

The results of modal analysis in three different cases, namely DTU 10 MW, NREL 5 MW and vestas 1.75 MW, which are a part of results reported in

papers 3, 4 and 5 are shown in the following.

1- DTU 10 MW 3-DOF model

The PSD spectrum of angular velocity error function obtained from 10 MW drivetrain model and its capability in extracting the 1^{st} and 2^{nd} torsional natural frequencies of the drivetrain compared to angular displacement and angular acceleration error functions is shown in Figures 5.2b-6.2b. The angular acceleration error function shows a higher performance in revealing the higher frequency modes (the 2^{nd} mode). The higher frequency modes have usually a lower impact on the response, which complicates the disclosure of those frequencies. The PSD spectrum of the input torque applied on the drivetrain MBS model is shown in Fig. 5.2a. This torque contains the majority of frequency components and can excite the drivetrain natural frequencies. Two methods based on monitoring the variations of natural frequencies and amplitude of response at natural frequencies between two different drivetrain operations are proposed in paper 4 [28] for estimating the damping coefficient from the torsional measurements. The estimated values of damping coefficients at the 1^{st} mode in two different operating speeds with two different loading conditions, by using the two methods proposed in paper 4 [28], are listed in Table 5.1, which show a good agreement between the estimated values and the actual value from the reference model.

Table 5.1: Estimation of damping coefficient at the 1^{st} mode of DTU 10 MW model for different operating speeds and loading conditions [28]

Operation	$\omega\,(rad/s)$	$\Omega^1_{peak}\,(rad/s)$	$\lvert e^{\omega}_{tot}(\Omega^1_{peak})\rvert$	ζ (reference model)	ζ (method 1)	ζ (method 2)
ω_1	0.9	8.67	0.159	0.21	0.21	0.18
ω_2	0.7	8.46	0.171	0.26	0.25	0.23

2- NREL 5 MW 14-DOF simulation model

The undamped natural frequencies of the healthy drivetrain system based on the 14-DOF torsional model are listed in the Table 5.2. As explained by equation 5.1, the torsional response error function can be defined between different bodies in the drivetrain model. For example, the undamped natural frequencies estimated from the angular acceleration error function for the 2^{nd} gearbox stage are shown in Figure 5.3. It is worth noting that the damping in this equivalent model is set to be zero, so that the estimated frequencies are directly giving the undamped natural frequencies.

3- Vestas 1.75 MW operational data

The PSD spectrum of angular velocity error function of the drivetrain operational data of Vestas V66 1.75 MW turbine for a rated operation compared to angular displacement and acceleration error functions is shown in Figures 5.4a-5.4c, which shows the observability of both the drivetrain and blade

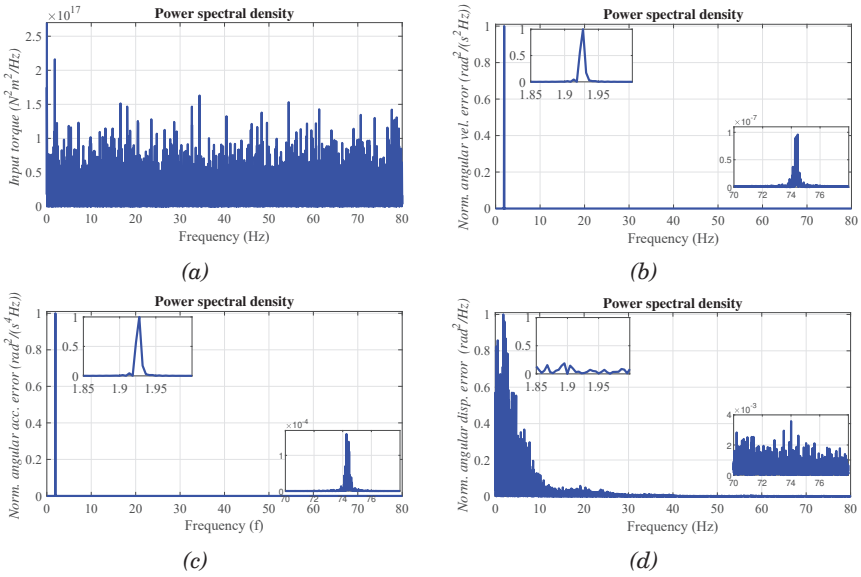

Figure 5.2: Simulation results of estimating drivetrain torsional natural frequencies based on DTU 10 MW floating wind turbine model [27] (paper 3). (a) PSD of τ^{rotor}. (b) PSD of e^{vel}_{tot}. (c) PSD of e^{acc}_{tot}. (d) PSD of e^{dis}_{tot}.

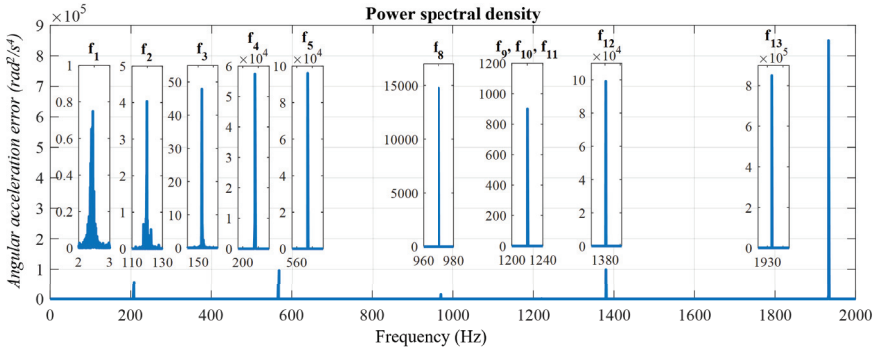

Figure 5.3: Estimation of torsional modes by using the error function defined based on the gearbox 2^{nd} stage torsional responses of NREL 5 MW wind turbine drivetrain [29].

natural frequencies, which are 2.6 Hz and 3.6 Hz, respectively. The results are validated by comparing the natural frequencies with the 1^{st} drivetrain

Table 5.2: 14-DOF drivetrain model natural frequencies of NREL 5 MW [29]

Mode	1	2	3	4	5	6	7	8	9	10	11	12	13	14
Actual	0	2	120	153	208	567	716	716	971	1224	1232	1232	1384	1942
Estimated	0	2	118	153	208	567	706	706	970	1220	1220	1220	1381	1933

and 1^{st} blade edgewise natural frequencies of another turbine with the same drivetrain technology and power range as reported in [66]. As it can be seen, angular acceleration performs slightly better in the extraction of characteristic frequencies of higher values. A comparison between the angular velocity error function PSD in two different operating speeds is shown in Figure 5.4d. As it can be seen, the higher damping coefficient in lower speeds has resulted in a lower damped natural frequency. Furthermore, at the drivetrain natural frequency, the response amplitude reacts more to the variation of damping. In other words, for a lower rotor speed which corresponds to a higher damping, the amplitude of response at the natural frequency reduces more compared with the amplitude of response at the other harmonics. The high-pass filtered low-speed shaft angular velocity measurement is also shown in Figure 5.4e. The filtered signal shows some degree of competence with the angular velocity error function in extracting the torsional properties, *i.e.* the drivetrain and the blade edgewise natural frequencies.

5.3 Proposed drivetrain system-level fault diagnosis approach

Variations in drivetrain dynamic properties and their relationships with progressive faults in system and component levels are reported in paper 4 [28] and paper 5 [29], respectively.

In papers 3 and 4, the diagnosis of drivetrain system-level faults is investigated. To this purpose, an equivalent 3-DOF model is proved to be sufficient for setting up the analytical relations for detecting the drivetrain faults at a system level based on monitoring the variations of the first and second nonrigid modes of the drivetrain system. Therefore, the analytical relationship between the drivetrain dynamic properties and the reduced order model parameters are obtained by deriving the related nonlinear equations and applying the normalized local sensitivity analysis to extract meaningful fault detection criteria for different stages of progressive faults. The methodology which is summarized in the flowchart in Figure 5.1, is briefly discussed in the following.

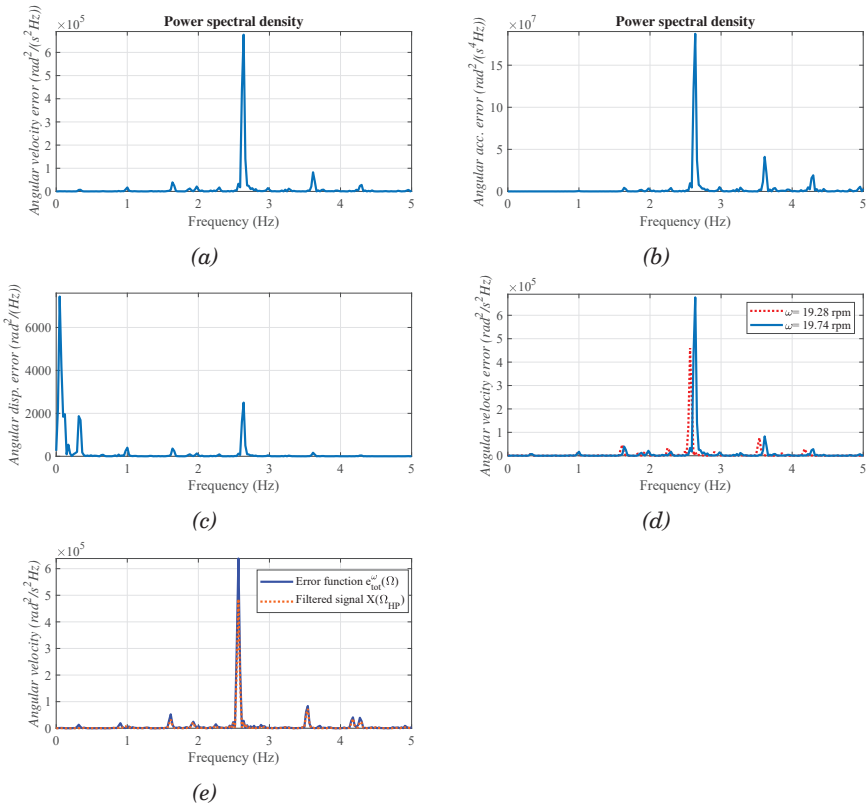

Figure 5.4: Modal analysis based on Vestas V66 1.75 MW drivetrain torsional response [27] (paper 3). (a) PSD of e^{ω}_{tot}. (b) PSD of e^{α}_{tot}. (c) PSD of e^{θ}_{tot}. (d) PSD of e^{ω}_{tot} in two different operations. (e) Comparison of $X(\Omega_{HP})$ and $e^{\omega}_{tot}(\Omega)$ performances.

5.3.1 3-DOF equivalent model dynamic properties as a function of model parameters

The two undamped natural frequencies (nonrigid modes) based on 3-DOF lumped-mass-spring model of a geared drivetrain, as functions of model parameters, can be calculated by

$$\Omega_1^{tor} = \sqrt{\frac{k_L}{2J_r} + \frac{k_L + k_H}{2J_{gr}} + \frac{k_H}{2J_{gn}} - \sqrt{(\frac{-k_L}{2J_r} - \frac{k_L - k_H}{2J_{gr}} + \frac{k_H}{2J_{gn}})^2 + \frac{k_L k_H}{J_{gr}^2}}}, \tag{5.7a}$$

$$\Omega_2^{tor} = \sqrt{\frac{k_L}{2J_r} + \frac{k_L + k_H}{2J_{gr}} + \frac{k_H}{2J_{gn}} + \sqrt{(\frac{-k_L}{2J_r} - \frac{k_L - k_H}{2J_{gr}} + \frac{k_H}{2J_{gn}})^2 + \frac{k_L k_H}{J_{gr}^2}}}, \tag{5.7b}$$

where Ω_1^{tor} and Ω_2^{tor} are the 1^{st} and 2^{nd} natural frequencies, k_L and k_H are the torsional stiffness of low- and high-speed shafts, and J_r, J_{gr} and J_{gn} are the moment of inertia of rotor, gearbox and generator, respectively.

The two normal mode shapes related to the two non-rigid modes of the under consideration drivetrain model, as functions of model parameters, which are scaled to unity length are

$$\Psi_{rot}^{\Omega_1} = \frac{\sqrt{\frac{k_L^2}{\frac{k_H^2}{(k_H - J_{gn}A)^2} + \frac{k_L^2}{(k_L - J_r A)^2} + 1)}}}{k_L - J_r A}, \quad \Psi_{rot}^{\Omega_2} = \frac{\sqrt{\frac{k_L^2}{\frac{k_H^2}{(k_H - J_{gn}B)^2} + \frac{k_L^2}{(k_L - J_r B)^2} + 1}}}{k_L - J_r B}, \tag{5.8a}$$

$$\Psi_{gear}^{\Omega_1} = \sqrt{\frac{1}{\frac{k_H^2}{(k_H - J_{gn}A)^2} + \frac{k_L^2}{(k_L - J_r A)^2} + 1}}, \quad \Psi_{gear}^{\Omega_2} = \sqrt{\frac{1}{\frac{k_H^2}{(k_H - J_{gn}B)^2} + \frac{k_L^2}{(k_L - J_r B)^2} + 1}}, \tag{5.8b}$$

$$\Psi_{gen}^{\Omega_1} = \frac{\sqrt{\frac{k_H^2}{\frac{k_H^2}{(k_H - J_{gn}A)^2} + \frac{k_L^2}{(k_L - J_r A)^2} + 1}}}{k_H - J_{gn}A}, \quad \Psi_{gen}^{\Omega_2} = \frac{\sqrt{\frac{k_H^2}{\frac{k_H^2}{(k_H - J_{gn}B)^2} + \frac{k_L^2}{(k_L - J_r B)^2} + 1}}}{k_H - J_{gn}B}, \tag{5.8c}$$

where

$$A = -\sqrt{(\frac{k_H}{2J_{gn}} - \frac{k_L}{2J_r} + \frac{k_H - k_L}{2J_{gr}})^2 + \frac{k_H k_L}{J_{gr}^2}} + \frac{k_H}{2J_{gn}} + \frac{k_L}{2J_r} + \frac{k_H + k_L}{2J_{gr}},$$

$$B = \sqrt{(\frac{k_H}{2J_{gn}} - \frac{k_L}{2J_r} + \frac{k_H - k_L}{2J_{gr}})^2 + \frac{k_H k_L}{J_{gr}^2}} + \frac{k_H}{2J_{gn}} + \frac{k_L}{2J_r} + \frac{k_H + k_L}{2J_{gr}},$$

$\Psi_{rot}^{\Omega_1}$, $\Psi_{gear}^{\Omega_1}$ and $\Psi_{gen}^{\Omega_1}$ are normal modes at rotor, gearbox and generator due to the 1^{st} mode. $\Psi_{rot}^{\Omega_2}$, $\Psi_{gear}^{\Omega_2}$ and $\Psi_{gen}^{\Omega_2}$ are the same parameters for the 2^{nd} mode.

The amplitude of the angular velocity residual function at the two natural frequencies in the general case of a damped system has the relationship with the system parameters and rotor and generator torques as

$$|e^{\omega}_{tot}(\Omega^{tor}_1)|=\frac{\sqrt{|T_g(\omega 1)|^2\sqrt{FA+H+J_r^2J_{gr}^2A^2}\sqrt{A}+|T_r(\omega 1)|^2\sqrt{EA+G+J_{gr}^2J_{gn}^2A^2}\sqrt{A}}}{\sqrt[4]{A^2I^2+(J_r\sqrt{E}+c_LJ_{gr}J_{gn})^2A^3+D^2(J_r+J_{gr}+J_{gn})^2A+k_L^2k_H^2(J_r+J_{gr}+J_{gn})^2+J_r^2J_{gr}^2J_{gn}^2A^4}}, \tag{5.9a}$$

$$|e^{\omega}_{tot}(\Omega^{tor}_2)|=\frac{\sqrt{|T_g(\omega 2)|^2\sqrt{FB+H+J_r^2J_{gr}^2B^2}\sqrt{B}+|T_r(\omega 2)|^2\sqrt{EB+G+J_{gr}^2J_{gn}^2B^2}\sqrt{B}}}{\sqrt[4]{B^2I^2+B^3(J_r\sqrt{E}+c_LJ_{gr}J_{gn})^2+k_L^2k_H^2(J_r+J_{gr}+J_{gn})^2+D^2(J_r+J_{gr}+J_{gn})^2B+J_r^2J_{gr}^2J_{gn}^2B^4}}, \tag{5.9b}$$

where

$D = c_Lk_H + c_Hk_L$, $E = (c_LJ_{gn} + c_HJ_{gr} + c_HJ_{gn})^2$, $F = (c_LJ_r + c_LJ_{gr} + c_HJ_r)^2$, $G = (J_{gr}k_H + J_{gn}k_L + J_{gn}k_H)^2$, $H = (J_rk_L + J_rk_H + J_{gr}k_L)^2$ and $I = c_Lc_HJ_r + c_Lc_HJ_{gr} + c_Lc_HJ_{gn} + J_rJ_{gr}k_H + J_rJ_{gn}k_L + J_rJ_{gn}k_H + J_{gr}J_{gn}k_L$.

5.3.2 Sensitivity analysis

It was shown that the estimated modes and the amplitude of response at those frequencies are connected to the system parameters and faults. In order to establish this relationship to be used in the proposed fault detection approach, sensitivity analysis is employed. The different categories of drivetrain system-level faults and their influences on the 3-DOF model parameters are discussed in paper 4 [28]. This part is aimed to use the closed-form mathematical relationships between the drivetrain dynamic properties and amplitude of response with the drivetrain reduced-order model parameters supported by sensitivity analyses for a subsequent use in the proposed fault diagnosis algorithm, based on the general 3-DOF torsional model of drivetrain. In order to achieve the above described purposes, two different sets of sensitivity analyses are performed in this section. First, a sensitivity analysis is performed on torsional frequencies and normal mode shapes of the equivalent undamped system to extract drivetrain system-level condition monitoring features. Second, a sensitivity analysis is performed on the amplitude of response at the natural frequencies primarily to estimate the damping coefficient and subsequently the undamped natural frequencies which are required for the first analysis, and secondarily to validate the condition monitoring features obtained in the first sensitivity analysis.

Local sensitivity analysis determines how a small perturbation around an input parameter value influences the value of the output. In the proposed fault diagnosis approach, in order to find the parameters with the highest impact on the drivetrain dynamic characteristics, local sensitivity analysis is employed for two reasons. First, the motivation of this work is detecting faults in an early stage of progress for preventive maintenance purposes.

Therefore, variations in the drivetrain system parameters is expected to happen with a slight change around the nominal values. Second, local sensitivity analysis derives a closed form expression for the sensitivity value which is valuable for implementation purposes. Local sensitivity is defined as the partial derivative of the output function with respect to the input parameters [67] as

$$S_{k,l}^{Loc} = \frac{\delta y_k}{\delta x_l},\ y_k \in \{y_1, ..., y_p\}\ and\ x_l \in \{x_1, ..., x_q\}, \tag{5.10}$$

In the above equation, y_k is the k^{th} output and x_l is the l^{th} input. In order to neutralize the impact of large/small inputs and small/large outputs, the local sensitivity can be normalized by the nominal values of inputs and outputs as

$$S_{k,l}^{Norm} = \frac{x_l^{ref}}{y_k^{ref}} \frac{\delta y_k}{\delta x_l}, \tag{5.11}$$

In the above equation, x_l^{ref} and y_k^{ref} are the nominal values of x_l and y_k. In the 3-DOF torsional model, the input and output vectors for sensitivity analysis are

$$x = \{k_L,\ k_H,\ J_r,\ J_{gr},\ J_{gn},\ c_L,\ c_H,\ T_r,\ T_g\}, \tag{5.12a}$$

$$y = \{\Omega_1^{tor},\ \Omega_2^{tor},\ \Psi_{rot}^{\Omega_1},\ \Psi_{rot}^{\Omega_2},\ \Psi_{gear}^{\Omega_1},\ \Psi_{gear}^{\Omega_2},\ \Psi_{gen}^{\Omega_1},\ \Psi_{gen}^{\Omega_2},\ |e_{tot}^{\omega}(\Omega_1^{tor})|,\ |e_{tot}^{\omega}(\Omega_2^{tor})|\}. \tag{5.12b}$$

The closed form of equations after applying normalized local sensitivity analysis to eqs. (5.7), (5.8) and (5.9) to find the sensitivity of drivetrain system dynamic properties and amplitude of response at the natural frequencies to the equivalent model parameters based on 3-DOF model are reported in paper 4 [28].

5.3.3 Results of proposed fault diagnosis approach validation

As discussed in [28], drivetrain system-level faults represent themselves by the variations of 3-DOF model equivalent stiffness and inertia parameters.

The detection of the faults which influence the stiffness the most is possible in the proposed approach by monitoring the consequences of these faults on the drivetrain torsional modes based on the results of sensitivity analysis. In order to simulate the stiffness related faults, the torsional stiffness

of the main and high-speed shafts in the SIMPACK model is reduced in four steps from 5 to 50%. The resultant variations in the natural frequencies and normal modes are listed in the Tables 5.3 and 5.4.

Table 5.3: Main shaft fault cases [28].

Fault case	$\frac{k_L}{k_L^n}$	$\frac{\Omega_1^{tor}}{\Omega_1^{tor,n}}$	$\frac{\Omega_2^{tor}}{\Omega_2^{tor,n}}$	$\frac{\Psi_{rot}^{\Omega_1}}{\Psi_{rot}^{\Omega_1,n}}$	$\frac{\Psi_{rot}^{\Omega_2}}{\Psi_{rot}^{\Omega_2,n}}$	$\frac{\Psi_{gear}^{\Omega_1}}{\Psi_{gear}^{\Omega_1,n}}$	$\frac{\Psi_{gear}^{\Omega_2}}{\Psi_{gear}^{\Omega_2,n}}$	$\frac{\Psi_{gen}^{\Omega_1}}{\Psi_{gen}^{\Omega_1,n}}$	$\frac{\Psi_{gen}^{\Omega_2}}{\Psi_{gen}^{\Omega_2,n}}$
$LC0$	1	1	1	1	1	1	1	1	1
$LC1$	0.95	0.975	1.000	1.000	0.950	1.000	1.000	1.000	1.000
$LC2$	0.85	0.923	0.999	1.000	0.851	1.001	1.000	1.000	1.001
$LC3$	0.7	0.838	0.999	1.000	0.000	1.003	1.000	1.000	1.003
$LC4$	0.5	0.709	0.998	1.000	0.000	1.005	1.000	1.000	1.005

Table 5.4: High-speed shaft fault cases [28].

Fault case	$\frac{k_H}{k_H^n}$	$\frac{\Omega_1^{tor}}{\Omega_1^{tor,n}}$	$\frac{\Omega_2^{tor}}{\Omega_2^{tor,n}}$	$\frac{\Psi_{rot}^{\Omega_1}}{\Psi_{rot}^{\Omega_1,n}}$	$\frac{\Psi_{rot}^{\Omega_2}}{\Psi_{rot}^{\Omega_2,n}}$	$\frac{\Psi_{gear}^{\Omega_1}}{\Psi_{gear}^{\Omega_1,n}}$	$\frac{\Psi_{gear}^{\Omega_2}}{\Psi_{gear}^{\Omega_2,n}}$	$\frac{\Psi_{gen}^{\Omega_1}}{\Psi_{gen}^{\Omega_1,n}}$	$\frac{\Psi_{gen}^{\Omega_2}}{\Psi_{gen}^{\Omega_2,n}}$
$LC0$	1	1	1	1	1	1	1	1	1
$LC1$	0.95	1.000	0.975	1.000	1.052	1.000	1.000	1.000	1.000
$LC2$	0.85	0.999	0.923	1.000	1.175	0.998	1.000	1.000	0.998
$LC3$	0.7	0.998	0.838	1.000	1.423	0.996	1.000	1.000	0.996
$LC4$	0.5	0.996	0.710	0.993	1.983	0.991	1.000	1.000	0.991

As it can be seen from these tables, the simulation results agree with the results obtained from the analytical sensitivity analysis of natural frequencies and normal modes as reported in paper 4 [28]. The fault detection features are obtained from the physical model, and the threshold for these physical features can accordingly be specified based on the aforedescribed sensitivity analysis applied to a specific drivetrain. As an example of stiffness-related faults, a shaft crack causes the reduced torsional stiffness of the shaft and the changed drivetrain torsional natural frequencies. The reduction of the 1^{st} natural frequency due to a crack in the main shaft is demonstrated in Figure 5.5a. As it can be seen, for the two operations with the same loading conditions, one for the normal system and the other for the system with a crack in the main shaft, the amplitude of response at the 1^{st} natural frequency is higher in the system with the cracked shaft compared to the normal system, which agrees with the results of the analytical sensitivity analysis

of the amplitude of response as reported in paper 4 [28]. The influence of a crack in high-speed shaft and its consequence in the drop of the 2^{nd} natural frequency is shown in Figure 5.5b. A crack in the high-speed shaft causes an increased amplitude of response at the 2^{nd} natural frequency, which agrees with the analytical sensitivity analysis results related to the amplitude of response at the 2^{nd} mode as reported in paper 4 [28]. Figures 5.5a and 5.5b are normalized with respect to the normal system results.

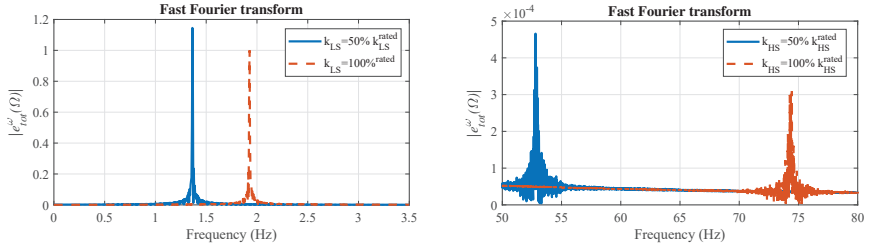

(a) *(b)*

Figure 5.5: Simulation results of stiffness-related faults based on DTU 10 MW floating wind turbine model [28] (paper 4). (a) Fault in low-speed shaft. (b) Fault in high-speed shaft.

The detection of inertia-related faults is also possible by monitoring the consequences on the drivetrain torsional modes based on the sensitivity analysis results. In here, in order to simulate the severe unbalance faults, the inertia of the associated component is increased in three steps from 5 to 20%. The subsequent changes in the drivetrain modes are listed and shown in the Tables 5.5- 5.7, which show that the simulation results agree with the analytical sensitivity analysis results as presented in paper 4 [28].

Table 5.5: Inertia-related fault cases (rotor).

Fault case	$\frac{J_r}{J_r^h}$	$\frac{\Omega_1^{tor}}{\Omega_1^{tor,n}}$	$\frac{\Omega_2^{tor}}{\Omega_2^{tor,n}}$	$\frac{\Psi_{rot}^{\Omega_1}}{\Psi_{rot}^{\Omega_1,n}}$	$\frac{\Psi_{rot}^{\Omega_2}}{\Psi_{rot}^{\Omega_2,n}}$	$\frac{\Psi_{gear}^{\Omega_1}}{\Psi_{gear}^{\Omega_1,n}}$	$\frac{\Psi_{gear}^{\Omega_2}}{\Psi_{gear}^{\Omega_2,n}}$	$\frac{\Psi_{gen}^{\Omega_1}}{\Psi_{gen}^{\Omega_1,n}}$	$\frac{\Psi_{gen}^{\Omega_2}}{\Psi_{gen}^{\Omega_2,n}}$
$LC0$	1	1	1	1	1	1	1	1	1
$LC1$	1.05	1.000	1.000	0.952	0.952	1.000	1.000	1.000	1.000
$LC2$	1.10	0.999	1.000	0.909	0.909	1.000	1.000	1.000	1.000
$LC3$	1.20	0.998	1.000	0.833	0.833	1.000	1.000	1.000	1.000

As an example of inertia-related faults, unbalance in the rotor, gearbox or generator results in an increase in the associated equivalent inertia of

Table 5.6: Inertia-related fault cases (gearbox).

Fault case	$\frac{J_{gr}}{J_{gr}^{n}}$	$\frac{\Omega_1^{tor}}{\Omega_1^{tor,n}}$	$\frac{\Omega_2^{tor}}{\Omega_2^{tor,n}}$	$\frac{\Psi_{rot}^{\Omega_1}}{\Psi_{rot}^{\Omega_1,n}}$	$\frac{\Psi_{rot}^{\Omega_2}}{\Psi_{rot}^{\Omega_2,n}}$	$\frac{\Psi_{gear}^{\Omega_1}}{\Psi_{gear}^{\Omega_1,n}}$	$\frac{\Psi_{gear}^{\Omega_2}}{\Psi_{gear}^{\Omega_2,n}}$	$\frac{\Psi_{gen}^{\Omega_1}}{\Psi_{gen}^{\Omega_1,n}}$	$\frac{\Psi_{gen}^{\Omega_2}}{\Psi_{gen}^{\Omega_2,n}}$
$LC0$	1	1	1	1	1	1	1	1	1
$LC1$	1.05	0.998	0.978	1.004	1.046	1.000	1.000	1.000	1.050
$LC2$	1.10	0.997	0.957	1.007	1.092	1.000	1.000	1.000	1.100
$LC3$	1.20	0.993	0.919	1.015	1.183	1.000	1.000	1.000	1.200

Table 5.7: Inertia-related fault cases (generator).

Fault case	$\frac{J_{gn}}{J_{gn}^{n}}$	$\frac{\Omega_1^{tor}}{\Omega_1^{tor,n}}$	$\frac{\Omega_2^{tor}}{\Omega_2^{tor,n}}$	$\frac{\Psi_{rot}^{\Omega_1}}{\Psi_{rot}^{\Omega_1,n}}$	$\frac{\Psi_{rot}^{\Omega_2}}{\Psi_{rot}^{\Omega_2,n}}$	$\frac{\Psi_{gear}^{\Omega_1}}{\Psi_{gear}^{\Omega_1,n}}$	$\frac{\Psi_{gear}^{\Omega_2}}{\Psi_{gear}^{\Omega_2,n}}$	$\frac{\Psi_{gen}^{\Omega_1}}{\Psi_{gen}^{\Omega_1,n}}$	$\frac{\Psi_{gen}^{\Omega_2}}{\Psi_{gen}^{\Omega_2,n}}$
$LC0$	1	1	1	1	1	1	1	1	1
$LC1$	1.05	0.978	0.998	1.046	1.003	1.000	1.000	1.000	0.952
$LC2$	1.10	0.958	0.997	1.093	1.007	1.000	1.000	1.000	0.909
$LC3$	1.20	0.920	0.994	1.186	1.012	1.000	1.000	1.000	0.833

the component in the model. The variation of inertia is different dependent on the severity of unbalance. A slight unbalance can cause a very slight change in the inertia and subsequently a slight change in the modes which makes the detection challenging by the proposed approach. The reduction of 1^{st} and 2^{nd} natural frequency due to the increase of the inertia of generator and gearbox as a result of unbalance faults in generator and gearbox are respectively shown in Figures 5.6a and 5.6b. The influence of increase of rotor inertia, which can model the rotor unbalance fault, on the simultaneous reduction of 1^{st} and 2^{nd} normal mode shapes in rotor position is also shown in Figure 5.6c. All these three figures are normalized with respect to the normal system results.

In paper 5 [29], by using a higher DOF torsional model of NREL 5 MW drivetrain system, the influence of pitting faults in sun-planet gears and ring-planet gears of the 1^{st} and 2^{nd} gearbox stage and their influences on the deviation of the drivetrain natural frequencies is investigated, which shows that monitoring the variations of the natural frequencies can also be used for detecting the drivetrain faults in a component level, *e.g.* the gearbox subcomponents.

The experimental studies are related to the torsional measurements of the drivetrain system of Vestas 1.75 MW turbine. The deviation of 1^{st} nat-

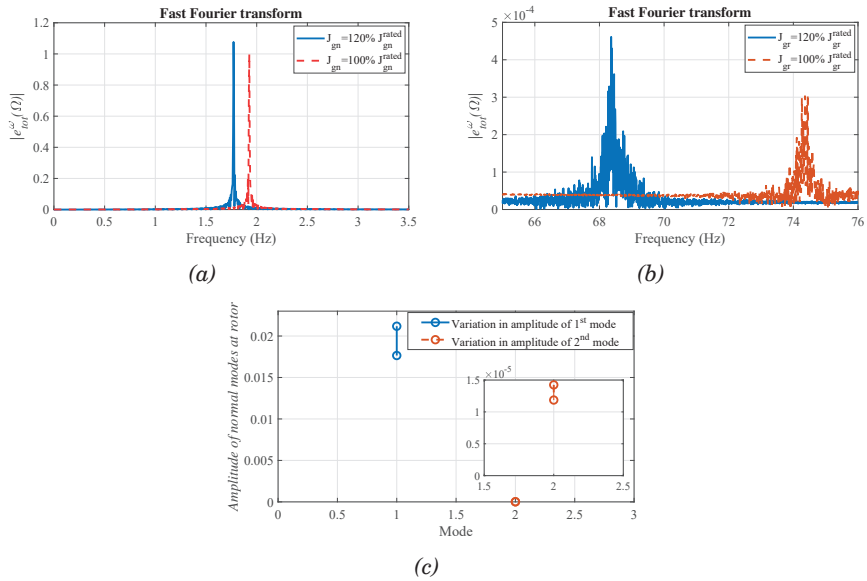

Figure 5.6: Simulation results of inertia-related faults based on DTU 10 MW floating wind turbine model [28] (paper 4). (a) Fault in generator. (b) Fault in gearbox. (c) Fault in rotor.

ural frequency apparently due to a low-speed shaft fatigue crack is shown in Figure 5.7a, which shows the capability of method in detecting the shaft abnormalities in the early stages of progression. As it can be seen, the reduction of the natural frequency at the same operational speed is observed, which can be due to a reduction in the low-speed shaft stiffness as a consequence of an early stage fault in the main shaft. The cracked shaft can represent a periodic reduction in the shaft stiffness due to nonlinear effects such as breathing of the crack. Dependent on the type of crack the variation of the stiffness of the different directions of lateral, axial and torsional could be different, because the stiffness change is dependent on the direction of bending moment at the crack cross-section. Due to the coupling phenomena in a cracked shaft (*i.e.* bending–torsion and longitudinal–torsion), the variations of longitudinal and bending stiffness parameters - they have relationship with the type and depth of crack- also influence the torsional stiffness in later fault stages. Therefore, the assumption made for modelling of a crack with constant torsional stiffness asymmetry seems to be realistic. The performance of the proposed method in the detection of main shaft

faults is compared with three conventional methods in literature based on accelerometers measurements, namely the frequency domain indicator based on observing twice the running frequency component and the subharmonic resonance crack4, crack3; the variable phase-difference between the time-domain measurements of the accelerometers placed on the two sides of shaft at the shaft rotational frequency component; and the RMS of time domain acceleration based on standard ISO 10816-21. The frequency spectra of the two accelerometers which are placed on the two main bearings which support the main shaft are shown in Figure 5.7b. The under consideration turbine has been working with the nominal rotational speed equal to $0.33Hz$ in the low-speed side. As it can be seen, the main revolution frequency, the double frequency and the subharmonics do not show a significant amplitude in the response. The insufficiency of frequency domain analysis in different operating speeds in detecting shaft faults in the general rotor system is also reported in [68]. The other drawback with frequency domain analysis based on our observations is that due to the low-frequency content of the low-speed shaft faults, they can be mistaken with a wide range of excitation frequencies due to environmental and structural motions-induced vibrations which happen in the low-frequency range. Figure 5.7c shows the synchronized time-domain acceleration measurements of AC1 and AC2 which are band-pass filtered around the low-speed shaft rotational frequency. As it can be seen, the figure does not represent any variation in the phase difference between these two signals. Monitoring the variations of the phase difference of the frequency component $0.33Hz$ can be challenging due to the influence of the other frequency components which appear in response in this frequency range. As reported in paper 4 [28], the described abnormality cannot also be detected by using the third method which is the standard time-domain approach grounded on the evaluation of the RMS value of the time series data of the translational vibrations based on standard ISO 10816-21.

By the increase of the order of equivalent model, more dynamic properties (higher natural frequencies which are not seen by 3-DOF model) can be employed in the proposed analytical method, which can support a more detailed fault detection in the drivetrain. However, it can be challenging for currently available modal estimation approaches to observe higher modes which appear with a low amplitude in the frequency-domain response. In other words, the actual condition for the modal estimation problem is restrictive, so that some of the eigenfrequencies of the drivetrain system may not be observable, especially the higher eigenfrequencies which can be excited by the input torque with a lower energy. The application of higher DOF torsional models as more detailed equivalent models which can capture real-

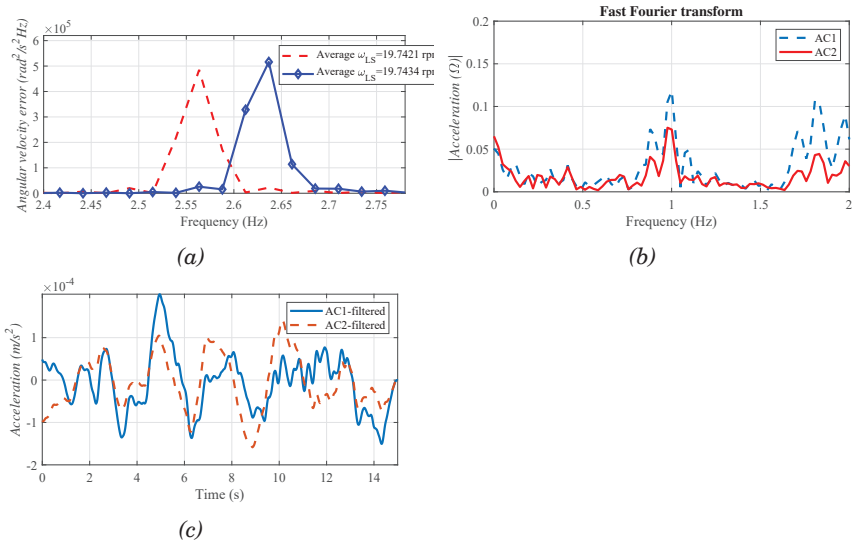

Figure 5.7: Experimental results of stiffness-related faults based on Vestas 1.75 MW drivetrain operational data [28] (paper 4). (a) Fault in main shaft: influence on 1^{st} mode. (b) Fault in main shaft: FFT of accelerometers. (c) Fault in main shaft: phase difference.

time variations in mesh stiffness and inertia of individual gears and intermediate shafts, to detect faults in those subcomponents by taking into account the components internal dynamics is studied in paper 5 [29]. Deriving the analytical model for extracting sufficient fault detecting features to diagnose the drivetrain faults in a component-level is looked as the future work.

In the next chapter, the discussion on torsional vibrations is continued but for a different purpose which is monitoring the remaining useful lifetime of the drivetrain components, by using digital twin modeling approaches.

Chapter 6

Digital twin-based fault prognosis by torsional measurements

6.1 General

In this chapter, digital twin-based fault prognosis of the drivetrain components by using the torsional measurements is discussed. Fault prognosis in this context means the near real-time estimation of the remaining useful lifetime (RUL) of the drivetrain components. Digital twin in this context consists of torsional dynamic models, online measurements and fatigue damage estimation, which are used for RUL estimation.

This chapter summarizes the methodology and reports a part of the results of the studies performed by Moghadam *et al.* [29] in paper 5, and Moghadam and Nejad [30] in paper 6. The method is designed in the general form for multi-degree-of-freedom (n-DOF) torsional model of the drivetrain. Then the method is developed for the estimation of RUL in different components of the drivetrain system. *In paper 6* [30], the method is developed based on 3-DOF equivalent torsional model of drivetrain as the drivetrain digital twin (DT) for monitoring the residual life of main and high-speed shafts, where the fatigue damage due to cyclic torsional-bending load is focused. *In paper 5* [29], the method is developed by using 14-DOF torsional model as DT of the drivetrain system for estimating the real-time degradation of the gears in the gearbox due to pitting fatigue damage and the gear pairs contact loads.

The degradation models are based on proven physics-based approaches

for the estimation of fatigue damage, which are supported by statistical approaches and stochastic models to address uncertainties to improve the accuracy. These methods which rely on real-time measurements, are computationally fast, can apply to different drivetrain components and are not restricted by the operational conditions.

In the following sections, the drivetrain DT model and the online estimation of equivalent reduced order model (ROM) parameters by using the torsional response and aerodynamic torque observer is discussed. Then, in the rest of this chapter, the design of real-time load observers for the drivetrain components by using DT model and operational measurements, the estimation of equivalent stress and then the degradation model is explained. The proposed DT model estimation approach and its application for monitoring drivetrain components residual life is evaluated by the simulation studies based on the drivetrain systems of DTU 10 MW and NREL 5 MW reference wind turbines.

The research contributions of this PhD work which are covered by this chapter are:

- Computationally fast digital twin models of the drivetrain system based on the torsional measurements and computationally inexpensive equivalent torsional models are proposed, which are aimed at monitoring the residual life of the components. The digital twin model based on 14-DOF equivalent of the drivetrain system is proposed for remaining useful lifetime (RUL) monitoring of the gearbox, which is tested for estimating the residual life of the gears of NREL 5 MW gearbox model and validated by comparing the results with high-fidelity simulation models. The digital twin model based on 3-DOF equivalent model is also proposed for estimating the residual life of main and high-speed shafts, which is tested by DTU 10 MW model. The proposed digital twin models leverage stochastic physics-based degradation models for estimating RUL in the drivetrain components by using the online estimated reduced order model (ROM), real-time torsional measurements, designed load observers and equivalent stress estimation approaches. These models take into consideration the various sources of uncertainty by using statistical approaches and stochastic models, namely Kalman filtering, Monte Carlo simulations and assuming fatigue damage as a random variable.

- The online estimation of the parameters of drivetrain equivalent models of different degrees of freedom by using the torsional response and the estimated values of drivetrain input torques is discussed. The pro-

posed robust least square error (LSE) estimator defined based on minimizing the difference between the equivalent model and the real-time measurements provides the best unbiased estimation of the coefficients in the linear regression model. Confidence intervals for estimation error of the ROM parameters are provided by using stochastic models supported by Monte Carlo simulations.

6.2 Estimation of drivetrain equivalent model by using the torsional measurements

The proposed algorithm for estimating the drivetrain equivalent ROM parameters and dynamic properties is described in this section.

6.2.1 Estimation of moment of inertia matrix

The general damped n-DOF torsional dynamical model of drivetrain can be represented by the following equation. The summation of the moments on each inertia in the lumped parameter model yields n equations of the form [69]

$$j_i\ddot{\boldsymbol{\theta}}_i(t)+C_i\left(\dot{\boldsymbol{\theta}}_i(t)-\dot{\boldsymbol{\theta}}_{i-1}(t)\right)-C_{i+1}\left(\dot{\boldsymbol{\theta}}_{i+1}(t)-\dot{\boldsymbol{\theta}}_i(t)\right)+k_i(\boldsymbol{\theta}_i(t)-\boldsymbol{\theta}_{i-1}(t))- k_{i+1}(\boldsymbol{\theta}_{i+1}(t)-\boldsymbol{\theta}_i(t))=T_i(t),\quad for\ i=(1,\ldots,n). \tag{6.1}$$

In the above equation, $\boldsymbol{\theta}_i$ is the angular displacement of i^{th} body. j_i is the inertia of i^{th} body. k_i is the equivalent stiffness between $(i-1)^{th}$ and i^{th} bodies. k_{i+1} is the equivalent stiffness between i^{th} and $(i+1)^{th}$ bodies. T_i is the external excitation applied to the i^{th} body. By using a matrix form representation, these set of equations can be rewritten as

$$\mathrm{J}\ddot{\boldsymbol{\Theta}}\ (\boldsymbol{t})+\mathrm{C}\dot{\boldsymbol{\Theta}}(\boldsymbol{t})+\mathrm{K}\boldsymbol{\Theta}(\boldsymbol{t})=\mathrm{T}(t). \tag{6.2}$$

In the above equation, **J**, **C** and **K** are the moment of inertia, damping and stiffness matrices with the size $n\times n$. $\boldsymbol{\Theta}$ and T are the response and load vectors with the size $n\times 1$, where each element of these two vectors represents a time series data. This model alongside the torsional measurements provide the inputs for the drivetrain model parameter estimation approach. The optimization variables are **J**, **C** and **K** matrices which are the drivetrain equivalent lumped model parameters. The sparsity of the matrix variables **J**, **C** and **K** are specified based on the drivetrain topology and is imposed to the optimization problem. Assuming that the load and response time series

are known, the parameter estimation problem turns to the minimization of the *L2*-norm of error. The error function is defined by

$$\boldsymbol{E}(t) \triangleq \widehat{\mathrm{J}}\ddot{\boldsymbol{\Theta}}(t) + \widehat{\mathrm{C}}\dot{\boldsymbol{\Theta}}(t) + \widehat{\mathrm{K}}\boldsymbol{\Theta}(t) - \mathrm{T(t)}. \tag{6.3}$$

Therefore, the least square error (LSE) estimator is defined to estimate the equivalent model parameters by minimizing the error function E between the model and measurements as

$$\begin{aligned} \widehat{\mathrm{J}}^{\mathrm{LS}}, \widehat{\mathrm{K}}^{\mathrm{LS}}, \widehat{\mathrm{C}}^{\mathrm{LS}} \in \arg \quad & \min\{\|\boldsymbol{E}\|_{\mathbf{2}}\} \\ & \mathrm{J,K,C} \geq \mathbf{0} \\ & \mathrm{J}_{l,m} \in \boldsymbol{S}^{\mathrm{J}} \\ & \mathrm{K}_{l,m} \in \boldsymbol{S}^{\mathrm{K}} \\ & \mathrm{C}_{l,m} \in \boldsymbol{S}^{\mathrm{C}} \end{aligned} . \tag{6.4}$$

In the above equation, $\boldsymbol{S}^{\mathrm{J}}$, $\boldsymbol{S}^{\mathrm{K}}$ and $\boldsymbol{S}^{\mathrm{C}}$ are the sparsity sets of matrices **J**, **K** and **C**. The matrix **J** is diagonal. **K** and **C** are non-diagonal symmetric matrices which are not full rank. The latter may cause computational difficulty for the above quadratic matrix optimization problem, and subsequently there is a possibility of divergence of the numerical solver. The larger perturbations due to the singular terms into the calculations than the numerically stable counterpart can cause larger errors in the solution. In order to simultaneously remove the coupling between the equations due to the **K** and **C** terms, cope with the error arisen from the ill-condition terms of model, and reduce the computational complexity by reduction of the number of variables, a summation operation is applied to the set of dynamic equations (6.1) of each inertia, which results in the elimination of stiffness and damping from the resultant scalar optimization problem. The latter leads to the following error function in terms of the inertia variables j_i as the model scalar variables and the torsional measurements time-series as the inputs, by assuming rotor as the reference of the rotary coordinate [29, 30].

$$\boldsymbol{e}(t) = j_1\dot{\boldsymbol{\Omega}}_1(t) + \cdots + u_{1,i}j_i\dot{\boldsymbol{\Omega}}_i(t) + \cdots + u_{1,n}j_n\dot{\boldsymbol{\Omega}}_n(t) - T_r(t) - u_{1,n}T_{gn}(t). \tag{6.5}$$

In the above equation, $\dot{\boldsymbol{\Omega}}_i$ is the time series of angular acceleration and j_i is the moment of inertia of the i^{th} DOF. T_r and T_{gn} are the time series of the rotor and generator torques, respectively. The response used in this equation is the angular acceleration which can be obtained by applying a derivation operation to the angular velocity measurements, or the second derivation to the angular displacement measurements. The sign of $u_{1,i}$ is determined based on the direction of rotation of j_i. Since the real-time values of response are known, the inertia parameters can be estimated by minimizing

the square error between the model and measurements. The LSE estimator constructed based on the difference between the estimated values as the model outputs and the actual value as the sensor measurements provides the best unbiased estimation of the coefficients in a linear regression model. The LSE function results in the following quadratic scalar optimization problem as

$$\hat{\mathbf{J}}^{\mathrm{LS}} = \arg \min_{j \geq 0} \{\|e\|_{\mathbf{2}}\} \quad . \tag{6.6}$$

This estimator is robust to the measurement noises, and can provide a good approximation even with less than n input data samples (underdetermined case). For the case of more than n samples (overdetermined case), this estimator helps to obtain more accurate estimation than solving the linear equations, when the input measurements are subject to independent and identically distributed (IID) Gaussian noise. In other words, the total LSE technique is able to correct the system with minimum perturbation [70]. The above convex multi-variate scalar optimization problem can be solved numerically by Matlab CVX, so that the global optimizer $j^{LS} = \{j_1, \ldots, j_n\}$ is estimated. Since this *L2*-norm regression optimization problem is in a quadratic convex form, the results which are the estimated values of the drivetrain ROM inertia parameters are the global optimizers of the problem.

For the special case of Gaussian noise, the LSE problem is mathematically equivalent to the maximum likelihood (ML) estimator [30]. The ML estimator is restricted by the assumption that the form of the distribution of random noise defined by the error function $\mathbf{e}(t)$ is known, so that the likelihood function can be constructed. Based on the extensive simulations, the error calculated from the torsional measurements in the under consideration application shows a near Gaussian distribution. Therefore, both LSE and ML estimators are expected to lead to the similar set of results.

As discussed earlier, the inputs of the optimization problem defined by equation 6.6 are the torsional response and the rotor and generator torques. The generator torque is a measurement available in the turbine for the generator control purposes. The generator torque is estimated from the generator electrical measurements, which is available in turbine main control unit. The aerodynamic torque applied to the drivetrain simulation model is obtained from the global simulations. However, in reality, the real value of applied aerodynamic torque is not available, but a estimation can be available by using the turbine operational measurements and the general information of the airfoil. The estimated torque can then be applied as the input to the drivetrain model identification approach. The algorithms for estimating the rotor and generator torques from the turbine operational measurements are

discussed by Moghadam and Nejad [30] in paper 6.

6.2.2 Estimation of stiffness matrix

The proposed method for estimating drivetrain system undamped natural frequencies from the torsional measurements was discussed in chapter 5. Therefore, as the next step, the stiffness parameters of the model are estimated by using the estimated inertia parameters from the LSE optimization problem and the estimated resonance frequencies from the torsional measurements. The undamped natural frequencies are a nonlinear function of inertia and stiffness as defined by

$$\boldsymbol{\omega}_i \ (for\ i = 1,\ldots,n) = \sqrt{eig(-\mathrm{J}^{-1}\mathrm{K})}. \tag{6.7}$$

Therefore, the stiffness matrix $\mathbf{K}$ is the root of the function g_i which is defined by the following nonlinear equation as [29, 30]

$$\boldsymbol{g}_i = {\boldsymbol{\omega}_i}^2 - eig(-\mathrm{J}^{-1}\mathrm{K}),\ (for\ i = 1,\ldots,n). \tag{6.8}$$

By imposing the sparsity and symmetricity to matrix $\mathbf{K}$ from the lumped model, it is possible to find the global optimizer $\mathbf{K}$ numerically by using Matlab fsolve. The latter also helps to reduce commutation cost of this matrix algebraic equation by reducing the number of variables from n^2 to n. The matrix $\mathrm{J}^{-1}\mathrm{K}$ is not symmetric in the general case which may give the sense that there are multiple answers for $\mathbf{K}$ from this equation. However, the fact that $-\mathrm{J}^{-1}\mathrm{K}$ is positive definite, shows that this matrix is a small perturbation of a symmetric matrix with positive eigenvalues, which keeps the eigenvalues positive [71].

The usual condition for the estimation problem is more restrictive. In other words, it is possible that only some of the eigenfrequencies of the drivetrain system can be estimated by employing the aforedescribed modal estimation approach, especially the higher eigenfrequencies which are excited with a lower energy of the input torque. In this case, the matrix $\mathbf{K}$ can be estimated by using the following optimization problem in terms of the first i eigenfrequencies as defined by using the following least square error estimator as [29, 30]

$$\widehat{\mathrm{k}}^{\mathrm{LS}} = \arg \min_{\boldsymbol{\Lambda} \in \Lambda} \{\| \boldsymbol{\lambda}_i - eig(\boldsymbol{\Lambda},\ i)\|^{\mathbf{2}}\}\ . \tag{6.9}$$

In the above equation, $\widehat{k}^{LS}$ is the set of nonzero elements of matrix K which are estimated by the above nonlinear matrix optimization problem. The sign of the elements of k are forced in the optimization problem. $\boldsymbol{\Lambda}$ is the

variable of this optimization problem, which is a function of the unknown variable K as $\mathbf{\Lambda} = -\mathrm{J}^{-1}\mathrm{K}$. $\boldsymbol{\lambda}_i$ is the set of i ($\mathrm{i} \in \{1,\ldots,\mathrm{n}\}$) smallest magnitude eigenvalues which are known from the modal estimation, $\boldsymbol{\lambda}_i = \{{\omega_1}^2,\ldots,{\omega_i}^2\}$. $eig(\mathbf{\Lambda}, i)$ is the set of i ($\mathrm{i} \in \{1,\ldots,\mathrm{n}\}$) smallest magnitude eigenvalues defined in terms of matrix J and the unknown matrix K. The feasible set Λ is defined by

$$\Lambda = \{\mathbf{\Lambda} : \mathbf{\Lambda} \in \mathbb{R}^{n\times \mathrm{n}},\ \ \mathrm{K} \geq \mathbf{0},\ \ \mathbf{\Lambda}_{l,m} = 0,\ \forall\ \mathbf{\Lambda}_{l,m} \in \boldsymbol{S}^{\mathbf{\Lambda}}\}, \tag{6.10}$$

In the above equation, $\boldsymbol{S}^{\mathbf{\Lambda}}$ is the sparsity set of matrix $\mathbf{\Lambda}$. The positive definiteness and sparsity of $\mathbf{\Lambda}$ are the constraints imposed to this problem. For the set of positive semidefinite matrices, this problem is convex so that the solution gives the global optimizer. However, $\mathbf{\Lambda}$ is not symmetric in general so that the definition of the problem is nonconvex for the numerical solvers and convex optimization tools are not able to numerically solve the problem. In order to solve the aforedescribed optimization problem, Matlab fmincon solver applicable for nonlinear nonconvex problems is used.

For the system with n-DOF, the system has $n-1$ nonrigid torsional modes. The latter leads to $n-1$ nonlinear equations which are the undamped natural frequencies as nonlinear functions of equivalent model inertia and stiffness parameters. These set of nonlinear equations are numerically solved, and n equivalent stiffness seen by each body are estimated. The estimated values of stiffness parameters are the main diagonal of the matrix. When the degree of the model increases, it is not easy to access the closed form of the n scalar nonlinear equations. However, the equations can still be solved numerically in the matrix form. By the increase of the degree of model, the computational complexity of algorithm increases, but it can provide more detailed DT model for condition monitoring of a wider range of drivetrain subcomponents.

In [30], 3-DOF model is used for RUL monitoring of the drivetrain main and high-speed shafts. In this case, the nonlinear matrix equation represented by eq. (6.9) is reduced to the two nonlinear scalar equations for the two nonrigid modes as [27]

$$F1(\mathrm{k_L},\mathrm{k_H}) = \omega_1 - \sqrt{\frac{\mathrm{k_L}}{2\mathrm{J_r}} + \frac{\mathrm{k_L}+\mathrm{k_H}}{2\mathrm{J_{gr}}} + \frac{\mathrm{k_H}}{2\mathrm{J_{gn}}} - \sqrt{\left(\frac{-\mathrm{k_L}}{2\mathrm{J_r}} - \frac{\mathrm{k_L}-\mathrm{k_H}}{2\mathrm{J_{gr}}} + \frac{\mathrm{k_H}}{2\mathrm{J_{gn}}}\right)^2 + \frac{\mathrm{k_L k_H}}{\mathrm{J_{gr}^2}}}}, \tag{6.11a}$$

$$F2(\mathrm{k_L},\mathrm{k_H}) = \omega_2 - \sqrt{\frac{\mathrm{k_L}}{2\mathrm{J_r}} + \frac{\mathrm{k_L}+\mathrm{k_H}}{2\mathrm{J_{gr}}} + \frac{\mathrm{k_H}}{2\mathrm{J_{gn}}} + \sqrt{\left(\frac{-\mathrm{k_L}}{2\mathrm{J_r}} - \frac{\mathrm{k_L}-\mathrm{k_H}}{2\mathrm{J_{gr}}} + \frac{\mathrm{k_H}}{2\mathrm{J_{gn}}}\right)^2 + \frac{\mathrm{k_L k_H}}{\mathrm{J_{gr}^2}}}}. \tag{6.11b}$$

By solving these two nonlinear equations, the values of k_L and k_H which are respectively the stiffness of main and high-speed shafts are estimated. For all $k_L, k_H \in R^+$, there is a unique solution for the above set of nonlinear

equations which ease solving the equations numerically. The proposed algorithm for estimating the equivalent model parameters of the 3-DOF model based on the detailed explanation given in the above text is summarized in the flowchart in Figure 6.1.

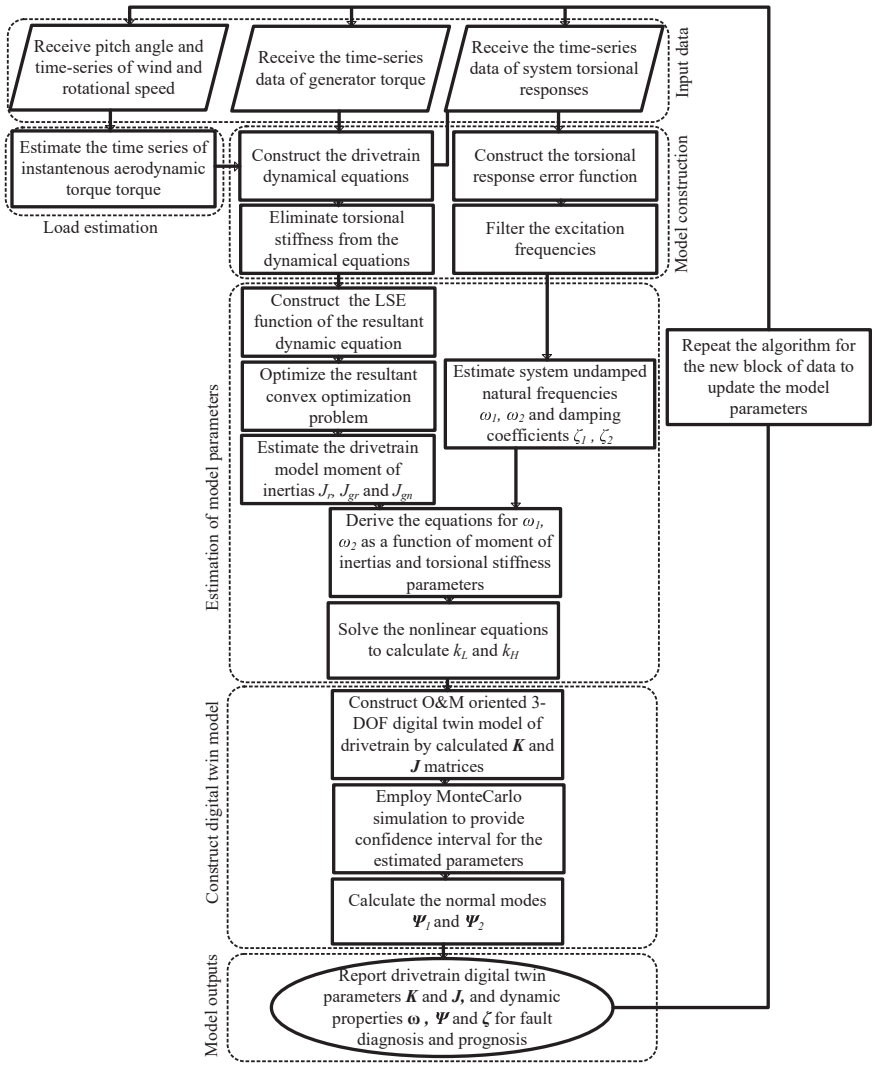

Figure 6.1: Proposed algorithm for estimation of drivetrain equivalent model parameters [30].

In [29], the algorithm is developed for 14-DOF model to be used for RUL monitoring of the different gears of the planetary/parallel gear stages of the drivetrain gearbox. For this case, the nonlinear matrix equation represented by the equation (6.9) is numerically solved to estimate the stiffness parameters.

6.2.3 Results of ROM model estimation

The results of applying the proposed algorithm for estimation of the equivalent 3-DOF model of DTU 10 MW drivetrain are investigated in here. The validation criterion for the estimated model parameters is the relative error percentage of less than *5%*. In order to identify the 3-DOF model, five parameters, namely J_r, J_{gr}, J_{gn}, k_L and k_H which are respectively the equivalent rotor inertia, gearbox inertia, generator inertia, main shaft stiffness and high-speed shaft stiffness should be specified. The estimated parameters and the errors of estimation versus the number of samples (2, 3, 5, 7, 10, 100, 1000) for the three different drivetrain operational conditions (EC1, EC2 and EC3, [30]) by using the actual value of input torque are shown in Figure 6.2.

The procedure explained by paper 6 [30] is followed to provide an analytical criterion/margin of the error for the proposed parameter estimation approach. With respect to the fact that the error time series at each test case meets the conditions of IID central limit theorem (CLT), in order to attain a reliable value of error in each test case, the number of data blocks for each test case is selected to ensure that with the confidence *99%*, the error places in the interval $\hat{\mu}_l \pm 2.58\frac{s}{\sqrt{l}}$. Therefore, the reported estimated parameters and errors are the most expected values with the specified confidence interval. For the case of fewer number of samples in each data block, the variance of errors is higher, which calls for a higher number of data blocks to realize the specified confidence level. In order to realize the confidence *99%* for the interval $\pm 5\%$ around the average estimated error, the minimum required number of data blocks at each test can be calculated by $l > 2662.56(\frac{s}{\hat{\mu}})^2$.

As it can be seen in Figure 6.2, the average estimation error is less than *1%* when the number of algorithm input samples (the length of each data block) is more than *5*. By increasing the number of samples, the error tends to zero. In addition, the method is not sensitive to the turbine operational conditions, and demonstrates a similar performance under different environmental conditions. By reducing the number of input measurement samples from *1000* to *10*, the computational time reduces by about *70%*. The saving in the computation time by reduction of the number of samples is expected to

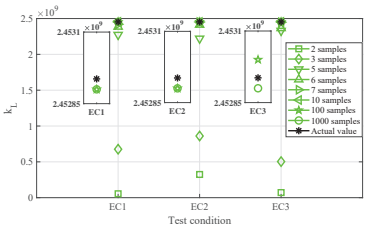

(a) Estimated main shaft stiffness vs. EC_i

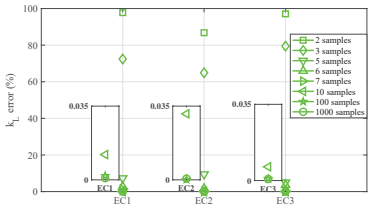

(b) Error in estimated main shaft stiffness vs. EC_i

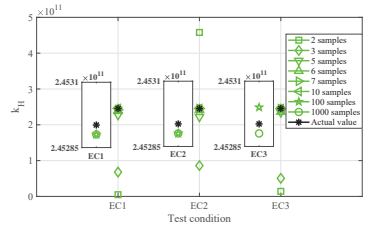

(c) Estimated high-speed shaft stiffness vs. EC_i

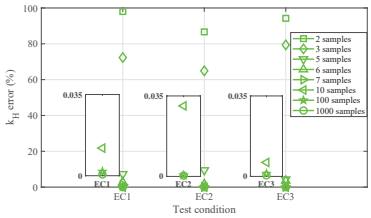

(d) Error in estimated high-speed shaft stiffness vs. EC_i

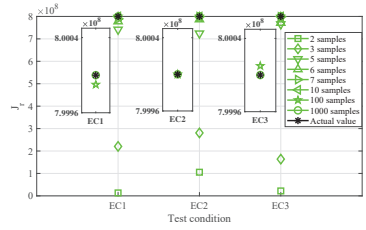

(e) Estimated rotor inertia versus EC_i

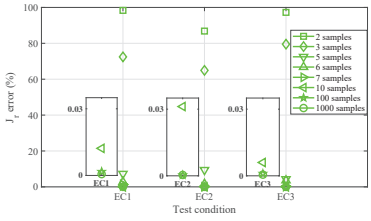

(f) Error in estimated rotor inertia vs. EC_i

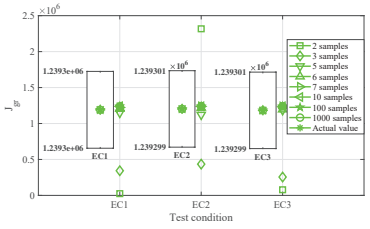

(g) Estimated gearbox inertia versus EC_i

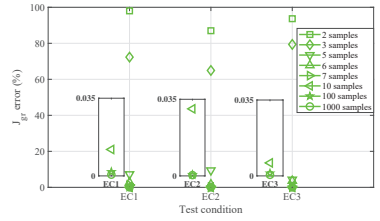

(h) Error in estimated gearbox inertia vs. EC_i

be more significant when the number of estimation variables (the degree of ROM) increases. The use of *10* samples with the sampling frequency *300Hz*,

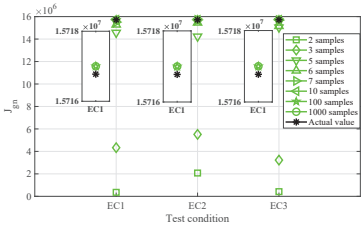

(i) Estimated generator inertia vs. EC_i

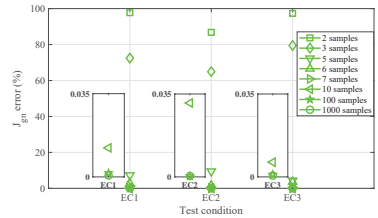

(j) Error in estimated generator inertia vs. EC_i

Figure 6.2: Estimated ROM model parameters of DTU 10 MW drivetrain, by using the actual aerodynamic torque [30] (paper 6). (a) k_L, (b) k_L relative error, (c) k_H, (d) k_H relative error, (e) J_r, (f) J_r relative error, (g) J_{gr}, (h) J_{gr} relative error, (i) J_{gn}, (j) J_{gn} relative error.

means the estimation of parameters in only the fraction of a second, which shows the possibility of algorithm to be executed in real-time.

The performance of proposed algorithm when the estimate value of aerodynamic torque instead of the actual value is applied as input to the algorithm, is shown in Figure 6.3. The latter is to address the uncertainty in the input torque for the proposed system identification algorithm. The estimated torque is calculated in real-time by an aerodynamic torque observer based on the turbine and blades online information by using the theory explained in paper 6 [30]. As it can be seen, for the case of using the estimated torque, the method needs more input data to maintain the 5% threshold set for the estimation error. The reason is that in case of few samples, the LSE estimator is more sensitive to the error of torque estimation of the individual samples. The error tends mostly to reduce by the increase of the input samples.

The performance of proposed system identification approach in tracking the variations in the system parameters in five different fault cases, namely faults in the main shaft, high-speed shaft, rotor, gearbox and generator is shown in Figure 6.4. More details about the simulated fault scenarios can be found in paper 6 [30]. These simulation cases are designed to evaluate the capability of the proposed algorithm in tracking the variations of the system parameters which are representing different system-level fault cases. Variations in each equivalent model parameter can represent a specific class of the drivetrain faults. The results shown in Figure 6.4 prove that the proposed DT model parameter estimation algorithm can track the variations in system perfectly.

The results related to the estimation of the parameters of the 14-DOF

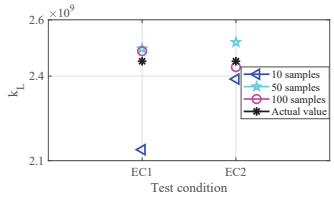

(a) Estimated main shaft stiffness vs. EC_i

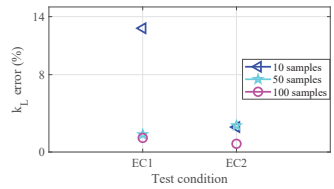

(b) Error in estimated main shaft stiffness

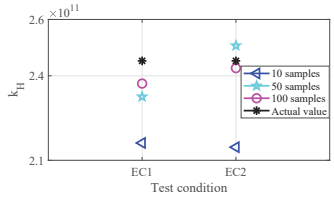

(c) Estimated high-speed shaft stiffness vs. EC_i

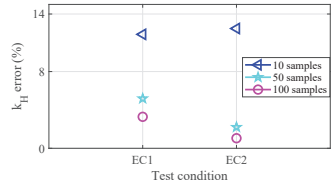

(d) Error in estimated high-speed shaft stiffness

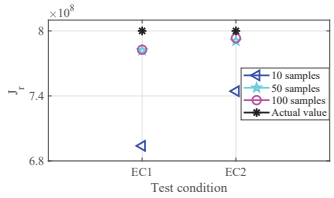

(e) Estimated rotor inertia vs. EC_i

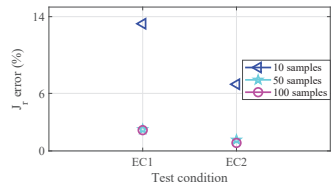

(f) Error in estimated rotor inertia vs. EC_i

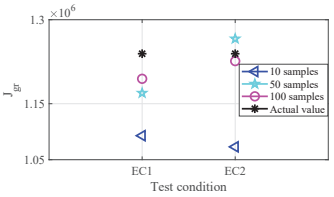

(g) Estimated gearbox inertia vs. EC_i

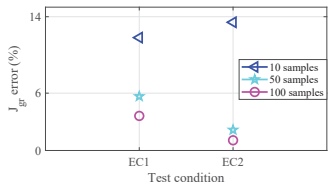

(h) Error in estimated gearbox inertia vs. EC_i

equivalent torsional lumped parameter model of NREL 5 MW drivetrain by using the proposed approach are shown in Table 6.1, which show that the estimation error of model parameters by using the proposed method is less than 1 %. The details about the 14-DOF model and the definition of the parameters are presented in paper 5 [29]. The results related to the estimation of equivalent model parameters in the case that only some of natural frequencies are known, based on solving the optimization problem in equation

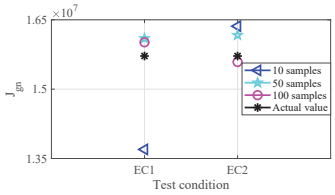

(i) Estimated generator inertia vs. EC_i

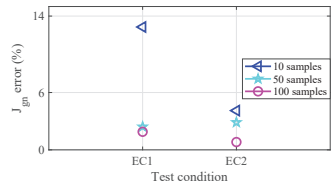

(j) Error in estimated generator inertia vs. EC_i

Figure 6.3: Estimated ROM parameters of DTU 10 MW drivetrain, by using the estimated aerodynamic torque [30] (paper 6). (a) k_L, (b) k_L relative error, (c) k_H, (d) k_H relative error, (e) J_r, (f) J_r relative error, (g) J_{gr}, (h) J_{gr} relative error, (i) J_{gn}, (j) J_{gn} relative error.

6.9, is reported in paper 5 [29]. In a stability perspective, the LSE estimator outperforms the first method which is based on solving the nonlinear equation 6.8, because the eigenfrequencies of $\mathbf{\Lambda}$ in the LSE estimator are forced to be positive, which ensures the convergence of the numerical solver. In other words, the LSE estimator is more robust to the input data, and is recommended also in the case that all the frequency modes are available.

6.3 Estimation of load and stress in the drivetrain components

6.3.1 Estimation of load and stress in main and high-speed shafts

The estimation of load and stress in the drivetrain components is possible by the real-time operational data and the online estimated ROM model, which both feed the designed load observers aimed at estimating the real-time load in the drivetrain components. Then the value of load is used to calculate stress and damage in the components. The algorithm can be adjusted for lifetime monitoring of different components of the drivetrain dependent on the degree of the DT model. The algorithm based on 3-DOF DT model is able to estimate the near real-time load in the main and high-speed shafts and measures the residual life of shafts by taking into account the variations of the shafts loading. To achieve this purpose, two torque observers are designed to estimate the main and high-speed shafts torques by using the torsional measurements and updated values of torsional stiffness parameters from the DT model. Then by using the estimated loads, the maximum

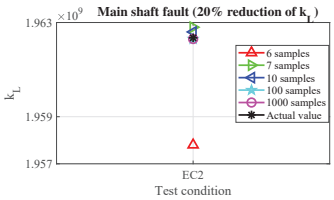

(a) Tracking main shaft stiffness variation

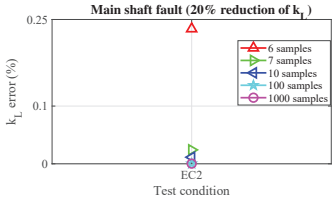

(b) Error in tracking main shaft stiffness variation

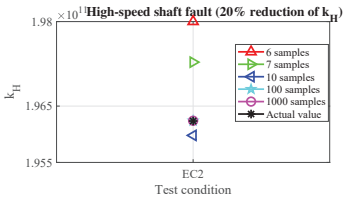

(c) Tracking HS shaft stiffness variation

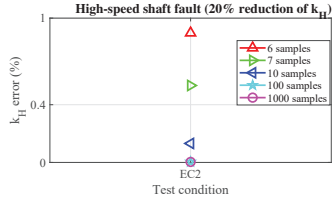

(d) Error in tracking HS shaft stiffness variation

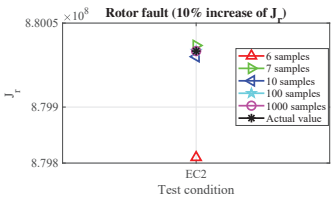

(e) Tracking rotor inertia variation

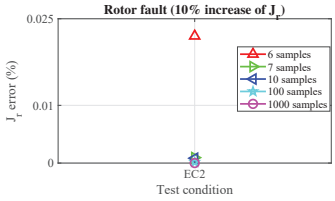

(f) Error in tracking rotor inertia variation

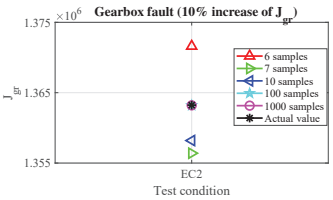

(g) Tracking gearbox inertia variation

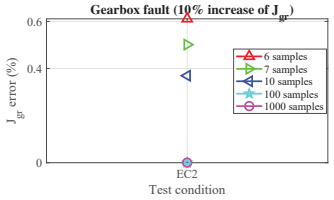

(h) Error in tracking gearbox inertia variation

equivalent stress throughout the two shafts is calculated, which provides the inputs for estimating the fatigue damage and residual life of the two shafts. In order to account for statistical uncertainties in load estimation approach, the influence of measurement noise and uncertainties in estimated model parameters are mitigated by employing Kalman filtering. This technique is used to preprocess the input torsional response applied to the degradation

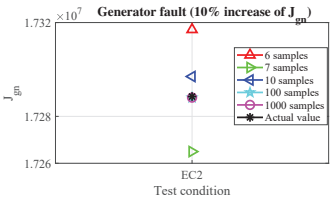

(i) Tracking generator inertia variation

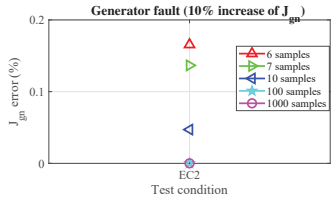

(j) Error in tracking generator inertia variation

Figure 6.4: Estimated ROM model parameters in different fault scenarios [30] (paper 6). (a) k_L, (b) k_L relative error, (c) k_H, (d) k_H relative error, (e) J_r, (f) J_r relative error, (g) J_{gr}, (h) J_{gr} relative error, (i) J_{gn}, (j) J_{gn} relative error.

model, by cancelling background noises and estimated model uncertainties.

The assumed linear state-space model as the input numerical model applied to the Kalman filter is obtained by applying the generalized coordinate approach. The details about the Kalman filter design can be found in paper 6 [30].

The torsional moment on the main and high-speed shafts is estimated based on the following equations

$$\mathrm{T_{LSS}} = \mathrm{k_{LS}}(\theta_\mathrm{r} - \theta_\mathrm{gr}) + \mathrm{c_{LS}}(\Omega_\mathrm{r} - \Omega_\mathrm{gr}), \tag{6.12a}$$

$$\mathrm{T_{HSS}} = \mathrm{k_{HS}}(\theta_\mathrm{gr} - \theta_\mathrm{gn}) + \mathrm{c_{HS}}(\Omega_\mathrm{gr} - \Omega_\mathrm{gn}). \tag{6.12b}$$

In the above equations, T_{LSS} and T_{HSS} are respectively the equivalent torque on the main and high-speed shafts. θ_r, Ω_r, θ_{gr}, Ω_{gr}, θ_{gn} and Ω_{gn} are the angular displacement and velocity of rotor, gearbox and generator, respectively. The shear stress of the shaft can then be calculated by [72]

$$\tau = \frac{Tc}{J}. \tag{6.13}$$

In the above equation, T is the online torsional moment which is estimated by equation 6.12, c is the radial distance from the shaft center line. J is the polar moment of inertia around the shaft axis defined by

$$J = \frac{\pi}{2}(d_o^4 - d_i^4). \tag{6.14}$$

In the above equation, d_i and d_o are respectively the inner and outer radius of the shaft. Therefore, the maximum shear stress happens on the shaft surface. Due to the large mass of main shaft, the bending stress can take a

Table 6.1: Estimation of NREL 5 MW drivetrain 14-DOF equivalent model parameters by using the proposed approach [29].

Digital twin model parameters							
Inertia				**Stiffness**			
	Actual	**Estimated**	**Error (%)**		**Actual**	**Estimated**	**Error (%)**
$\boldsymbol{j}_1$	5.7e7	5.7e7	0.0	$\boldsymbol{k}_{R-R}$	9.3e8	9.3e8	0.3
$\boldsymbol{j}_2$	1.1e4	1.1e4	0.2	$\boldsymbol{k}_{c1-c1}$	6.8e10	6.8e10	0.0
$\boldsymbol{j}_3$	2.2e2	2.2e2	0.2	$\boldsymbol{k}_{p11-p11}$	4.4e8	4.4e8	0.2
$\boldsymbol{j}_4$	2.2e2	2.2e2	0.2	$\boldsymbol{k}_{p12-p12}$	4.4e8	4.4e8	0.2
$\boldsymbol{j}_5$	2.2e2	2.2e2	0.2	$\boldsymbol{k}_{p13-p13}$	4.4e8	4.4e8	0.2
$\boldsymbol{j}_6$	3.5e2	3.5e2	0.2	$\boldsymbol{k}_{s1-s1}$	8.7e9	8.6e9	0.1
$\boldsymbol{j}_7$	2.7e3	2.7e3	0.1	$\boldsymbol{k}_{c2-c2}$	9.3e10	9.3e10	0.2
$\boldsymbol{j}_8$	2.1e2	2.1e2	0.1	$\boldsymbol{k}_{p21-p21}$	1.3e10	1.3e10	0.3
$\boldsymbol{j}_9$	2.1e2	2.1e2	0.1	$\boldsymbol{k}_{p22-p22}$	1.3e10	1.3e10	0.3
$\boldsymbol{j}_{10}$	2.1e2	2.1e2	0.1	$\boldsymbol{k}_{p23-p23}$	1.3e10	1.3e10	0.3
$\boldsymbol{j}_{11}$	1.5e1	1.5e1	0.2	$\boldsymbol{k}_{s2-s2}$	2.0e9	2.0e9	0.2
$\boldsymbol{j}_{12}$	1.6e3	1.6e3	0.0	$\boldsymbol{k}_{W-W}$	6.0e9	6.0e9	0.2
$\boldsymbol{j}_{13}$	8.0e1	8.0e1	0.0	$\boldsymbol{k}_{P-P}$	4.7e8	4.7e8	0.3
$\boldsymbol{j}_{14}$	5.4e3	5.4e3	0.0	$\boldsymbol{k}_{G-G}$	9.6e7	9.6e7	0.3

significant value which is calculated by [72]

$$\sigma = \frac{Mc}{J}. \tag{6.15}$$

In the above equation, M is the bending moment of the shaft due to the shaft weight. By using a distributed mass model, the maximum bending moment which happens in the center point of the shaft on the surface area can be calculated by

$$M^{max} = \frac{WL^2}{8}. \tag{6.16}$$

In the above equation, W is the mass per unit length of the shaft, and L is the length of the shaft. Therefore, the maximum bending and shear stresses

happen simultaneously on the surface of the middle of the shaft as

$$\tau_{\mathrm{LSS}}^{\max} = \frac{2}{\pi} \frac{\mathrm{d_o^{LSS}}(\mathrm{k_{LS}}(\theta_{\mathrm{r}} - \theta_{\mathrm{gr}}) + \mathrm{c_{LS}}(\Omega_{\mathrm{r}} - \Omega_{\mathrm{gr}}))}{(\mathrm{d_o^{LSS}})^4 - (\mathrm{d_i^{LSS}})^4}, \tag{6.17a}$$

$$\tau_{\mathrm{HSS}}^{\max} = \frac{2}{\pi} \frac{\mathrm{d_o^{HSS}}(\mathrm{k_{HS}}(\theta_{\mathrm{gr}} - \theta_{\mathrm{gn}}) + \mathrm{c_{HS}}(\Omega_{\mathrm{gr}} - \Omega_{\mathrm{gn}}))}{(\mathrm{d_o^{HSS}})^4 - (\mathrm{d_i^{HSS}})^4}, \tag{6.17b}$$

$$\sigma^{\max} = \frac{\mathrm{W L^2 d_o}}{4\pi(\mathrm{d_o^4} - \mathrm{d_i^4})}. \tag{6.17c}$$

The equivalent stress is then estimated by applying von Mises theory. The equivalent stress due to the combined bending and torsion is maximum in the middle of the shaft on the surface. Von Mises stress under combined bending and torsion loading is calculated by [73]

$$\sigma_d = \sqrt{\sigma_{max}^2 + 3\tau_{max}^2}. \tag{6.18}$$

In the above equation, σ_d is von Mises stress, and τ_{max} and σ_{max} are respectively the maximum torsional and bending stresses.

The estimations of main shaft load and stress in three different cases, namely normal operations, fault in the main shaft, and overload conditions are illustrated in Figures 6.6 and 6.6, respectively. The early stage fault in the main shaft is modeled with the 10% reduction of the shaft stiffness. The overload is modeled with the 20% increase of the drivetrain torque. As it can be seen in these figures, in all the simulation scenarios, the error in the estimation of load and stress of the main shaft by using the proposed digital twin technique is less than 5%.

6.3.2 Estimation of contact load and stress at each gear stage

The most prevalent failures of the large gears in wind turbine drivetrain systems are due to gear tooth root bending and pitting fatigue damage [74]. For monitoring the RUL of the gears in this work, the degradation of the gears due to pitting fatigue damage and the gear pairs contact loads are taken into consideration. The contact loads on the gear pairs are estimated by using the load observers designed for the gear pairs based on the real-time estimated equivalent torsional model and torsional measurements. NREL 5 MW drivetrain and the 14-DOF equivalent model are employed in this section to investigate into the possibility of using the proposed DT technique for the real-time estimation of degradation and residual life of the gears of

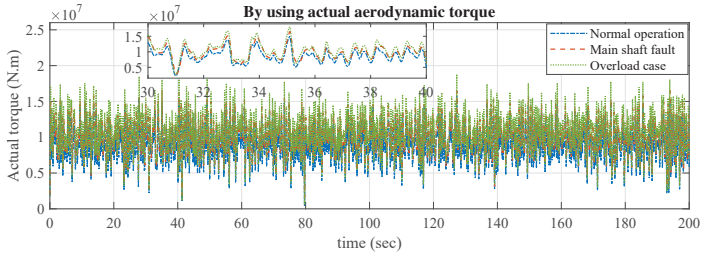

(a) Main shaft actual torque

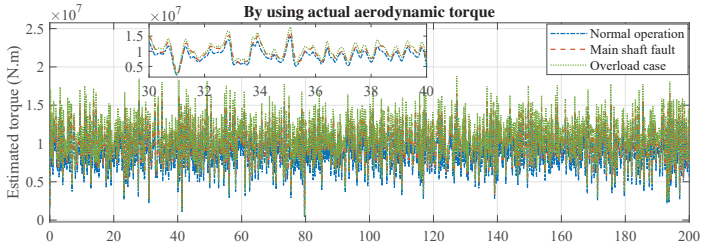

(b) Main shaft estimated torque

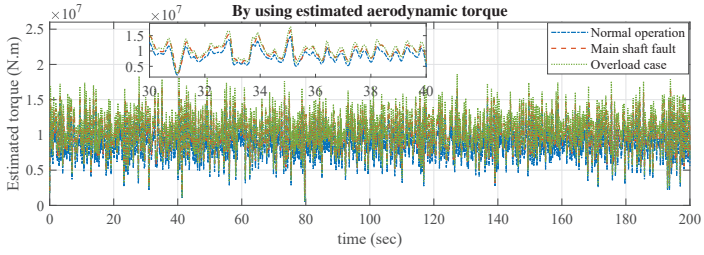

(c) Main shaft estimated torque

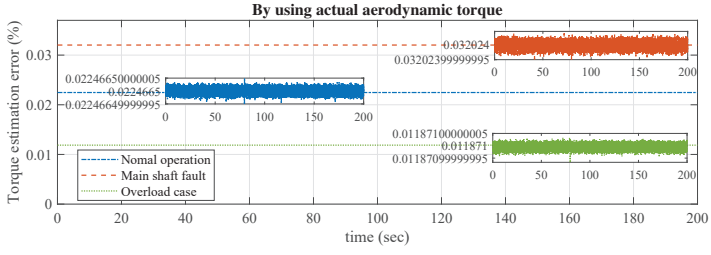

(d) Main shaft estimated torque error

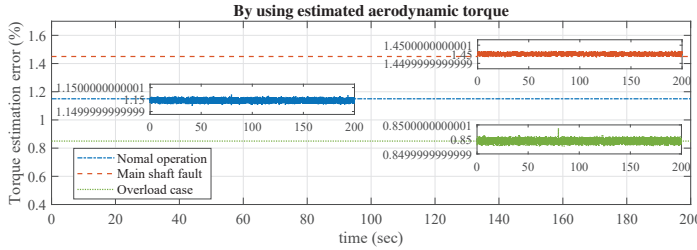

(e) Main shaft estimated torque error

Figure 6.5: Real-time torque on the main shaft of DTU 10 MW drivetrain model [30] (paper 6). (a) Actual torque, (b) Estimated torque in case of using actual aerodynamic torque, (c) Estimated torque in case of using estimated aerodynamic torque, (d) Torque estimation relative error in case of using actual aerodynamic torque, (e) Torque estimation relative error in case of using estimated aerodynamic torque.

wind turbine drivetrain gearbox due to pitting damage. The details about 14-DOF equivalent model are described in paper 5 [29].

In the gearbox of wind turbines, the input and output torques for planetary (parallel) stages are respectively the carrier (pinion) torque T_C (T_P) and the sun (wheel) torque T_s (T_W). The equations describing the internal dynamics of different gearbox stages as a function of gears mesh stiffness and inertia are as follows [29]

Planetary stage:

$$\begin{aligned} J_s\ddot{\theta}_s &= T_s - N_p r_s F_{sp}, \\ J_p\ddot{\theta}_p &= r_p(F_{pr} - F_{sp}) = -J_p\frac{r_s}{r_p}\ddot{\theta}_s, \\ m_p a_w\ddot{\theta}_c &= F_{pr} + F_{sp} - F_{pc} = m_p a_w\frac{r_s}{r_s+r_r}\ddot{\theta}_s, \\ J_c\ddot{\theta}_c &= T_c - N_p r_s F_{sp} = J_c\frac{r_s}{r_s+r_r}\ddot{\theta}_s. \end{aligned} \tag{6.19}$$

Parallel stage:

$$\begin{aligned} J_P\ddot{\theta}_P &= T_P - r_P F_{PW} = -J_P\frac{r_P}{r_W}\ddot{\theta}_W, \\ J_W\ddot{\theta}_W &= T_W - r_W F_{PW}. \end{aligned} \tag{6.20}$$

The detailed definition of the parameters in the above dynamic model is given in the description of 14-DOF model in paper 5 [29]. It is possible to obtain the relationship between the input and output torques at each stage by eliminating the internal forces between the elements. The resulted equations for both the planetary and parallel stages are

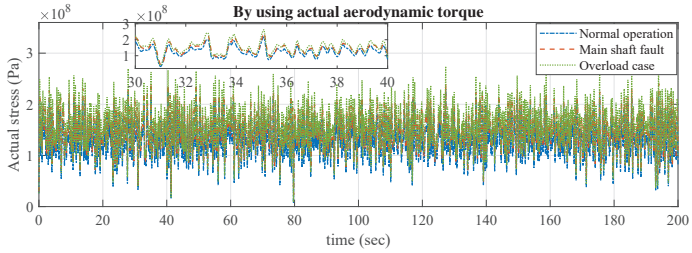

(a) Main shaft actual maximum stress.

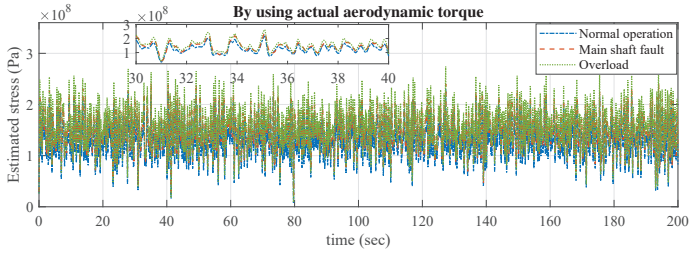

(b) Main shaft estimated maximum stress.

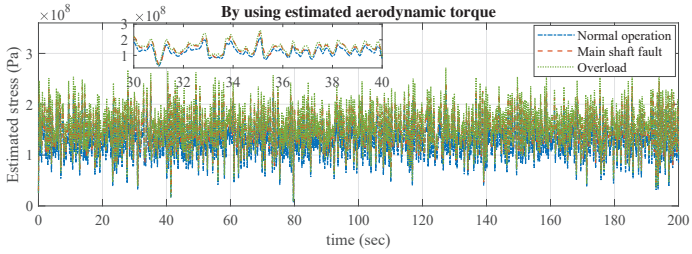

(c) Main shaft estimated maximum stress.

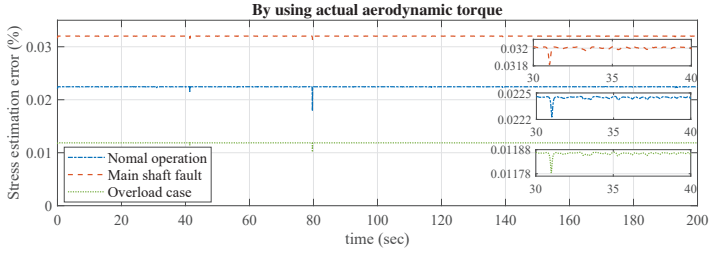

(d) Main shaft estimated stress error.

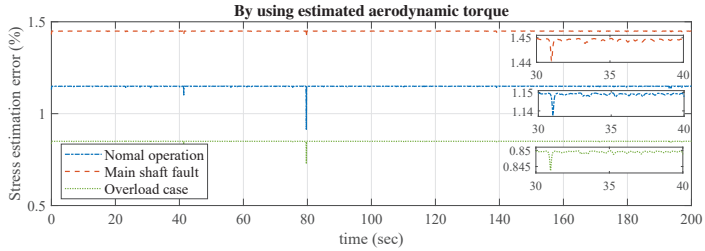

(e) Main shaft estimated stress error.

Figure 6.6: Real-time equivalent von Mises stress on the main shaft of DTU 10 MW drivetrain model [30] (paper 6). (a) Actual stress, (b) Estimated stress in case of using actual aerodynamic torque, (c) Estimated stress in case of using estimated aerodynamic torque, (d) Stress estimation relative error in case of using actual aerodynamic torque, (e) Stress estimation relative error in case of using estimated aerodynamic torque.

Planetary stage:

$$\begin{aligned} T_s &= J_{EQ}\ddot{\theta}_s - T_c\frac{r_s}{2a_w}, \text{ where} \\ J_{EQ}^{planetary} &= J_s + \frac{N_p r_s^2}{2}\left(J_p/r_p^2 + m_p\frac{a_w}{r_s+r_r}\right) + J_c\frac{r_s^2}{2a_w(r_s+r_r)}. \end{aligned} \tag{6.21}$$

Parallel stage:

$$\begin{aligned} T_W &= J_{EQ}\ddot{\theta}_W + T_P\frac{r_W}{r_P}, \text{ where} \\ J_{EQ}^{parallel} &= J_W + J_P\frac{r_W^2}{r_P^2}. \end{aligned} \tag{6.22}$$

In the above equations, $J_{EQ}^{planetary}$ is the equivalent mass moment of inertia in the planetary stage, having contributions from the sun, N_p planet gears and planet carrier. $J_{EQ}^{parallel}$ is the same parameter for the parallel stage. The torque transfer between stages is through the shafts, so that the transferred torque can be estimated by

$$T_{out} = T_{in} - J_S\ddot{\theta}_S. \tag{6.23}$$

In the above equation, $J_S\ddot{\theta}_S$ is the inertial torque from the shaft [42]. For NREL 5 MW drivetrain, the input and output torques of each stage are calculated by [29] (paper 5)

$$
\begin{aligned}
T_{in}^{stage1} = T_c^{stage1} = T_R - J_{LSS}\ddot{\theta}_R,\\
T_{in}^{stage2} = T_c^{stage2} = T_{out}^{stage1} - J_{ISS}\ddot{\theta}_s^{stage1},\\
T_{in}^{stage3} = T_P = T_G - J_{HSS}\ddot{\theta}_G,\\
T_{out}^{stage1} = T_s^{stage1} = J_{EQ}^{stage1}\ddot{\theta}_s^{stage1} - T_{in}^{stage1}\frac{r_s^{stage1}}{2a_w^{stage1}},\\
T_{out}^{stage2} = T_s^{stage2} = J_{EQ}^{stage2}\ddot{\theta}_s^{stage2} - T_{in}^{stage2}\frac{r_s^{stage2}}{2a_w^{stage2}},\\
T_{out}^{stage3} = T_W = J_{EQ}^{stage3}\ddot{\theta}_W - T_{in}^{stage3}\frac{r_W}{r_P}.
\end{aligned}
\tag{6.24}
$$

As it can be seen, the torques estimated at each gear stage are functions of drivetrain input torque, torsional response and the parameters of the equivalent model which are estimated in real-time by using the proposed system identification approach. The input torques estimated above are then used for estimating the stress at the different gear stages. Gear contact stresses are analyzed in this work following ISO 6336-2:2019 [75]. According to this standard, the contact stresses are

$$
\sigma_{Hi} = Z_{BD}Z_H Z_E Z Z_\beta \sqrt{K_A K_{\gamma i} K_{vi} K_{H\beta i} K_{H\alpha i}} \sqrt{\frac{2000 T_i}{d_1^2 b}\frac{u+1}{u}}. \tag{6.25}
$$

In the above equation, u is the gear-ratio of the pair, d_1 and b are reference diameter and face width of the pinion, respectively, T_i is the input torque. The other parameters account for different aspects of the problem, such as contact relations Z_{BD} and ratios Z, material properties Z_E, helix angle Z_β, mesh load K_γ, gear speed K_v, load distributions $K_{H\beta i}$ and $K_{H\alpha i}$. These factors are defined in [75]. Equation (6.25) can be rewritten as

$$
\sigma_{Hi} = C\sqrt{T_i}. \tag{6.26}
$$

In the above equation, C represents the design parameters in equation 6.25. This parameter can be roughly estimated from nominal conditions as $C = \sigma_{HN}/\sqrt{T_{iN}}$, so that equation (6.26) becomes

$$
\sigma_{Hi} = \sigma_{HN}\sqrt{\frac{T_i}{T_{iN}}}. \tag{6.27}
$$

In the above equation, σ_{HN} and T_{iN} are the nominal contact stress and torque. The estimated input and output torques of each stage estimated by using dynamic model described by equation 6.24 are shown in Figure 6.7. The estimated contact stress at the sun-plant gear pair of the second gearbox stage by using equation 6.27 is demonstrated in Figure 6.8. These results

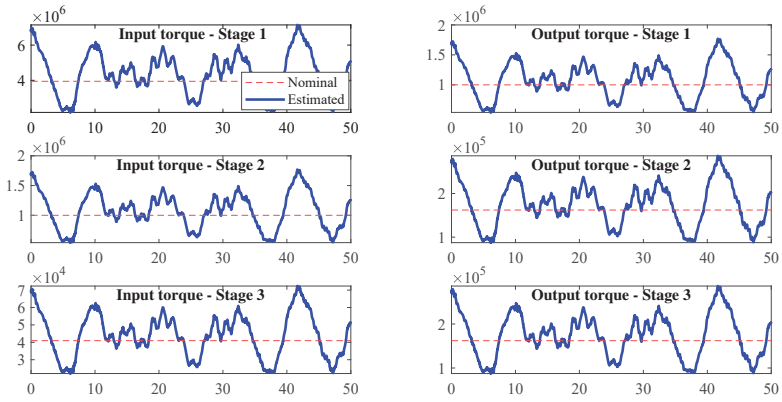

Figure 6.7: Estimated input and output torques of the 1^{st}, 2^{nd} and 3^{rd} gearbox stages of NREL 5 MW drivetrain.

are obtained based on the simulation studies of [29] (paper 5). The results show a fair agreement between the estimated stress by using the proposed DT approach and the estimated values from the drivetrain high-fidelity simulation models. It is worth noting that the proposed DT algorithm keeps the same number of stress cycles with the high-fidelity model though the range of cycles is slightly higher. The latter means that the proposed DT technique may slightly overestimate the fatigue damage of the gear.

6.4 Degradation model

6.4.1 Degradation model for residual life estimation

Stress-life method is used for estimating the fatigue damage. Stress-life method has shown proven performance for estimating fatigue in high-cycle applications with the number of cycles over $N > 10^3$ during the component lifetime. The estimated time series of maximum stress feeds the time-domain cycle counting approach based on rainflow approach. The rainflow cycle counting [76] is applied to calculate the number of cycles at different stress levels. Then damage is estimated in real-time and the residual life of the component is estimated. Miner's rule is used to calculate the accumulated fatigue damage of the drivetrain components.

Cycle counting is especially important for the broad-band stress signals to distinguish small cycles which are interruptions of larger ones. The outputs

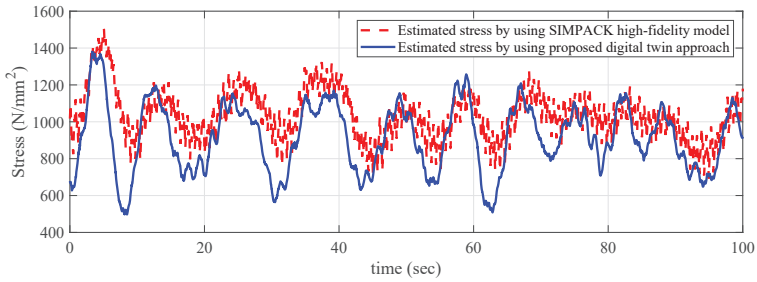

Figure 6.8: Validation of estimated sun-planet contact stress at the 2^{nd} stage of gearbox in NREL 5 MW drivetrain: comparison between the contact stress estimated by using the proposed digital twin approach and the contact stress obtained from high-fidelity SIMPACK simulation model.

are the amplitude stress levels σ_s, and the number of stress cycles at σ_s $for\ s = (1,\ldots,S)$. Goodman rule is employed to calculate the effective stress (the equivalent zero mean alternating stress) by considering the influence of nonzero mean stress level by means of the equation [77]

$$\sigma_s^e = \frac{\sigma_s}{1 - \frac{\sigma_m}{\sigma_u}},\ \forall\ s \in \{1,\ldots,S\}. \tag{6.28}$$

In the above equation, σ_m and σ_u are the mean stress and material yield strength, respectively. The accumulated damage for the data block t with S different stress levels σ_s^e ($s \in \{1,\ldots,S\}$) is calculated by using Miner's rule as

$$d^t = \sum_{s=1}^{S} \frac{n_s}{N_s}. \tag{6.29}$$

In this equation, n_s is the number of cycles at the stress level σ_s^e and N_s is the number of cycles to yield at stress level σ_s^e, where the relationship is defined by S-N curve characteristic as [78]

$$\sigma_s^e = a(2N_s)^b. \tag{6.30}$$

The absolute total online accumulated damage is calculated by

$$D = \sum_{t=1}^{Time} d^t. \tag{6.31}$$

In this equation, *Time* stands for the last data block which represents the current time. d^t represents the "short-term" damage, which is related to only

a specific environmental condition. Damage D characterizes the long-term damage which captures the influence of all possible environmental conditions [42]. The described damage estimation method can also be used to estimate the relative damage between different operation periods over the time, which informs both the operator and designer about the variations in degradation between different operational periods. It can also be used for estimating the relative damage between the different drivetrain components at the time, to give the operator information about the most vulnerable parts of the system at different periods of operation.

The aforedescribed deterministic damage estimation approach does not necessarily provide precise results. In order to improve the accuracy of estimation, stochastic models which can adequately address the uncertainties in the stress-life degradation estimation approach can be used in conjunction with the above described deterministic model-based approach.

The other significant source of uncertainty in the proposed residual life estimation approach arises from stress-life method [78] and the procedure employed to obtain S-N curve parameters a and b which represent the best-fitting estimates of experimental fatigue data [79]. In this thesis, in order to address the uncertainty in fatigue calculation due to material uncertainties, damage at each stress level is assumed as a random variable. In other words, in order to estimate damage for the t^{th} data block of the stress time series, d^t, the damage is calculated by assuming the S-N curve parameters a and b as random variables, so that for each stress level σ_i, the number of cycles to failure are estimated by randomly selecting a and b in the intervals $\pm 5\%$ of their nominal values.

A detailed analysis of stress signal which helps to obtain a confidence interval for the estimated expected value of damage is carried out by Moghadam and Nejad [30] in paper 6. Based on the results of this study, the stress time series of drivetrain components are assumed to be IID at each operating speed, which helps to obtain confidence interval for average damage, by using Monte Carlo simulation and the results of IID CLT [80]. With the confidence 95%, the average damage places in the interval

$$[\widehat{\mu}_{d^t} - 1.96 s_{d^t}/\sqrt{(k)} \quad \widehat{\mu}_{d^t} + 1.96 s_{d^t}/\sqrt{(k)}], \tag{6.32a}$$

$$\widehat{\mu}_{d^t} = \frac{1}{k}\sum_{i=1}^{k} d_i^t, \tag{6.32b}$$

$$s_{d^t} = \sqrt{\frac{1}{k-1}\sum_{i=1}^{k}(d_i^t - \widehat{\mu}_{d^t})^2}. \tag{6.32c}$$

In the above equations, k is the number of cases that the parameters of S-

N curve are randomly generated for estimation of d^t, so that $d_i^t = (d_1^t, ..., d_k^t)$. The value of k is selected to realize an interval $\pm 5\%$ around the mean value of d_i^t. $\widehat{\mu}_{d^t}$ and s_{d^t} are the average and variance estimates.

6.4.2 Degradation of main and high-speed shafts

The algorithm for estimating RUL of the main and high-speed shafts by using the proposed DT-based residual life monitoring approach is summarized by the flowchart in Figure 6.9. The proposed DT approach for estimating the two shafts residual life is based on the 3-DOF equivalent ROM of drivetrain.

The expected values of main shaft accumulated damage in different test scenarios for 3600 seconds of operation during normal, overload and faulty conditions are listed in Table 6.2. These simulation studies are based on DTU 10 MW drivetrain system. The S-N curve characteristics of the main shaft material used for the damage calculations are described in [30]. *Actual damage* in Table 6.2 represents the accumulated damage when the actual value of drivetrain parameters and input loads are accessed. *Estimated damage*$_\mathbf{1}$ is the damage estimated by using the proposed DT model and the actual value of drivetrain input loads. *Estimated damage*$_\mathbf{2}$ is the damage estimated when the DT model and estimated values of drivetrain input loads are applied. The estimated damage in all the different test scenarios agrees with the actual damage, with an exception for coupled fault and overload test case, where the proposed approach slightly underestimates the damage.

Table 6.2: Expected value of main shaft accumulated damage in DTU 10 MW drivetrain for different test scenarios for 3600 seconds of operation at rated rotor speed [30].

Test scenario	**Actual damage**	**Estimated damage$_1$**	**Estimated damage$_2$**
Normal operation	$1.8e^{-7}$	$1.8e^{-7}$	$1.8e^{-7}$
Overload (20%)	$1.1e^{-5}$	$1.1e^{-5}$	$1.1e^{-5}$
Fault (10%)	$8.3e^{-7}$	$8.3e^{-7}$	$8.3e^{-7}$
Overload and fault	$3.4e^{-5}$	$3.4e^{-5}$	$3.3e^{-5}$

6.4.3 Degradation of gears in the gearbox

The results of estimating RUL of the different gears in the gearbox by using the proposed DT approach are reported in Table 6.3. The proposed DT approach for estimation of the residual life of the gears is based on 14-DOF

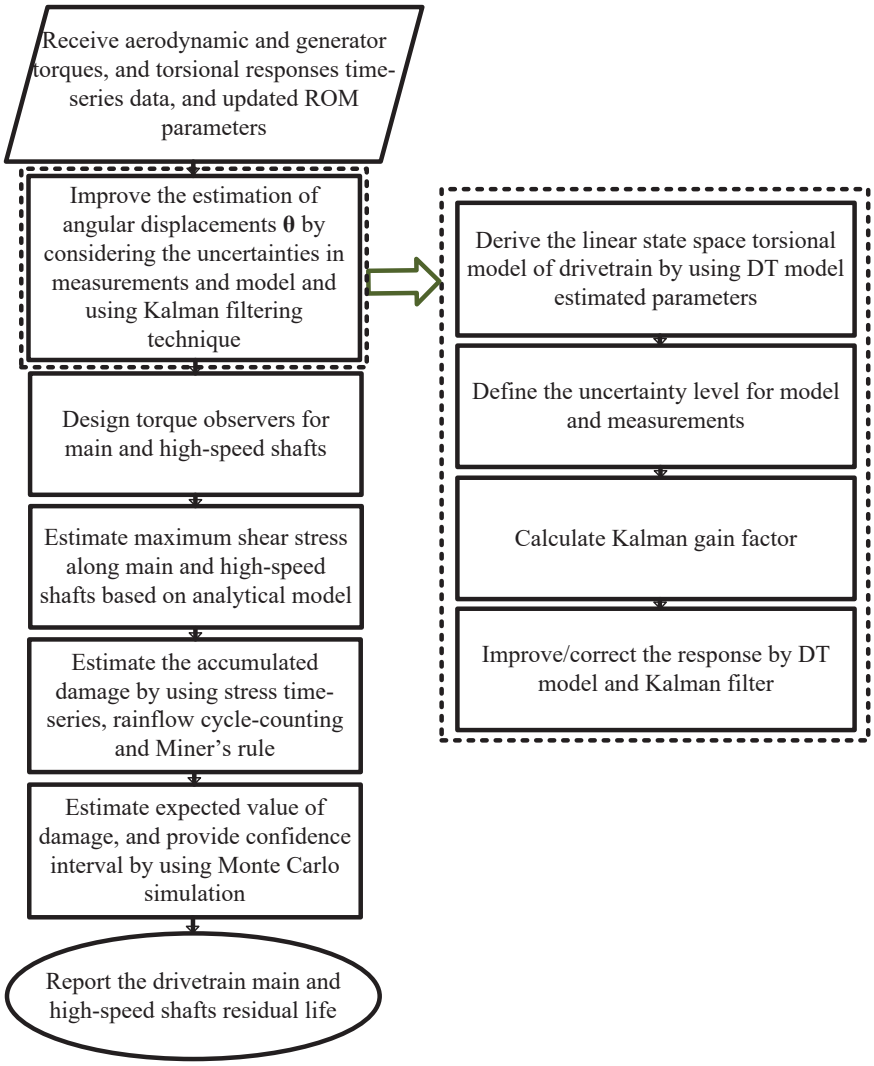

Figure 6.9: Algorithm for estimation of residual life of drivetrain main and high-speed shafts by using the estimated 3-DOF equivalent model, torsional measurements and stress-life method [30] (paper 6).

equivalent ROM of drivetrain. The SN curve characteristics for the gears pitting fatigue damage calculations are described in paper 5 [29]. The simulation studies are based on NREL 5 MW drivetrain system. The expected

values of the accumulated damage in different gears for 3600 seconds of operation during normal conditions at a rated drivetrain speed are reported in Table 6.3, which show an agreement between the actual and estimated values of damage.

Table 6.3: Expected value of different gears accumulated damage in NREL 5 MW drivetrain, for 3600 seconds of normal operation at rated rotor speed [29].

Gear	**Actual damage**	**Estimated damage**
1^{st} stage sun	$4.8e^{-6}$	$4.8e^{-6}$
2^{nd} stage sun	$4.6e^{-6}$	$4.6e^{-6}$
3^{rd} stage pinion	$7.6e^{-6}$	$7.6e^{-6}$

Chapter 7

Conclusions

7.1 Conclusions

This PhD thesis was aimed at proposing cost effective and computationally fast solutions for improving the condition monitoring of the drivetrain system of future offshore wind turbines.

In order to achieve this purpose, as the first step, the pros and cons of different drivetrain configurations were investigated by using a life cycle optimization approach. In this approach, the optimization was performed in both system and component levels by looking into the criteria obliged by the proposed life cycle assessment approach and taking into account the design, manufacturing and installation, and O&M costs together. It was shown that medium-speed permanent magnet synchronous generator (PMSG) drivetrain technology can offer a better compromise between total weight, raw material cost, size, efficiency and dynamic behavior analysis, so that it was selected as the main case study to test the condition monitoring methods designed and developed for the drivetrain of floating offshore wind turbines in this PhD project.

The fault diagnosis of the drivetrain by using the time and frequency domains analyses of the translational vibration measurements was investigated and the capability of these methods in observing the faults initiated by different sources was explained. A data-driven diagnosis solution was proposed by using the drivetrain translational vibration data based on modelling the drivetrain sensor network with the equivalent spatial probabilistic graphical model and assuming the multi-variate distribution which fits the drivetrain vibration measurements forming a Gaussian Markov random field, and leveraging the features that each graph in this field follows. The experimental and simulation studies proved the successful diagnosis of

faults in the drivetrain at component-level (fault in the main bearing based on the analysis of experimental data, and fault in the gearbox high-speed shaft bearing by using the data generated by simulation model), which were not observable by the standard time-domain approach based on the analysis of the RMS of acceleration measurements.

Then the innovative condition monitoring solutions of the drivetrain by using the torsional vibration measurements were focused. The main reason was developing methods based on using the sensors, communication infrastructure and processing power already available in turbine and farm levels, to propose cost-effective and easy to implement solutions to improve the drivetrain condition monitoring in system and component levels. The torsional measurements can be obtained by the encoders and possibly strain gauges which are used in drivetrain respectively for the controlling objective and the measurement of load. As the starting point to study about the feasibility of using the torsional vibration measurements for the drivetrain condition monitoring, the classical time and frequency domains analyses of the torsional measurements and the possibility of observing faults initiated by different sources were studied, and the performance was compared to the classical time and frequency domains analyses of translational vibrations. A frequency-domain data analysis tool based on monitoring the energy of vibration signal around the suspicious/defect frequency was also developed. The results of this study showed that the torsional vibration measurements can improve the condition monitoring based on translational vibrations by offering an earlier stage fault detection, supporting the root cause analysis and also giving feedback to the designer on the torsional excitation frequencies which can result in the accelerated degradation of the components over the time.

In the next step, the torsional vibrations were selected as the main focus of this PhD research. The possibility of using two methods based on torsional vibration measurements, namely torsional response error function and low-pass filtered torsional response function, to support the drivetrain system modal analysis was investigated. The results based on both experimental and simulation-based studies were used to prove the possibility of estimating the drivetrain natural frequencies by using the torsional vibration measurements, where the torsional responses obtained from higher-order drivetrain simulation models showed the possibility of observing the higher drivetrain frequency modes. The drivetrain faults were classified into two main categories of system and component levels. Then fault diagnosis algorithms based on monitoring the variations of the drivetrain dynamic properties, namely the undamped natural frequencies and normal mode shapes,

were studied. An algorithm for drivetrain fault diagnosis at system-level was developed based on the 3-DOF equivalent model of drivetrain supported by sensitivity analysis to measure the contribution of the different stages of progress of drivetrain system-level faults in the variation of drivetrain modes. The proposed method which was also implementable by using only one encoder data, was validated by both experimental and simulation studies. The results reported by simulation studies proved the successful detection of different types of system-level faults including the unbalance faults in rotor, generator and gearbox, and crack in main and high-speed shafts. The The results reported by experimental studies showed the possibility of observing an early stage fault in the main shaft which was not detectable by using the standard condition monitoring methods. Then higher order equivalent models were tested, and the influence of faults at the component level (more specifically, pitting faults in the different gears of the gearbox) on the drivetrain dynamic properties was shown by simulation studies. However, further studies to establish an analytical approach for the drivetrain fault diagnosis at component-level by monitoring the dynamic properties was considered as a future work.

A further step was taken in torsional vibrations-based condition monitoring to study the possibility of using torsional vibration measurements for prognosis of drivetrain faults, by investigating into approaches for the near real-time estimation of the remaining useful lifetime of the drivetrain components by using the torsional measurements. To this purpose, a digital twin modelling approach was proposed as the combination of the real-time equivalent torsional model, online torsional measurements and degradation model to estimate the online fatigue damage of the drivetrain components. A computationally fast algorithm was designed for estimating the drivetrain equivalent torsional reduced order model parameters by using the torsional measurements and employing a robust least square error estimator. The least-square error estimator was designed based on minimizing the square error between the equivalent model and measurements. The online estimated model and measurements were applied as input to the load observers to estimate the near real-time load and subsequently equivalent stress in the drivetrain components by taking into consideration the internal dynamics of the drivetrain components. Then the real-time degradation estimation for obtaining the residual life of the components was performed based on a proven physics-based approach grounded on the analysis of the stress life of the drivetrain components. The degradation estimation approach was supported by statistical approaches and stochastic models to address the two main sources of uncertainty in the proposed DT model arisen from first the

load estimation approach and second the estimation of fatigue damage by relying on the material properties obtained from the S-N curve, to improve the estimation accuracy and obtain a confidence interval for the estimated expected value of damage. The employed statistical approaches and stochastic models include but are not limited to Kalman filtering, Monte Carlo simulation, stochastic modelling of fatigue damage and model identification by using algorithms with robustive characteristics. In one of the studies, a digital twin model was developed based on 3-DOF equivalent lumped model for estimating the residual life of the main and high-speed shafts. In the other study, a digital twin model was proposed grounded on 14-DOF equivalent model for estimating the residual life of the gears of the drivetrain gearbox. The proposed digital twin models were evaluated by simulation studies and the results were validated by comparing the results of estimated stress from digital twin model with the estimated stress from high-fidelity simulation models. The combination of the proposed torsional digital twin model with translational models aimed at detecting faults in the drivetrain bearings was considered as the other future work.

7.2 Original contributions

This thesis deals with design and development of innovative and cost-effective solutions to improve the condition monitoring of the drivetrain system of future offshore wind turbines. The main contributions of the thesis can be summarized as follow:

• *Establishing a drivetrain system optimization approach which ensures an optimized overall cost, weight, size, and improved efficiency and reliability*

Drivetrain cost optimization by using a life cycle assessment approach was introduced. Many researchers have done optimization, but we did in a life cycle perspective which is more holistic and valuable. A new analytical design approach was proposed for the optimized design of PMSG based on the optimization of the active material cost. An analytical design model of the gearbox was presented, and a new optimization approach was proposed to optimize the gearbox weight. A comprehensive comparison between the design, raw material cost, weight, size, efficiency and reliability of DDPMSG, MSPMSG and HSPMSG drivetrain technologies was presented. The first torsional natural frequency of the three under consideration PMSG-based drivetrain configurations was calculated, and the feasibility of application in floating offshore wind turbines was investigated.

• *Developing a drivetrain fault diagnosis method at component level based on the translational vibrations by using the combination of physics-based and data-driven approaches, and monitoring the variations of drivetrain statistical properties*

A statistical learning approach based on the graphical model of drivetrain obtained from Lagrangian approach was proposed for fault detection in the wind turbine drivetrain components. Fulfilling Gaussian Markov Random Field (GMRF) properties in the drivetrain vibration measurements motivated using the features any graph in this field obeys, namely the stationarity of the inverse of covariance matrix in a GMRF and its conditional dependence properties were used to achieve a drivetrain computationally fast abnormality detection approach. The method was able to diagnose the faults that were not detectable by standard condition monitoring approaches. The latter was shown by both experimental and simulation studies.

• *Classifying the different sources of excitation in drivetrain condition monitoring analyses and proposing the efficient vibration-based diagnosis solutions based on the source of excitation*

An experimental comparison between different available solutions for detecting drivetrain bearings and gears defects initiated by different sources of excitation was performed. Torsional vibrations residual function which is recently proposed in literature of vibration-based condition monitoring of wind turbine drivetrain was experimentally validated by time and frequency domain analysis of torsional versus translational vibrations. To this purpose, Different frequency-domain tools for detecting abnormalities in the drivetrain system, namely FFT, PSD and envelope PSD spectrums and analysis of the energy of the signal at the defect frequencies were employed experimentally by using operational measurements.

• *Designing methods for drivetrain modal analysis by means of torsional vibrations*

Drivetrain modal analysis by using the different types of torsional measurements was introduced. The proposed modal analysis approach was analytically proved. The performance of the proposed modal analysis approaches was demonstrated by using both experimental studies based on the operational data and simulation studies. Two different simulation studies based on two different drivetrain systems and two different equivalent models (a simplified 3-DOF and a more complex 14-DOF models) of drivetrain were carried out, and the possibility of observing the system natural frequencies by using different functions of torsional measurements was investigated. An

analytical approach for estimating the damping coefficients associated with the different natural frequencies and operating speeds by analyzing the variations of amplitude of torsional response residual function at the natural frequencies and variations of damped natural frequencies in different operating speeds was proposed.

• *Designing methods for drivetrain fault diagnosis at both system and component levels based on monitoring the variations of the drivetrain dynamic properties*

A drivetrain condition monitoring approach was proposed which works based on monitoring the variations of the system dynamic properties and the amplitude of response at the natural frequencies. The drivetrain system fault detection features were extracted by leveraging sensitivity analysis. The method was tested by using both operational and simulation data obtained respectively from Vestas 1.75 MW and DTU 10 MW wind turbine drivetrains. The results were showing that the state of progression of different categories of drivetrain faults at system-level are observable in an early stage by the fault diagnosis method developed based on 3-DOF equivalent torsional model of the drivetrain, only by tracking the faults consequent variations in the drivetrain dynamic properties. The analytical equations of 3-DOF drivetrain model supported by sensitivity analysis were used to extract the fault detection features which were shown to be sufficient to detect the drivetrain faults at a system level. Then the possibility of extending this work to the drivetrain fault diagnosis at component-level by using higher DOF models of the drivetrain was demonstrated by the simulation studies.

• *Establishing the digital twin approach for fault prognosis of the drivetrain components by using the drivetrain torsional measurements*

Computationally fast digital twin models of the drivetrain system based on the torsional measurements and computationally inexpensive equivalent torsional models were proposed, which were aimed at monitoring the residual life of the components. The digital twin model based on 14-DOF equivalent of the drivetrain system was proposed for remaining useful lifetime (RUL) monitoring of the gearbox, which was tested for estimating the residual life of the gears of NREL 5 MW gearbox model and validated by comparing the results with high-fidelity simulation models. The digital twin model based on 3-DOF equivalent model was also proposed for estimating the residual life of main and high-speed shafts, which was tested by DTU 10 MW model. The proposed digital twin models leveraged stochastic physics-based degradation models for estimating RUL in the drivetrain components

by using the online estimated reduced order model (ROM), real-time torsional measurements, designed load observers and equivalent stress estimation approaches. These models take into consideration the various sources of uncertainty by using statistical approaches and stochastic models, namely Kalman filtering, Monte Carlo simulations and assuming fatigue damage as a random variable.

• *Designing a robust and computationally fast method for estimating the parameters of drivetrain equivalent models of different degrees of complexity by using the torsional measurements, for fault diagnosis and prognosis applications*

The online estimation of the parameters of drivetrain equivalent models of different degrees of freedom by using the torsional response and the estimated values of drivetrain input torques was discussed. The proposed robust least square error (LSE) estimator defined based on minimizing the difference between the equivalent model and the real-time measurements provided the best unbiased estimation of the coefficients in the linear regression model. Confidence intervals for estimation error of the ROM parameters were provided by using stochastic models supported by Monte Carlo simulations.

7.3 Recommendations for future works

• *Further development of proposed drivetrain fault diagnosis approach based on monitoring the drivetrain dynamic properties for detection of the faults at component level*

The proposed fault diagnosis approach and the associated feature space were analytically designed for detecting system-level faults based on a 3-DOF equivalent model of drivetrain. The component-level fault diagnosis was studied heuristically relying on limited simulation studies, which showed the potential of this method for detection of the faults in the gears. Analytical methods based on higher DOF equivalent models of drivetrain to obtain an analytical feature space for detecting drivetrain faults at component level is the area that is needed to be investigated more in future.

• *Further development of the proposed fault prognosis approach based on torsional digital twin models and torsional measurements for prognosis of the faults in the drivetrain bearings*

Combining the proposed torsional digital twin models with translational

models for prognosis of the fault in the drivetrain bearings has a high potential to be investigate further in the future.

• *Applying and testing the proposed fault diagnosis and prognosis approaches to other fields of application*

The methods developed in this PhD thesis were originally design for the drivetrain system of floating offshore wind turbines. However, these methods have a potential to be adjusted and applied to the other application domains *e.g.* for condition monitoring of ship propulsion systems and steam turbines.

• *Extending the data-driven statistical learning approach proposed in this PhD project for condition monitoring of the drivetrain, to the monitoring of the whole turbine and monitoring of the wind farm*

The proposed data-driven drivetrain condition monitoring method which relies on translational vibrations, has a high potential to capture the interactions between different turbine subsystems. The latter can be used to find the abnormalities in the turbine subsystems based on monitoring the variation of the correlations between turbine subsystems due to system faults or unexpected operations, which has a good potential to improve the operation and maintenance of future floating offshore wind turbines.

References

[1] European Commission Press release. Boosting offshore renewable energy for a climate neutral europe. https://ec.europa.eu/commission/presscorner/detail/en/IP_20_2096. [Online; accessed 19 November 2020].

[2] Philipp Beiter, Walter Musial, Patrick Duffy, Aubryn Cooperman, Matthew Shields, Donna Heimiller, and Michael Optis. The cost of floating offshore wind energy in california between 2019 and 2032.

[3] Anastasia Ioannou, Andrew Angus, and Feargal Brennan. Parametric CAPEX, OPEX, and LCOE expressions for offshore wind farms based on global deployment parameters. *Energy Sources, Part B: Economics, Planning, and Policy*, 13(5):281–290, 2018.

[4] Sebastian Pfaffel, Stefan Faulstich, and Kurt Rohrig. Performance and reliability of wind turbines: A review. *Energies*, 10(11):1904, 2017.

[5] Arnljot Hoyland and Marvin Rausand. *System reliability theory: models and statistical methods*, volume 420. John Wiley & Sons, 2009.

[6] Farid K Moghadam and Amir R Nejad. Evaluation of PMSG-based drivetrain technologies for 10-MW floating offshore wind turbines: Pros and cons in a life cycle perspective. *Wind Energy*, 2020.

[7] Christian Bak, Frederik Zahle, Robert Bitsche, Taeseong Kim, Anders Yde, Lars Christian Henriksen, Morten Hartvig Hansen, Jose Pedro Albergaria Amaral Blasques, Mac Gaunaa, and Anand Natarajan. The DTU 10-MW reference wind turbine. In *Danish Wind Power Research 2013*, 2013.

[8] Evan Gaertner, Jennifer Rinker, Latha Sethuraman, Frederik Zahle, Benjamin Anderson, Garrett E Barter, Nikhar J Abbas, Fanzhong Meng, Pietro Bortolotti, Witold Skrzypinski, et al. Iea wind tcp task

37: Definition of the iea 15-megawatt offshore reference wind turbine. Technical report, National Renewable Energy Lab.(NREL), Golden, CO (United States), 2020.

[9] Latha Sethuraman, Michael Maness, and Katherine Dykes. Optimized generator designs for the DTU 10-MW offshore wind turbine using generatorse. In *35th Wind Energy Symposium*, page 0922, 2017.

[10] Jesse Agwandus Andrawus. *Maintenance optimisation for wind turbines*. PhD thesis, 2008.

[11] Johann Mayer and Dieter Gerling. Simulation of arbitrary fault-conditions in pm-machines by generalized unsymmetrical modeling. In *2012 XXth International Conference on Electrical Machines*, pages 2866–2872. IEEE, 2012.

[12] AW Morgan and D Wyllie. A survey of rolling-bearing failures. In *Proceedings of the Institution of Mechanical Engineers, Conference Proceedings*, volume 184, pages 48–56. SAGE Publications Sage UK: London, England, 1969.

[13] Mostafa Valavi, Arne Nysveen, Robert Nilssen, Robert D Lorenz, and Terje Rølvåg. Influence of pole and slot combinations on magnetic forces and vibration in low-speed pm wind generators. *IEEE Transactions on Magnetics*, 50(5):1–11, 2013.

[14] Astrid Røkke. *Permanent magnet generators for marine current tidal turbines*. PhD thesis, 2017.

[15] Amir Rasekhi Nejad, Zhen Gao, and Torgeir Moan. Fatigue reliability-based inspection and maintenance planning of gearbox components in wind turbine drivetrains. *Energy Procedia*, 53:248–257, 2014.

[16] TE Tallian. On competing failure modes in rolling contact. *ASLE transactions*, 10(4):418–439, 1967.

[17] Pierre Tchakoua, René Wamkeue, Mohand Ouhrouche, Fouad Slaoui-Hasnaoui, Tommy Andy Tameghe, and Gabriel Ekemb. Wind turbine condition monitoring: State-of-the-art review, new trends, and future challenges. *Energies*, 7(4):2595–2630, 2014.

[18] Fausto Pedro García Márquez, Andrew Mark Tobias, Jesús María Pinar Pérez, and Mayorkinos Papaelias. Condition monitoring of wind turbines: Techniques and methods. *Renewable Energy*, 46:169–178, 2012.

[19] Sheryl M Gracewski and Nigel D Ramoutar. Vibration measurement. *Handbook of Measurement in Science and Engineering*, pages 367–432, 2012.

[20] Estefania Artigao, Andres Honrubia-Escribano, and Emilio Gomez-Lazaro. Current signature analysis to monitor dfig wind turbine generators: A case study. *Renewable Energy*, 116:5–14, 2018.

[21] Slim Soua, Paul Van Lieshout, Asanka Perera, Tat-Hean Gan, and Bryan Bridge. Determination of the combined vibrational and acoustic emission signature of a wind turbine gearbox and generator shaft in service as a pre-requisite for effective condition monitoring. *Renewable Energy*, 51:175–181, 2013.

[22] Wenxian Yang, Peter J Tavner, Christopher J Crabtree, Y Feng, and Y Qiu. Wind turbine condition monitoring: technical and commercial challenges. *Wind Energy*, 17(5):673–693, 2014.

[23] Oliver Tonks and Qing Wang. The detection of wind turbine shaft misalignment using temperature monitoring. *CIRP Journal of Manufacturing Science and Technology*, 17:71–79, 2017.

[24] Yanhui Feng, Yingning Qiu, Christopher J Crabtree, Hui Long, and Peter J Tavner. Monitoring wind turbine gearboxes. *Wind Energy*, 16(5):728–740, 2013.

[25] Amir R Nejad, Peter Fogh Odgaard, and Torgeir Moan. Conceptual study of a gearbox fault detection method applied on a 5-MW spar-type floating wind turbine. *Wind Energy*, 21(11):1064–1075, 2018.

[26] Amir Rasekhi Nejad, Erin E Bachynski, Marit I Kvittem, Chenyu Luan, Zhen Gao, and Torgeir Moan. Stochastic dynamic load effect and fatigue damage analysis of drivetrains in land-based and tlp, spar and semi-submersible floating wind turbines. *Marine Structures*, 42:137–153, 2015.

[27] Farid K Moghadam and Amir R Nejad. Natural frequency estimation by using torsional response, and applications for wind turbine drivetrain fault diagnosis. In *Journal of Physics: Conference Series*, volume 1618, page 022019. IOP Publishing, 2020.

[28] Farid K Moghadam and Amir R Nejad. Theoretical and experimental study of wind turbine drivetrain fault diagnosis by using torsional vi-

brations and modal estimation. *Under review by Elsevier Journal of Sound and Vibration*, 2021.

[29] Farid K Moghadam, Geraldo F Rebouças, and Amir R Nejad. Digital twin modeling for predictive maintenance of floating offshore wind turbine drivetrains. *Accepted to Springer Journal of Forschung im Ingenieurwesen*, 2021.

[30] Farid K Moghadam and Amir R Nejad. Online condition monitoring of floating wind turbines drivetrain by using digital twin modeling approach. *Under review by Elsevier Journal of Mechanical Systems and Signal Processing*, 2021.

[31] John Marius Hegseth and Erin E Bachynski. A semi-analytical frequency domain model for efficient design evaluation of spar floating wind turbines. *Marine Structures*, 64:186–210, 2019.

[32] Sintef. Sima. `https://www.sintef.no/en/software/sima/`.

[33] Harald Ormberg and Erin E Bachynski. Global analysis of floating wind turbines: Code development, model sensitivity and benchmark study. In *The 22nd International Offshore and Polar Engineering Conference*. International Society of Offshore and Polar Engineers, 2012.

[34] Jason Jonkman, Sandy Butterfield, Walter Musial, and George Scott. Definition of a 5-MW reference wind turbine for offshore system development. Technical report, National Renewable Energy Lab.(NREL), Golden, CO (United States), 2009.

[35] Amir R Nejad, Erin E Bachynski, and Torgeir Moan. Effect of axial acceleration on drivetrain responses in a spar-type floating wind turbine. *Journal of Offshore Mechanics and Arctic Engineering*, 141(3), 2019.

[36] Amir Rasekhi Nejad, Yi Guo, Zhen Gao, and Torgeir Moan. Development of a 5-MW reference gearbox for offshore wind turbines. *Wind Energy*, 19(6):1089–1106, 2016.

[37] Farid K Moghadam and Amir R Nejad. Drivetrain fault detection of multi-megawatt offshore wind turbines by statistical learning. *To be submitted*, 2021.

[38] IEC 61400-1. Wind turbines, part 1: Design requirements, 2005.

[39] H Polinder, D Bang, RPJOM Van Rooij, AS McDonald, and MA Mueller. 10-MW wind turbine direct-drive generator design with pitch or active speed stall control. In *2007 IEEE International Electric Machines & Drives Conference*, volume 2, pages 1390–1395. IEEE, 2007.

[40] Shuaishuai Wang, Amir R Nejad, and Torgeir Moan. On design, modelling, and analysis of a 10-MW medium-speed drivetrain for offshore wind turbines. *Wind Energy*, 23(4):1099–1117, 2020.

[41] Hui Li, Zhe Chen, and Henk Polinder. Optimization of multibrid permanent-magnet wind generator systems. *IEEE transactions on energy conversion*, 24(1):82–92, 2009.

[42] Nejad A.R., Gao Z., and Moan T. On long-term fatigue damage and reliability analysis of gears under wind loads in offshore wind turbine drivetrains. *International Journal of Fatigue*, 61:116–128, 2014.

[43] MR Dubois, H Polinder, and JA Ferreira. Comparison of generator topologies for direct-drive wind turbines. *Proceedings of the 2000 NORPIE*, pages 22–26, 2000.

[44] ISO 10816-21. Mechanical vibration, evaluation of machine vibration by measurements on non–rotating parts: horizontal axis wind turbines with gearbox, 2015.

[45] ISO 13373-1. Condition monitoring and diagnostics of machines—vibration condition monitoring—part 1: General procedures, 2002.

[46] Akilu Yunusa-Kaltungo and Jyoti K Sinha. Coherent composite hos analysis of rotating machines with different support flexibilities. In *Vibration Engineering and Technology of Machinery*, pages 145–153. Springer, 2015.

[47] J Mathew and RJ Alfredson. The condition monitoring of rolling element bearings using vibration analysis. *Journal of vibration, acoustics, stress, and reliability in design*, 106(3):447–453, 1984.

[48] P Večeř, Marcel Kreidl, and R Šmíd. Condition indicators for gearbox condition monitoring systems. *Acta Polytechnica*, 45(6), 2005.

[49] CJ Stander, PS Heyns, and W Schoombie. Using vibration monitoring for local fault detection on gears operating under fluctuating load conditions. *Mechanical Systems and Signal Processing*, 16(6):1005–1024, 2002.

[50] Z Hameed, YS Hong, YM Cho, SH Ahn, and CK Song. Condition monitoring and fault detection of wind turbines and related algorithms: A review. *Renewable and Sustainable energy reviews*, 13(1):1–39, 2009.

[51] Fangzhou Cheng, Jun Wang, Liyan Qu, and Wei Qiao. Rotor-current-based fault diagnosis for dfig wind turbine drivetrain gearboxes using frequency analysis and a deep classifier. *IEEE transactions on industry applications*, 54(2):1062–1071, 2017.

[52] Chinmaya Kar and AR Mohanty. Monitoring gear vibrations through motor current signature analysis and wavelet transform. *Mechanical systems and signal processing*, 20(1):158–187, 2006.

[53] Zijun Zhang, Anoop Verma, and Andrew Kusiak. Fault analysis and condition monitoring of the wind turbine gearbox. *IEEE transactions on energy conversion*, 27(2):526–535, 2012.

[54] Pavan Kumar Kankar, Satish C Sharma, and Suraj Prakash Harsha. Vibration-based fault diagnosis of a rotor bearing system using artificial neural network and support vector machine. *International Journal of Modelling, Identification and Control*, 15(3):185–198, 2012.

[55] Jürgen Herp, Niels L Pedersen, and Esmaeil S Nadimi. Assessment of early stopping through statistical health prognostic models for empirical rul estimation in wind turbine main bearing failure monitoring. *Energies*, 13(1):83, 2020.

[56] Cédric Peeters, Patrick Guillaume, and Jan Helsen. Vibration-based bearing fault detection for operations and maintenance cost reduction in wind energy. *Renewable Energy*, 116:74–87, 2018.

[57] Baoping Tang, Wenyi Liu, and Tao Song. Wind turbine fault diagnosis based on morlet wavelet transformation and wigner-ville distribution. *Renewable Energy*, 35(12):2862–2866, 2010.

[58] Wilson Q Wang, Fathy Ismail, and M Farid Golnaraghi. Assessment of gear damage monitoring techniques using vibration measurements. *Mechanical Systems and Signal Processing*, 15(5):905–922, 2001.

[59] R Uma Maheswari and R Umamaheswari. Trends in non-stationary signal processing techniques applied to vibration analysis of wind turbine drive train–a contemporary survey. *Mechanical Systems and Signal Processing*, 85:296–311, 2017.

[60] VN Patel, N Tandon, and RK Pandey. Defect detection in deep groove ball bearing in presence of external vibration using envelope analysis and duffing oscillator. *Measurement*, 45(5):960–970, 2012.

[61] Farid K Moghadam and Amir R. Nejad. Experimental validation of angular velocity measurements for wind turbines drivetrain condition monitoring. In *International Conference on Offshore Mechanics and Arctic Engineering*, volume 59353, page V001T01A035. American Society of Mechanical Engineers, 2019.

[62] Henrik Stensgaard Toft, John Dalsgaard Sørensen, and Dick Veldkamp. Assessment of load extrapolation methods for wind turbines. *Journal of solar energy engineering*, 133(2), 2011.

[63] Ami Wiesel and Alfred O Hero. Distributed covariance estimation in gaussian graphical models. *IEEE Transactions on Signal Processing*, 60(1):211–220, 2011.

[64] Tsuyoshi Idé, Aurelie C Lozano, Naoki Abe, and Yan Liu. Proximity-based anomaly detection using sparse structure learning. In *Proceedings of the 2009 SIAM international conference on data mining*, pages 97–108. SIAM, 2009.

[65] Sankar K Roy, AR Mohanty, and CS Kumar. Amplitude demodulation of instantaneous angular speed for fault detection in multistage gearbox. In *Vibration Engineering and Technology of Machinery*, pages 951–961. Springer, 2015.

[66] John Licari, Carlos E Ugalde-Loo, Janaka B Ekanayake, and Nicholas Jenkins. Damping of torsional vibrations in a variable-speed wind turbine. *IEEE Transactions on Energy Conversion*, 28(1):172–180, 2012.

[67] Andrea Saltelli, Stefano Tarantola, and KP-S Chan. A quantitative model-independent method for global sensitivity analysis of model output. *Technometrics*, 41(1):39–56, 1999.

[68] Yang Liu, Yulai Zhao, Zi-Qiang Lang, Jintao Li, Xinxin Yan, and Siyao Zhao. Weighted contribution rate of nonlinear output frequency response functions and its application to rotor system fault diagnosis. *Journal of Sound and Vibration*, 460:114882, 2019.

[69] Daniel J Inman and Ramesh Chandra Singh. *Engineering vibration*, volume 3. Prentice Hall Englewood Cliffs, NJ, 1994.

[70] Mert Pilanci, Orhan Arikan, and Mustafa C Pinar. Structured least squares problems and robust estimators. *IEEE transactions on signal processing*, 58(5):2453–2465, 2010.

[71] Gene H Golub and Charles Van Loan. Unsymmetric positive definite linear systems. *Linear Algebra and its Applications*, 28:85–97, 1979.

[72] Russell Charles Hibbeler and SC Fan. *Mechanics of materials*, volume 8. Prentice Hall, 2011.

[73] B Engel and Sara Salman Hassan Al-Maeeni. Failure analysis and fatigue life estimation of a shaft of a rotary draw bending machine. *constraints*, 3:1785–1790, 2017.

[74] Carlo Gorla, Francesco Rosa, Edoardo Conrado, and Horacio Albertini. Bending and contact fatigue strength of innovative steels for large gears. *Proceedings of the Institution of Mechanical Engineers, Part C: Journal of Mechanical Engineering Science*, 228(14):2469–2482, 2014.

[75] ISO6336-2. Calculation of load capacity of spur and helical gears, part 2: calculation of surface durability (pitting), 2006.

[76] Stephen D Downing and DF Socie. Simple rainflow counting algorithms. *International journal of fatigue*, 4(1):31–40, 1982.

[77] James F Manwell, Jon G McGowan, and Anthony L Rogers. *Wind energy explained: theory, design and application*. John Wiley & Sons, 2010.

[78] Richard Gordon Budynas, J Keith Nisbett, et al. *Shigley's mechanical engineering design*, volume 8. McGraw-Hill New York, 2008.

[79] Bruno Sudret, Zakoua Guédé, Patrick Hornet, Jean-Michel Stéphan, and Maurice Lemaire. Probabilistic assessment of fatigue life including statistical uncertainties in the sn curve. In *Proceedings of the 17th International Conference on Structural Mechanics in Reactor Technology*, 2003.

[80] Art B Owen. Monte carlo theory, methods and examples. *Monte Carlo Theory, Methods and Examples. Art Owen*, 2013.

Appendix A

Appended papers

A.1 Paper 1

Paper 1:
Evaluation of PMSG-based drivetrain technologies for 10-MW floating offshore wind turbines: Pros and cons in a life cycle perspective.
Authors: Farid Khazaeli Moghadam, Amir Rasekhi Nejad
Published in *Wind Energy*, 2020, DOI: 10.1002/we.2499.

Received: 2 May 2019 | Revised: 13 February 2020 | Accepted: 2 March 2020
DOI: 10.1002/we.2499

WILEY

RESEARCH ARTICLE

Evaluation of PMSG-based drivetrain technologies for 10-MW floating offshore wind turbines: Pros and cons in a life cycle perspective

Farid K. Moghadam | Amir R. Nejad

Department of Marine Technology, Norwegian University of Science and Technology, Trondheim, Norway

Correspondence
Farid K. Moghadam, Department of Marine Technology, Norwegian University of Science and Technology, Trondheim, Norway.
Email: farid.k.moghadam@ntnu.no

[Correction added on 20 April 2020, after first online publication: Peer review history statement has been added.]

Abstract

This paper presents an in depth evaluation and comparison of three different drivetrain choices based on permanent-magnet synchronous generator (PMSG) technology for 10-MW offshore wind turbines. The life cycle approach is suggested to evaluate the performance of the different under consideration drivetrain topologies. Furthermore, the design of the drivetrain is studied through optimized designs for the generator and gearbox. The proposed drivetrain analytical optimization approach supported by numerical simulations shows that application of gearbox in 10-MW offshore wind turbines can help to reduce weight, raw material cost, and size and simultaneously improve the efficiency. The possibility of resonance with the first torsional natural frequency of drivetrain for the different designed drivetrain systems, the influence of gear ratio, and the feasibility of the application for a spar floating platform are also discussed. This study gives evidence on how gearbox can mitigate the torque oscillation consequences on the other components and how the latter can influence the reliability of drivetrain.

KEYWORDS

drivetrain optimization, floating offshore wind turbine, life cycle assessment, permanent-magnet synchronous generator

1 | INTRODUCTION

The capacity of offshore wind turbines and the distance from shores is rising rapidly, so that multigigawatt offshore wind farms based on multimegawatt floating turbines show potentials to be one of the dominant sources of power production in the future. The latter is due to availability of better wind resources, less turbulence, steadier winds, and less wind shear; easier transportation of larger turbines on the sea; technological developments in power electronic converters and direct current (DC) power transmission technologies; the establishments of required market infrastructures; and technological achievements in installation of turbines in deep waters, which lead to a considerable drop in the levelized cost of energy (LCOE) of offshore wind turbines. In spite of significant improvements, there are still no unanimous decision about the drivetrain system technology in offshore wind turbines.[1,2] Offshore wind reaches to 10-MW turbines or even higher, but there are still different interests between manufacturers in the selection of drivetrain technology. One reason is that the drivetrain in wind originally comes from available experiences in other industries, which has been modified over time. The latter has then been upscaled for higher powers with some modifications to reduce the production costs and improve the dynamic response. Because the wind turbines are developed for a wide range of power in various onshore/offshore, fixed/floating, two-/three-bladed rotors, upwind/downwind, high/medium/low wind, fix/variable speed, stall/active yaw, and stall/active pitch applications, a customized design of the drivetrain for the cost reduction and performance improvement is inevitable. Therefore, there is a need for a special drivetrain design for each power class for different applications to have the lowest manufacturing, installation, and

The peer review history for this article is available at https://publons.com/publon/10.1002/we.2499.

maintenance costs and simultaneously achieve the most reliable and efficient operation. The optimization of the drivetrain system also influences on the turbine design, because the size and weight of drivetrain is a main constraint in design of nacelle.

Even though the drivetrain system has an important share in manufacturing and maintenance of the turbine, and even if there are some researches conducted on the optimization of the components of the drivetrain, there is no analytical study about a system-level optimization of the drivetrain for 10-MW floating wind turbine applications as of the authors' knowledge. The proof for this claim is the different technology interests in offshore wind turbine industry. Because the drivetrain is a complex electromechanical system, the optimization of this system is a multidisciplinary task that calls for external system-level and internal component-level optimization problems. The other circumstance is that the optimizations need to be performed over the life cycle of the system, consisting of design, manufacturing and installation, and operation and maintenance (O&M). In this paper, different permanent magnet synchronous generator (PMSG)-based drivetrain technologies, that is, direct-drive permanent-magnet synchronous generator (DDPMSG), medium-speed permanent-magnet synchronous generator (MSPMSG), and high-speed permanent-magnet synchronous generator (HSPMSG), are designed and compared. This work is a starting point for the optimization of drivetrain systems for large offshore wind turbines from design, manufacturing, and O&M perspectives. It will be shown that a thoughtful selection of technology can considerably reduce the drivetrain weight and cost, while improving the overall efficiency and dynamic response. The numerical results show that the drivetrain system based on MSPMSG could be the most promising choice for 10-MW floating offshore wind turbines.

Four assumptions are made in this research:

1. There are some limitations such as availability of a technology, vendors, and raw materials that influence on companies' drivetrain selection. The latter will not be discussed in this research.
2. The purpose of analytical design of the drivetrain components is to provide input data for the comparison study between different drivetrain technologies. Complementary component-level detailed design steps such as finite element analysis for more detailed electromagnetic, structural, and thermal designs are not in the scope of this research.
3. Reliability calculations for under consideration drivetrain systems are not in the scope of this paper, but how the failure modes are affected by the drivetrain technology is discussed.
4. For each drivetrain technology, the conventional configuration is considered in this study. Some innovative wind turbine drivetrain systems, such as gearbox integrated main-bearing (used eg in Areva Multibrid M5000 medium-speed technology) and hub-supported drivetrain (used eg in GE Haliade 150-6MW direct-drive technology) based on more compact and lightweight designs, are not the focus of this work.

The study is carried out on the basis of the most conventional drivetrain configurations available in the market, and the results provide a baseline for any further investigations on 10-MW PMSG-based wind turbine drivetrain systems. The life cycle approach for performance assessment of the different drivetrain topologies based on the PMSG technology over the design lifetime is introduced. Over the life cycle, the research focus will be on design, manufacturing, and operation supported by an analytical model of the drivetrain components. On this basis, the contributions of this paper are the following:

1. Drivetrain performance assessment using the life cycle approach is introduced.
2. A new drivetrain optimization approach is proposed, which ensures an optimized overall cost and weight, improves the reliability and efficiency, and simultaneously assesses the feasibility of the design.
3. A new analytical design approach is proposed for the optimized design of PMSG based on the optimization of the active material cost. The optimization problem is solved numerically, and the global optimizer is determined. The design is validated by ANSYS-RMxprt software.
4. An analytical design model of the gearbox is presented, and a new optimization approach is proposed to optimize the gearbox weight. KISSsoft software is used to validate the feasibility of the design.
5. A comprehensive comparison between the design, raw material cost, weight, size, efficiency, and reliability of DDPMSG, MSPMSG, and HSPMSG drivetrain technologies is presented.
6. The first torsional natural frequency of three under consideration drivetrain technologies is calculated, and the feasibility of application in floating offshore wind turbines is investigated.

The selection of drivetrain technology is a multidisciplinary task that needs to compromise between the criteria obliged by the life cycle assessment approach. By using DDPMSG, the generator will be larger, heavier, and more expensive, which can also increase the weight and the cost of nacelle, tower, and platform consequently. The latter also affects the installation and maintenance costs. The first research problem would be if the extra weight of a low-speed generator could compensate the weight reduction due to the gearbox removal. The second question is if the elimination of gearbox can improve the reliability because the nullification of one of the subsystems in a serial system seems to help reach a higher reliability if the reliability of components is fixed. The third challenge is if the gearbox removal can improve the drivetrain efficiency using the same justification that was provided for the reliability. The last question is which topology can safely work with floating offshore platform, which is expected to be widely used in high-power offshore wind turbines. This research uses analytical models of the drivetrain components along with numerical optimization techniques and deals with the described research problems. It is analytically proven that for the under consideration range of speed and power, gearbox helps to improve the operation and reduce the raw material cost of drivetrain. The main focus of this work is studying about the design interactions and dynamic couplings between gearbox and generator in offshore floating wind turbines' drivetrain systems. Higher level details of the drivetrain design including the design of main bearings, high-speed and low-speed shafts, and bedplate are

not discussed in this work. The weight of bedplate has an important role on the drivetrain overall weight. The bedplate sizing depends on a wide range of parameters including drivetrain technology, rotor weight, rotor overhang, main shaft dimension, main bearings weight, gearbox weight, generator weight, converter weight, and transformer weight. In addition to individual component weights that the bedplate must support, the bedplate model must take into account rotor loads. For the design of bedplate for the under consideration drivetrain systems, readers are referred to Guo et al.[3,4]

The paper is organized as follows: The state-of-the-art of wind turbine drivetrain technologies for offshore and onshore applications is presented in Section 2. In Section 3, the drivetrain life cycle performance assessment approach and the proposed drivetrain optimization algorithm are described. The analytical design and optimization procedure of the three under consideration PMSGs, that is, DDPMSG, MSPMSG, and HSPMSG, and the associated gearboxes are elaborated in the same section. Numerical simulations to validate the optimized generators and gearboxes design and a detailed comparison study between the under consideration drivetrain systems concerning cost, weight, operation, and performance are presented in Section 4. The paper is concluded in Section 5.

2 | STATE-OF-THE-ART TECHNOLOGIES

A review on commercialized drivetrain system technologies of wind turbines with a power higher than 4 MW is performed in this section. The dominant drivetrain technologies for the under consideration power are DDPMSG, MSPMSG, direct-drive wound rotor synchronous generator (DDWRSG), medium-speed wound rotor synchronous generator (MSWRSG), high-speed doubly fed induction generator (HSDFIG), and high-speed squirrel cage induction generator (HSSCIG) (Table 1). DDPMSG is the dominant technology of Siemens Gamesa (power range 6-8 MW) and GE (power range 6-12 MW) for fixed/floating platforms. MSPMSG is MHI Vestas' solution for the power higher than 8 MW, Aeorodyn for 6 MW, and Adwen and Areva for 8 and 5 MW, respectively. MSWRSG is Aerodyn's alternative for 8 MW. HSSCIG is the technology used by both Siemens and Vestas (power range 3-4 MW). HSDFIG is the technology used by Senvion and REpower for 6.2 MW offshore. DDWRSG is the Enercon technology interest for the power up to 8 MW but for onshore applications. Some research-scale offshore drivetrain designs prototyping in the 5 to 12 MW range have also been considered in this study. An overview of the most recent application of different drivetrain technologies is shown in Table 2. Based on this summary, all these technologies show potentials for the drivetrain in offshore wind turbines. Even though the most recent literature recommends DDPMSG because of efficiency and reliability considerations,[5] the diversity in drivetrain technology interests in both industry and academia shows that other factors influence on the selection of the wind turbine drivetrain. In the meantime, there are many other technologies that have not been commercialized. For instance, direct-drive and medium-speed DFIG with a high number of poles are less efficient due to a high excitation loss.[6] Brushless DFIG is not an efficient machine due to a low-power torque density compared with typical induction and synchronous generators.[7] Superconducting direct-drive synchronous generators are still far from being commercialized regarding standardization and some open paths to explore regarding cost and reliability.[8] An overview on the commercialized turbines (see Table 2) and the reference turbines developed by research institutions and universities[9,10] shows a unanimous interest in PMSG for high-power offshore wind turbine drivetrain systems. Higher efficiency due to external excitation circuit removal, higher reliability and availability, and less maintenance costs due to the compactness and lightweight design and brushes elimination are the motivations.[10] Different designs for permanent-magnet generators are proposed in the literature. The latter includes vernier/conventional generators, axial/radial flux, surface-mounted/interior rotor magnets, slotted/slotless stator, inner/outer rotor, distributed/concentrated winding, and integer-/fractional-slot winding machines.[11] However, still, the commercialized designs for wind turbine drivetrain systems, that is, radial flux, inner rotor, and surface-mounted PMSGs, are the focus of this research.

In the continued section, the priorities which may be considered by the different turbine manufacturers in selection of the PMSG drivetrain technology is analytically studied. It is aimed to find which PMSG-based drivetrain topology will probably be the future trend based on the analysis of the available choices. The power range and turbine platform are emphasized as the other important criteria which affect the drivetrain technology chosen by different manufacturers.

3 | METHODOLOGY

For this study, the DTU 10 MW reference wind turbine is used.[9] The parameters of the DTU turbine used for the drivetrain studies are listed in Table 3. The other parameters related to the drivetrain components are updated based on the designed generators and gearboxes in this paper.

3.1 | Life cycle approach

In the life cycle performance assessment approach, to have a meaningful comparison between different drivetrain technologies, the overall costs and benefits are evaluated over the design lifetime, and the outcome is expressed by using levelized values as equivalent costs and benefits at the regular intervals during all the system life. By using this method, the costs and revenues of various drivetrain technologies are needed to be studied over design, manufacturing, installation, O&M, life extension, and decommissioning[12] (see Figure 1). The optimal configuration is the one that gives the highest profit over the cycle.

In design, concerns related to design, for example, complexities in design, maximal design utilization, and higher degree of adaptation to site-specific conditions, reliability, and controllability, are important. A preliminary failure modes study about the generator and gearbox in PMSG drivetrain is summarized in Table 4. It is interesting to observe that the most of failure modes can be rooted back to design stage. In

TABLE 1 State-of-the-art of drivetrain technologies in multimegawatt onshore and offshore wind turbines at a glance (up to 10 MW)

Technology	Layout
1. High-speed squirrel cage induction generator • Merits: cheap, simple generator design • Drawbacks: sensitive to transients, low efficiency	
2. High-speed doubly fed induction generator • Merits: cheap, fractional converter • Drawbacks: sensitive to transients, low efficiency	
3. Direct-drive wound rotor synchronous generator • Merits: cheap • Drawbacks: brushes, low efficiency, higher weight	
4. Medium-speed wound rotor synchronous generator • Merits: cheap • Drawbacks: brushes, low efficiency	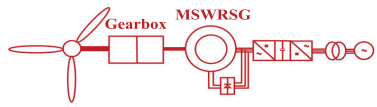
5. Direct-drive permanent-magnet synchronous generator • Merits: low maintenance, high efficiency • Drawbacks: expensive	
6. Medium-speed permanent-magnet synchronous generator • Merits: low maintenance, high efficiency, less weight for higher powers • Drawbacks: expensive	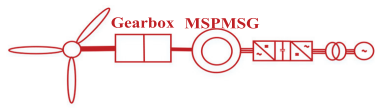

reliability-based design, one should look at the reliability of a drivetrain design considering failure modes to ensure a safe and reliable operation over the operating speed and torque range. However, the failure modes depend on the drivetrain technology. Furthermore, regarding specific operating conditions, some modes are of a higher importance. The failure functions will then be defined for the components and subsequently the drivetrain system based on a criticality analysis of the failure modes of the components. The impacts of uncertainty sources such as wind, wave, material strength model, and power grid can be modelled by using safety factors in a deterministic design or applying a multiplicative model of uncertainties in a stochastic design approach.[18] The outcome of reliability-based design will specify the expected lifetime of drivetrain system. For new systems and applications, for example, PMSG-based drivetrain systems for 10 MW spar floating offshore wind turbine, due to the lack of standards for the design load cases, design is more challenging, which requires to leverage the similar experiences accompanied by a wide range of numerical simulations. As a design study in this paper, the first torsional natural frequency of under consideration PMSG-based drivetrain systems is studied, and design remarks are given about the feasibility of using these technologies in floating platforms.

In manufacturing and installation, weight, compactness, and special manufacturing and installation requirements should be taken into consideration. An example of more manufacturing efforts is in manufacturing DDPMSG, where the too high pole count causes small rotor poles with fine stator slotting, which makes manufacturing expensive. About installation efforts, for instance, less weight drivetrain technology and the consequent reduced weight nacelle and tower help to reach less cost transportation and craning requirements. For more clarification, a promising solution for a floating wind turbine transport and installation is to preassemble the whole turbine in one piece in the shipyard, towing to the

TABLE 2 Drivetrain most conventional technologies

HSSCIG	HSDFIG	DDWRSG	MSWRSG	DDPMSG	MSPMSG
SWT-4.0-130	GE 5.3-153	EN136-4.2	SCD 8.0/168	SG 8.0-167 DD	V164-10.0MW
Siemens	General Electric	Envision	Aerodyn	Siemens	Vestas
4 MW	5.3 MW	4.2 MW	8 MW	8 MW	10 MW
Offshore/onshore	Onshore	Offshore/onshore	Offshore	Offshore	Offshore
Geared (1:119)	Geared (NA)	Direct-drive	Geared (1:27)	Direct-drive	Geared (1:38)
V136-4.2 MW	6.2M126	E-126 7.580	NA	YZ150/10.0	Adwen AD 8-180
Vestas	Senvion	Enercon	NA	Swiss Electric	Adwen
4 MW	6.2 MW	7.6 MW	NA	10 MW	8 MW
Onshore	Offshore	Onshore	NA	Offshore	Offshore
Geared (NA)	Geared (1:97)	Direct-drive	NA	Direct-drive	Geared (1:41)

Abbreviations: DDPMSG, direct-drive permanent-magnet synchronous generator; DDWRSG,direct-drive wound rotor synchronous generator; HSDFIG, high-speed doubly fed induction generator; HSSCIG, high-speed squirrel cage induction generator; MSPMSG,medium-speed permanent-magnet synchronous generator; MSWRSG, medium-speed wound rotor synchronous generator.

Parameter	Value
Rated power (MW)	10
Rated rotor speed (rpm)	9.6
Rated wind speed (m/s)	11.4
Equivalent driveshaft linear spring constant (N.m/rad)	2,452,936,425
Rotor moment of inertia J_r $(kg.m^2)$	8×10^8

TABLE 3 Turbine specification[9]

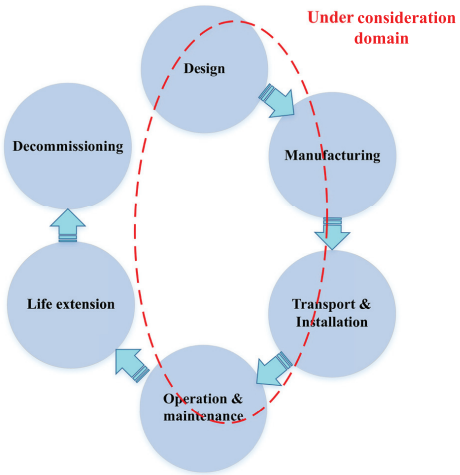

FIGURE 1 Drivetrain life cycle assessment approach [Colour figure can be viewed at wileyonlinelibrary.com]

offshore deployment site, and using a large floating crane to hook up with mooring systems,[19] where the most important limitation is the turbine weight. A significant part of this paper is dedicated to the optimization of weight, raw material cost, and size for under consideration drivetrain technologies as a necessary input to study manufacturing and installation costs.

In O&M, performance, efficiency, reliability, availability, and maintenance costs are required to be addressed. In offshore wind turbine applications, especially in high-power floating installations in deep waters, due to farther distance from shores, broader ranges of excitation sources and motions, and utilization of large, massive, and expensive components, any improvement in efficiency, reliability, and availability can help to reduce cost of electricity. It is reported that O&M contributes in order of 30% of LCOE in offshore wind turbines.[20] In *performance*, the quality of generator output power is concentrated, where the generator technology and the power frequency converter play a significant role. In *efficiency*, improving the efficiency of the drivetrain is discussed. It is needed to evaluate which technology and configuration will give a greater efficiency, which helps to reduce the electricity cost. Therefore, there will be a need to look into all the individual components of the drivetrain system. Then, the overall efficiency in the rated power is calculated/compared for the different technologies. In *reliability*, the failure rates of different drivetrain components and fault tolerance properties of each technology is required to be analyzed. Therefore, the failure modes of the subcomponents must be listed, so that the components and subsequently the drivetrain systems could be studied/sorted according to the

TABLE 4 Basic failure modes study of PMSG drivetrain components

PMSG[11,13-15]	Gearbox[16,17]
Possible faults	**Possible faults**
Mechanical faults	*Gear fault*
Blocking bearings	*Shaft fault*
Stucking filings in the air gap	*Bearing fault*
Electrical faults	Shaft misalignment
Short circuit faults	Shaft bending
Finite resistance circuit faults	Shaft loose
Open circuit faults	*Housing fault*
Magnetic faults	*Fastener fault*
Demagnetization of rotor magnets	*Seal fault*
Detachment of rotor magnets	**Fault reasons**
Fault reasons	Underestimated design loads
Overcurrent	Torque overloads
Voltage sags, swells, and harmonics	Material defects
Cooling and lubrication system maloperation	Manufacturing errors
Sensors and communication network maloperation	Dirt in the lubricant or poor lubrication
Rotor torque oscillation by wave-/wind-induced moments	Damage during transportation and assembly
Electromagnetic torque oscillations	Misalignment of components in the shaft
Poor or contaminated bearing lubrication	**Failure modes**
Bearing installation problems	Gear wear; scuffing and contact fatigue (fatigue)
Failure modes	Gear plastic deform; crack; fracture; bending (ultimate = fatigue)
Stator winding insulation fail (fatigue, ultimate)	Bearing spalling : excessive load = poor lubrication (fatigue)
Demagnetization: magnet heating (ultimate)	Bear: smearing : foreign objects trapped within (fatigue)
Demagnetization: increased flux density (ultimate)	Bear: worn surface : skewed roller = lubrication (fatigue)
Phase/path cutoff (fatigue, ultimate)	Bear: partial chipping of rings = roller : excessive load (fatigue)
Stator tooth fretting damage/crack (fatigue/ultimate)	Bear: ring split = crack : excessive load = loose fit (fatigue)
Detached magnet: raised centrifugal forces (fatigue)	Bear: fretting corrosion : fluctuating load = lubrication (fatigue)
Bearing pitting and sanding (fatigue)	Bear: electrical pitting : sparks by electric current (fatigue)
Bearing brinelling/false brinelling (fatigue)	Bear: damaged retainer : heavy vibration = speed change (fatigue) different

Abbreviation: PMSG, permanent-magnet synchronous generator.

highest to the lowest probability of failure regarding the most critical failure modes. The latter can be based on the failure reports if enough event logs and trouble shooting reports of the operation are available. It can also be based on the post processing of real operational data measured from the system[21] to calculate the fatigue damage and remaining useful life of the system. The latter could be supported by sufficient simulated models under the different load cases dependent on the application. In general, a combination of these two approaches is used. Obtaining the vulnerability map for each component considering the critical failure modes, which indicates the subcomponents from the highest to lowest probability of damage is the basis for reliability-based maintenance. The latter supported by lifetime-predicting models will give an insight about the reliability and remaining lifetime of the system, which is needed to be done for the different drivetrain technologies. In *availability*, the downtimes of the wind turbine due to the drivetrain shutdowns, including downtimes for periodic maintenance or unscheduled repairs for different technologies, are needed to be discussed. Furthermore, the possibility of using modular design for different gearboxes and generators for reduction of downtime in different drivetrain technologies relates to availability studies. In order to compare reliability and availability of different technologies, a detailed analysis of each component's failure modes, probability of failure, and the downtimes is required. Maintenance costs will relate to the failure rate of components, labor, parts, operations, equipment, and facilities.[22] The technology of high-power floating offshore wind turbines is new, and there are only few operational turbines of this type. An accurate O&M comparison between different technologies relies on an access to operational data of the same system under the same load cases; however, approximated analyses can be attained based on available experiences in lower power ranges, similar experiences from other industries, some limited data in access from the same operational turbines and applications, scaled-down laboratory-based systems, supported by high-fidelity simulation models and theoretical analyses. Each drivetrain technology is finally needed to be scored based on O&M criteria, namely, efficiency, reliability, availability, and maintenance costs. The other fact that makes O&M analysis more difficult is that each drivetrain technology is a different dynamic system with different responses. To maintain the tip speed ratio of larger rotors in higher powers to reach the highest power coefficient, the nominal rotational speed of rotor is reduced, which causes different dynamic responses even for the turbines of the same technology but a different rated power. Moreover, floating offshore platforms encounter turbines into different motions induced by the synergistic impacts of wind and wave, the gravity of the turbine, and the floating platform. The lower rotor speed and more diverse and higher amplitude excitations necessitate a special O&M study for the drivetrain in high-power floating applications. In this research, for the under consideration PMSG-based drivetrain topologies, the overall efficiency is calculated/compared considering the efficiency of the individual components. As a reliability analysis, the drivetrain failure modes affected by the rotor torque and generator electromagnetic torque oscillations of different technologies are discussed and compared. Unequal

TABLE 5 Case study technologies

Technology	Type 1 (DDPMSG)	Type 2 (MSPMSG)	Type 3 (HSPMSG)
Rated power(MW)	10	10	10
Application	Floating offshore	Floating offshore	Floating offshore
Generator	PMSG	PMSG	PMSG
Gearbox	Direct-drive	Three stages (1:50)	Three stages (1:156)

Abbreviations: DDPMSG, direct-drive permanent-magnet synchronous generator; HSPMSG, high-speed permanent-magnet synchronous generator; MSPMSG, medium-speed permanent-magnet synchronous generator; PMSG, permanent-magnet synchronous generator.

cogging torque values in different drivetrain technologies cause different rotational vibration performances. The part of the life cycle that is emphasized is specified in Figure 1.

3.2 | Proposed drivetrain design optimization

The selection of drivetrain technology is a multidisciplinary task that needs to make compromises between the criteria obliged by the life cycle approach. As explained earlier, PMSG is the promising technology for high-power offshore wind turbines. Because 10 MW PMSG-based drivetrain can be realized by different gear ratios, it is needed to assess different gear ratios over the life cycle. Gear ratio as per definition in IEC 61400-4 is $\frac{n}{n_r}$, where n and n_r are the speeds of input and output shafts, respectively.[23] The three under consideration drivetrain topologies are DDPMSG, MSPMSG, and HSPMSG technologies, which are specified in Table 5). The 2D view of PMSG overall design that is used for the three under consideration drivetrain technologies is shown in Figure 2A. DDPMSG is a direct-drive technology. MSPMSG is the medium-speed drivetrain technology, which can be realized by either two or three stages. The operational high-power medium-speed technologies are often based on hybrid gearboxes containing three stages, including planetary gears in the upwind stages and parallel gear pairs, which can be used to realize the gear ratio 1 : 36 to 1 : 108. The mentioned gearbox topology is selected for the MSPMSG drivetrain technology in the paper. HSPMSG is a high-speed drivetrain technology. The gearbox for the high-speed technology can be realized by three planetary stages with a gear ratio variable from 1 : 108 to 1 : 216. The gearbox topology for the MSPMSG and HSPMSG drivetrain technologies is shown in Figures 2B and 2C. In industry, based on the rule of thumb, the conventional parallel stage is used for realization of the inverse of gear ratio $1 < \alpha < 3$, and a conventional planetary stage is used for $3 < \alpha < 6$. For $1 < \alpha < 3$, the industry interest is in using a parallel stage. The reason that planetary gear is not dominant for $1 < \alpha < 3$ is due to more complex design and manufacturing, more difficult access for maintenance, and difficulty in fault detection and condition monitoring. Therefore, for the realization of the gear ratio 1 : 50 suggested in DTU 10-MW turbine design, the gearbox topology based on two planetary gear stages and one parallel stage is studied in the paper as the most conventional topology to realize the similar gear ratios in the medium-speed wind turbine drivetrain systems but for lower power ranges. In the power range 10 MW in a medium-speed application, there is no agreed topology and gear ratio in the gearbox design. Some manufacturers have recently used other design topologies to meet better the requirements of offshore application by a less weight and more robust design under load variations, for example, Vestas V164-9.5MW and Adwen AD 8MW-180 have used three-stage compound planetary stages and two-stage compound planetary stages, respectively, to realized the gear-ratios 1 : 38 and 1 : 41. Because no reference was found, which prohibits the utilization of three planetary stages to realize an MS gearbox, another MS topology based on three planetaries is also studied. For the HS design with the assumed gear ratio 156, the most practical way to realize the gearbox is using three planetary stages.

Larger generator in DDPMSG technology causes more costly manufacturing, installation, and maintenance. Even though the general idea is that a direct-drive generator is more reliable, available, and efficient due to a gearbox removal (eg, in Polinder et al[20,25] and Zhang et al[24]), the different generators and gearboxes in DDPMSG, MSPMSG, and HSPMSG drivetrain technologies result in different dynamic responses, efficiencies, and weights of the components and the drivetrain, which calls for an analytical study before judging about operations and economics. Generator and gearbox are focused. The other significant components are converter system and main bearings. The main bearings in the under consideration technologies are the same because they are placed on low-speed side. The power converter system depends on rated power and voltage. Because the three generators are designed for the same power factor and consequently apparent power, the rated power of the converters is the same. However, the increased design voltage in MSPMSG and HSPMSG drivetrains compared with DDPMSG helps to reach a higher efficiency for the power converter with less effort due to reduction of switching losses, but the increased voltage raises the power converter cost due to the increased cost of the switches, DC link, and some auxiliary circuits. The changes in the overall drivetrain efficiency and cost due to power converter are neglected.

The algorithm of the proposed PMSG drivetrains evaluation is demonstrated by the flowchart in Figure 3. From the conceptual design perspective, the gearbox affects both the input torque and speed of the generator. The latter are among the critical parameters in design of generator so that the size of generator is directly proportional to these parameters. In each iteration of the proposed drivetrain optimization approach, the gear ratio is fixed by the outer loop. Therefore, the optimization problem of each drivetrain technology is broken into two decoupled problems of gearbox and generator optimizations. As a result, for each drivetrain topology, two internal component-level optimization problems are solved. The first problem looks for the optimized design of the generator. The generator optimization problem is designed to ensure the minimization of cost of active material while maximizing the generator torque density. The second problem is a cost (weight) optimization of the

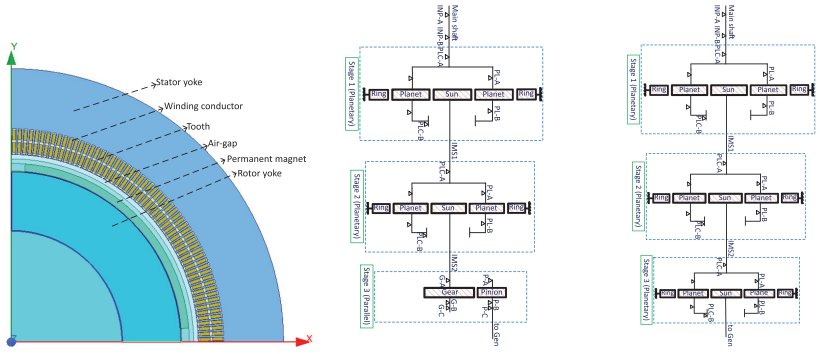

(A) PMSG (B) MSPMSG gearbox (C) HSPMSG gearbox

FIGURE 2 Topology of generator and gearbox in this study. HSPMSG, high-speed permanent-magnet synchronous generator; MSPMSG, medium-speed permanent-magnet synchronous generator; PMSG, permanent-magnet synchronous generator [Colour figure can be viewed at wileyonlinelibrary.com]

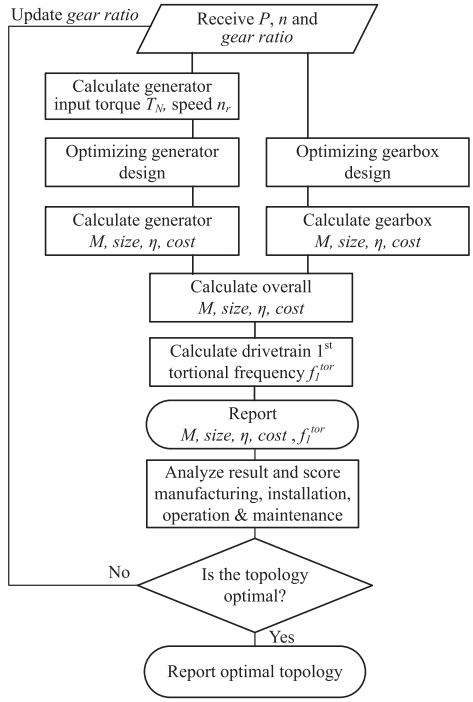

FIGURE 3 Proposed drivetrain optimization approach

multistage gearbox. Drivetrain performance-based and reliability-oriented constraints are imposed to the component-level optimization problems to ensure the feasibility of the generator and gearbox proposed designs and a fair comparison between the under consideration drivetrain technologies. Finally, the designed drivetrain systems are compared with respect to total weight, cost, size, efficiency, and dynamic responses.

3.2.1 | Generator optimization

As discussed in Section 2, PMSG is the dominant technology for high-power offshore wind turbines. Some motivations are as follows:

1. Armature reaction is smaller in a permanent-magnet generator with surface-mounted magnets than in electrically excited generators, due to a larger air gap;

2. Losses of the field winding in electrically excited generators cause lower efficiency in these generators compared with permanent-magnet generators;
3. Besides reducing losses, the permanent-magnet generators lead to a lighter design. For the same power and frequency, compared with an electrically excited generator, a permanent-magnet generator can be realized with a smaller diameter, which is really helpful for design of high-power direct-drive generators for wind turbines[26]; and
4. It is believed that permanent-magnet generators are more reliable than electrically excited generators. One reason is that excitation circuits, the associated power electronics semiconductor devices, and the commutation rings and brushes cause a high portion of failures and downtimes in electrically excited generators, while they are not needed for permanent-magnet generators. The possible faults regarding the application of magnets, including magnets demagnetization and detachment can, to a great extent, be avoided by a proper design approach.

A three-phase radial flux, inner rotor, surface-mounted, slotted machine with laminated stator/rotor cores and distributed winding is the reference generator technology studied in this section. Reluctance torque, which is an important source of torque pulsations, is negligible in surface-mounted PMSGs. Low weight, simple design, and low-armature reaction are some other benefits of surface-mounted technologies.

Different objective functions with different sets of optimization variables are suggested in the literature for optimized design of PMSGs. Li et al[27] suggests the cost of the active material, Dubois et al[28] recommends the ratio of the cost of active material to torque density, and Røkke et al[11] proposes the cost of the active materials including the housing and the cost of the energy lost in the machine over its lifetime to be used to optimize the PMSG design.

In the continued part, an analytical design based on the minimization of the ratio of cost of active material to torque density is used to find the optimized design of the generator in DDPMSG, MSPMSG, and HSPMSG technologies. The latter ensures the minimum cost while maximizing the electromagnetic (developed) torque density and utilization of the generator weight. The proposed analytical model represents the cost function and the design constraints as a function of five geometrical variables. The design procedure for the three under consideration generators is the same, but the parameters and constraints are adapted based on the operating voltage and speed.

The cost function C of the generator optimization problem is defined as

$$C_{\text{generator}}(\boldsymbol{x}) = \arg\min_{x}\left(\frac{\text{cost}_{\text{active}}(\boldsymbol{x})}{T_d(\boldsymbol{x})}\right), \tag{1a}$$

$$cost_{active}(\boldsymbol{x}) = cost_{fe}(\boldsymbol{x}) + cost_{cu}(\boldsymbol{x}) + cost_{pm}(\boldsymbol{x}), \tag{1b}$$

$$T_d(\boldsymbol{x}) = \frac{T_N}{V(\boldsymbol{x})}, \tag{1c}$$

where x is a vector that represents the optimization variables. $cost_{active}$ is the cost of active materials in generator construction in Euro. The cost of active materials consists of the cost of iron used in rotor and stator yokes and stator teeth, copper of the stator windings, and the surface-mounted permanent magnets. $cost_{fe}$ is the total cost of iron, $cost_{cu}$ is the cost of copper, and $cost_{magnet}$ is the cost of magnet material. T_N is the nominal torque in $kN.m$, and V is the generator active volume in m^3. T_d is the generator torque density in $kN.m/m^3$. The variables in Equation (1) are defined by

$$\boldsymbol{x} = [x_1, x_2, x_3, x_4, x_5]^T = [D_s, L_s, b_s, h_s, h_m]^T, \tag{2a}$$

$$cost_{cu} = c_{cu} m_{cu}, \tag{2b}$$

$$cost_{pm} = c_{pm} m_{pm}, \tag{2c}$$

$$cost_{fe} = c_{fe} m_{fe}, \tag{2d}$$

$$V = \pi \frac{D_{so}^2}{4} L_e, \tag{2e}$$

where the five optimization variables D_s, L_s, b_s, h_s, and h_m are the air gap diameter, active length of generator, slot width, slot height, and magnet height, respectively. c_{fe}, m_{fe}, c_{cu}, m_{cu}, c_{pm}, and m_{pm} are the specific costs and total weights of core, copper, and magnet, respectively. The design of surface-mounted PMSG deals with the determination of a high number of variables related to the generator geometry and operation. In the proposed optimized design approach, it was observed that all the generator design variables can be either defined as a function of the five geometrical optimization variables, or considered constant, or can change in optimization problem outer loops. The latter helped to turn a nonlinear and strongly nonconvex problem to a convex problem to be able to find a global optimizer. The other generator design variables, which are not assumed as a optimization variable, are classified into three different groups: first, those that can be written as a function of the five optimization variables, such as flux densities in air gap and teeth; second, the design variables that are assumed constant, for example, air gap thickness, which is fixed at the minimum value regarding the mechanical construction considerations of large permanent-magnet generators, and maximum flux densities in rotor and stator yokes; third, those variables that are updated/changed in outer loops to find their optimal values, for example, magnetic pole embrace $\left(\frac{b_m}{\tau_p}\right)$ and number of slots per pole and phase (q), but in each internal optimization take constant values. The

definition of m_{cu} in terms of the five optimization variables ($x_1, \ldots, x_5$) is given in Equation (3a). The role of winding overhang, the slot wedge, and the insulation thickness is considered in the model. The weight of copper is proportional to the length and the cross section of the winding. The length is dependent on the generator length, the pole pitch, and the overhang, which is proportional to the voltage. The definition of m_{pm} in terms of the optimization variables is given in Equation (3b). $b_m\tau_p$ in this equation models the ratio of the pole surface that is covered by the magnet material to the all pole surface, which could take different values by using an optimization outer loop. The definition of the three components of m_{fe}, which respectively model the iron used for stator teeth, stator yoke, and the rotor core in terms of the optimization variables, is given in Equation (3c). The other variables in this equation are either constant or change by using external optimization loops. V in Equation (3d) is the overall volume of the generator, which is a function of generator equivalent length L_e and the stator outer diameter D_{so}. The generator equivalent length is a function of core length and air gap. The stator outer diameter is also a function of D_s, h_s, and stator yoke height h_{sy}. In Equation (3d), V is written in terms of the optimization variables.

$$m_{cu}(\boldsymbol{x}) = N\left(2x_2 + 2.5\left(\frac{\pi x_1}{p}\right) + 0.05\left(\frac{V_{ph}}{1000}\right) + 0.150\right)\left((x_3 - 2h_i)\frac{x_4 - h_w - 4h_i}{Q}\right)\rho_{cu}, \tag{3a}$$

$$m_{pm}(\boldsymbol{x}) = p\left(\frac{b_m}{\tau_p}\frac{\pi x_1}{p}\right)x_2 x_5 \rho_{pm}, \tag{3b}$$

$$m_{fe}(\boldsymbol{x}) = Q\left(\frac{\pi x_1}{Q} - x_3\right)x_4 x_2 \rho_{fe} + \tag{3c}$$

$$\pi\left(x_1 + 2x_4 + \frac{B_r x_5}{\frac{\mu_{pm}\pi x_1}{Q\left(\frac{\pi x_1}{Q} - \frac{x_3^2}{5(\delta + \frac{x_5}{\mu_{pm}}) + x_3}\right)}\left(\delta + \frac{x_5}{\mu_{pm}}\right)}\frac{4}{\pi}\sin\left(\frac{\pi b_m}{2\tau_p}\right)\frac{b_m}{\tau_p}\frac{\pi x_1}{p}\frac{x_2 + 2\delta}{2k_{fe}\hat{B}_{sy}x_2}\right)$$
$$\times \frac{B_r x_5}{\frac{\mu_{pm}\pi x_1}{Q\left(\frac{\pi x_1}{Q} - \frac{x_3^2}{5(\delta + \frac{x_5}{\mu_{pm}}) + x_3}\right)}\left(\delta + \frac{x_5}{\mu_{pm}}\right)}\frac{4}{\pi}\sin\left(\frac{\pi b_m}{2\tau_p}\right)\frac{b_m}{\tau_p}\frac{\pi x_1}{p}\frac{x_2 + 2\delta}{2k_{fe}\hat{B}_{sy}x_2}x_2\rho_{fe}$$
$$+\pi\left(x_1 - 2\delta - 2x_5 - \frac{B_r x_5}{\frac{\mu_{pm}\pi x_1}{Q\left(\frac{\pi x_1}{Q} - \frac{x_3^2}{5(\delta + \frac{x_5}{\mu_{pm}}) + x_3}\right)}\left(\delta + \frac{x_5}{\mu_{pm}}\right)}\frac{4}{\pi}\sin\left(\frac{\pi b_m}{2\tau_p}\right)\frac{b_m}{\tau_p}\frac{\pi x_1}{p}\frac{x_2 + 2\delta}{2k_{fe}\hat{B}_{ry}x_2}\right)$$
$$\times \frac{B_r x_5}{\frac{\mu_{pm}\pi x_1}{Q\left(\frac{\pi x_1}{Q} - \frac{x_3^2}{5\left(\delta + \frac{x_5}{\mu_{pm}}\right) + x_3}\right)}\left(\delta + \frac{x_5}{\mu_{pm}}\right)}\frac{4}{\pi}\sin\left(\frac{\pi b_m}{2\tau_p}\right)\frac{b_m}{\tau_p}\frac{\pi x_1}{p}\frac{x_2 + 2\delta}{2k_{fe}\hat{B}_{ry}x_2}x_2\rho_{fe},$$

$$V(\boldsymbol{x}) = \frac{\pi}{4}\left(x_1 + 2x_4 + 2\left(\frac{B_r x_5}{\frac{\mu_{pm}\pi x_1}{Q\left(\frac{\pi x_1}{Q} - \frac{x_3^2}{5(\delta + \frac{x_5}{\mu_{pm}}) + x_3}\right)}\left(\delta + \frac{x_5}{\mu_{pm}}\right)}\frac{4}{\pi}\sin\left(\frac{\pi b_m}{2\tau_p}\right)\frac{b_m}{\tau_p}\frac{\pi x_1}{p}\frac{x_2 + 2\delta}{2k_{fe}\hat{B}_{sy}x_2}\right)\right)^2 \tag{3d}$$
$$\times (x_2 + 2\delta).$$

The definition of the variables used in the the above equations is given in Table 6. For more details on the design variables and their dependencies with the defined optimization variables, readers are referred to Grauers et al.[26] The results of the described optimization problem provide the detailed geometry, material consumption, cost, and the operational criteria such as efficiency, decoupled generator losses, power factor, flux densities, electrical and thermal loadings, induced and terminal voltages, and torque oscillations. The generator optimization problem including the objective function and the constraints is highly nonlinear. Because the resultant is a constrained nonlinear multivariable nonconvex problem in terms of the optimization variables, convex programming tools cannot be useful. Because the constraints are of a high number and mostly nonlinear, duality theories and associated dual problems add to the complexity of optimization. Problem reduction, using linear optimization,[11] and application of heuristic approaches, for example, genetic algorithm[27] are some alternatives suggested in the literature. Our observations show that the aforedescribed disciplined nonconvex problem shows a convex shape in a multidimensional graphical illustration of the objective function and constraints in the predefined range of optimization variables so that the problem is convex on a portion of its domain that is the feasible region regarding the constraints. Therefore, a global optimizer for this optimization problem could be found. MATLAB *fmincon* numerical optimization solver using sequential quadratic programming (SQP) algorithm is used to find the globally optimized design.

The objective function C is optimized subject to a wide range of specific electrical loading, magnetic loading, insulation and mechanical forces mitigation requirements, current density, armature thermal loading, power factor, and efficiency-based constraints to ensure a feasible design for the three generators. The carter factor is modelled in terms of the design variables in the optimization problems. The generators are assumed

TABLE 6 Generator optimization results

Generator Specifications	DDPMSG	MSPMSG	HSPMSG
Technical specification			
Number of poles p	200	12	4
Rated output power P_e (Mw)	10.003	10.004	10.000
Rated input torque T_N (MN.m)	10.689	0.202	0.065
Rated rotational speed n_r (rpm)	9.6	480	1497.6
Rated RMS line voltage V_L (kV)	3.471	10.438	10.452
Rated generator output frequency f (Hz)	16	48	49.92
Efficiency η (%)	93.09	98.41	98.34
Specific electric loading A (A/mm)	109.99	107.72	106.41
Armature current density J_s (A/mm^2)	4.66	5.02	4.99
Armature thermal load (A^2/mm^3)	512.24	540.98	531.07
Cogging torque (N.m)	958.54	0.23	0.01
Maximum air-gap flux density $\hat{B}_s$ (T)	0.46	0.52	0.49
Maximum magnet flux density $\hat{B}_m$ (T)	0.48	0.58	0.64
Maximum statorteeth flux density $\hat{B}_t$ (T)	0.95	1.43	1.36
Maximum statoryoke flux density $\hat{B}_{sy}$ (T)	1.10	1.11	1.07
Maximum rotoryoke flux density $\hat{B}_{ry}$ (T)	1.10	1.11	1.10
Total loss (kw)	742.52	161.55	168.87
Dimension specification			
Air gap diameter D_s (m)	10.622	2.547	1.743
Active length L_s (m)	1.498	0.512	0.391
Slot width b_s (mm)	27.5	11.5	11.2
Slot height h_s (mm)	86.9	62.8	65.8
Stator yoke height h_{sy} (mm)	27.30	148.65	333.05
Rotor yoke height h_{ry} (mm)	48.25	167.65	361.25
Magnet width b_m (mm)	140.72	552.61	1082.83
Magnet height h_m (mm)	21	19.7	38.9
number of slots Q	600	432	288
Number of slots per pole & phase q	1	12	24
Mechanical air-gap height δ (mm)	10	2	2
Polepitch τ_p (mm)	166.85	666.67	1368.70

continues.

to be equipped with integrated water cooling, which helps to increase the limits of the electrical loading constraint. The winding insulation class *N* with an average temperature rise of 130° C for the rated operation and the maximum hot-spot temperature 200° C is considered for the design limits and power loss calculations. No restriction regarding generator frame sizes is imposed to the problem. It is assumed that the generators outputs are connected to infinite bus. In a real case, the outputs are connected to a converter as an external circuit. The converter's dedicated controller controls the phase angle and amplitude of armature output current to attain higher power factors, maximizing the generator output active power. The generators are all designed for an induced voltage less than the rated terminal voltage, which helps to minimize the permanent-magnet material consumption and weight of generator and to reduce the generator core losses. The optimized design based on the proposed analytical model is performed by MATLAB and validated using ANSYS-RMxprt software to ensure that the generators can stably deliver the desired output power and voltage.

The generator structure weight consists of cooling system, beams, cylinder, shaft, and bearings. Different models for the weight is suggested in the literature.[26] In Hartviksen,[29] the generator structure weight is estimated with a sum of cylinder and beams weights. Because the beams weight is proportional to the generator diameter and the cylinder weight has a relation with the multiplication of the diameter and length, the following experimental equation is used to estimate the weight of structure compared with a known structure weight of a similar generator with the same range of power:

$$m_{str} = \frac{1}{2} m_{str}^0 \left(\left(\frac{D_{so}}{D_{so}^0} \right)^2 + \frac{L_s}{L_s{}^0} \right), \tag{4}$$

where m_{str}^0, D_{so}^0, and $L_s{}^0$ are the weight, outer diameter, and length of the reference generator. The data of reference generator, which is a 10-MW DDPMSG, are obtained from Polinder et al.[30]

3.2.2 | Gearbox optimization

In this section, the objective function is minimization of the cost of active material in gearbox by optimizing the stage gear ratios. The gearbox cost function for a typical three-stage configuration is defined by

$$C_{\text{gearbox}}(\boldsymbol{u}) = \arg\ \min \left(cost_{\text{gear}}(\boldsymbol{u}) \right), \tag{5a}$$

TABLE 6 continued

Generator Specifications	DDPMSG	MSPMSG	HSPMSG
Wedge height h_w (mm)	3	2	2
Stator outer diameter D_{so} (m)	10.857	2.973	2.544
Rotor inner diameter D_{ri} (m)	10.464	2.1677	0.9384
Equivalent core length L_e (m)	1.518	0.516	0.395
Slot pitch τ_s (mm)	55.62	18.52	19.01
Winding specification			
Winding layers	2	2	2
Winding type	Full pitch	Full pitch	Full pitch
Parallel branches	1	1	1
Conductors per slot	2	2	2
Winding connection	star	star	star
Number of winding turns N	600	432	288
Insulation thickness h_i, mm/kv	1	1	1
Material properties			
Magnet density ρ_{pm} (kg/m^3)	7400	7400	7400
Relative permeability of magnet μ_{pm}	1.1	1.1	1.1
Magnet residual flux density B_r	1.23	1.23	1.23
Magnet specific cost c_{pm} (Euro/kg)	80	80	80
Core density ρ_{fe} (kg/m^3)	7650	7650	7650
Relative permeability	B-H curve	B-H curve	B-H curve
Core specific cost c_{fe} (Euro/kg)	16	16	16
Copper density ρ_{cu} (kg/m^3)	8900	8900	8900
Copper specific cost c_{cu} (Euro/kg)	27	27	27
Design parameters			
Core stacking factor k_{fe}	0.97	0.97	0.97
Magnetic pole embrace $(\frac{b_m}{\tau_p})$	0.85	0.85	0.85
Weight and cost specification			
Armature copper weight M_{cu} (ton)	12.077	2.109	2.211
Permanent magnet weight M_M (ton)	6.552	0.494	0.487
Armature core weight M_{fe} (ton)	27.777	5.824	7.206
Rotor core weight M_{fe} (ton)	9.984	4.085	3.703
Total active material weight M_{Active} (ton)	56.390	12.513	13.608
Approximated structure weight $M_{structure}$ (ton)	267.85	52.52	39.79
Total weight M_{tot} (ton)	324.24	65.03	53.40
Total active material cost c_{Active} (MEuro)	1.45	0.25	0.27
Total raw material cost c_{total} (MEuro)	5.74	1.09	0.91

Abbreviations: DPMSG, direct-drive permanent-magnet synchronous generator; HSPMSG, high-speed permanent-magnet synchronous generator; MSPMSG, medium-speed permanent-magnet synchronous generator.

$$cost_{gear}(\boldsymbol{u}) = cost_{stage1}(\boldsymbol{u}) + cost_{stage2}(\boldsymbol{u}) + cost_{stage3}(\boldsymbol{u}), \tag{5b}$$

where u is vector of the optimization variables. $cost_{gear}$ is total raw material cost of the gears of gearbox stages in Euro. The variables in Equation (5) are described as

$$\boldsymbol{u} = [u_1, u_2, u_3]^T, \tag{6a}$$

$$cost_{stage}^{planetary} = c_{gear} m_{gear}^{planetary}, \tag{6b}$$

$$cost_{stage}^{parallel} = c_{gear} m_{gear}^{parallel}, \tag{6c}$$

where c_{gear} is the unit cost of the gears material and $m_{gear}^{planetary}$ and $m_{gear}^{parallel}$ represent the weights of planetary and parallel stages, respectively, which is defined as the function of optimization variables using the model described in Nejad et al[31] as

$$m_{gear}^{planetary}(u) = \frac{2\rho_{fe} Q_S}{k}\left(\frac{1}{B} + \frac{1}{B\left(\frac{u}{2}-1\right)} + \left(\frac{u}{2}-1\right) + \left(\frac{u}{2}-1\right)^2 + k_r\frac{(u-1)^2}{B} + k_r\frac{(u-1)^2}{B\left(\frac{u}{2}-1\right)}\right), \tag{7a}$$

$$m_{gear}^{parallel}(u) = \frac{2\rho_{fe} Q_P}{k}\left(1 + \frac{1}{u} + u + u^2\right), \tag{7b}$$

where Q_s and Q_p are the input torques to the sun and pinion for planetary and parallel stages, respectively. u is the gear ratio, B is number of planets of the planetary stage, and k_r is a ring scaling factor of the planetary stage. k is the intensity of tooth loads factor. The overall active material weight for a sample three-stage gearbox with two planetary and one parallel stages is calculated as

$$\begin{aligned} m_{gears}(u) = & \frac{2\rho_{fe}Q_0}{k}\frac{1}{u_1}\left(\frac{1}{B}+\frac{1}{B\left(\frac{u_1}{2}-1\right)}+\left(\frac{u_1}{2}-1\right)+\left(\frac{u_1}{2}-1\right)^2+k_r\frac{(u_1-1)^2}{B}+k_r\frac{(u_1-1)^2}{B\left(\frac{u_1}{2}-1\right)}\right) \\ & +\frac{2\rho_{fe}Q_0}{k}\frac{1}{u_1u_2}\left(\frac{1}{B}+\frac{1}{B\left(\frac{u_2}{2}-1\right)}+\left(\frac{u_2}{2}-1\right)+\left(\frac{u_2}{2}-1\right)^2+k_r\frac{(u_2-1)^2}{B}+k_r\frac{(u_2-1)^2}{B\left(\frac{u_2}{2}-1\right)}\right) \\ & +\frac{2\rho_{fe}Q_0}{k}\frac{1}{u_1u_2u_3}\left(1+\frac{1}{u_3}+u_3+u_3^2\right). \end{aligned} \tag{8}$$

Equation (8) is obtained by the sum of the weights of two planetary stages and one parallel stage as described in Equation (7). The input torque applied on the sun/pinion of each gearbox stage is replaced in the weight function of the stage by applying the gear ratio of the previous stages on the main shaft torque Q_0. To derive Equation (8), it is important to notice the sun/pinion is the output gear of the planetary/parallel gear stage.

The above described optimization problem is solved subject to constraints related to the gear ratio of each stage and the overall gear ratio. The outputs of the problem are the optimized gear ratios, weight, and cost. The resultant is a constrained nonlinear multivariable nonconvex optimization problem. Because the aforedescribed disciplined nonconvex problem shows a convex behavior in multidimensional graphical illustration of the objective function and constraints in the defined range of optimization variables, it is possible to find the global optimizer. MATLAB *fmincon* numerical optimization solver is used to find the global optimizer.

The replacement of the third parallel stage in MSPMSG drivetrain with a planetary stage in HSPMSG helps to reach higher gear ratios and reduce weight and size with compact design features of planetary gears. The disadvantages of planetary gearboxes are their complexity and sensitivity to manufacturing errors and elastic deformations in the shafts, bearings, and gearbox cage so that a planetary gearbox performs the best only if equal load sharing between planets is achieved.[32] The optimized three-planetary stages gearbox for HSPMSG drivetrain and two-planetary and one-parallel stage gearbox for MSPMSG drivetrain based on the explained model and the proposed optimization approach are evaluated as the case studies in Section 4. The gearboxes optimized designs are validated using the KISSsoft gear design software, and the overall geometry, weight, cost, and efficiency are compared for the different topologies.

3.2.3 | The first torsional natural frequency of drivetrain

To ensure that the different designed drivetrain technologies execute a safe operation without any danger of resonance due to external/internal excitations, the first torsional natural frequency of three under consideration drivetrain systems is studied. The first torsional frequency is calculated by using a simplified two-mass model. The gearbox is modelled with the gear ratio and the stiffness of the connecting links to the rotor and generator are modelled, but the moment of inertia and stiffness of the gearbox are neglected. The moment of inertia of the gearbox is negligible compared with the moment of inertia of the generator so that it does not have any considerable impact on the first drivetrain torsional mode. The first torsional frequency by using a two-mass model is calculated by[33]

$$f_1^{tor} = \frac{1}{2\pi}\sqrt{k_{eq}\frac{J_r+\alpha^2J_{gen}}{\alpha^2J_rJ_{gen}}}, \quad k_{eq} = \frac{\alpha^2k_rk_{gen}}{k_r+\alpha^2k_{gen}}, \tag{9}$$

where k_{eq} is the equivalent shaft stiffness in the rotor side, J_r and J_{gen} are the moment of inertia of rotor and generator, k_r and k_{gen} are the shaft stiffness of rotor and generator, and α is inverse of the gear ratio.

The first torsional natural frequency of drivetrain of the three under consideration topologies obtained by the above model is validated by using a three-mass model in Simpack software, which models the moment inertia of the gearbox to see how it can influence the first mode.

4 | NUMERICAL SIMULATIONS

4.1 | Optimized generator specification

The results of the three optimized generator designs based on DDPMSG, MSPMSG, and HSPMSG using the proposed analytical approach are listed in Table 6. The three optimized designed generators are validated by ANSYS-RMxprt. The terminal voltage and power-angle characteristics of the designed generators, which show that the three generators can stably deliver the designed power with the target voltage, are shown in Figure 4. The power angle characteristic shows the relation between the power output of the generator P_e and the power angle δ. The power angle is the angle between the generator induced voltage at the air gap and the terminal voltage. When the input mechanical power increases, the power angle increases to counterbalance the input power by the increase of the generated electrical power, where there is a $\delta = \pi/2$ *rad*

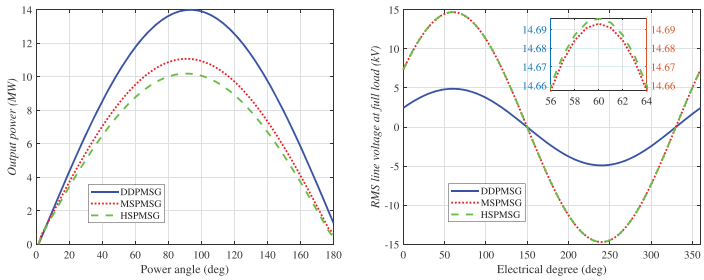

FIGURE 4 Characteristic curves of the designed generators. DDPMSG, direct-drive permanent-magnet synchronous generator; HSPMSG, high-speed permanent-magnet synchronous generator; MSPMSG, medium-speed permanent-magnet synchronous generator [Colour figure can be viewed at wileyonlinelibrary.com]

limit that any exceedance causes a loss of synchronism and instability. The curve demonstrated in Figure 4A is the power-angle characteristic obtained from the validated model in ANSYS-RMxprt software and shows that the three designed generators are all able to deliver the designed 10 MW power but at different power angles. The designed points on the power-angle characteristic of the generators are the optimal operation by the consideration of efficiency and power factor in the optimization problem under a rated operation. The operating point in the three designs also has a safe distance from the power angle limit $\delta = \pi/2\ rad$. Although the designed generators can give higher power especially in DDPMSG, it will not result in a desirable operation regarding a much lower efficiency. The frequency converter can also influence on the power factor and subsequently the power angle. The generator terminal voltage is also an important constraint in the optimized design problem so that the designed generators must be able to deliver the rated power at the rated voltage level, which the generator is designed for. Figure 4B shows one cycle of the terminal line voltage ($V_{Line} = \sqrt{3}V_{Phase}$) of the three designed generators validated by ANSYS-RMxprt.

As it can be seen in Table 6, a transition from the low-speed to high-speed generator helps to save weight by reduction of diameter and length of the generator although the required stator and rotor yokes height increases. For higher speed generators, the reduction of the number of poles still decreases the diameter and length of machine; however, the rise in the stator and rotor yokes height exceeds the amount of weight saved by the reduced diameter and length. Consequently, the weight of active material in HSPMSG is increased, but the total weight including the weight of structure is still less than MSPMSG technology. Considerable reduction of weight and raw material cost in the generators designed for higher operational speeds and improved efficiency and torque oscillations are observed based on the simulation results.

The efficiency of generator in the optimized analytical design approach is considered as a constraint so that the design solution has to fulfill the minimum requirements regarding the power loss and efficiency. For this purpose, in the design code, the components of generator power loss consisting of winding loss, rotor and stator cores losses (hysteresis and eddy current losses), magnet losses, additional losses (stray losses), and friction and windage losses are modelled at rated load operation. The optimized design is then validated by the ANSYS-RMxprt analytical design software to ensure that the designed generator can supply the designed power at the specified voltage. This software makes it possible to check a wide range of parameters related to the generator operation including but not limited to flux densities in different places, electric loading, thermal loading, induced and terminal voltage, power factor, total harmonic distortion, power losses, and efficiency. The values of efficiency given in the paper are the verified results obtained by ANSYS. It is worth noting that maintaining the same efficiency for the low-speed generator needs more increase in volume compared with higher speed generators. The latter makes high-efficiency DDPMSG technology for high-power applications infeasible or inefficient. The voltage and frequency for the design of DDPMSG are selected less than the two other generators, to help the minimum weight and cost design. The design voltages are selected so that the output voltage of converter place in a standard voltage level based on the standards.[34,35] Regarding the reduced rotational speed in DDPMSG and the direct relationship between the induced voltage and speed, it is not efficient to design the direct-drive generator with the same voltage level used for medium-speed and high-speed generators design. The relative root mean square (RMS) value of the fundamental component of the induced voltage is given by[27]

$$E_r = \sqrt{2}k_w\omega_s N_{ph}\frac{D_s}{2}L_e B_\delta^1, \tag{10}$$

where k_w is the winding factor, ω_s is the rotational speed in rad/s, and B_δ^1 is the RMS value of the fundamental component of the air gap flux density. Therefore, the increase of induced voltage means the rise in the number of turns (more winding weight), the length of the machine (more core weight), and the air gap flux density (more magnet weight). The latter increases the weight and cost of design. A power transformer in the wind turbine is used to adjust the converter output voltage to the voltage at point of common coupling (PCC) so that the reduced voltage of DDPMSG and consequently the reduced converter output voltage does not cause any problem if the voltage is selected among the standard voltages.

The design for a reduced output frequency also helps to reduce the number of poles and consequently the diameter and weight of generator. The latter is possible, because the power converter can adjust the output frequency if the frequency is in the converter operating range. Therefore, the design of DDPMSG for a lower voltage level and frequency is practical and results in the minimum weight design of the direct-drive generator. The other two machines, that is, MSPMSG and HSPMSG are designed for the same standard voltage level. Similar loading conditions

TABLE 7 Gearbox optimization results

Gearbox Specifications	MSPMSG		HSPMSG
Technical specification			
Type	Two planetaries and one parallel	Three planetaries	Three planetaries
Overall gear ratio	1:50	1:50	1:156
Rated power (MW)	10	10	10
Rated input shaft speed n (rpm)	9.6	9.6	9.6
Rated input shaft torque Q (MN.m)	9.947	9.947	9.947
Efficiency η (%)	97.3	97.3	98.1
Gear specification of the first stage			
Gear type	Planetary	Planetary	Planetary
Gear ratio	1:3.524	1:3.231	1:4.333
Number of planets	5	5	5
Normal module	32	45	28
Normal pressure angle (degree)	23.3	27.1	24.6
Helix angle (degree)	0	0	0
Center distance a (m)	0.917	1.140	1.027
Sun gear facewidth b_1 (m)	0.533	0.316	0.568
Planets facewidth b_2 (m)	0.514	0.297	0.552
Ring gear facewidth b_3 (m)	0.533	0.316	0.568
Number of teeth, sun	33	31	34
Number of teeth, planet	23	17	37
Number of teeth, ring	82	69	111
Profile shift coefficient, sun	0.217	0.664	0.446
Profile shift coefficient, planet	0.493	0.907	0.866
Profile shift coefficient, ring	0.249	0.312	0.555
Weight m_{gear}^{S1} (ton)	17.53	15.01	28.11
Efficiency η (%)	99	98.9	99.4
Gear specification of the second stage			
Gear type	Planetary	Planetary	Planetary
Gear ratio	1:4.804	1:3.4560	1:6
Number of planets	3	3	3
Normal module	25	28	25
Normal pressure angle (degree)	24.3	23.7	23.4
Helix angle (degree)	0	0	0
Center distance a (m)	0.696	0.819	0.704

continues.

are considered for design of the three generators to reach a fair comparison between them. Mechanical losses including friction and windage are neglected.

4.2 | Optimized gearbox specification

The optimized medium-speed and high-speed gearboxes specifications including the geometrical and technical data of the stages, respectively for 10-MW MSPMSG and HSPMSG wind turbine drivetrain systems using the analytical model described in Section 3 are specified in Table 7. The results validated using KISSsoft software show that even though the multistage gearbox for the HSPMSG drivetrain is designed for a higher gear ratio, it can still slightly reduce the total weight and improve the efficiency of the gearbox. The change in the weight scaling factor applied to model the structure weight of the two different gearboxes can slightly affect the results about the gearbox weight. As it can be seen, a transition from medium-speed to high-speed gearbox can help to slightly improve the efficiency and weight. To provide a fair comparison, because there was no reference found, which prohibits the utilization of three planetary stages instead of two planetary and one parallel stages to realize a medium-speed gearbox, the optimized results of another medium-speed topology based on three planetary stages is added to Table 7.

The values of gearbox efficiency are the validated values calculated by KISSsoft after the implementation of the optimized model in the software environment. KISSsoft is an analytical tool that calculates the power loss and heat dissipation of each gear stage according to the ISO/TR 14179 standard. The software analytical efficiency calculations are elaborated by Langhart et al.[36]

4.3 | Comparison between different PMSG-based drivetrain technologies

The overall drivetrain weight, cost, and efficiency for DDPMSG, MSPMSG, and HSPMSG are summarized in Table 8 and graphically compared in Figures 5A to 5C. As it can be seen, moving from the direct-drive technology towards the medium-speed, the drive train weight, raw material cost,

TABLE 7 continued.

Gearbox Specifications		MSPMSG	HSPMSG
Sun gear facewidth b_1 (m)	0.466	0.331	0.415
Planets facewidth b_2 (m)	0.450	0.316	0.401
Ring gear facewidth b_3 (m)	0.466	0.331	0.415
Number of teeth, sun	23	34	19
Number of teeth, planet	31	23	36
Number of teeth, ring	88	83	95
Profile shift coefficient, sun	0.176	0.283	0.430
Profile shift coefficient, planet	0.754	0.535	0.285
Profile shift coefficient, ring	-0.157	-0.137	0.772
Weight m_{gear}^{S2} (ton)	9.06	6.74	9.26
Efficiency η (%)	99.2	99.2	99.3
Gear specification of the third stage			
Gear type	Parallel	Planetary	Planetary
Gear ratio	1:2.95	1:4.4775	1:6
Number of planets	…	3	3
Normal module	40	18	14
Normal pressure angle (degree)	20	22.7	23.3
Helix angle (degree)	0	0	0
Center distance a (m)	1.177	0.495	0.394
Sun/pinion facewidth b_1 (m)	0.622	0.223	0.201
Planets/gear facewidth b_2 (m)	0.599	0.212	0.195
Ring facewidth b_3 (m)	…	0.223	0.201
Number of teeth, sun /pinion	15	25	19
Number of teeth, planet/gear	44	29	36
Number of teeth, ring	…	86	95
Profile shift coefficient, sun/pinion	0.377	0.092	0.225
Profile shift coefficient, planet /gear	-0.451	0.441	0.471
Profile shift coefficient, ring	…	0.405	0.595
Weight m_{gear}^{S3} (ton)	12.28	2.04	1.43
Efficiency η (%)	99.1	99.2	99.4
Design parameters			
Intensity of tooth loads factor	4×10^6	4×10^6	4×10^6
Ring scaling factor	0.4	0.4	0.4
Housing, bearings & lubrication scale factor	0.2	0.2	0.2
Material properties			
Material	Case carburized steel	Case carburized steel	Case carburized steel
Density (kg/m^3)	7850	7850	7850
Specific cost c_{gear} (Euro/kg)	16	16	16
Weight and cost specification			
Total gears weight (ton)	38.87	23.79	38.80
Moment of inertia ($Mkg.m^2$)	1.24	0.25	0.36
Total weight (ton)	46.64	28.55	46.56
Total raw material cost (MEuro)	0.75	0.46	0.74

Abbreviations: DPMSG, direct-drive permanent-magnet synchronous generator; HSPMSG, high-speed permanent-magnet synchronous generator.

efficiency and electromagnetic torque oscillations are significantly improved. A transition from the medium-speed to the high-speed generator still helps to improve all the aforementioned properties.

To reduce fatigue damage and noise and comply with standard limits, a suppression to the permissible level 2% for electromagnetic torque oscillations is required.[37] Torque oscillation in surface-mounted PMSGs mainly comes from two sources[38,39]:

1. Cogging effect due to the variable permeance of the air gap and
2. Distortion of sinusoidal distribution of air gap flux density due to saturation, current ripple resulting from pulse width modulation (PWM), and low power quality of the grid.

Cogging torque resulting from cogging effect is an important component of torque oscillations in PMSGs, which can be improved by the proper design. As it can be seen in Table 8, the designed generators fulfill the torque oscillation requirements. However, the ratio of the cogging to the average torque reduces by the increase of gear ratio. The fundamental cogging frequency for the PMSG with integer-slot windings and

TABLE 8 Drivetrain optimization results

Drivetrain Technology	DDPMSG	MSPMSG		HSPMSG
Gearbox configuration	No gearbox	Planetary-planetary-parallel	Three planetaries	Three planetaries
Generator weight (ton)	324.24	65.03	65.03	53.40
Generator cost (MEuro)	5.74	1.09	1.09	0.91
Gearbox weight (ton)	0	46.64	28.55	46.56
Gearbox cost (MEuro)	0	0.75	0.46	0.74
Total weight (ton)	324.24	111.67	93.58	99.96
Total cost (MEuro)	5.74	1.84	1.55	1.66
Electromagnetic torque oscillation (%)	0.00897	0.00011	0.00011	0.00001
Rated efficiency (%)	93.09	95.75	95.75	96.47

Abbreviations: DPMSG, direct-drive permanent-magnet synchronous generator; HSPMSG, high-speed permanent-magnet synchronous generator; MSPMSG, medium-speed permanent-magnet synchronous generator.

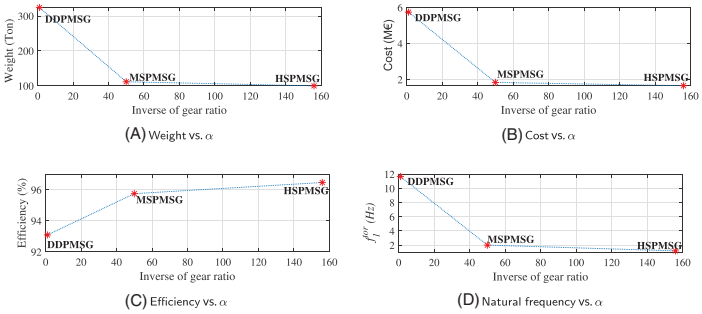

FIGURE 5 Comparison between different drivetrain technologies: DDPMSG, MSPMSG and HSPMSG. DPMSG, direct-drive permanent-magnet synchronous generator; HSPMSG, high-speed permanent-magnet synchronous generator; MSPMSG, medium-speed permanent-magnet synchronous generator [Colour figure can be viewed at wileyonlinelibrary.com]

surface-mounted magnets is calculated by[40]

$$f_{cog} = Q\frac{2f_{in}}{p}, \tag{11}$$

where Q is number of slots, f_{in} is generator input frequency, and p is number of poles. It can be seen that the cogging torque frequency depends on the input speed, but in rated operation, the cogging torque frequencies for DDPMSG, MSPMSG, and HSPMSG are 0.96, 57, and 3600 Hz, respectively. The higher cogging torque frequency of higher speed generators reduces the probability of coincidence on the natural frequencies of the drivetrain main bearings and the generator bearings' inner ring, outer ring, and rolling elements (see the associated failure modes in Table 4). Regarding the higher shaft first torsional natural frequency in DDPMSG, it is doubted that the cogging frequency can coincide this frequency. The type of main bearings in the wind turbines are mostly spherical roller bearings. These bearings have different defect frequencies due to out-of-round rotating, roller irregularity, and outer and inner race irregularities. For the under consideration 10-MW turbine, the defect frequency of these modes can start from a fraction of hertz and rise up to few hertz. The cogging torque in DDPMSG can cause fatigue damage to bearing components due to the possibility of coincidence with main bearing defect frequencies. For higher speed generators in MSPMSG and HSPMSG technologies, it is also possible that cogging torque coincides the gears mesh frequencies, which can affect the gear teeth fatigue life. However, in the designed medium-speed and high-speed gearboxes, the mesh frequencies of generator side gear stage are 120 and 474 Hz, respectively, which keep a safe distance from the rated fundamental cogging torque frequencies. The presence of gearbox results in a longer transmission path between the external excitation source initiated from the rotor (aerodynamic torque and forces) and the generator side (electromagnetic torque and forces), which are transmitted to the generator and rotor side components, respectively, which can reduce the amplitude of drivetrain external excitations. The latter can affect the probability of failure of generator and rotor side components (eg, main bearings) due to those external excitations. The increased defect frequencies of the generator bearings due to the rise in the rotational speed naturally immunizes these components against the loads applied on the drivetrain by rotor as a result of synergistic impacts of wind, waves, and structural motions, which all appear with a low frequency content. The latter shows some potentials to improve the reliability of main bearings and generator in the drivetrain, although the appearance of gearbox as a new serial component has a negative impact on the reliability of drivetrain. Therefore, it is challenging to compare the overall reliability of the under consideration drivetrain systems. In the continued part, the possibility of resonance by using the three designed drivetrain systems is investigated.

There is a coupling between gearbox and generator in the geared wind turbine drivetrain systems used for reducing torsional vibration and accommodating misalignment. The coupling between generator and gearbox could suppress the high-frequency excitations initiated by the generator due to distortion of air gap flux in order not to be transmitted to the rest of the drivetrain. Those frequencies happen mostly in harmonics of generator output frequency. The cogging frequency in MSPMSG and HSPMSG has a high-frequency nature and is isolated by the coupling from the rest of the drivetrain although there is not any possibility for this frequency to coincide with the first torsional frequency

TABLE 9 The first torsional natural frequency of drivetrain, and the excitation sources

Drivetrain Technology	DDPMSG	MSPMSG	HSPMSG
Generator moment of inertia J_{gen} (kg.m^2)	456965.65	6286.71	1888.30
First torsional natural frequency -by two mass model (Hz)	11.66	2.01	1.20
First torsional natural frequency -by three mass model in Simpack (Hz)	11.66	1.93	1.19
1P rotational frequency (Hz)	0-0.16	0-0.16	0-0.16
3P rotational frequency (Hz)	0-0.48	0-0.48	0-0.48
Wind (Hz)	0-0.02	0-0.02	0-0.02
Wave (Hz)	0.05-0.2	0.05-0.2	0.05-0.2
Electromagnetic torque oscillations (Hz)	0-10000	0-10000	0-10000
Gear mesh frequency-first harmonic at rated speed (Hz)	…	18-120	23-474
Bearing defect frequency-first harmonic at rated speed (Hz)	0.16-8	0.16-170	0.16-500

Abbreviations: DPMSG, direct-drive permanent-magnet synchronous generator; HSPMSG, high-speed permanent-magnet synchronous generator; MSPMSG, medium-speed permanent-magnet synchronous generator.

due to the high-frequency nature of cogging torque in geared drivetrain technologies. In DDPMSG, there is normally no mechanical torsional vibration isolator in the drivetrain system. As a result, the generator torsional vibrations including low frequency (due to cogging torque) and higher frequencies (due to saturation, power converter switching, and power grid) transmit to the rotor side of the drivetrain. The latter can influence on the drivetrain lifetime specially in higher powers with smaller values of the first drivetrain torsional frequency, generator cogging torque frequency, and generator output frequency.

Active vibration dampers are another drivetrain torsional vibration damping mechanism, which are used to mitigate the impact of the significant torsional vibrations on the drivetrain due to aerodynamic torque oscillations (usually, the frequencies that are considered to be damped by active dampers are the first drivetrain torsional mode and first blade in plane mode) by compensation of them in the generator electromagnetic torque set point. These dampers are generally band-pass filters, which are tuned around some prespecified frequencies. If these mechanical oscillations do not get compensated in the generator torque, the consequent electric power oscillations not only reduces the power quality but also can interact with power system modes and cause resonances with the electric circuits frequencies, which can cause high voltages and currents and damage the electric components. Instead of these compensations on torque through active dampers, some turbines use passive parallel band-stop filters in the frequency converter system to filter the frequencies of the aerodynamic torque oscillations from the output electric power. To our best knowledge, the active dampers do not influence on the torsional vibrations initiated by generator. In direct-drive technologies, due to the lack of coupling, there is no mechanism to suppress the transmission of generator vibrations to the rotor side. In 10-MW DDPMSG, the cogging frequency can coincide with the defect frequencies of the main bearings and there is no mechanism reported in the literature of direct-drive drivetrain systems to isolate this low frequency range excitations that are initiated from the generator side.

4.4 | The first torsional natural frequency of drivetrain and resonance analysis

ANSYS-Maxwell moment of inertia calculation package is used to obtain a good estimation of the generator moment of inertia for the designed generators. The first torsional frequency of designed DDPMSG, MSPMSG, and HSPMSG drivetrains is presented in Table 9 and graphically illustrated in Figure 5D. The rotor and tower flexibilities are neglected in the calculation of the first torsional frequencies.

The excitations that influence on the drivetrain operation come from different sources, for example, turbine rotational motion, motions induced by structural resonances, wind- and wave-induced motions, the electromagnetic torque oscillation resulted by cogging torque/saturation/converter system/power grid, and the drivetrain internal excitations due to the gears mesh frequencies and the bearings defect frequencies. For the drivetrain system, the most unfavorable operating condition happens when the rotor rotational frequency (1P) coincides the drivetrain first torsional frequency. The other source of excitation that can affect the rotor torque comes from the tower shadow effect, which occurs with blade passing frequency 3P. The tower bending (TB) frequency excited by the 1P or 3P rotational frequencies is another source of excitation in a spar floating platform.[41] An excited TB natural frequency causes motions that induce a moment component on the rotor torque. Wave is another excitation source in offshore wind turbines so that waves at sea have significant energy at periods of 5 to 20 seconds. An example of wave impacts is nacelle side-side motion developed by sway and rolling motions, which has a low frequency inherent. The natural periods of wind excitations also change from a fraction of a minute for turbulent fluctuations to some hours due to diurnal effects. The impacts of the generator cogging torque on the drivetrain components was discussed earlier. The power grid and converter system are the other excitation sources that influence on the generator electromagnetic torque and consequently the moment on the shaft. The latter can have different reasons, for example, grid voltage drops, swells and harmonics, and the harmonics in the current resulted by the PWM frequency converter,[42] which happen with higher frequencies potentially starting from the first or the higher order harmonics of $\frac{np}{120}$ up to a few thousands of hertz depending on the grid power quality, converter topology, the modulation technique, and switching frequency.[43] n is the generator rotational speed. The internal excitations due to any excited bearing frequencies (main bearings, gearbox, and generator bearings) or gear mesh frequencies of the gearbox stages can work as an impact that could excite the system natural frequencies and the defect frequencies of the other components. The excitation sources with the same frequencies can cause more complicated impacts. Combined impacts of different excitations with the same

TABLE 10 Environmental conditions for drivetrain analysis

EC	1	2	3	4
U_w (m/s)	7	9	11	15
H_s (m)	2.5	3.5	3.5	3.5
T_p (s)	6.5	7.5	7.5	11.5

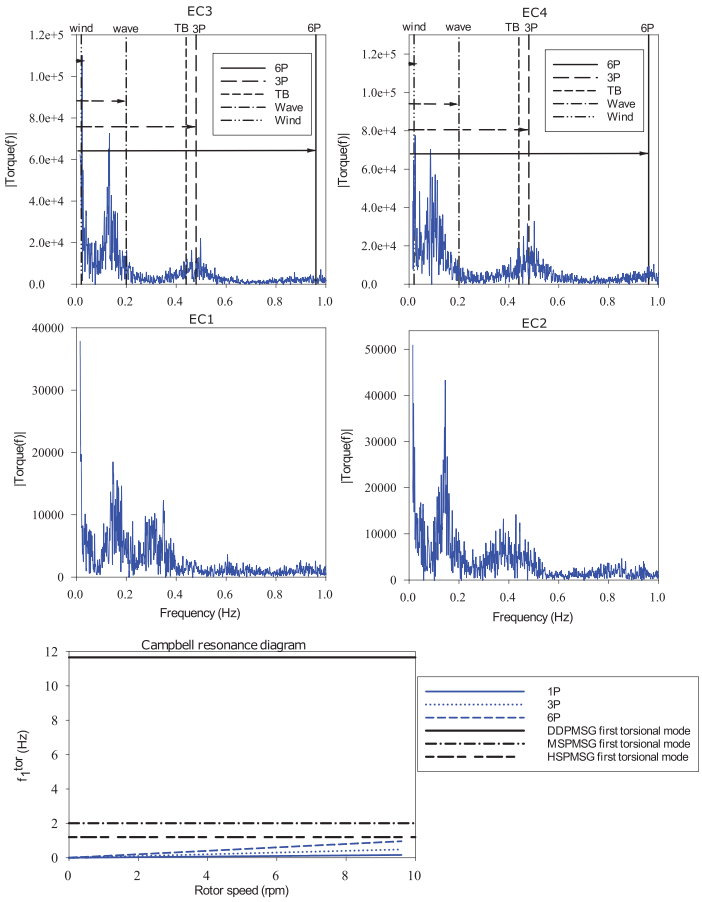

FIGURE 6 Rotor torque frequency spectrum analysis of 10-MW spar floating offshore wind turbine in different environmental conditions and associated resonance diagram. DPMSG, direct-drive permanent-magnet synchronous generator; HSPMSG, high-speed permanent-magnet synchronous generator; MSPMSG, medium-speed permanent-magnet synchronous generator [Colour figure can be viewed at wileyonlinelibrary.com]

frequencies can result in a coupled effect by producing other frequencies described as beating effect in Thomson.[44] An overview of the excitation sources for 10-MW spar floating wind turbine is presented in Table 9.

In order to determine which loads can excite the first torsional natural frequency of drivetrain, an effective approach could be to study the drivetrain response by using a frequency-domain analysis. For this purpose, the rotor torque data of the DTU 10MW reference wind turbine with a spar floating platform obtained from SIMA global simulation software is used, and the impacts on the drivetrain are studied using a decoupled analysis. Decoupled analysis approach is explained in detail in Nejad et al.[45] This model is very useful to study the consequences of the drivetrain torsional excitations induced by aerodynamic loads and structural motions. The specification of the spar floating platform used in the global simulations is given by Hegseth et al.[41] To study the impact of wind and wave, four different environmental conditions are simulated as listed in Table 10. For different wind speeds U_w within the operational range of the turbine, the most probable values of significant wave height H_s and peak period T_p are selected for the global simulations. In order to analyze how the different loads influence on the response, the frequency spectrum of rotor torque for the different operating conditions is shown in Figure 6. The frequency spectrum of the signal in frequencies lower than 1 Hz is selected and shown because the most significant energy of the rotor torque was observed in this range. The possible resonances due to external excitations for the three optimally designed drivetrain systems are demonstrated by the Campbell diagram in Figure 6.

The torque components induced by tower shadow, TB, wind, and wave are depicted in the figure. As it can be seen, the wave- and wind-induced components are very low frequency so that they cannot excite the torsional modes of any of the three under consideration drivetrain systems. The other excitations with considerable energy (including 1P, TB, 3P, and 6P) happen at the frequencies less than 1 Hz so that none of the designed DDPMSG, MSPMSG, and HSPMSG drivetrain technologies are affected by aerodynamic loads and structural excitations. A larger distance between the drivetrain natural frequency and the aerodynamic loads is an advantage of lower speed generator technologies, where DDPMSG outperforms the other drivetrain systems. On the other side, for the drivetrain with higher first torsional frequency, it would be more susceptible to excitations with generator torsional vibration frequencies, especially in the direct drive technology in which there is no coupling between the generator and rotor to suppress the generator electromagnetic torque vibrations. In lower speed generator technologies, in order to reduce the generator size, the number of poles is reduced. Consequently, the generator output frequency is reduced. For instance, the generator output frequency of the DDPMSG design in the paper is 16 Hz. The generator reduced output frequency and simultaneously increased first torsional frequency (eg, 11.66 Hz for the designed DDPMSG), which is a drawback of drivetrain technologies based on lower speed generators. During operations at speeds lower than the rated value, it is quite possible that the frequency of the generator-induced voltage coincides with the first natural frequency, which is not a recommended operation. Operations at this speed or any transition over it can cause large vibrations in the system. The nontorsional excitation sources , for example, bearings and gears, have also a potential to induce torque vibrations at bearing defect frequencies and gear mesh frequencies, respectively. The higher the value of the first torsional frequency, the more the possibility of coincidence with those frequencies. For example, in DDPMSG, it is possible that the second harmonic of main bearings roller irregularity frequency coincides with the first torsional frequency. From this perspective, higher speed generators could exhibit a higher performance. Therefore, with respect to dynamic response and resonance possibility, MSPMSG seems to be a better compromise.

5 | DISCUSSIONS AND CONCLUDING REMARKS

The optimized analytical 10-MW drivetrain designs for three different PMSG-based drivetrain topologies, that is, DDPMSG, MSPMSG, and HSPMSG, were explained and compared, and the feasibility of application in spar floating offshore wind turbines was studied. The results showed that utilization of gearbox can improve both the economics and operations of the wind turbine in 10-MW floating offshore wind turbines based on the following proven reasons:

1. It helps to reduce the weight of the drivetrain system,
2. It reduces the raw material cost of the drivetrain,
3. It can result in a better dynamic performance and reduce the possibility of resonance in the drivetrain due to the coincidence of the excitation frequencies (initiated by aerodynamic torque and electromagnetic torque) with the first drivetrain torsional frequency and the individual components defect frequencies,
4. Higher speed generator technologies in MSPMSG and HSPMSG drivetrain systems help to improve the overall drivetrain efficiency.

By considering the interactions between the drivetrain components, it was discussed how a medium-speed gearbox can improve some drivetrain failure modes concerning with the generator and the main bearings. However, new failure modes due to the presence of gearbox will also appear in the geared drivetrain systems. Regarding the lack of any operational data at this power range, the weakness of simulation tools in modelling of such complex dynamical system, and insufficient knowledge on loads in floating applications, it is challenging to compare the reliability of different drivetrain technologies. Future work will be devoted on investigating the optimal gear ratio for the PMSG drivetrain for 10-MWturbine and comparing the expected lifetime of different PMSG drivetrain systems by a thorough reliability analysis for floating offshore applications.

ACKNOWLEDGMENT

The authors would like to thank John Marius Hegseth of Norwegian University of Science and Technology, Trondheim, Norway, for providing the 10-MW spar floating wind turbine global analysis simulation results.

ORCID

Farid K. Moghadam https://orcid.org/0000-0002-0795-6887
Amir R. Nejad https://orcid.org/0000-0003-0391-8696

REFERENCES

1. IRENA I. *Renewable Power Generation Costs in 2017*. Abu Dhabi: International Renewable Energy Agency; 2018.
2. Note on technology costs for offshore wind farms and the background for updating CAPEX and OPEX in the technology catalogue datasheets. Danish Energy Agency; 2018.
3. Guo Y, Parsons T, King R, Dykes K, Veers P. *Analytical Formulation for Sizing and Estimating the Dimensions andWeight of Wind Turbine Hub and Drivetrain Components*. Golden, CO (United States): National Renewable Energy Lab.(NREL); 2015.

4. Guo Y, Parsons T, Dykes K, King R. A systems engineering analysis of threeâĂŘpoint and fourâĂŘpoint wind turbine drivetrain configurations. *Wind Energy*. 2017;20(3):537-50.
5. McKenna R, Ostman P, Leye VD, Fichtner W. Key challenges and prospects for large wind turbines. *Renew Sustain Energy Rev*. 2016;53:1212-1221.
6. Cheng M, Zhu Y. The state of the art of wind energy conversion systems and technologies: a review. *Energy Convers Manag*. 2014;88:332-347.
7. Gorginpour H, Oraee H, McMahon R. Electromagnetic-thermal design optimization of the brushless doubly fed induction generator. *IEEE Trans Ind Electron*. 2014;61:1710-1721.
8. Abrahamsen A, Liu D, Magnusson N, et al. Comparison of levelized cost of energy of superconducting direct drive generators for a 10-MW offshore wind turbine. *IEEE Trans Appl Supercond*. 2018;28:1-5.
9. Bak C, Zahle F, Bitsche R, et al. Description of the DTU 10 MW reference wind turbine. *DTU Wind Energy Report-I-0092*; 2013.
10. Sethuraman L, Maness M, Dykes K. Optimized generator designs for the DTU 10-MW offshore wind turbine using GeneratorSE. In: 35th Wind Energy Symposium; 2017:0922.
11. Rkke A. Permanent Magnet Generators for Marine Current Tidal Turbines. *Ph.D ,thesis*. Norway; 2017.
12. Torsvik J, Nejad A, Pedersen E. Main bearings in large offshore wind turbines: development trends, design and analysis requirements. *J Phys Conf Ser*. 2018;1037:042020.
13. Mayer J, Gerling D. Simulation of arbitrary fault-conditions in PM-machines by generalized unsymmetrical modeling. In: IEEE XXth International Conference on Electrical Machines; 2012:2866-2872.
14. Morgan AW, Wyllie D. A survey of rolling-bearing failures. In: Proceedings of the Institution of Mechanical Engineers, Conference Proceedings, Vol. 184; 1969:48-56.
15. Valavi M, Nysveen A, Nilssen R, Lorenz R, Rlvg T. Influence of pole and slot combinations on magnetic forces and vibration in low-speed PM wind generators. *IEEE Trans Mag*. 2014;5:1-1.
16. Nejad A, Gao Z, Moan T. Fatigue reliability-based inspection and maintenance planning of gearbox components in wind turbine drivetrains. *Energy Procedia*. 2014;53:248-57.
17. Tallian T. On competing failure modes in rolling contact. *ASLE Trans*. 1967;4:418-39.
18. Nejad A, Gao Z, Moan T. On long-term fatigue damage and reliability analysis of gears under wind loads in offshore wind turbine drivetrains. *Int J Fatigue*. 2014;61:116-28.
19. Gao Z, Bingham H, Ingram H, et al. Committee V. 4: Offshore Renewable Energy. In: In Proceedings of the 20th International Ship and Offshore Structures Congress (ISSC 2018), Vol. 2 IOS Press; 2018:193-277.
20. Polinder H, Ferreira J, Jensen B, Abrahamsen A, Atallah K, McMahon R. Trends in wind turbine generator systems. *IEEE Trans Emerging Sel Topics Power Elect*. 2013;1:174-185.
21. Moghadam F, R Nejad A. Experimental Validation of Angular Velocity Measurements for Wind Turbines Drivetrain Condition Monitoring. In: ASME 2019 2nd International Offshore Wind Technical Conference 2019 Dec 13 American Society of Mechanical Engineers Digital Collection; 1-9.
22. Manwell J, McGowan J, Rogers A. *Wind Energy Explained: Theory, Design and Application*: John Wiley & Sons; 2010.
23. IEC 61400-4. Wind turbines part 4: Standard for design and specification of gearboxes; 2012.
24. Zhang Z, Matveev A, Øvrebø S, Nilssen R, Nysveen A. State of the art in generator technology for offshore wind energy conversion systems. In: IEEE International Electric Machines Drives Conference (IEMDC) IEEE; 2011:1131-1136.
25. Polinder H, Pijl A, Vilder G, Tavner PJ. Comparison of direct-drive and geared generator concepts for wind turbines. *IEEE Trans Energy Convers*. 2007;21:725-733.
26. Grauers A. Design of Direct-Driven Permanent-Magnet Generators for Wind Turbines. *Ph.D thesis*. Sweden: Chalmers University of Technology; 1996.
27. Li H, Chen Z, Polinder H. Optimization of multibrid permanent-magnet wind generator systems. *IEEE Trans Energy Conv*. 2009;24:82-92.
28. Dubois MR, Polinder H, Ferreira JA. Comparison of generator topologies for direct-drive wind turbines. In: Proc. 2000 Nordic Countries Pow. And Indust. Elec; 2000:22-26.
29. Hartviksen H. *Application of scaling laws for direct drive permanent magnet generators in wind turbines*, *Master thesis*. Norway: Norwegian University of Science and Technology; 2015.
30. Polinder H, Bang D, Van Rooij R, McDonald A, Mueller M, 10 MW. wind turbine direct-drive generator design with pitch or active speed stall control. *IEEE Int Elect Mach Drives Conf (IEMDC)*. 2007;2:1390-1395.
31. Nejad A, Guo Y, Gao Z, Moan T. Development of a 5MW reference gearbox for offshorewind turbines. *Wind Energy*. 2016;19:1089-1106.
32. Nejad A, Xing Y, Guo Y, Gao Z, Keller J, Moan T. Effects of floating sun gear in a wind turbine's planetary gearbox with geometrical imperfections. *Wind Energy*. 2015;18:2105-2120.
33. Nejad AR. Modelling and analysis of drivetrains in offshore wind turbines. *Offshore Wind Energy Technology*; 2018:37.
34. Voltages. IEC Standard IEC 60038; 2009.
35. Rotating electrical machines rating and performance. IEC 60034-1; 2017.
36. Langhart J, Ha T. How to get most realistic efficiency calculation for gearboxes. Power Transmission Engineering; 2015.
37. Moghadam F, Ebrahimi S, Oraee A, Velni JM. Vector control optimization of DFIGs under unbalanced conditions. *Int Trans Elect Energy Syst*. 2018;28:e2583.
38. Gieras JF. Permanent magnet motor technology: design and applications. CRC press; 2009.
39. Miliani E, Ayad MY, Depernet D, Kauffmann JM. Experimental analysis of a six phase permanent magnet synchronous generator in a variable speed constant frequency generating system. In: In APEC 07-Twenty-Second Annual IEEE Applied Power Electronics Conference and Exposition; 2007:1727-1732.
40. Gieras JF. Permanent magnet motor technology: design and applications. CRC press; 2009.
41. Hegseth JM, Bachynski EE. A semi-analytical frequency domain model for efficient design evaluation of spar floating wind turbines. *Marine Struct*. 2019;64:186-210.

42. Kato S, Inui Y, Michihira M, Tsuyoshi A. A low-cost wind generator system with a permanent magnet synchronous generator and diode rectifiers. In: Proceedings of the International Conference on Renewable Energy and Power Quality (ICREPQ'07). 2007:38-44.
43. Hung JY, Ding Z. Design of currents to reduce torque ripple in brushless permanent magnet motors. *IEE Proc B (Electric Power Appl)*. 1993;40:260-266.
44. Thomson W. Theory of vibration with applications. CRC press; 2018.
45. Nejad AR, Bachynski EE, Moan T. Effect of axial acceleration on drivetrain responses in a spar-type floating wind turbine. *ASME J Offshore Mech Arct Eng*. 2019;141:031901-031907.

How to cite this article: Moghadam FK, Nejad AR. Evaluation of PMSG-based drivetrain technologies for 10 MW floating offshore wind turbines: pros and cons in a life-cycle perspective. *Wind Energy*. 2020;23:1542–1563. https://doi.org/10.1002/we.2499

A.2 Paper 2

Paper 2:
Experimental validation of angular velocity measurements for wind turbines drivetrain condition monitoring.
Authors: Farid Khazaeli Moghadam, Amir Rasekhi Nejad
Published in *Proceedings of the ASME 2019 2nd International Offshore Wind Technical Conference IOWTC2019*, November 3-6, St. Julian's, Malta, 2019, IOWTC2019-7620, V001T01A035; 9 pages.

A.3 Paper 3

Paper 3:
Natural frequency estimation by using torsional response, and applications for wind turbine drivetrain fault diagnosis.
Authors: Farid Khazaeli Moghadam, Amir Rasekhi Nejad
Published in *In Journal of Physics: Conference Series*, September 2020, Vol. 1618, No. 2, p. 022019. IOP Publishing.

Natural frequency estimation by using torsional response, and applications for wind turbine drivetrain fault diagnosis

Natural frequency estimation by using torsional response, and applications for wind turbine drivetrain fault diagnosis

Farid K. Moghadam and Amir R. Nejad

Norwegian University of Science and Technology, Trondheim, Norway

E-mail: farid.k.moghadam@ntnu.no

Abstract. A method based on torsional vibration measurements for a system-level condition monitoring of the drivetrain system is developed in this paper. The latter is tested by using a $10MW$ wind turbine drivetrain simulation model, and experimentally validated by the drivetrain operational data obtained from a $1.75MW$ turbine. The method relies on the estimation of the drivetrain torsional natural frequencies by using the torsional responses residual function and subsequent monitoring of the variations in the eigenfrequencies and normal modes. In other words, an abnormal deviation from the reference values of these dynamic parameters can be translated into a meaningful interpretation on the propagation of a specific fault in the driveline. Local sensitivity analysis is employed to establish a relationship between different types of drivetrain faults and the system dynamic properties.

1 Introduction

Multi-megawatt offshore wind turbines are considered as a solution for the large-scale realization of renewable power generations. Offshore wind industry still suffers from longer downtime, high cost for repair and replacement of this system and higher risk of loss of turbine. The latter is due to the larger components and the difficulty to access the system in offshore environments, and a wider range of excitations due to the synergistic impacts of waves, currents and wind turbulences which call for innovative approaches to have a better understanding about the system dynamics and excitations. The focus of this research is proposing a system-level drivetrain condition monitoring (CM) solution by estimation and monitoring of the system dynamic properties. The latter is performed by developing a numerical model of the drivetrain as a dynamic system based on its measured torsional response and the subsequent estimation of torsional frequencies. The motivation is to reduce operational expenditure (OPEX) and subsequently levelized cost of energy (LCOE) to make offshore wind power competitive with land-based wind turbines.

Variations in the drivetrain can be monitored by tracking the changes in the modal parameters (resonance frequencies, damping ratios, and mode shapes) of the dominant modes of this system [1]. Operational modal analysis (OMA) approaches are proposed for characterization of the dynamic behavior (modal parameters) of wind turbine drivetrain in the recent literature by using the translational vibration measurements [1], which generally suffer from a high possibility that harmonics be misinterpreted as the eigenfrequencies [1, 2]. Drivetrain is a complex dynamical system with different sources of external excitations and components defect frequencies,and the

OMA techniques are still not matured enough for such a system. The latter has made OMA technique less-efficient for condition-based maintenance.

The possibility of estimating the drivetrain torsional natural frequencies by using the angular velocity residual function and the subsequent application for health monitoring of the drivetrain, blades and tower is discussed in this paper. Natural frequencies appear on torsional response (*e.g.* angular velocity) due to the impulsive behavior of wind which can act as a physical hammer which excites the system torsional frequencies. In addition, some wind and wave induced structural motions such as excited tower bending and blade in plane modes can act as torsional excitation sources and induce some torsional vibrations on the drivetrain torsional response. The latter makes the angular velocity measurements also applicable for health monitoring of tower and blades. The drivetrain system torsional response and the natural frequencies are proposed in the literature for detecting faults initiated by torsional sources. Patel *et al.* [3] proposes the use of angular displacement to support the lateral response to recognise the rubbing faults in the drivetrain, so that the excited torsional frequency and the amplitude of response in the natural frequency and the side bands are utilized to characterize the fault. Feng *et al.* [4] proposes the use of the measurements of torque instead of transverse vibration signals to diagnose planetary gearbox local/distributed faults, because they are free from the amplitude modulation effect caused by time variant vibration transfer paths, thus they have simpler spectral structure than transverse signals. Lebold *et al.* [5] suggests monitoring the characteristic changes in torsional natural frequencies, and claims that those changes are associated with the shaft crack propagation. Kia *et al.* [6] proposes the estimated electromagnetic torque of the electrical machine as a noninvasive torsional measurement in the drivetrain to monitor the torsional stress on the components including shaft, bearings, and gearbox, and the method is used to detect a gear failure. The electromagnetic torque estimation is commonly used in electrical drives to control the electrical machine, and implementation of the method does not need any additional sensor. Not only the drivetrain faults, but also rotor and tower excited modes can cause a torsional oscillation observable on the drivetrain torsional response [7, 8]. The amplitude of blade edgewise and tower bending natural frequencies can provide insights about resonances in these components. The monitoring of the variations of these components frequencies is also useful for some other purposes such as ice detection in blades, and health monitoring of blades (detect root cracks within turbine blades) and tower. The idea of using angular velocity measurements for the drivetrain fault detection is originally proposed by Nejad *et al.* [9]. The input data is provided from the encoders on the drivetrain used for the turbine control, and is normally in access in both the turbine and the farm levels. Therefore, any algorithm based on those measurements can simply be integrated in either turbine or farm control to support the online health monitoring of the drivetrain. Moghadam *et al.* [8] experimentally tests the potential of using the encoder measurements to detect different faults initiated by the different excitation sources, compared to a conventional method based on accelerometers.

In the proposed drivetrain condition monitoring approach of this paper, it is assumed that faults in the driveline (*e.g.* shaft cracks, unbalance and looseness) reveal themselves by variations in the system stiffness and moment of inertia. Therefore by monitoring the consequences of variations of drivetrain parameters (*i.e.* stiffness and moment of inertia matrices) in change of the drivetrain dynamic properties (*i.e.* natural frequencies, mode shapes and damping matrix), it is possible to monitor the progress of faults. For this purpose, a sensitivity analysis helps to realize what are the most influential parameters on the variability of the drivetrain dynamic properties. The main contributions of this work are:

(i) Estimation of the wind turbine drivetrain torsional natural frequencies by using the system torsional responses,

(ii) Estimation of the drivetrain damping in the torsional natural frequencies,

(iii) Proposing a method for driveline health monitoring without any additional sensor, based

on monitoring the variations in the estimated drivetrain dynamic properties.

2 Methodology

2.1 Torsional natural frequency estimation theory

The torsional response of equivalent one-degree-of-freedom rotational system in the non-dimensional form can be expressed by

$$\theta = \frac{\frac{\tau_0}{k_t}}{\sqrt{(1-(\frac{\omega}{\omega_n})^2)^2 + (2\zeta_t(\frac{\omega}{\omega_n}))^2}}, \tag{1}$$

where θ is the angular position and τ_0 is the amplitude of the excitation momentum. For this case, ω_n is the natural torsional frequency of the system. k_t is the torsional stiffness of the shaft, and ζ_t is the torsional damping ratio. An amplified frequency in the drivetrain torsional response can be due to a significant excitation amplitude or coincidence of excitation frequency with natural frequencies.

Natural frequencies appear on torsional responses *e.g.* angular velocity measurements due to impulsive behavior of wind which excites those frequencies. An initial velocity applied on a system as described by Thomson *et al.*[10] can play a role as an impact which is able to excite the system torsional frequencies. In the wind turbine, the ceaseless variations of wind results in continual variations in angular velocity which is physically similar to an initial velocity applied to the system. Though these variations in speed and subsequently torque are of a very low frequency and slow dynamics, but it introduces considerable energy in different frequencies including the characteristic frequencies of the system. Due to the existence of damping in a physical system, the measured natural frequencies from the torsional response are the damped frequencies. Our observations show that the angular velocity measurements can help to measure the drivetrain and the blade edgewise natural frequencies. By filtering the shafts revolution frequencies, components defect frequencies and excitations (very low frequency due to wind, low frequency due to wave tower shadow effect, and high frequency due to generator), the drivetrain torsional natural frequencies, and some torsional induced motions due to excited edgewise rotor blade and tower bending modes are acquired. Based on a primary knowledge on the torsional frequencies for each power range, it is possible to separate the observed natural frequencies for drivetrain, blades and tower. The variations in the natural frequencies and normal modes can be used as criteria for the severity of some sorts of faults in the drivetrain. To estimate the damped natural frequencies, angular velocity residual/error function is proposed. The input of this method is provided by two encoders located at the high- and low-speed shafts of drivetrain, and subsequently the residual function is constructed based on the subtraction of these two signals. Some drivetrains are only equipped with one angular velocity measurement on the shaft, so that the implementation of the method might require an additional moderate sampling frequency encoder to provide the sufficient inputs. The angular velocity residual function $e^{\omega}_{\mathrm{tot}}$ from the high-speed side is expressed by

$e^{\omega}_{tot} = \omega_{HS} - a_1 a_2 a_3 \omega_{LS}$, where ω_{HS} and ω_{LS} are the rotational speed in rad/s obtained from the high- and low-speed encoders, respectively. a_1, a_2 and a_3 are the inverse of gear ratios of the gearbox stages. The error function main feature is cancellation of the impacts of the excitations which are transferred to the drivetrain from the housing, from the resultant torsional response. Angular displacement and acceleration are the other torsional responses of the drivetrain system which could theoretically be used similar to angular velocity to obtain the system torsional parameters. For this purpose, similar to $e^{\omega}_{\mathrm{tot}}$, the angular displacement error function $e^{\theta}_{\mathrm{tot}}$ and the angular acceleration error function $e^{\alpha}_{\mathrm{tot}}$ are defined by

$e^{\theta}_{tot} = \theta_{HS} - a_1 a_2 a_3 \theta_{LS}$, $\mathrm{e}^{\alpha}_{tot} = \alpha_{HS} - a_1 a_2 a_3 \alpha_{LS}$.

In particular, angular acceleration is the torsional response which has a direct relation with the applied load, and contains useful information on how the applied torque interacts with the

system. The frequency domain analytics Fourier transform and power spectral density (PSD) are used for analysis of the defined torsional response error functions. The Fourier series of $e^{\omega}_{\mathrm{tot}}$, $e^{\alpha}_{\mathrm{tot}}$ and $e^{\theta}_{\mathrm{tot}}$ are defined by

$$e^{\omega}_{tot}(\Omega) = \sum_{n=-\infty}^{\infty} C_n e^{ik_n\Omega},\ e^{\alpha}_{tot}(\Omega) = \sum_{n=-\infty}^{\infty} C_n (ik_n) e^{ik_n\Omega},\ e^{\theta}_{tot}(\Omega) = \sum_{n=-\infty}^{\infty} C_n (ik_n)^{-1} e^{ik_n\Omega}$$

Differentiation and integration are linear operations that are distributive over addition. As it can be seen, in $e^{\alpha}_{\mathrm{tot}}$ compared to $e^{\omega}_{\mathrm{tot}}$, the amplitude of the frequency components higher than 1 Hz is magnified with the gain k_{n}, and the frequencies lower than 1 Hz are weakened with the same proportion. In $e^{\theta}_{\mathrm{tot}}$ compared to $e^{\omega}_{\mathrm{tot}}$, the amplitude of the frequency components lower than 1 Hz is magnified with the gain k_{n}^{-1}, and the frequencies higher than 1 Hz are weakened with the same proportion.

The 1^{st} natural frequency of the drivetrain systems of the same technology decreases as the rated power increases. However, even for 10 MW wind turbine which is the highest commercially available and even for the high-speed technologies which have lower first natural frequencies, the first torsional frequency is higher than 1 Hz [11]. Therefore, the angular acceleration error functions theoretically outperforms the other two approaches in highlighting the torsional frequencies. The other benefit is weakening the frequencies lower than 1 Hz which appear in the drivetrain torsional response mostly due to wave and wind turbulence and does not contain any information on the natural frequencies. However, an additional derivation operation is required to attain acceleration from the velocity measurements which increases the computational cost of this method.

To evaluate the observability of natural frequencies on the torsional response error functions and the subsequent application for drivetrain condition monitoring, a simplified model of drivetrain is useful. The 1^{st} and 2^{nd} undamped natural frequencies (nonrigid modes) based on a simplified three-mass spring and three degrees of freedom (DOF) torsional model of a geared drivetrain is calculated by

$$\omega_n^1 = \sqrt{\frac{k_{LS}}{2J_{rot}} + \frac{k_{LS}+k_{HS}}{2J_{gear}} + \frac{k_{HS}}{2J_{gen}} - \sqrt{(\frac{-k_{LS}}{2J_{rot}} - \frac{k_{LS}-k_{HS}}{2J_{gear}} + \frac{k_{HS}}{2J_{gen}})^2 + \frac{k_{LS}k_{HS}}{J_{gear}^2}}}, \tag{2a}$$

$$\omega_n^2 = \sqrt{\frac{k_{LS}}{2J_{rot}} + \frac{k_{LS}+k_{HS}}{2J_{gear}} + \frac{k_{HS}}{2J_{gen}} + \sqrt{(\frac{-k_{LS}}{2J_{rot}} - \frac{k_{LS}-k_{HS}}{2J_{gear}} + \frac{k_{HS}}{2J_{gen}})^2 + \frac{k_{LS}k_{HS}}{J_{gear}^2}}}, \tag{2b}$$

where ω_{n}^1 and ω_{n}^2 are the 1^{st} and 2^{nd} natural frequencies, k_{LS} and k_{HS} are the torsional stiffness of low- and high-speed shafts, and J_{rot}, J_{gear} and J_{gen} are the moment of inertia of rotor, gearbox and generator, respectively.

2.1.1 Simulation based validation For the simulation studies, DTU 10 MW reference wind turbine is selected. In order to evaluate if the input torque is able to excite the drivetrain natural frequencies and subsequently to study the possibility of observing those frequencies in the different drivetrain torsional responses, an effective approach is involving decoupled simulation technique [12] and engaging frequency-domain data analytics. For this purpose, the rotor torque data of 10 MW turbine with a spar floating platform obtained from SIMA global simulation software is used, and the impacts on the drivetrain is studied using a decoupled analysis. The operating condition for this simulation is close to the rated operation with an average wind speed $U_w = 11\ m/s$, significant wave height $H_s = 3.5\ m$ and peak period $T_p = 7.5\ s$. The natural frequencies of the under consideration drivetrain is calculated by using a 3-DOF torsional model and eq. (2), and validated by Simpack multi-body simulation software. In this torsional model, rotor, gearbox and generator are modelled with equivalent moment of inertia, and the low-

and high-speed shafts are each modelled with a constant torsional stiffness. The generator and gearbox specifications are used from the optimized medium-speed 10 MW drivetrain system proposed in [11]. The parameters of this model are listed in Table 1. The natural frequencies of this model are 1.9 Hz and 73.9 Hz. The torsional responses of rotor and generator shafts are obtained from the Simpack simulated model to investigate possibility of observing the natural frequencies from the angular velocity, acceleration and displacement error functions.

Table 1: Model specification

Parameter	**Value**
Equivalent rotor moment of inertia J_{rot} $(kg.m^2)$	$800,000,000$
Equivalent gearbox moment of inertia J_{gear} $(kg.m^2)$	$1,239,300$
Equivalent generator moment of inertia J_{gen} $(kg.m^2)$	$15,716,775$
Equivalent low-speed shaft torsional stiffness K_{rot}^{gear} $(N.m/rad)$	$2,452,936,425$
Equivalent high-speed shaft torsional stiffness K_{gear}^{gen} $(N.m/rad)$	$245,293,642,500$

2.1.2 Experimental validation The operational data from Vestas V66-1.750MW turbine is used for the experimental study. To test the method, an additional encoder is installed on the low-speed shaft. In PSD of the angular velocity error function of the operational data, in addition to the natural frequencies, some other frequency components are also expected to be observed. However, by a prior knowledge about the defect frequencies and the other torsional excitation sources, and by subsequently filtering those frequencies, it is possible to distinguish the natural frequencies. The benefits with measuring the natural frequencies by this noninvasive method are the low implementation cost, and the possibility of obtaining the precise values of natural frequencies by including the system nonlinearities, and translational impacts on the rotation transferred through the bed-plate and torque arm.

2.2 Estimation of damping in the drivetrain

As discussed earlier, the natural frequencies measured by the approach proposed in Section 2.1 are the damped natural frequencies ω_d which have the relation $\omega_{\mathrm{d}}^i = \sqrt{(1-(\zeta^i)^2)}\omega_{\mathrm{n}}^i$ with the undamped frequency ω_{n}, with ζ^i the damping coefficient ($\zeta^i = c^i/c_{\mathrm{c}}^i$) for the i^{th} mode. c and c_{c} are actual and critical dampings. More precisely, the estimated natural frequencies are the extreme values of the response. The response extreme values from the simplified model in eq. (2.1), will occur at $\omega_{\mathrm{peak}}^i = \sqrt{(1-2(\zeta^i)^2)}\omega_{\mathrm{n}}^i$. ζ^i takes different values in different operating speeds. For two different operating speeds, for each frequency mode, damping in the system natural frequency of the two operations is related to the measured natural frequencies by eq. (3a)

$$\frac{\omega_{peak}^{i,t_1,\omega_1}}{\omega_{peak}^{i,t_2,\omega_2}} = \sqrt{\frac{1-(\zeta^{i,t_1,\omega_1})^2}{1-(\zeta^{i,t_2,\omega_2})^2}}, \quad (3a) \qquad \frac{\theta_{\omega_{peak}}^{i,t_1,\omega_1}}{\theta_{\omega_{peak}}^{i,t_2,\omega_2}} = \frac{\tau_0^{t_1}}{\tau_0^{t_2}}\frac{\zeta^{i,t_2,\omega_2}}{\zeta^{i,t_1,\omega_1}}\frac{\sqrt{1-(\zeta^{i,t_2,\omega_2})^2}}{\sqrt{1-(\zeta^{i,t_1,\omega_1})^2}}, \quad (3b) \qquad (3)$$

with $\omega_{\mathrm{peak}}^{i,t_1,\omega_1}$ the drivetrain eigenfrequency estimated during operation in the time period t_1 and the turbine speed ω_1. $\omega_{\mathrm{peak}}^{i,t_2,\omega_2}$ is the same parameter estimated during the time period t_2 and the speed ω_2. According to eq. (1), there is a relationship as shown in eq.(3b) between the amplitude of response and damping ratio at the measured natural frequencies for the two different operations. $\theta_{\omega_{\mathrm{peak}}}^{i,t_1,\omega_1}$ is the response amplitude in the i^{th} frequency mode in the operating point $\begin{bmatrix} t_1 \\ \omega_1 \end{bmatrix}$, and $\theta_{\omega_{\mathrm{peak}}}^{i,t_2,\omega_2}$ is the same parameter for the operating condition $\begin{bmatrix} t_2 \\ \omega_2 \end{bmatrix}$. To derive eq. (3$b$), it is assumed that the two operating points are close enough so that the stiffness and moment of inertia stay constant. As a result, the undamped natural frequency does not change. By using eqs (3a) and (3b), the absolute values of the damping coefficient of the system in the

natural frequency in different operating conditions can be estimated. The latter can be used to monitor damping in different operating speeds and helps to track the variations of damping over the system lifetime, which provides the input for retuning active dampers and helps to improve the system dynamic response. It is worth noting that the estimated damping by this methods also includes the effects of the rotor aerodynamic damping and active electric damping introduced by the generator control. Therefore, the resultant of damping of shafts, components, coupling and active dampers in the system natural frequencies can be observed which gives a good feedback for drivetrain design and also the operator for calibration of active damper parameters.

As it is shown in Section 2.3, the 1^{st} and 2^{nd} modes are affected to a great extent by the torsional stiffness of the low- and high-speed shafts, respectively. The damping of the first and second modes is also mostly dominated by the damping introduced by low- and high-speed shafts, respectively. Therefore, the estimated damping coefficients can be used to estimate the actual damping of the related shafts in the reduced order model of drivetrain.

The different damping behaviors in the system natural frequency compared to the harmonics in the torsional response is the criterion suggested for validating the natural frequencies estimated by the proposed method in Section 2.1. Based on eq. (1), damping is more significantly reducing the amplitude of response in the natural frequency compared to the harmonics, which helps to distinguish the natural frequency from the other harmonics. In other words, the ratio of amplitude of response at natural frequency in two different operating speeds is higher/lower (depended on if the speed drops or rises) than this ratio at harmonics.

2.3 Sensitivity analysis

A shaft crack results in reduction of the torsional stiffness of the shaft [13]. A change in the stiffness of the shafts also influences on the drivetrain system frequency modes. Therefore, by obtaining the mathematical relation between the stiffness of different shafts and the system natural frequencies, it is possible to monitor their conditions by monitoring variations in the natural frequencies. The other parameter which can influence on the drivetrain natural frequencies is the moment of inertia of the drivetrain components. Variations in the moment of inertia matrix represents the other category of faults in the driveline with the unbalance and looseness as the foremost. This category of faults are characterized by the increase of moment of inertia due to an additional force that is generated in those conditions and based on the parallel axis theorem. The mathematical relation between the drivetrain torsional natural frequencies and the moment of inertia of components can help to detect and localize these faults.

The variations in stiffness and moment of inertia can result in similar natural frequency variation patterns. Therefore, to distinguish between variations in the natural frequencies because of variations in the shafts' stiffness with those due to variations in moment of inertia matrix (source of fault), determining the correlation between the system parameters and the normalized mode shapes can provide a useful direction to find the source of fault. To check how the variations in stiffness and moment of inertia influence on the variability of system natural torsional frequencies and mode shapes, a sensitivity analysis is performed. There are two classes of sensitivity analysis methods, namely local and global sensitivity analysis. Morio *et al.*[14] has reported the same kind of results by using these two method for simple models. Local sensitivity determines how a small perturbation near an input parameter value influences the value of the output. In this Section, in order to find the parameters with the greatest impact on the drivetrain dynamic characteristics local sensitivity analysis is employed due to two main reasons. First, the motivation of this work is detecting faults in early stages for predictive maintenance purposes so that variations in the drivetrain system parameters happen with a slight change around the set point values. Second, local sensitivity analysis derives a closed form expression for the sensitivity value which makes the result more reliable and easier to implement. Local sensitivity is defined as the partial derivative of the output function with respect to the input parameters [15] as

$S_{i,j}^{Loc} = \frac{\delta y_i}{\delta x_j},\ y_i \in \{y_1, ..., y_p\}\ and\ x_j \in \{x_1, ..., x_q\}$, where y_i is the i^{th} output and x_j is the j^{th} input. To neutralize the impact of large/small inputs and small/large outputs, the local sensitivity can be normalized by the nominal values of inputs and outputs by

$S_{i,j}^{Norm} = \frac{x_j^{ref}}{y_i^{ref}} \frac{\delta y_i}{\delta x_j}$, with x_j^{ref} and y_i^{ref} as the nominal values of x_j and y_i. For the 3-DOF torsional model described in Section 2.1, the input and output vectors for sensitivity analysis are $x = \{k_\mathrm{LS},\ k_\mathrm{HS},\ J_\mathrm{rot},\ J_\mathrm{gear},\ J_\mathrm{gen}\}$ and $y = \{f_1^{tor},\ f_2^{tor}\}$. By applying normalized local sensitivity theory on eq. (2) we will have

$$S_{1,1}^{norm} = \frac{k_{LS}}{4} \frac{\frac{(\frac{1}{J_{gear}}+\frac{1}{J_{rot}})A-\frac{k_{HS}}{J_{gear}^2}}{\sqrt{A^2+\frac{k_{LS}k_{HS}}{J_{gear}^2}}} + \frac{1}{J_{gear}} + \frac{1}{J_{rot}}}{-\sqrt{A^2+\frac{k_{LS}k_{HS}}{J_{gear}^2}}+B}, \quad S_{2,1}^{norm} = \frac{k_{LS}}{4} \frac{(\frac{1}{J_{gear}} - \frac{(\frac{1}{J_{gear}}+\frac{1}{J_{rot}})A-\frac{k_{HS}}{J_{gear}^2}}{\sqrt{A^2+\frac{k_{LS}k_{HS}}{J_{gear}^2}}} + \frac{1}{J_{rot}})}{\sqrt{A^2+\frac{k_{LS}k_{HS}}{J_{gear}^2}}+B}, \tag{4a}$$

$$S_{1,2}^{norm} = \frac{k_{HS}}{4} \frac{\frac{1}{J_{gen}} - \frac{(\frac{1}{J_{gear}}+\frac{1}{J_{rot}})A+\frac{k_{LS}}{J_{gear}^2}}{\sqrt{A^2+\frac{k_{LS}k_{HS}}{J_{gear}^2}}} + \frac{1}{J_{gear}}}{-\sqrt{A^2+\frac{k_{LS}k_{HS}}{J_{gear}^2}}+B}, \quad S_{2,2}^{norm} = \frac{k_{HS}}{4} \frac{\frac{(\frac{1}{J_{gen}}+\frac{1}{J_{gear}})A+\frac{k_{LS}}{J_{gear}^2}}{\sqrt{A^2+\frac{k_{LS}k_{HS}}{J_{gear}^2}}} + \frac{1}{J_{gen}} + \frac{1}{J_{gear}}}{\sqrt{A^2+\frac{k_{LS}k_{HS}}{J_{gear}^2}}+B}, \tag{4b}$$

$$S_{1,3}^{norm} = -\frac{J_{rot}}{4} \frac{\frac{k_{LS}}{J_{rot}^2} + \frac{k_{LS}A}{J_{rot}^2\sqrt{A^2+\frac{k_{LS}k_{HS}}{J_{gear}^2}}}}{-\sqrt{A^2+\frac{k_{LS}k_{HS}}{J_{gear}^2}}+B}, \quad S_{2,3}^{norm} = -\frac{J_{rot}}{4} \frac{\frac{k_{LS}}{J_{rot}^2} - \frac{k_{LS}A}{J_{rot}^2\sqrt{A^2+\frac{k_{LS}k_{HS}}{J_{gear}^2}}})}{\sqrt{A^2+\frac{k_{LS}k_{HS}}{J_{gear}^2}}+B}, \tag{4c}$$

$$S_{1,4}^{norm} = -\frac{J_{gear}}{4} \frac{\frac{k_{HS}+k_{LS}}{J_{gear}^2} - \frac{\frac{2k_{LS}k_{HS}}{J_{gear}^3}+\frac{(k_{HS}-k_{LS})A}{J_{gear}^2}}{\sqrt{A^2+\frac{k_{LS}k_{HS}}{J_{gear}^2}}}}{-\sqrt{A^2+\frac{k_{LS}k_{HS}}{J_{gear}^2}}+B}, \quad S_{2,4}^{norm} = -\frac{J_{gear}}{4} \frac{\frac{\frac{2k_{LS}k_{HS}}{J_{gear}^3}+\frac{(k_{HS}-k_{LS})A}{J_{gear}^2}}{\sqrt{A^2+\frac{k_{LS}k_{HS}}{J_{gear}^2}}} + \frac{k_{HS}+k_{LS}}{J_{gear}^2}}{\sqrt{A^2+\frac{k_{LS}k_{HS}}{J_{gear}^2}}+B}, \tag{4d}$$

$$S_{1,5}^{norm} = -\frac{J_{gen}}{4} \frac{\frac{k_{HS}}{J_{gen}^2} - \frac{k_{HS}A}{J_{gen}^2\sqrt{A^2+\frac{k_{LS}k_{HS}}{J_{gear}^2}}}}{-\sqrt{A^2+\frac{k_{LS}k_{HS}}{J_{gear}^2}}+B}, \quad S_{2,5}^{norm} = -\frac{J_{gen}}{4} \frac{\frac{k_{HS}}{J_{gen}^2} + \frac{k_{HS}A}{J_{gen}^2\sqrt{A^2+\frac{k_{LS}k_{HS}}{J_{gear}^2}}}}{\sqrt{A^2+\frac{k_{LS}k_{HS}}{J_{gear}^2}}+B}, \tag{4e}$$

where $A = \frac{k_{HS}}{2J_{gen}} - \frac{k_{LS}}{2J_{rot}} + \frac{k_{HS}-k_{LS}}{2J_{gear}}$ and $B = \frac{k_{HS}}{2J_{gen}} + \frac{k_{LS}}{2J_{rot}} + \frac{k_{HS}+k_{LS}}{2J_{gear}}$.

A schematic figure representing the proposed driveline condition monitoring method is illustrated in Fig. 1. $EN1$ and $EN2$ in this figure are the angular velocity measurement sensors placed on the low- and high-speed shafts, respectively. The algorithm which summarizes the proposed approach is depicted in Fig. 2. $\varphi^{1,m}$ and $\varphi^{2,m}$ are the normal modes related to the 1^{st} and 2^{nd} natural frequencies, respectively. m varies from 1 up to the degree of the model. τ and $\tau_{\varphi\mathrm{m}}$ are the low-limit threshold natural frequency and normal mode for normal operations. It is worth noting that the natural frequencies estimated and subsequently used in the condition monitoring algorithm are the damped natural frequencies which are directly estimated from the operational measurements of system torsional response. In order to eliminate the influence of different damping values as a result of different turbine operational speeds, the estimated natural frequencies and the associated thresholds are engaged in the proposed algorithm based on the operational speed.

3 Results

3.1 Simulation results

The PSD spectrum of angular velocity error function obtained from 10 MW drivetrain model in Simpack and its capability in highlighting the torsional natural frequencies is shown in Fig.

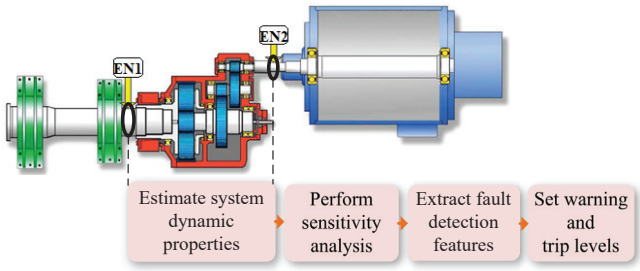

Figure 1: Schematic of the proposed condition monitoring method.

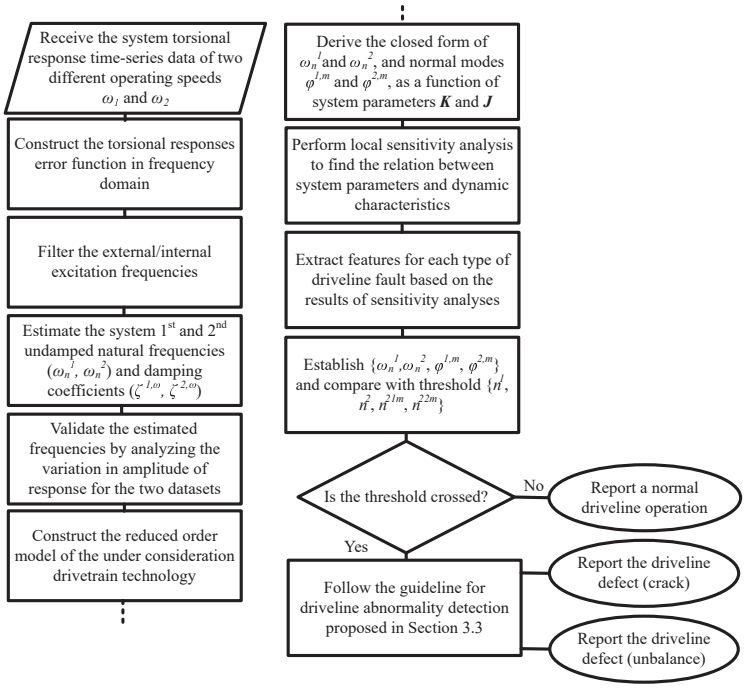

Figure 2: Flowchart of the proposed algorithm for driveline condition monitoring.

3. In this figure, the performance of angular velocity error function in extracting the 1^{st} and 2^{nd} torsional natural frequencies of the drivetrain is compared with angular displacement and angular acceleration error functions. As it can be seen, acceleration error function outperforms in revealing the higher frequency modes (the 2^{nd} mode). The higher modes have usually a lower impact on the response, which impedes disclosure of those frequencies. The PSD spectrum of input torque obtained from the global simulation and applied on the Simpack drivetrain model is shown in Fig. 3a. This input contains the majority of frequency components and can excite the drivetrain natural frequencies. In this simulation study, the model is undamped. Therefore, the estimated frequencies are the undamped frequencies. As discussed in Section 2.2, for a damped system, the estimated frequencies are the peak frequencies which can be translated to

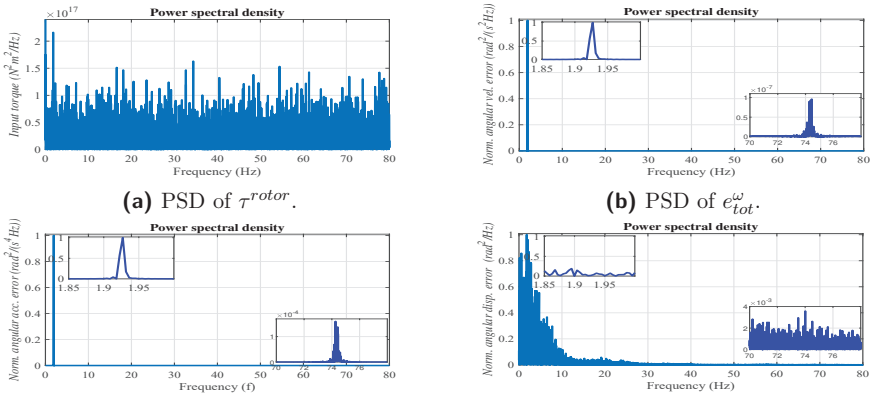

(a) PSD of τ^{rotor}. **(b)** PSD of e^{ω}_{tot}.

(c) PSD of e^{α}_{tot}. **(d)** PSD of e^{θ}_{tot}.

Figure 3: Simulation results based on 10 MW floating wind turbine model.

the undamped natural frequencies by using the estimated damping coefficients from the theory elaborated in the same Section. ω_{n} can also be approximated with ω_{peak} if $\zeta << 1$ which may not be an unrealistic assumption for multi-megawatt wind turbine drivetrain systems.

3.2 Experimental results

The PSD spectrum of angular velocity error function of the Vestas drivetrain operational data for a rated operation is shown in Fig. 4, which shows the observability of both the drivetrain and blade natural frequencies. The results are validated by comparing with the 1^{st} drivetrain and 1^{st} blade edgewise natural frequencies of another turbine with the same drivetrain technology and a similar power range reported in [16]. The performance of angular velocity error function is compared with angular displacement and acceleration error functions. As it can be seen, angular acceleration shows a slightly higher performance in amplification and extraction of characteristic frequencies of higher values.

A comparison between the angular velocity error function PSD in two different operating speeds is shown in Fig. 4d. As it can be seen, the higher damping coefficient in lower speeds results in a lower damped natural frequency as discussed in Section 2.2. Furthermore, at the drivetrain natural frequency, the amplitude reacts more significantly to the variation in damping. In other words, the amplitude of response at the natural frequency reduces more compared with other harmonics, for a lower rotor speed which corresponds to a higher damping.

3.3 Sensitivity analysis results

The results of the normalized local sensitivity analyses with natural frequencies (f_1^{tor}, f_2^{tor}) and normal modes (ϕ_1, ϕ_2) as the outputs and shaft stiffnesses ($K_{\mathrm{LS}}, K_{\mathrm{HS}}$) as the inputs are shown in Table 2. The reported numbers show the normalized sensitivity values and also the variations of outputs (in %) for the input parameters changed by $\pm 5\%$ of their rated values. As it can be seen, there is a direct relationship between the 1^{st} frequency and K_{LS}, and the 2^{nd} frequency and K_{HS}. Therefore, variations in the natural frequencies can be translated into the variations in the shaft stiffness and subsequently the defects in the drivetrain shafts. The influence of the shafts defect (stiffness variation) on amplitude of oscillation due to the 1^{st} mode is negligible. However, the stiffness variation results in variations in the amplitude of oscillation in rotor due to the 2^{nd} mode.

The results of the sensitivity analyses with natural frequencies and normal modes as the outputs

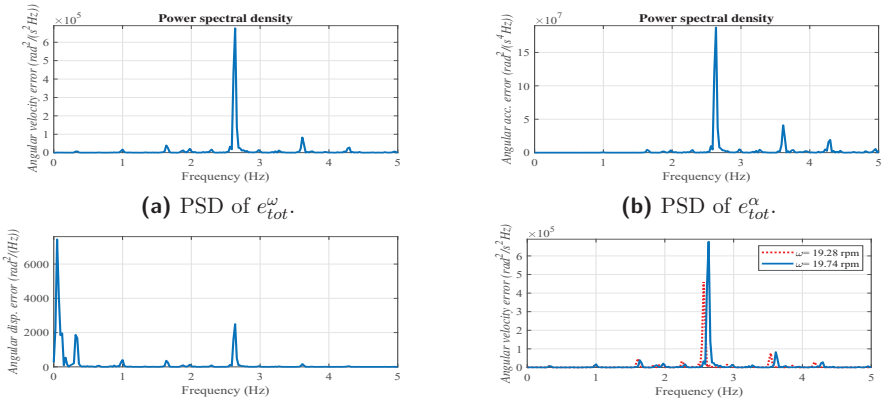

(a) PSD of e^{ω}_{tot}. **(b)** PSD of e^{α}_{tot}.

(c) PSD of e^{θ}_{tot}. **(d)** velocity (different operations).

Figure 4: Experimental results based on 1.75 MW Vestas turbine operational data.

Table 2: Sensitivity of natural frequencies, amplitude of oscillation due to the 1^{st} mode, and amplitude of oscillation due to the 2^{nd} mode to torsional stiffness.

Sensitivity \ Variable	$K_{LS}(\pm5\%)$	$K_{HS}(\pm5\%)$	K_{LS} *and* K_{HS} $(\pm5\%)$
f_1^{tor}	$0.50(\pm2.48\%)$	$0.00(\pm0.02\%)$	$0.50(\pm2.50\%)$
f_2^{tor}	$0.00(\pm0.02\%)$	$0.50(\pm2.48\%)$	$0.50(\pm2.50\%)$
ϕ_1^{rot}	$0.00(\pm0.02\%)$	$0.00(\mp0.02\%)$	$0.00(0.00\%)$
ϕ_1^{gear}	$0.00(\mp0.02\%)$	$0.00(\pm0.02\%)$	$0.00(0.00\%)$
ϕ_1^{gen}	$0.00(\pm0.02\%)$	$0.00(\mp0.02\%)$	$0.00(0.00\%)$
ϕ_2^{rot}	$0.99(\pm4.96\%)$	$-0.99(\mp4.97\%)$	$0.00(0.00\%)$
ϕ_2^{gear}	$0.00(0.00\%)$	$0.00(0.00\%)$	$0.00(0.00\%)$
ϕ_2^{gen}	$-0.01(\mp0.05\%)$	$0.01(\pm0.05\%)$	$0.00(0.00\%)$

and moment of inertia ($J_{\text{rot}}, J_{\text{gear}}, J_{\text{gen}}$) as the inputs are shown in Table 3. As it can be seen, there is an inverse relationship between the 1^{st} frequency and J_{gen}, and the 2^{nd} frequency and J_{gear}, so that the reduction of natural frequencies can be due to a rise in the moment of inertia. To distinguish between the drop in natural frequencies due to variation in stiffness and moment of inertia, the results should be interpreted together with monitoring the variations of normal modes. The simultaneous drop of the 1^{st} frequency and the amplitude of oscillation at rotor due to the 2^{nd} mode represents a problem in low-speed shaft. The drop of the 2^{nd} frequency and the simultaneous rise in amplitude of oscillation at rotor due to the 2^{nd} mode discloses the problems in high-speed shaft. The drop of the 1^{st} frequency, the simultaneous rise in amplitude of oscillation at rotor due to the 1^{st} mode and drop in amplitude of oscillation at generator due to the 2^{nd} mode reveal unbalances in generator side. The drop of the 2^{nd} frequency and a simultaneous rise in amplitude of oscillation at both rotor and generator due to the 2^{nd} mode can be used as the criteria to detect an unbalance in gearbox. However, unbalance in rotor represents it self mainly by variations in normal modes with minor influence on the natural frequencies,so that a simultaneous drop in amplitude of oscillation at rotor due to 1^{st} and 2^{nd} modes are indicators of rotor unbalance.

4 Conclusions

The potentials of using drivetrain torsional responses for estimation of the drivetrain torsional natural frequencies and heath monitoring of the driveline was discussed, and evaluated by both experimental and simulation studies. Local sensitivity analysis was engaged to find the

Table 3: Sensitivity of natural frequencies, amplitude of oscillation due to the 1^{st} mode, and amplitude of oscillation due to the 2^{nd} mode to moment of inertia.

Sensitivity \ Variable	$J_{rot}(\pm5\%)$	$J_{gear}(\pm5\%)$	$J_{gen}(\pm5\%)$	$J_{rot}(\pm5\%)$ $J_{gear}(\pm5\%)$	$J_{gear}(\pm5\%)$ $J_{gen}(\pm5\%)$	$J_{rot}(\pm5\%)$ $J_{gen}(\pm5\%)$	$J_{rot}(\pm5\%)$ $J_{gear}(\pm5\%)$ $J_{gen}(\pm5\%)$
f_1^{tor}	$-0.01(\mp0.05\%)$	$-0.03(\mp0.17\%)$	$-0.45(\mp2.25\%)$	$-0.40(\mp0.22\%)$	$-0.49(\mp2.44\%)$	$-0.46(\mp2.32\%)$	$-0.50(\mp2.50\%)$
f_2^{tor}	$0.00(0.00\%)$	$-0.45(\mp2.25\%)$	$-0.04(\mp0.18\%)$	$-0.45(\mp2.25\%)$	$-0.49(\mp2.44\%)$	$-0.04(\mp0.18\%)$	$-0.49(\mp2.44\%)$
ϕ_1^{rot}	$-1.00(\mp5.01\%)$	$0.07(\pm0.35\%)$	$0.93(\pm4.63\%)$	$-0.93(\mp4.66\%)$	$1.00(\pm4.98\%)$	$-0.07(\mp0.37\%)$	$0.00(\mp0.02\%)$
ϕ_1^{gear}	$0.00(0.00\%)$	$0.00(0.00\%)$	$0.00(0.00\%)$	$0.00(0.00\%)$	$0.00(0.00\%)$	$0.00(0.00\%)$	$0.00(0.00\%)$
ϕ_1^{gen}	$0.00(0.00\%)$	$0.00(0.00\%)$	$0.00(0.00\%)$	$0.00(0.00\%)$	$0.00(0.00\%)$	$0.00(0.00\%)$	$0.00(0.00\%)$
ϕ_2^{rot}	$-1.00(\mp5.01\%)$	$0.89(\pm4.47\%)$	$0.08(\pm0.39\%)$	$-0.10(\mp0.52\%)$	$0.97(\pm4.85\%)$	$-0.92(\mp4.62\%)$	$-0.03(\mp0.14\%)$
ϕ_2^{gear}	$0.00(0.00\%)$	$-0.01(\mp0.03\%)$	$0.01(\pm0.03\%)$	$-0.01(\mp0.03\%)$	$0.00(0.00\%)$	$0.01(\pm0.03\%)$	$0.00(0.00\%)$
ϕ_2^{gen}	$0.00(0.00\%)$	$0.96(\pm4.82\%)$	$-1.00(\mp4.98\%)$	$0.96(\pm4.82\%)$	$-0.03(\mp0.15\%)$	$-1.00(\mp4.98\%)$	$-0.03(\mp0.15\%)$

mathematical relation between the variations in dynamic properties of the system and variations in drivetrain parameters. In order to detect and localize the driveline faults, one should look into the variations in the system natural frequencies and the amplitude of oscillation due to the frequency modes. Future work will be focused on applying the proposed approach on more detailed models of the drivetrain to cover more diversity of faults in the driveline, and using the technique for prognosis of the driveline faults in various drivetrain technologies.

References

[1] El-Kafafy, M., Gioia, N., Guillaume, P. and Helsen, J., 2019. Long-term automatic tracking of the modal parameters of an offshore wind turbine drivetrain system in standstill condition. *In Rotating Machinery, Vibro-Acoustics & Laser Vibrometry*, Vol. 7 (pp. 91-99).

[2] El-Kafafy, M., Colanero, L., Gioia, N., Devriendt, C., Guillaume, P. and Helsen, J., 2017. Modal parameters estimation of an offshore wind turbine using measured acceleration signals from the drivetrain. *In Struc. Health Monitoring& Damage Detection*, 7, pp.41-48.

[3] Patel, T.H. and Darpe, A.K., 2009. Coupled bending-torsional vibration analysis of rotor with rub and crack. *Journal of Sound and Vibration*, 326(3-5), pp.740-752.

[4] Feng, Z. and Zuo, M.J., 2013. Fault diagnosis of planetary gearboxes via torsional vibration signal analysis. *Mechanical Systems and Signal Processing*, 36(2), pp.401-421.

[5] Lebold, M.S., Maynard, K., Reichard, K., Trethewey, M., Bieryla, D., Lissenden, C. and Dobbins, D., 2004, March. Using torsional vibration analysis as a synergistic method for crack detection in rotating equipment. *IEEE Aerospace Conf. Proc.*, Vol. 6, pp. 3517-3527.

[6] Kia, S.H., Henao, H. and Capolino, G.A., 2009. Torsional vibration assessment using induction machine electromagnetic torque estimation. *IEEE Transactions on Industrial Electronics*, 57(1), pp.209-219.

[7] Lu, B., Li, Y., Wu, X. and Yang, Z., 2009, June. A review of recent advances in wind turbine condition monitoring and fault diagnosis. *In 2009 IEEE Power Electronics and Machines in Wind Applications*, pp. 1-7.

[8] Moghadam, F.K., and Nejad, A.R., 2019. Experimental validation of angular velocity measurements for wind turbines drivetrain condition monitoring. *Accepted by Proceedings of 2^{nd} International Offshore Wind Technical Conference (IOWTC) 2019.*

[9] Nejad, A.R., Odgaard, P.F. and Moan, T., 2018. Conceptual study of a gearbox fault detection method applied on a 5-MW spar-type floating wind turbine. *Wind Energy*, 21(11), pp.1064-1075.

[10] Thomson, W., 2018. Theory of vibration with applications. CrC Press.

[11] Moghadam, F.K., and Nejad, A.R., 2019. Evaluation of PMSG-based drivetrain

technologies for 10 MW floating offshore wind turbines: pros and cons in a life-cycle perspective. *Accepted by Wind Energy*.

[12] Nejad, A.R., Bachynski, E.E. and Moan, T., 2019. Effect of axial acceleration on drivetrain responses in a spar-type floating wind turbine. *Journal of Offshore Mechanics and Arctic Engineering*, 141(3).

[13] Lissenden, C.J., Tissot, S.P., Trethewey, M.W. and Maynard, K.P., 2007. Torsion response of a cracked stainless steel shaft. *Fatigue and fracture of engineering materials and structures*, 30(8), pp.734-747.

[14] Morio, J., 2011. Global and local sensitivity analysis methods for a physical system. *European Journal of Physics*. 32. 1577.

[15] Saltelli, A., Tarantola, S. and Chan, K.S., 1999. A quantitative model-independent method for global sensitivity analysis of model output. *Technometrics*, 41(1), pp.39-56.

[16] Licari, J., Ugalde-Loo, C.E., Ekanayake, J.B. and Jenkins, N., 2012. Damping of torsional vibrations in a variable-speed wind turbine. *IEEE Transactions on Energy Conversion*, 28(1), pp.172-180.

A.4 Paper 4

Paper 4:
Theoretical and experimental study of wind turbine drivetrain fault diagnosis by using torsional vibrations and modal estimation.
Authors: Farid Khazaeli Moghadam, Amir Rasekhi Nejad
Under review at Elsevier Journal of Sound and Vibration.

Theoretical and experimental study of wind turbine drivetrain fault diagnosis by using torsional vibrations and modal estimation

Farid K. Moghadam and Amir R. Nejad

Department of Marine Technology, Norwegian University of Science and Technology, Trondheim, Norway

Abstract

This paper provides an analytical proof and the theoretical development of the idea of using the torsional vibration measurements for a system-level condition monitoring of the drivetrain system. The developed drivetrain condition monitoring approach based on torsional measurements error function is tested by using a $10MW$ geared wind turbine drivetrain simulation model embedded on a floating platform, and experimentally validated by the drivetrain operational measurements obtained from a $1.75MW$ turbine. The method relies on modal estimation of the drivetrain system by using the torsional measurements and subsequent monitoring of the variations in the system eigenfrequencies and normal modes. In the proposed condition monitoring approach, it is shown that any abnormal deviation from the reference values of the drivetrain system dynamic properties can be translated into the progression of a specific fault in the system. In order to extract the condition monitoring features, local sensitivity analysis is engaged to establish a relationship between different categories of drivetrain faults with the system dynamic properties and the amplitude of torsional response, which helps with both to identify the state of the progressive faults and to localize them. Sensitivity analysis is also employed along with the estimated torsional modes for estimation of damping coefficients from the amplitude of response at the natural frequencies and their subsequent use for estimation of undamped natural frequencies which are later used in the proposed condition monitoring approach.

Keywords: drivetrain system, torsional measurements, modal estimation, fault detection, sensitivity analysis, floating wind turbines

1. Introduction

Both predictive and condition-based maintenances are proposed in the literature as potential game changers and measures which could be taken to flatten the gap between OPEX in offshore and land-based wind turbines aimed at realizing the EU 2050 plan by reduction of downtime and subsequently levelized cost of energy (LCOE) of offshore wind [1]. The motivation of this research is reducing the costly operation and maintenance of offshore turbines - more specifically the drivetrain system of floating offshore wind turbines - and improving the risk of investment by using condition-based maintenance and a subsequent reduction in downtime as one of the most influential consequences of drivetrain failures. The latter is investigated based on developing the methods which can use only the existing sensors, database, communication network and can be implemented for both online and offline monitoring purposes. The condition monitoring system is in addition to the performance monitoring, and the concept behind is monitoring

of the conditions of the turbine systems with the highest risk of loss of turbine availability considering both likelihood and consequence of failures, because monitoring the condition of all systems may be economically and technologically infeasible. According to the study by Pfaffel *et al.* [2] which provides a cautious comparison on reliability characteristics of both onshore and offshore wind turbines, drivetrain system which in general includes all rotating components in power conversion system *i.e.* hub, rotor, main bearings, gearbox, generator and power converter accounts for 57% of turbine total failures and 65% of turbine total downtime. These numbers are expected to be higher in floating offshore turbines. The latter is due to more costly marine operations specially in deep waters, the larger and more expensive components, and a wider range of excitation sources due to the synergistic impacts of waves, currents and wind turbulences which call for innovative approaches to achieve a better understanding about the system dynamics and excitation sources. The focus of this research is proposing a system-level drivetrain condition monitoring (CM) solution by the drivetrain modal estimation and a subsequent monitoring of abnormal variations of system modes. This goal is performed by developing a numerical model of the drivetrain as a dynamic system based on its measured torsional response and the subsequent estimation of the drivetrain torsional modes. In contrast with the other systems (*e.g.* bridges and buildings), the dynamic properties of the drivetrain do not experience a significant change over normal operations. The latter can be used to monitor any abnormality caused by faults. Therefore, variations in the drivetrain can be monitored by tracking the changes in the modal parameters (resonance frequencies, damping ratios, and normal modes(both amplitude and phase)) of the dominant modes of this system [3]. Estimation of mechanical systems dynamical characteristics is mainly based on operational modal analysis (OMA) which is challenging for drivetrain as a complex dynamical system. The latter is mainly based on translational vibration measurements [4], and the reported results in the literature show the high possibility of harmonics to be mistaken with the eigenfrequencies [3; 5]. Drivetrain is a complex rotational system with different sources of external excitation and components defect frequencies. The uncertainties in the estimated modes have made OMA technique less-efficient for condition-based maintenance.

The current condition monitoring approaches of the wind turbine drivetrain are based on one or a combination of five categories of techniques, namely vibration analysis [6], electrical signature (current and power signals) [7], acoustic emissions analysis [8], thermography [9] and temperature analysis [10], and analysis of oil particles [11]. Today, vibration analysis is mainly based on system translational responses obtained by accelerometers (*e.g.* see [12]) with a minor attention to torsional measurements. The only commercially available drivetrain condition monitoring based on torsional measurements is associated with the measurement of torque as the system applied load [13]. The latter is not widely used due to the matter of cost, technological limitations related to operating speed and torque ranges and shafts dimensions, intrusive nature of the torque measurement techniques, and also a lack of a standardized approach and the immature and insufficient knowledge to analyze and extract features from the torsional measurements.

Frequency response function (FRF) is a common tool which is used for modal estimation by the estimation of a system transfer function. However, the complexity of the drivetrain system and inadequacy of models in considering the internal dynamics and interactions between systems, nonlinear and synergistic impacts of different excitation sources, uncertainties in estimation of loads are some reasons which cause inexplicable harmonics and limit the application of FRF for the estimation of drivetrain dynamic properties. In this work, the modal estimation

and fault detection are based on the system torsional responses. An anterior estimation of the drivetrain loads can provide more options to the proposed algorithm. The possibility of observing drivetrain torsional natural frequencies in the torsional response is reported in [14] for different applications such as jet engine high-pressure disk, a hydro station turbine and a coal-fired power plant. The possibility of observing blade natural frequencies in drivetrain shaft torsional response and the potentials for condition monitoring of the blades is also reported in [14; 15]. Suominen *et al.* [16] has reported the visibility of ship propulsion system natural frequencies in the torque measurements of the propulsion shaft due to the propeller blade contact with ice. However, these reports are based on observations on experimental studies and are not reliant on an analytical torsional model of the drivetrain systems.

The drivetrain system torsional response and the natural frequencies are proposed in the literature for detecting faults initiated by torsional sources. Patel *et al.* [17] proposes the use of angular displacement to support the lateral response to recognise the rubbing faults in the drivetrain, so that the excited torsional frequency and the amplitude of response in the natural frequency and the side bands are utilized to characterize the fault. Feng *et al.* [18] proposes the use of the measurements of torque instead of transverse vibration signals to diagnose planetary gearbox local/distributed faults, because they are free from the amplitude modulation effect caused by time variant vibration transfer paths, thus they have simpler spectral content than transverse signals. Lebold *et al.* [19] suggests monitoring the characteristic changes in torsional natural frequencies, and claims that those changes are associated with the shaft crack propagation. Kia *et al.* [20] proposes the estimated electromagnetic torque of the electrical machine as a noninvasive torsional measurement in the drivetrain to monitor the torsional stress on the components including shaft, bearings, and gearbox, and the method is used to detect a gear failure. The electromagnetic torque estimation is commonly used in electrical drives to control the electrical machine, and implementation of the method does not need any additional sensor. Not only the drivetrain faults, but also rotor and tower excited modes may result in frequency components in the drivetrain torsional response [21]. The amplitude of response at blade edgewise and tower bending natural frequencies can provide insights about resonances in these components. The monitoring of the variations of these components frequencies is also useful for some other purposes such as ice detection in blades, and health monitoring of blades (detect root cracks within turbine blades) and tower. The idea of using angular velocity measurements for the wind turbine drivetrain fault detection was originally proposed by Nejad *et al.* [22]. The input data is provided by the encoders installed on the drivetrain for the turbine control purposes. The latter is normally accessible in both turbine and farm levels, which helps to realize condition monitoring by means of supervisory control and data acquisition (SCADA) system available measurements. Therefore, any algorithm based on those measurements can be integrated into either turbine or farm control to support the online condition monitoring of the drivetrain. Moghadam *et al.* [15] has experimentally evaluated the possibility of detecting some categories of faults in early stages by a direct utilization of torsional response, and the results of the study are compared to a conventional method based on translational vibrations obtained by accelerometers. The authors demonstrated how torsional measurements can complement the conventional approaches by providing insights on the excitation sources which are significantly influencing on the drivetrain lifetime which is useful as both a design feedback and earlier stage fault detection.

Even though the torsional response cannot directly be used for monitoring of some sort of faults, it contains the drivetrain system-level dynamic properties which can provide a near real-time

modal estimation of system. From this perspective, torsional measurements are indirectly used for the drivetrain system condition monitoring purposes. For this purpose, these measurements are first used to estimate the dynamic properties of the drivetrain as a rotational system. These properties are only related to the system physical parameters and not the loading or specific operational condition, so that they can be used in the second step to monitor the variations in the drivetrain, which can be translated into a fault in case of passing a prespecified level. Moghadam *et al.* [23] has started an analytical approach to turn torsional measurements into meaningful features for fault detection purposes by specification of the analytical relationship between the system natural frequency variations and faults, and a subsequent potential for detection of system faults. The current work is dedicated to the theoretical development and simulation/experimental validation of the idea originally proposed by [23] for the modal estimation of the drivetrain by using torsional measurements, and a subsequent use of this idea to develop a method for the drivetrain system-level condition monitoring. The influence of shaft crack propagation on the torsional natural frequency was discovered by [14; 24]. However, those studies lack an analytical model which describes the variations in order to establish a meaningful feature for monitoring the condition of crack. For this feature to be used as a criterion as a shaft cracking monitoring technique, a sufficient model should be provided to be able to relate the variations to the state of the fault. In addition, there are other categories of system-level faults which can also influence drivetrain torsional modes which are not considered in earlier studies.

The condition monitoring of the drivetrain at system level by using the estimated torsional natural frequencies, the normal modes, the amplitude of response in the natural frequencies and the damping of the system at natural frequencies in different operations is discussed in this paper. For this purpose, online operational measurements of the drivetrain different torsional responses including the angular velocity residual function and filtered angular velocity are employed. Drivetrain faults at system level can influence the drivetrain model parameters, so that they can be categorized into the faults that change the torsional stiffness most (*e.g.* crack in the shafts and bearing wear specially in gearbox), and faults that change mostly the inertia of the drivetrain (changes in mass balance/distrinution which can be due to *e.g.* loss of mass, wear and unbalance; and also change in the axis of rotation which can be due to *e.g.* misalignment and looseness). Regarding the relation of inertia with the square of the center of mass distance from the center of rotation, the faults which variate the center of rotation demonstrate more significant influence on the inertia and thus are more influential on the torsional dynamic properties. Among the faults that influence the inertia of the bodies in drivetrain equivalent model, there are some types which have more considerable impact on the boundary conditions between rotating and stationary elements and thus influence more drivetrain lateral responses than the torsional response (*e.g.* looseness (pedestal, shaft and bearings, coupling), [25]). The latter influences significantly lateral stiffness parameters and the lateral responses of the drivetrain, so that the detection of those faults by using the lateral response and monitoring the variations of system lateral properties could be a practical approach. Even though these faults can cause a small variation of the torsional parameters, the impact may not be significant enough for fault detection purposes. For example, a pedestal looseness may cause increased rubbing which leads to a nonlinear small increase of torsional stiffness.

By specification of the parameter in the equivalent reduced order model which will be significantly influenced by a fault, it is possible to look for the expected consequences of the associated variations of the parameter as a result of fault on the system dynamic properties,

as the condition monitoring indicators. The *first category* of faults, which are detectable by the proposed CM approach, influence the torsional stiffness. Cracks in the drivetrain shafts are one of the most influential faults in this category. The initial cracks occur due to material imperfections and temperature variations in the parts of main shaft with severe stress concentration, which can grow worse under large alternating loads due to wind turbulence. To detect the shaft cracks of different relative depths, an approach based on nonlinear output FRF is proposed by [26] and experimentally tested on a simple double-disk rotor system, where the linear displacements and the bending moments are the under consideration responses but the torsional vibrations are neglected. In shaft crack faults, variation in stiffness is influenced by the crack depth and the shape of the crack front. The latter makes the detection of different types of cracks quite challenging so that a detection method suitable for one type of crack cannot be generalized to the other types. This fault does not take place as frequently as shaft unbalance or misalignment but the consequences are very high, so that the detection in very early stages is of a high importance. If shaft cracks are not detected in early stages, the later stages of this category of faults may cause severe damage of the shaft and the occurrence of considerable secondary faults with high risk of injuries for the plant personnel. As discussed by Chatterton *et al.* [27], crack detection by using translational/axial vibrations obtained from accelerometers is challenging due to the influence of the dynamic effects caused by different components and their consequent induced vibrations. The interpretation of the data in these methods is also dependent on a deep understanding of the type of crack, its physical properties and the specific operational conditions so that the realization of an online monitoring may not be possible. The frequency and time domains analysis of accelerometers is the conventional approach to detect increased vibrations in the component-level in higher stages of a progressive fault (*e.g.* gear tooth and rolling element bearing fatigue issues). The *second category* of faults detectable by the proposed approach influence the inertia of the components in the equivalent model. In this group, misalignment and unbalance are significantly more common than the other faults. Unbalance in the rotor blades is one of the most influential and prevalent faults which can be due to different reasons *e.g.* excessive weight following a blade repair, icing, water penetration through cracks and loose material moving inside the blades. The latter causes loss in the power production. The reason for placing an emphasis on the rotor unbalance is that the highest unbalance in the drivetrain arises from the component with the highest moment of inertia which is the rotor assembly in the wind turbine drivetrain. The mass unbalance also causes additional loads on the entire structure and specially the drivetrain components so that it results in a periodic torsional (in earlier stages) and transversal (in later stages) oscillations in the wind turbine's drivetrain. It directly increases the wear of the blade on the drivetrain bearings and gears by generating asymmetrical loads. The rotor mass unbalance can be measured by monitoring its consequent variations in the drivetrain dynamic properties. As a prognostic measure, the unbalance mass can be estimated and if the detected unbalance exceeds a limit, the rotor blades should be balanced with a balancing device.

Condition monitoring is mostly designed in component level, which is helping when the fault is propagated to the individual components and causes physical changes in the component level. However, the root cause of a wide range of faults are system-level issues such as unbalance, misalignment, looseness and shaft cracks. In the proposed drivetrain CM approach of this paper, it is assumed that system-level drivetrain faults (*e.g.* shaft cracks and unbalance) can reveal themselves by variations in the system stiffness and moment of inertia. Therefore, by monitoring the consequences of variations of drivetrain parameters (*i.e.* stiffness and moment of inertia matrices) in change of the drivetrain dynamic properties (*i.e.* natural frequencies,

mode shapes and damping coefficients), it is possible to monitor the progress of faults. For this purpose, an analytical model of the drivetrain which represents the relationship between the system parameters and dynamic properties and a subsequent sensitivity analysis helps to realize what are the most influential system parameters/faults which can variate the drivetrain dynamic properties. *In the feature selection algorithm*, the torsional dynamical model of the drivetrain and the local sensitivity analysis are engaged. The algorithm is designed to an extent that could offer robust, fast and accurate online monitoring.

The main focus of this work are on geared drivetrain systems used for wind turbines. Based on the theoretical studies in this research work, a 3-DOF equivalent torsional model of the geared drivetrain is sufficient for detection of the drivetrain faults at a system-level, because system-level faults represent themselves mainly by changing the torsional stiffness and the moment of inertia parameters of the 3-DOF equivalent model. In the first step of the work, the proposed modal estimation approach by using the torsional measurements is presented, which is proved in the general case for a n-DOF torsional model of the drivetrain, followed by a detailed parametric proof based on 3-DOF model. As the second step of this research, the analytical relationship between the 3-DOF equivalent model parameters and drivetrain dynamic properties is established, which helps to identify the drivetrain system condition/state-of-operation by monitoring the variations in the drivetrain dynamic properties (undamped natural frequencies and normal modes) which can be estimated from the operational measurements by using the proposed modal estimation approach or the other approaches proposed by the literature. The other reason for sticking to 3-DOF model, is that the closed form parametric expressions of the drivetrain dynamic properties as a function of equivalent model parameters can be obtained for this simplified model. Those expressions are the required inputs for the proposed fault detection approach based on monitoring the variations of the drivetrain dynamic properties. Those expressions provide quantifiable fault detection features, which are implementable in microcontrollers and can be integrated with turbine fully automated control and monitoring systems. By the increase of the order of equivalent model, more dynamic properties (higher natural frequencies which are not seen by 3-DOF model) can be employed, which can support a more detailed fault detection in the drivetrain. However, it is a little challenging for currently available modal estimation approaches to observe higher modes which appear with a low amplitude in the frequency-domain response. In other words, the real conditions for the modal estimation problem is restrictive, so that the higher eigenfrequencies of the drivetrain system, which are excited by the input torque with a low energy, may not be observable.

The proposed method in this paper can detect stiffness or inertia related faults by monitoring the consequences of faults on online estimated modes and amplitude of response. The method is computationally inexpensive since it relies on only few data samples and a moderate data resolution and sampling frequency. On this basis, the main contributions of this work are:

1. Analytical proof of a drivetrain modal estimation approach by using torsional measurements,
2. Introducing an analytical approach for estimation of damping coefficients of the system modes by analyzing the amplitude of torsional response error function at the natural frequencies,
3. Theoretical development and simulation/experimental validation of a drivetrain system-level fault diagnosis approach based on estimated modal parameters, and comparison with other methods in the literature.

The paper is organized as follows: Modal estimation by using torsional measurements is analytically elaborated in Section 2. An analytical approach for drivetrain condition monitoring by using torsional response and the estimated modes is proposed and discussed in details in Section 3. The proposed drivetrain modal estimation and condition monitoring approach are validated and compared with the approaches in the literature through simulation/experimental studies in Section 4. The paper is concluded in Section 5.

2. Modal estimation by using torsional measurements

2.1. Torsional natural frequency estimation theory

Drivetrain is often modelled as one-degree-of-freedom (1-DOF) rotational system in global dynamic response tools. The forced torsional vibration response of the equivalent 1-DOF damped rotational model of drivetrain influenced by the random excitation $\tau(t)$ in frequency domain and non-dimensional form can be expressed by

$$|\theta(\Omega)| = \frac{\frac{|\tau(\Omega)|}{k_t}}{\sqrt{(1-(\frac{\Omega}{\Omega_n})^2)^2 + (2\zeta_t^{\omega}(\frac{\Omega}{\Omega_n}))^2}}, \tag{1}$$

where $\theta(\Omega)$ and $\tau(\Omega)$ are the Fourier transforms of angular position and the excitation torque, respectively. Ω_n is the undamped torsional natural frequency of the system, k_t is the torsional stiffness of the shaft, and ζ_t is the torsional damping coefficient of the mode Ω_n at the operating speed ω. As it can be seen, an amplified frequency in the drivetrain torsional response can be due to a significant excitation amplitude or the vicinity of excitation frequency with natural frequencies.

Natural frequencies appear in torsional responses *e.g.* angular velocity measurements due to impulsive behavior of wind which excites those frequencies. An initial velocity applied on a system as described by Thomson *et al.*[28] can play a role as an impact which is able to excite the system torsional frequencies. In the wind turbine, the ceaseless variations of wind results in continual variations in angular velocity which is physically similar to an initial velocity applied to the system. Even though these variations in speed and subsequently torque happen in very low frequency, they can introduce considerable energy in different frequencies including the characteristic frequencies of the system. Due to the existence of damping in a real system, the measured natural frequencies from the torsional response are the damped frequencies. By filtering the shafts revolution frequencies, components defect frequencies and excitations (very low frequency due to wind, low frequency due to wave tower shadow effect, and high frequency due to generator), the drivetrain torsional natural frequencies, and some torsional induced motions due to excited edgewise rotor blade and tower bending modes are acquired. Based on a primary knowledge on the torsional frequencies for each power range, it is possible to separate the observed natural frequencies for drivetrain, blades and tower. The variations in the natural frequencies and normal modes can be used as criteria to identify some sorts of faults in the drivetrain. To estimate the damped natural frequencies, angular velocity residual/error function is proposed. The input of this method is provided by two encoders located at the high- and low-speed shafts of drivetrain, and subsequently the residual function is constructed based on the subtraction of these two signals. Some drivetrain systems are only equipped with one angular velocity measurement on the shaft, so that the implementation of the method may

require an additional moderate resolution encoder to provide the sufficient inputs. The angular velocity residual function e^{ω}_{tot} from the high-speed side is expressed by

$$e^{\omega}_{tot} = \omega_{HS} - a_1 a_2 a_3 \omega_{LS}, \tag{2}$$

where ω_{HS} and ω_{LS} are the rotational speed in rad/s obtained from the high- and low-speed encoders, respectively. a_1, a_2 and a_3 are the inverse of gear ratios of the gearbox stages. The error function main feature is cancellation of the impacts of the excitations which are transferred to the drivetrain from the housing, from the resultant torsional response. Angular displacement and acceleration are the other torsional responses of the drivetrain system which could theoretically be used similar to angular velocity to obtain the system torsional parameters. For this purpose, similar to e^{ω}_{tot}, the angular position error function e^{θ}_{tot} and the angular acceleration error function e^{α}_{tot} are defined by

$$e^{\theta}_{tot} = \theta_{HS} - a_1 a_2 a_3 \theta_{LS}, \quad e^{\alpha}_{tot} = \alpha_{HS} - a_1 a_2 a_3 \alpha_{LS}. \tag{3}$$

In particular, angular acceleration is the torsional response which has a direct relation with the applied, and contains useful information on how the applied torque interacts with the system. If acceleration or displacement is used for evaluation, the assessment criteria tends to vary with frequency, because the relation between them and velocity is proportional to frequency. The Fourier series of e^{ω}_{tot}, e^{α}_{tot} and e^{θ}_{tot} are defined by $e^{\omega}_{tot}(\Omega) = \sum_{n=-\infty}^{\infty} C_n e^{ik_n\Omega}$, $e^{\alpha}_{tot}(\Omega) = \sum_{n=-\infty}^{\infty} C_n (ik_n) e^{ik_n\Omega}$, $e^{\theta}_{tot}(\Omega) = \sum_{n=-\infty}^{\infty} C_n (ik_n)^{-1} e^{ik_n\Omega}$. Differentiation and integration are linear operations that are distributive over addition. As it can be seen, in e^{α}_{tot} compared to e^{ω}_{tot}, the amplitude of the frequency components higher than $1Hz$ is magnified with the gain k_n, and the frequencies lower than $1Hz$ are weakened with the same proportion. In e^{θ}_{tot} compared to e^{ω}_{tot}, the amplitude of the frequency components lower than $1Hz$ is magnified with the gain k_n^{-1}, and the frequencies higher than $1Hz$ are weakened with the same proportion. The 1^{st} natural frequency of the drivetrain systems of the same technology decreases as the rated power increases. However, even for $10MW$ wind turbine which is the biggest commercially available and even for the high-speed technologies which have lower first natural frequencies, the 1^{st} torsional frequency is higher than $1Hz$ [31]. Therefore, the angular acceleration error function is theoretically slightly better than the other two approaches in highlighting the torsional frequencies. The other benefit is weakening the frequencies lower than $1Hz$ which appear in the drivetrain torsional response mostly due to wind turbulence and structural motions, but do not contain any information on the drivetrain natural frequencies. However, an additional derivation operation is required to attain acceleration from the velocity measurements which increases the computational cost of this method.

A limitation with aforedescribed approach is the dependency on two encoders, because in several turbines there is only one encoder available located in the low speed shaft. As discussed earlier, one of the significant features of the error function is cancellation of the influences of structural motions from the torsional response. The latter results in a clean signal which is able to highlight the system characteristic frequencies. Those motions are mainly influenced by wind, wave and structural resonances, and natural frequencies of structural motions and low frequency interactions between rotor, tower and support structure and have a low frequency content.

Therefore, the filtered angular velocity of low speed shaft has some potentials in highlighting the drivetrain torsional frequencies. The filtered signal $X(\Omega_{HP})$ is extracted by

$$X(\Omega) = a_1 a_2 a_3 \omega_{LS}(\Omega), \quad X(\Omega_{HP}) = X(\Omega) H(\Omega_{HP}), \tag{4}$$

where $H(\Omega_{HP})$ is the transfer function of the high-pass filter applied to the low speed shaft encoder signal to attenuate the low frequency noises resulted wind induced low frequency motions. The performance of filtered angular velocity of low speed shaft in highlighting the torsional frequencies compared to the different torsional response error functions is tested with both simulation and operational measurements as reported in Section .

In order to capture better the drivetrain dynamics at system level for the subsequent use for drivetrain fault diagnosis at system level while minimizing the computational complexity of the model, 3-DOF torsional model is offered and the performance of the model is evaluated throughout the paper. For this purpose, to evaluate the observability of natural frequencies on the torsional response error functions and the subsequent application for drivetrain condition monitoring, a 3-DOF torsional model of the damped drivetrain is engaged. The 1^{st} and 2^{nd} undamped natural frequencies (nonrigid modes) based on 3-DOF lumped-mass-spring model of a geared drivetrain can be calculated by the equations reported in Appendix A. The eigenvectors of the damped drivetrain model take complex values. By assuming damping equal to zero, the normal modes take real values which show the relative angular motion of the different inertias in the model. The closed form of two normal modes related to the two non-rigid modes of the under consideration drivetrain model which are scaled to unity length are reported in Appendix A.

Both undamped frequencies and normal modes are unique for the system so that any deviation of the parameters can indicate variations in the drivetrain system which can be used for fault detection. The continued discussion is dedicated on an analytical proof of the idea of observing natural frequencies from the torsional response. The theory is first presented for the general form of response obtained from the general n-DOF torsional drivetrain model. Then the possibility of observing torsional modes in amplitude of angular velocity error function based on a 3-DOF model is mathematically proven to be used in the proposed model-based fault detection approach.

Theorem 1. *Torsional natural frequencies belong to the set of extreme points of the torsional response in the frequency domain.*

Proof. The general form of the discrete multi-DOF torsional model of drivetrain with n degrees of freedom in the time domain is defined by

$$\mathbf{J}\ddot{\theta} + \mathbf{C}\dot{\theta} + \mathbf{K}\theta = T(t), \tag{5}$$

where $\mathbf{J}$, $\mathbf{C}$ and $\mathbf{K}$ are the moment of inertia, damping and stiffness matrices with the size $n \times n$. θ and T are the response and load vectors with the size $n \times 1$, where each element of these two vectors represent a time series data. The representation in frequency domain by using the frequency variable S and Laplace transform will be

$$[\mathbf{J}S^2 + \mathbf{C}S + \mathbf{K}]_{n\times n}[\Theta(S)]_{n\times 1} = T(S)_{n\times 1}. \tag{6}$$

By replacing the characteristic equation $\mathbf{J}S^2+\mathbf{C}S+\mathbf{K}$ with $\mathbf{M}$, the frequency domain response $\Theta(S)$ will be

$$\Theta(S) = \frac{adj(\mathbf{M})}{det(\mathbf{M})}T(S), \tag{7}$$

where $adj(\mathbf{M})$ is the adjugate of $\mathbf{M}$ which is a polynomial function with the matrix variable $\mathbf{M}$. $det(\mathbf{M})$ is the determinant of the system characteristic equation. As it can be seen, the roots of the $det(\mathbf{M})$ are the extreme points of response $\Theta(S)$. However, the roots of the determinant of characteristic equation of a system are the system's eigenfrequencies. Therefore, the torsional natural frequencies of the system belong to the set of extreme points of the response. In the undamped system ($\mathbf{C} = \mathbf{0}$), the roots will be pure imaginary which represent the undamped natural frequencies Ω_n^i. In the general damped system, the roots are the damped natural frequencies Ω_d^i with the following relation with the undamped frequencies

$$\Omega_d^i = \zeta^i\Omega_n^i + j\Omega_n^i\sqrt{1-(\zeta^i)^2} \quad i \in 1,..,n. \tag{8}$$

The torsional natural frequencies in both cases of damped or undamped system based on the provided proof which refers to the general form of damped system are the extreme points of the response frequency domain function.

Thus, we complete the proof of Theorem 1.

The other extreme points of $\Theta(S)$ are due to the load dynamics, the system unmodelled internal dynamics and the interactions between these two. As discussed earlier, in order to pick out the natural frequencies, other harmonics which also demonstrate themselves as other extreme points in response must be filtered. For this purpose, the response error function is engaged which is able to filter the influences of the loads transferred to the drivetrain through the structure, which is very useful specially in offshore wind turbines equipped with floating support structures which can induce a wider range of harmonics in the drivetrain response.

The typical signal for frequency domain fault detection study is the amplitude of response. In the following part, the possibility of using the Theorem 1 results for the amplitude of torsional response and more specifically the amplitude of angular velocity error function is investigated. For this purpose, the general 3-DOF damped torsional model of the geared drivetrain system is selected, and the possibility of observing natural frequencies in the amplitude of angular velocity error function in the frequency domain is analytically evaluated.

The amplitude of angular positions at the different places of the drivetrain based on the equiv-

alent 3-DOF torsional model of drivetrain transferred to the rotor side are as

$$|\theta_r(\Omega)| = \sqrt{\frac{\Big\{(-\Omega^4 J_{gr}J_{gn} + \Omega^2(c_L c_H + \sqrt{G}) - k_L k_H)^2 + \Omega^2(\Omega^2\sqrt{E} - D)^2\Big\}|Tr(\Omega)|^2 + \Big\{(-\Omega^2 c_L c_H + k_L k_H)^2 + \Omega^2 D^2\Big\}|T_g(\Omega)|^2}{\Omega^4\Big(\Omega^4 J_r J_{gr} J_{gn} - \Omega^2 I + k_L k_H (J_r + J_{gr} + J_{gn})\Big)^2 + \Omega^6\Big(\Omega^2(J_r\sqrt{E} + c_L J_{gr} J_{gn}) - D(J_r + J_{gr} + J_{gn})\Big)^2}}, \tag{9a}$$

$$|\theta_{gr}(\Omega)| = \sqrt{\frac{\Big\{(-\Omega^2(c_L c_H + k_L J_{gn}) + k_L k_H)^2 + \Omega^2(\Omega^2 c_L J_{gn} - D)^2\Big\}|Tr(\Omega)|^2 + \Big\{(\Omega^2(c_L c_H + k_H J_r) - k_H k_L)^2 + \Omega^2(\Omega^2 c_H J_r - D)^2\Big\}|T_g(\Omega)|^2}{\Omega^4\Big(\Omega^4 J_r J_{gr} J_{gn} - \Omega^2 I + k_L k_H (J_r + J_{gr} + J_{gn})\Big)^2 + \Omega^6\Big(\Omega^2(J_r\sqrt{E} + c_L J_{gr} J_{gn}) - D(J_r + J_{gr} + J_{gn})\Big)^2}}, \tag{9b}$$

$$|\theta_{gn}(\Omega)| = \sqrt{\frac{\Big\{(-\Omega^2 c_L c_H + k_L k_H)^2 + \Omega^2 D^2\Big\}|Tr(\Omega)|^2 + \Big\{(-\Omega^4 J_r J_{gr} + \Omega^2(c_L c_H + \sqrt{H}) - k_L k_H)^2 + \Omega^2(\Omega^2\sqrt{F} - D)^2\Big\}|T_g(\Omega)|^2}{\Omega^4\Big(\Omega^4 J_r J_{gr} J_{gn} - \Omega^2 I + k_L k_H (J_r + J_{gr} + J_{gn})\Big)^2 + \Omega^6\Big(\Omega^2(J_r\sqrt{E} + c_L J_{gr} J_{gn}) - D(J_r + J_{gr} + J_{gn})\Big)^2}}, \tag{9c}$$

where

$D = c_L k_H + c_H k_L$, $E = (c_L J_{gn} + c_H J_{gr} + c_H J_{gn})^2$, $F = (c_L J_r + c_L J_{gr} + c_H J_r)^2$, $G = (J_{gr}k_H + J_{gn}k_L + J_{gn}k_H)^2$, $H = (J_r k_L + J_r k_H + J_{gr}k_L)^2$ and $I = c_L c_H J_r + c_L c_H J_{gr} + c_L c_H J_{gn} + J_r J_{gr} k_H + J_r J_{gn} k_L + J_r J_{gn} k_H + J_{gr} J_{gn} k_L$.

$\theta_r(\Omega)$, $\theta_{gr}(\Omega)$ and $\theta_{gn}(\Omega)$ are the angular positions at rotor, gearbox and generator, respectively. c_L and c_H are the actual damping of low- and high-speed shafts.

The amplitude of angular velocity error function in the general form by using the Laplace operator S can be defined as a function of angular positions as follows

$$|e^{\omega}_{tot}(S)| = |S(\theta_r(S) - \theta_{gn}(S))|. \tag{10}$$

By replacing the angular positions in eq. (10), the result will be

$$|e^{\omega}_{tot}(S)| = \sqrt{\frac{(A_1^2|S|^6 + A_2^2|S|^4 + A_3^2|S|^2)|T_r(S)|^2 + (A_4^2|S|^6 + A_5^2|S|^4 + A_6^2|S|^2)|T_g(S)|^2}{A_7^2|S|^8 + A_8^2|S|^6 + A_9^2|S|^4 + A_{10}^2|S|^2 + A_{11}^2}}, \tag{11}$$

where

$A_1 = J_{gr}J_{gn}$, $A_2 = c_L J_{gn} + c_H J_{gr} + c_H J_{gn}$, $A_3 = J_{gr}k_H + J_{gn}k_L + J_{gn}k_H$, $A_4 = J_r J_{gr}$, $A_5 = c_L J_r + c_L J_{gr} + c_H J_r$, $A_6 = J_r k_L + J_r k_H + J_{gr}k_L$, $A_7 = J_r J_{gr} J_{gn}$, $A_8 = c_L J_r J_{gn} + c_H J_r J_{gr} + c_L J_{gr} J_{gn} + c_H J_r J_{gn}$, $A_9 = c_L c_H J_r + c_L c_H J_{gr} + c_L c_H J_{gn} + J_r J_{gr} k_H + J_r J_{gn} k_L + J_r J_{gn} k_H + J_{gr} J_{gn} k_L$, $A_{10} = c_L J_r k_H + c_H J_r k_L + c_L J_{gr} k_H + c_H J_{gr} k_L + c_L J_{gn} k_H + c_H J_{gn} k_L$, $A_{11} = J_r k_L k_H + J_{gr} k_L k_H + J_{gn} k_L k_H$.

The denominator of angular velocity error function $e^{\omega}_{tot}(S)$ based on the described model finds the form as

$$D(e^{\omega}_{tot}(S)) = (A_7S^4 + A_8S^3 + A_9S^2 + A_{10}S + A_{11})S^2. \tag{12}$$

The roots of the above function are the poles of $e^{\omega}_{tot}(S)$ which belong to the set of extreme points of the response. By replacing $S = j\Omega$ for the equivalent undamped system, $D(e^{\omega}_{tot}(\Omega))$ will find the form of a complex equation. To find the roots of the resulted complex equation, the absolute value of this equation is set to be zero which turns to the following polynomial equation

$$(A_7\Omega^6 - A_9\Omega^4 + A_{11}\Omega^2)^2 + (A_{10}\Omega^3 - A_8\Omega^5)^2 = 0. \tag{13}$$

The above equation can be reduced to a polynomial of the order of four by the change of variable $\gamma = \Omega^2$ and eliminating the rigid modes ($\Omega = 0$), which makes it possible to find the closed form solutions of the response poles. The resulted equation is

$$A_7^2\gamma^4 + (A_8^2 - 2A_7A_9)\gamma^3 + (A_9^2 + 2A_7A_{11} - 2A_8A_{10})\gamma^2 + (A_{10}^2 - 2A_9A_{11})\gamma + A_{11}^2 = 0. \tag{14}$$

By assuming damping equal to zero, and considering the positiveness of γ, the two acceptable answers are obtained. The results give four values for Ω which belong to the extreme points of response. The results are two pairs of imaginary poles which the absolute value of each pair coincides with one of the system torsional eigenfrequencies described by eq. (A.1).

The results can be extended to the damped system so that also in the damped system the poles of the response coincide with the eigenfrequencies of the system, where the poles take the complex form $S = \sigma + j\omega_d = \zeta\Omega_n + j\Omega_n\sqrt{1-(\zeta)^2}$. However, the absolute value of the poles will still be $|S| = \Omega_n$. By replacing Ω_n from eq. (A.1) instead of $|S|$ in eq. (11), the amplitude of response at the two natural frequencies in the general case of a damped system has the relationship with the system parameters and loads as

$$|e^{\omega}_{tot}(\Omega_1^{tor})| = \frac{\sqrt{|T_g(\omega 1)|^2\sqrt{FA + H + J_r^2J_{gr}^2A^2}\sqrt{A} + |T_r(\omega 1)|^2\sqrt{EA + G + J_{gr}^2J_{gn}^2A^2}\sqrt{A}}}{\sqrt[4]{A^2I^2 + (J_r\sqrt{E} + c_LJ_{gr}J_{gn})^2A^3 + D^2(J_r + J_{gr} + J_{gn})^2A + k_L^2k_H^2(J_r + J_{gr} + J_{gn})^2 + J_r^2J_{gr}^2J_{gn}^2A^4}}, \tag{15a}$$

$$|e^{\omega}_{tot}(\Omega_2^{tor})| = \frac{\sqrt{|T_g(\omega 2)|^2\sqrt{FB + H + J_r^2J_{gr}^2B^2}\sqrt{B} + |T_r(\omega 2)|^2\sqrt{EB + G + J_{gr}^2J_{gn}^2B^2}\sqrt{B}}}{\sqrt[4]{B^2I^2 + B^3(J_r\sqrt{E} + c_LJ_{gr}J_{gn})^2 + k_L^2k_H^2(J_r + J_{gr} + J_{gn})^2 + D^2(J_r + J_{gr} + J_{gn})^2B + J_r^2J_{gr}^2J_{gn}^2B^4}}, \tag{15b}$$

The frequency domain angular velocity error function of a theoretically undamped system under excitation at natural frequencies is unbounded. Therefore, performing a sensitivity analysis to find the relation between the variations of the amplitude of response at natural frequencies and the variations of system parameters which can represent the system faults is not possible.

However, a physical system in practice has damping. The response of a damped system at natural frequencies is bounded due to the influence of damping in the system. Therefore, monitoring the variations of the amplitude of response in the natural frequencies can be related to variations of the system parameters and faults. In the continued part, the possibility of using the amplitude of response of a damped system at natural frequencies for monitoring the variations in the system is discussed. The results of this study can also be used for estimation of damping in the system.

As it can be seen from eq. (15), in difference with the equations for the system natural frequencies and mode shapes, the amplitude of response at the first and second natural frequencies is proportional to not only the system parameters but also the loads. The latter limits the application of amplitude of response as a fault precursor. However, it can be used as a criterion to evaluate the results obtained by the proposed fault detection algorithm, so that it provides inputs for drivetrain condition monitoring based on monitoring the variations of amplitude of response at the natural frequencies in terms of variations in the system parameters by sensitivity analysis which is elaborated in Section 3. The results of analysis of amplitude of response also provides necessary inputs for the estimation of damping in the system.

By using the simplified model in eq. (1), the peak frequencies of the amplitude of response have the relation $\Omega_{peak} = \Omega_n\sqrt{1-2\zeta^2}$ with the associated undamped frequency. This result can be extended to the higher order systems and higher order natural frequencies. Our analytical study on the extreme points of the amplitude of response in higher order models shows that these points are highly nonlinear and complicated functions of system parameters which make the utilization of these equations computationally expensive. However, these points can be related to the undamped natural frequencies by using the damping coefficients as

$$\Omega^i_{peak} = \Omega^i_n\sqrt{1-2\zeta_i^2}. \tag{16}$$

The two following equations can be used to estimate the damping coefficients of different modes at different operating speeds, by using the peak frequencies and the amplitude of response at those frequencies, as follows:

$$\frac{\Omega^{i,t_1}_{peak}}{\Omega^{i,t_2}_{peak}} = \sqrt{\frac{1-2\zeta^2_{i,t_1}}{1-2\zeta^2_{i,t_2}}}, \tag{17a}$$

$$\frac{|e^{\omega}_{tot}(\Omega^{i,t_1}_{peak})|}{|e^{\omega}_{tot}(\Omega^{i,t_2}_{peak})|} = f(T_r, T_g, c_L, c_H, k_L, k_H, J_r, J_{gr}, J_{gn}), \tag{17b}$$

where $\zeta_{i,t}$ is the damping coefficient related to the mode i and operation t. $|e^{\omega}_{tot}(\Omega_{peak})|$ is the amplitude of response at the peak frequency. Both the peak frequency and amplitude of response at peak frequency are estimated from the frequency domain response based on the theory elaborated earlier in this Section. The eq. (17b) is long and nonlinear with dependency to all the system parameters and loads so that relating the variations in the amplitude of response to variations in damping coefficient seems to be a challenging task. The theory related to the employment of sensitivity analysis for relating the ratio of amplitude of response to the ratio of

damping coefficients from eq. (17) and the implementation of this approach will be discussed in the continued Sections. From the peak frequency and the approximated damping coefficient, the undamped frequency can be estimated by using eq. (16).

3. Drivetrain condition monitoring by using torsional measurements

The estimation of system modes by using the angular velocity error function was elaborated in Section 2. As discussed earlier, the estimated modes and the amplitude of response at those frequencies can be related to the system parameters and faults. In order to establish this relationship to be used in the proposed fault detection approach, sensitivity analysis is employed.

3.1. Sensitivity analysis

This part is aimed to obtain the closed form mathematical relationships between the drivetrain dynamic properties and amplitude of response with the drivetrain reduced-order model parameters through a sensitivity analysis for a subsequent use in the proposed fault diagnosis algorithm. Similar to in Section 2, the general 3-DOF damped torsional model of drivetrain is selected for the analytical studies in this Section.

As discussed earlier, faults like crack in shafts and rotor, coupling damage, or damage in gearbox are examples of potential faults which can change the drivetrain stiffness. For example, a shaft crack results in reduction of the torsional stiffness of the shaft [29]. A change in the stiffness influences the drivetrain system frequency modes. Therefore, by obtaining the mathematical relationship between the stiffness of different shafts and the system modes, it is possible to monitor their conditions by monitoring the variations in the system natural frequencies and normal modes. The other parameter which can influence the drivetrain torsional modes is the moment of inertia of the drivetrain components. Variations in the moment of inertia matrix represents the other category of faults in the driveline with the unbalance and loss of mass as the foremost. For example, unbalance faults are characterized by the increase of moment of inertia due to an additional force that is generated during those conditions based on the parallel axis theorem. The mathematical relationship between the drivetrain torsional natural frequencies and the moment of inertia of components can help to identify these faults. The variations in stiffness and inertia can result in similar natural frequency variation patterns. Therefore, to distinguish between variations in the natural frequencies because of variations in the shafts' stiffness with those due to variations in moment of inertia matrix (source of fault), determining the correlation between the system parameters and the normalized mode shapes can provide a useful direction to find the source of fault. The correlation between the amplitude of response at the system natural frequencies can also be useful in two ways: first, to estimate the damping coefficients and subsequently the undamped natural frequencies from the estimated natural frequencies; second, to confirm or repeal the results obtained about the system faults taken based on the analysis of natural frequencies and normal modes.

In order to achieve the above described purposes, two different sets of sensitivity analyses are performed in this Section. First, a sensitivity analysis on torsional frequencies and normal modes of the equivalent undamped system to extract drivetrain system-level condition monitoring features. Second, a sensitivity analysis on the amplitude of response at the natural frequencies primarily to estimate the damping coefficient and subsequently the undamped natural frequencies which are required for the first analysis, and then to support the condition monitoring features obtained in the first sensitivity analysis.

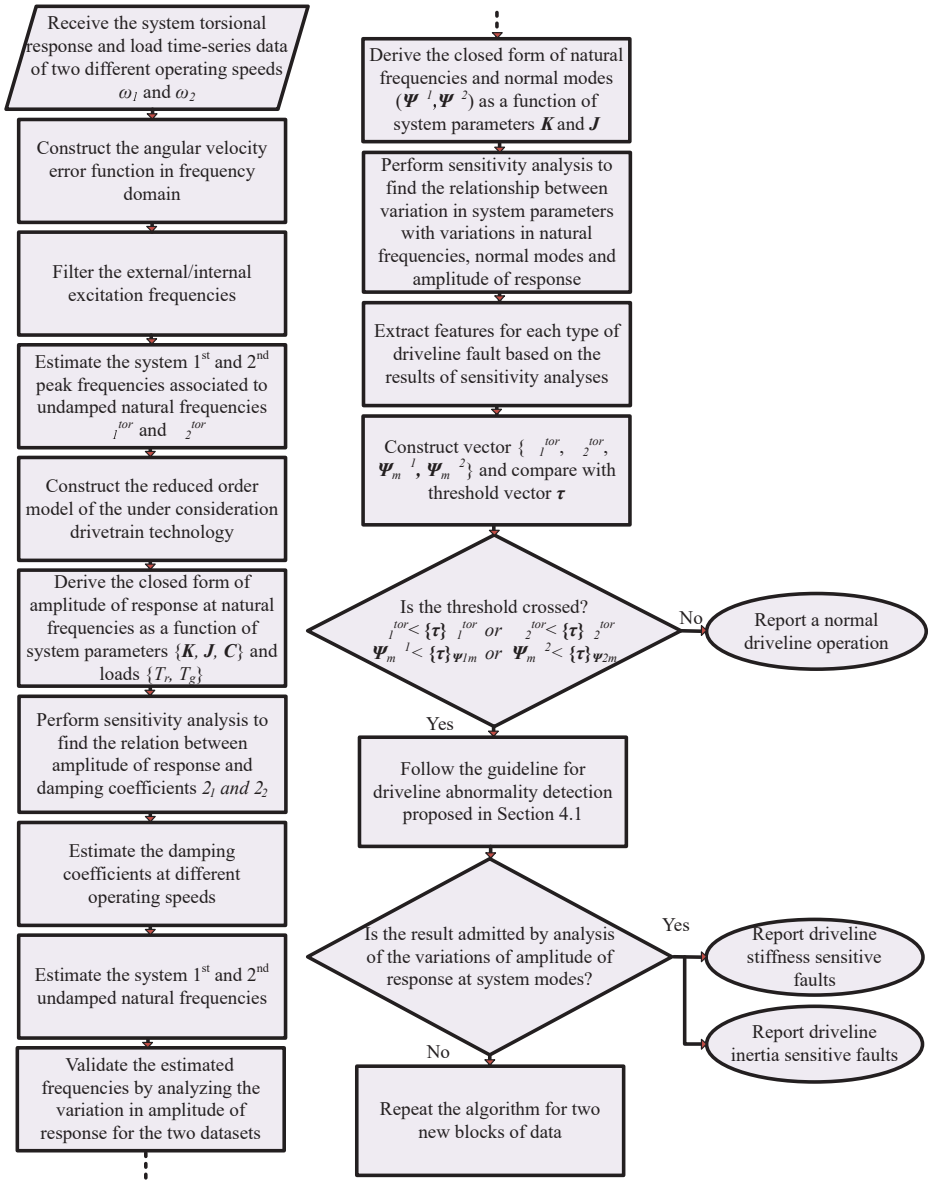

Figure 1: Proposed algorithm for driveline condition monitoring by using torsional measurements and estimated modes.

In order to check how the variations in stiffness and moment of inertia influence the system torsional natural frequencies and mode shapes, a sensitivity analysis is performed. There are two classes of sensitivity analysis methods, namely local and global sensitivity analysis. Morio *et al.*[30] has reported the same kind of results by using these two method for simple models. Local sensitivity determines how a small perturbation near an input parameter value influences the value of the output. In this Section, in order to find the parameters with the greatest impact on the drivetrain dynamic characteristics, local sensitivity analysis is employed due to two main reasons. First, the motivation of this work is detecting faults in early stages for predictive maintenance purposes so that variations in the drivetrain system parameters happen with a slight change around the set point values. Second, local sensitivity analysis derives a closed form expression for the sensitivity value which makes the result more reliable and easier to implement. Local sensitivity is defined as the partial derivative of the output function with respect to the input parameters [32] as

$$S_{k,l}^{Loc} = \frac{\delta y_k}{\delta x_l},\ y_k \in \{y_1, ..., y_p\}\ and\ x_l \in \{x_1, ..., x_q\}, \tag{18}$$

where y_k is the k^{th} output and x_l is the l^{th} input. To neutralize the impact of large/small inputs and small/large outputs, the local sensitivity can be normalized by the nominal values of inputs and outputs by

$$S_{k,l}^{Norm} = \frac{x_l^{ref}}{y_k^{ref}} \frac{\delta y_k}{\delta x_l}, \tag{19}$$

with x_l^{ref} and y_k^{ref} as the nominal values of x_l and y_k. For the 3-DOF torsional model described in Section 2.1, the input and output vectors for sensitivity analysis are

$$x = \{k_L,\ k_H,\ J_r,\ J_{gr},\ J_{gn},\ c_L,\ c_H,\ T_r,\ T_g\}, \tag{20a}$$

$$y = \{\Omega_1^{tor},\ \Omega_2^{tor},\ \Psi_{rot}^{\Omega_1},\ \Psi_{rot}^{\Omega_2},\ \Psi_{gear}^{\Omega_1},\ \Psi_{gear}^{\Omega_2},\ \Psi_{gen}^{\Omega_1},\ \Psi_{gen}^{\Omega_2},\ |e_{tot}^{\omega}(\Omega_1^{tor})|,\ |e_{tot}^{\omega}(\Omega_2^{tor})|\}. \tag{20b}$$

The closed form of equations after applying normalized local sensitivity theory on eqs. (A.1) and (A.2) are shown in Appendix B and Appendix C. A positive value in this analysis stands for a direct relationship between the input parameter and output, whereas a negative value represents that the parameter and output are inversely correlated. The normalized local sensitivity analysis can take different values. If the absolute value is equal to 1, it means that the relative variation in input parameter is equally transmitted to the output, whereas the absolute value higher than 1 shows that the relative variation is magnified in the output. However, the absolute value lower than 1 represents that the relative variations of the input is shrunk in the output.

In the second study, in order to find the parameters/variables which have the highest contribution in variations of the amplitude of response at the response peak frequencies, a local sensitivity analysis is performed. For this purpose, two methods are proposed. First, the peak

frequencies are approximated with the associated natural frequency and subsequently the eq. (15) is used. The closed form equations which specify the correlation between the angular velocity error function amplitude at the natural frequencies with the system parameters and loads are derived by performing local sensitivity analysis as shown in Appendix D. This approximation can be improved by using the approximated damping coefficients and updating the eq. (15) by using the eq. 16. Another approach which is based on numerical calculations and is also used later in the simulation studies for comparison purposes is to numerically find the peak frequencies of the the response in the eq. (11) and finding the sensitivity of the response equations to the parameters after replacing the numerically calculated frequencies in the response function. The precision in estimation of the damping coefficient by the two proposed methods compared to the approximation proposed in [23] is presented in simulation studies. In order to attain the accuracy of these methods, the results are compared to the exact values of the coefficients based on the model parameters.

The following procedure summarizes the modal estimation approach:

1. The torsional response error function (or interchangeably the low-pass filtered signal of a single torsional response) is generated. The response can be angular velocity/acceleration.
2. The resultant signal is preprocessed so that the defect frequencies of the components and structural motions-induced harmonics are filtered. The result will give the damped torsional natural frequencies of the drivetrain system.
3. The measured natural frequency is validated by the analysis of variations of amplitude of response in the suspicious frequencies at different operating speeds. In simple words, the variation of the amplitude of response in the system natural frequency (damped natural frequencies) due to the variation of damping coefficient is more significant compared to the variation of the amplitude of response in the harmonics. The variation of damping coefficient is due to the consistent variations in the operating speed in wind turbine drivetrains.
4. Damping at the natural frequency depends on the operating speed. The damping coefficient at two ensuing operations in two different speeds can be estimated by applying the theory developed in this Section and modeled by eq. 17, based on monitoring the variations of the natural frequency and amplitude of response between the two operations.
5. By using the estimated damped natural frequencies from torsional response and the estimated damping coefficient from the analysis of amplitude of response, the undamped natural frequencies are obtained, which provide inputs for the fault detection approach based on monitoring the variations of system dynamic properties.

The algorithm which summarizes the proposed drivetrain modal estimation and the ensuing condition monitoring approach is illustrated by the flowchart in Fig. 1. $\mathbf{\Psi}_m^{\Omega 1}$ and $\mathbf{\Psi}_m^{\Omega 2}$ are the normal modes related to the 1^{st} and 2^{nd} natural frequencies, respectively. m varies from 1 up to the degree of the model, which accounts for the different bodies in the equivalent reduced order model. $\boldsymbol{\tau}_{\Omega}^{tor}$ and $\boldsymbol{\tau}_{\Psi_m}$ are the low-limit threshold natural frequency and normal mode related to normal operations.

3.2. Test cases

3.2.1. Simulation based validation

For the simulation studies, DTU $10MW$ reference wind turbine is selected. In order to evaluate if the input torque is able to excite the drivetrain natural frequencies and subsequently to study the possibility of observing those frequencies in the different drivetrain torsional responses, an effective approach is involving decoupled simulation technique. For this purpose, the rotor torque data of a detailed model of $10MW$ turbine with a spar floating platform obtained from SIMA global simulation software [33] is used, and the impacts on the drivetrain is studied by using a decoupled analysis.

The decoupled simulation approach consists of two separated phases. In the first phase, global simulation analyses are performed under different environmental conditions. In the global simulation, the blades and hub assembly, the structural module including the flexible multi-body systems for tower and platform and the nacelle are modelled. This model is coping with combined aerodynamic and hydrodynamic loading by using numerical and probabilistic models of wind, waves and current in the global simulation software to capture the integrated effect of the loads and the wind turbine control system on the turbine model. The results of the global analysis in this study are the loads transmitted to the drivetrain by the rotor specified by the time series of the resultant moment on the rotor. The second phase of decoupled analysis is that the offline global simulation results will then be applied as inputs on the drivetrain model in Simpack multi-body simulation (MBS) software [34] to calculate and analyse the drivetrain components local dynamic responses for modal estimation and fault detection purposes. The drivetrain model in the second phase of decoupled simulation utilizes the components reduced order models. As a complementary step, the post processing of local responses provides useful information for the drivetrain secondary studies. Without loss of generality, a geared drivetrain technology is selected for the simulation studies. However, the 3-DOF reference model can also be used for direct-drive technology fault detection based on the proposed approach, where regarding the considerable mass of main shaft, it should be modelled as a separate mass to improve the model accuracy, and then a similar approach can be engaged.

The operating condition for the global simulation is close to the rated operation with an average wind speed $U_w = 11m/s$, significant wave height $H_s = 3.5m$ and peak period $T_p = 7.5s$. In the under consideration 3-DOF torsional model of the geared drivetrain, rotor, gearbox and generator are modelled with equivalent moment of inertia, and the low- and high-speed shafts are each modelled with constant torsional stiffnesses. The generator and gearbox specifications are used from the optimized $10MW$ medium-speed drivetrain system proposed in [31]. The parameters of this model are listed in the Table 1. The undamped natural frequencies of this model calculated by eq. (A.1), and validated by Simpack are $1.9Hz$ and $73.9Hz$. The actual damping of the low- and high-speed shafts are also assumed to be 5% and 10% of the low-speed shaft stiffness, respectively. The torsional responses of rotor and generator shafts are obtained from the MBS model to investigate possibility of observing the natural frequencies from the angular velocity, acceleration and displacement error functions. The proposed methods for estimation of damping coefficients in different operating speeds are tested on the damped model of under consideration $10MW$ geared drivetrain. The possibility of detecting different stages of system-level inertia and stiffness related faults from the torsional response obtained from the $10MW$ MBS model are investigated by using the proposed algorithm.

In order to capture the system dynamic properties in the proposed approach and to get statistically comparable results, the time interval of each block of data should be large enough to

capture the lowest natural frequency. The sampling frequency should be high enough to capture the higher frequency modes which are of significance, and on the other side is limited to the SCADA sampling frequency in case of implementation in the farm level. Since the realization of the method is based on the 1^{st} and 2^{nd} nonrigid modes, for observing these two modes, the required length of data block is only a fraction of one second and the required sampling frequency is around $400Hz$ for $10MW$ medium-speed drivetrain technology.

Table 1: $10MW$ medium-speed drivetrain 3-DOF model specification

Parameter	**Value**
Equivalent rotor moment of inertia J_r $(kg.m^2)$	$800,000,000$
Equivalent gearbox moment of inertia J_{gr} $(kg.m^2)$	$1,239,300$
Equivalent generator moment of inertia J_{gn} $(kg.m^2)$	$15,716,775$
Equivalent low-speed shaft torsional stiffness k_L $(N.m/rad)$	$2,452,936,425$
Equivalent high-speed shaft torsional stiffness k_H $(N.m/rad)$	$245,293,642,500$

3.2.2. Experimental validation

The operational data from Vestas V66-1.750MW turbine is used for the experimental study. To test the method, an additional encoder is installed on the low-speed shaft. The topology of the drivetrain is shown in Fig. 2. As it can be seen, the two encoders $EN1$ and $EN2$ are the torsional measurement sensors placed on the low- and high-speed shafts, respectively. $AC1$ and $AC2$ are the accelerometers placed on the two main bearings to measure the lateral vibrations for comparison of the proposed method based on torsional vibrations with conventional approaches in the literature which are mainly based on translational vibrations. The data sets include the drivetrain operations under different operating speeds in both normal and faulty cases.

In PSD of the angular velocity error function of the operational data, in addition to the natural frequencies, some other frequency components are also expected to be observed. However, by a prior knowledge about the defect frequencies and the other torsional excitation sources, and by subsequently filtering those frequencies, it is possible to distinguish the natural frequencies. The benefits with measuring the natural frequencies by this noninvasive method are the low implementation cost, and the possibility of obtaining the precise values of natural frequencies by including the system nonlinearities, and translational impacts on the rotation transferred through the bed-plate and torque arm.

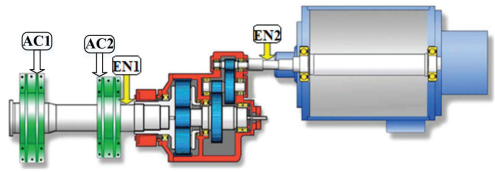

Figure 2: Vestas V66-1.750MW drivetrain topology, and vibration sensors placement.

4. Simulation/experimental studies

4.1. Sensitivity analysis results

The results of the normalized local sensitivity analyses with natural frequencies $(\Omega_1^{tor}, \Omega_2^{tor})$ and normal modes (ϕ_1, ϕ_2) as the outputs and shaft stiffnesses (k_L, k_H) as the inputs with variation

of only one model parameter at a time are shown in the Table 2. The interpretation of the local sensitivity analysis values is disclosed in Section 3.1. The reported numbers show the normalized sensitivity values which are calculated based on $10MW$ drivetrain model parameters. The values of the table in bold designate the absolute sensitivity values higher than 0.01, which is used as the criterion that the associated parameter and output are correlated. The values which are not highlighted designate the absolute sensitivity values lower than 0.01 representing a negligible sensitivity, so that the associated parameter and output are uncorrelated. As it can be seen, there is a direct relationship between the 1^{st} frequency and k_L, and the 2^{nd} frequency and k_H. Therefore, variations in the natural frequencies can be translated into the variations in the shaft stiffness and subsequently the defects in the drivetrain shafts. The influence of the shafts defect (stiffness variation) on the normal mode of the 1^{st} natural frequency is negligible. However, the stiffness variation results in variations in the normal mode element of the 2^{nd} natural frequency related to rotor. The results of the sensitivity analyses with natural frequencies and normal modes as the outputs and moment of inertia (J_r, J_{gr}, J_{gn}) as the inputs (variation of only one model parameter at a time) are shown in the Table 2. As it can be seen, there is an inverse relationship between the 1^{st} frequency and J_{gn}, and the 2^{nd} frequency and J_{gr}, so that the reduction of natural frequencies can be due to a rise in the moment of inertia. To distinguish between the drop in natural frequencies due to variation in stiffness and moment of inertia, the results should be interpreted together with monitoring the variations of normal modes. The simultaneous drop of the 1^{st} frequency and the normal mode element of the 2^{nd} frequency related to rotor represents an abnormality in low-speed shaft. The drop of the 2^{nd} frequency and the simultaneous rise in the normal mode element of the 2^{nd} frequency related to rotor discloses the problems in high-speed shaft. The drop of the 1^{st} frequency, the simultaneous rise in the normal mode element of the 1^{st} frequency related to rotor and drop in the normal mode element of the 2^{nd} frequency related to generator reveal unbalances in generator side. The drop of the 2^{nd} frequency and a simultaneous rise in the normal mode elements of the 2^{nd} frequency related to both generator and rotor can be used as the criteria to detect an unbalance in gearbox.

As discussed earlier in Section 3, another criterion which can be used in parallel to ascertain the validity of the above guideline is monitoring the variations of the amplitude of response at the natural frequencies based on the sensitivity analysis values reported in the Table 3 which will be discussed later in this Section. This criterion in difference with the criteria established in the above guideline needs an anterior estimation of the system loads. However, a good estimation of both the rotor and generator torques is available in wind turbine application. The rotor torque is estimated by using the blade aerodynamic equations and the input wind. The generator torque is estimated from the generator voltage and current measurements.

Sensitivity of the amplitude of frequency spectrum of angular velocity error function at the 1^{st} mode to system parameters and loads are summarized in the Table 3. The 2^{nd} column is related to the first method based on the approximation of peak frequencies with the associated natural frequencies, calculating the response equation at those frequencies, deriving the sensitivity equations of the resulted functions in terms of parameters, then updating the response based on the approximated damping coefficients and repeating the sequence to improve the accuracy of estimation. The results reported of the first method are obtained by only a single iteration. The use of this method based on the approximation of Ω_{peak} with Ω_n which is more accurate if $\zeta << 1$. However, the accuracy can be improved as explained by the correction which can be applied on the eq. (15) based on the estimated damping coefficients. The 3^{rd} column of this

Table 2: Sensitivity of natural frequencies and normal modes to variations of model parameter (stiffness and inertia).

Sensitivity \ Variable	k_L	k_H	J_r	J_{gr}	J_{gn}
Ω_1^{tor}	**0.50**	0.00	−0.01	**-0.03**	**-0.45**
Ω_2^{tor}	0.00	**0.50**	0.00	**-0.45**	**-0.04**
ϕ_1^{rot}	0.00	0.00	**-1.00**	**0.07**	**0.93**
ϕ_1^{gear}	0.00	0.00	0.00	0.00	0.00
ϕ_1^{gen}	0.00	0.00	0.00	0.00	0.00
ϕ_2^{rot}	0.99	**-0.99**	**-1.00**	**0.89**	**0.08**
ϕ_2^{gear}	0.00	0.00	0.00	−0.01	0.01
ϕ_2^{gen}	−0.01	0.01	0.00	**0.96**	**-1.00**

Table 3: Sensitivity of amplitude of response at 1^{st} and 2^{nd} modes to system parameters and loads.

Variable \ Sensitivity	Method 1 (1^{st} mode)	Method 2 (1^{st} mode)	Method 1 (2^{nd} mode)
J_r	**0.02**	**0.02**	0.01
J_{gr}	**-0.02**	−0.01	**0.21**
J_{gn}	**-0.21**	**-0.10**	**-0.47**
k_L	**-0.21**	**-0.34**	0.00
k_H	0.00	0.00	**-0.25**
c_L	**-0.08**	**-0.07**	0.00
c_H	0.00	0.00	−0.01
T_r	−0.01	−0.01	−0.01
T_g	**0.51**	**0.51**	**0.51**

table is related to the second method based on the numerical calculation of peak frequencies, deriving the response equation in those frequencies and finding the sensitivity of the resulted equations to the parameters and loads variations. The sensitivity of the amplitude of frequency spectrum of angular velocity error function at the 2^{nd} mode to system parameters and loads are also listed in the 4^{th} column of the same table.

As it can be seen from the Table 3, variation in amplitude of response at the 1^{st} mode is mainly dominated by generator torque, generator inertia, low-speed shaft stiffness and damping. The amplitude ratio at the 1^{st} mode for two different operations is directly influenced by load and inversely influenced by damping. Knowing that the system parameters are constant, by a prior knowledge about the load, variations in damping can be estimated. To estimate the damping coefficients from the amplitude of response based on the sensitivity analysis results, three different cases can be assumed for the simulations. All these cases are based on monitoring the variations of the response amplitude at the natural frequencies between two different operating points t_1 and t_2.

Case 1: The two operating points are close, so that the system parameters and load stay constant.

In this case, the variation in the amplitude ratio directly reflects the variation in the actual damping ratio which varies due to the variation of the operating speed. Those variations are correlated proportional with the numbers calculated by the sensitivity analysis. From this relationship, the variation in the damping coefficient is estimated. By using this information

Table 4: Estimation of damping coefficient at the 1^{st} mode for Case 1: loads do not change between the two operating points.

Operation	$\omega\ (rad/s)$	$\Omega^1_{peak}\ (rad/s)$	$\lvert\epsilon^{\omega}_{tot}(\Omega^1_{peak})\rvert$	ζ (reference model)	ζ (method 1)	ζ (method 2)	ζ (method in [23])
ω_1	0.9	8.67	0.159	0.21	0.20	0.16	0.48
ω_2	0.7	8.46	0.156	0.26	0.25	0.22	0.49

Table 5: Estimation of damping coefficient at the 1^{st} mode for Case 2: loads change between the two operating points.

Operation	$\omega\ (rad/s)$	$\Omega^1_{peak}\ (rad/s)$	$\lvert\epsilon^{\omega}_{tot}(\Omega^1_{peak})\rvert$	ζ (reference model)	ζ (method 1)	ζ (method 2)	ζ (method in [23])
ω_1	0.9	8.67	0.159	0.21	0.21	0.18	0.27
ω_2	0.7	8.46	0.171	0.26	0.25	0.23	0.31

along with eq. (17a), the two dampings of the two operations are estimated. It is worth noting that in Case 1, since the system parameters and subsequently the critical dampings are constant, the actual damping ratio is equal to the ratio of the damping coefficients between the two operations. The estimated values of damping coefficients at the 1^{st} mode in two different operating speeds which meet the conditions of Case 1, by using the two proposed methods which described in Section 3.1 compared to the approximation proposed in [23] are listed in the Table 4. The comparison of the three methods of estimating damping coefficients shows that the method 1 even based on one iteration outperforms the two other damping approximation approaches by demonstrating a much lower relative error.

Case 2: The load varies between the two operations but the system parameters stay constant.

In this case, the loads and dampings vary while the other system parameters are constrained to be constant. With an access to the estimated load it is still possible similar to in Case 1 to measure the variation in damping coefficients by using the local sensitivity analysis results and by relating the variation in response amplitude to the variation in load and damping, based on the proportions calculated by the sensitivity analysis. From this relationship, the variation in the damping coefficient and subsequently the two dampings of the two operations are estimated similar to in Case 1. The estimated values of damping coefficients at the 1^{st} mode in two different operating speeds which meet the conditions of Case 2, by using the two methods proposed in Section 3.1 are listed in the Table 5. It is assumed that during the second operating speed/condition, both the rotor and generator loads have been increased by 20% so that $\frac{T_r^{\omega_2}}{T_r^{\omega_1}} = \frac{T_g^{\omega_2}}{T_g^{\omega_1}} = 1.2$. Similar to in Case 1, the comparison of the three methods of estimating damping coefficients shows that the method 1 even with one iteration outperforms the two other damping approximation approaches.

Case 3: Both the load and parameters are changing.

In this case, the estimation of damping variation from the response is challenging because it needs a good estimation not only from the load but also the other system parameters. In this case, the amplitude of response may not give enough information to estimate the damping coefficients based on that, because the updated values for the system parameters may be unknown. However, assuming that the load can be estimated, the result of this study can be used to authenticate the conclusions made about the system faults from the analysis of natural frequencies and normal modes variations.

A similar set of sensitivity analysis is performed for the second mode which shows the sensitivity

of amplitude of response at the second natural frequency more significantly to the high-speed shaft stiffness, generator torque, and the moment of inertia of gearbox and generator with no considerable sensitivity to the damping at the second mode. Based on this study,the amplitude of response at the second frequency is not significantly influenced by the value of the dampings so that the amplitude of response is not recommended as a good criterion for estimation of damping coefficient of the second mode. Some other functions of the amplitude of response of different operations may offer less sensitivity to parameters variation which are more useful when the information on the system is low, which are not discussed in here. Another potential of monitoring the variations of amplitude of response at the estimated torsional natural frequencies is for estimation of the loads. In other words, for the same operational speed and system parameters, the natural frequencies and dampings will stay the same and variations of the amplitude of response at system torsional natural frequencies is directly connected to variations in generator torque which can be used for monitoring the variations of the torque. The latter is also not discussed more in this work.

The extracted features obtained by the sensitivity study for detecting the drivetrain faults are evaluated by both the MBS simulation model and the real operational data in the continued parts.

4.2. Simulation-base validation of proposed modal estimation and condition monitoring approach

The simulation-base validations relies on the data obtained from the multi-body simulation model of $10MW$ medium-speed PMSG drivetrain system in Simpack.

4.2.1. Estimation of natural frequencies from torsional measurements

The PSD spectrum of angular velocity error function obtained from $10MW$ drivetrain model and its capability in highlighting the torsional natural frequencies is shown in figures 3b-3d. In these three figures, the performance of angular velocity error function in extracting the 1^{st} and 2^{nd} torsional natural frequencies of the drivetrain is compared with angular displacement and angular acceleration error functions. As it can be seen, acceleration error function outperforms in revealing the higher frequency modes (the 2^{nd} mode). The higher modes have usually a lower impact on the response, which impedes disclosure of those frequencies. The PSD spectrum of the input torque applied on the drivetrain MBS model is shown in Fig. 3a. This torque which is obtained from the global simulation contains the majority of frequency components and can excite the drivetrain natural frequencies.

4.2.2. Diagnosis of drivetrain faults

The drivetrain faults at system-level vary the equivalent torsional model parameters, so that by monitoring the consequences of these variations on the drivetrain dynamic properties and amplitude of response at the natural frequencies these faults can be detected. For simulation purposes, the faults are simulated independently so that the correlations between the under consideration faults are neglected.

As discussed earlier, detection of stiffness changing related faults is possible in the proposed approach by monitoring the consequences of these faults on the drivetrain torsional modes based on the results of sensitivity analysis. As an example of stiffness-related faults, the growth of crack in the shaft causes the torsional stiffness of the shaft to decrease and this change will be reflected in the driveline torsional natural frequencies. The variations of the shafts stiffness from 5% are considered as the start of fatigue crack in the shaft. The latter is equivalent with

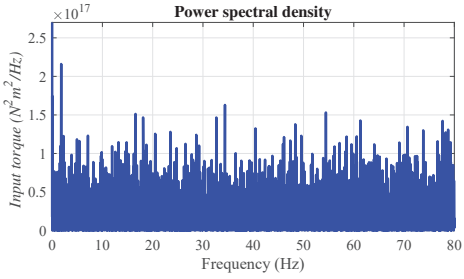
Power spectral density
Input torque (N^2m^2/Hz)
Frequency (Hz)

(a)

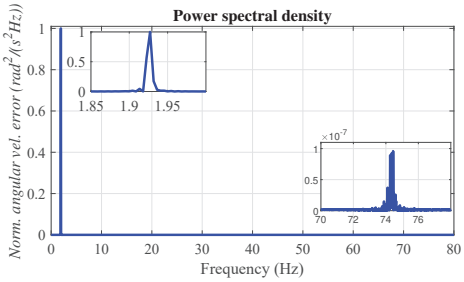
Power spectral density
Norm. angular vel. error ($rad^2/(s^2Hz)$)
Frequency (Hz)

(b)

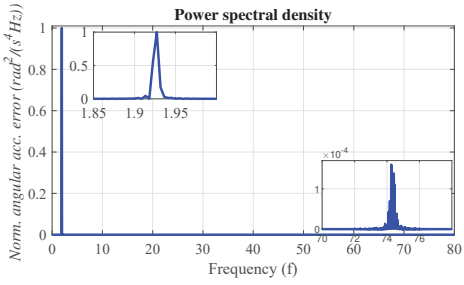
Power spectral density
Norm. angular acc. error ($rad^2/(s^4Hz)$)
Frequency (f)

(c)

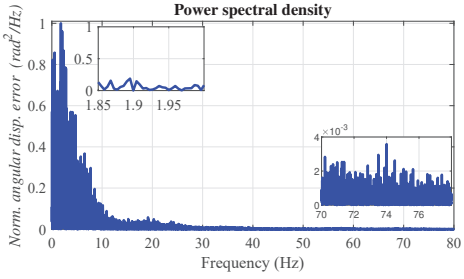
Power spectral density
Norm. angular disp. error (rad^2/Hz)
Frequency (Hz)

(d)

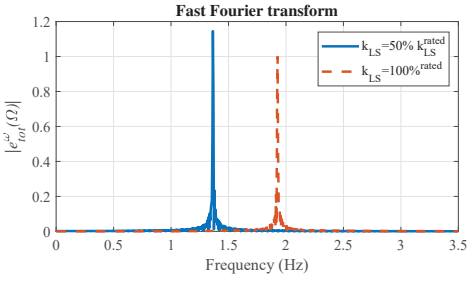
Fast Fourier transform
k_{LS}=50% k_{LS}^{rated}
k_{LS}=100% k_{LS}^{rated}
$|e_{tot}^{\omega}(\Omega)|$
Frequency (Hz)

(e)

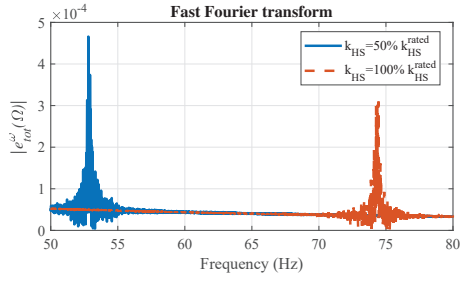
Fast Fourier transform
k_{HS}=50% k_{HS}^{rated}
k_{HS}=100% k_{HS}^{rated}
$|e_{tot}^{\omega}(\Omega)|$
Frequency (Hz)

(f)

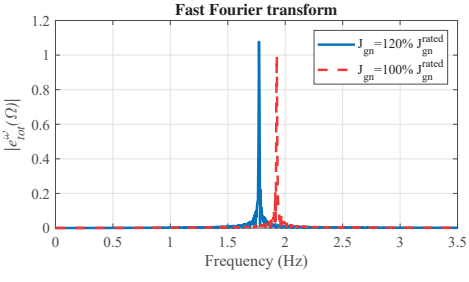
Fast Fourier transform
J_{gn}=120% J_{gn}^{rated}
J_{gn}=100% J_{gn}^{rated}
$|e_{tot}^{\omega}(\Omega)|$
Frequency (Hz)

(g)

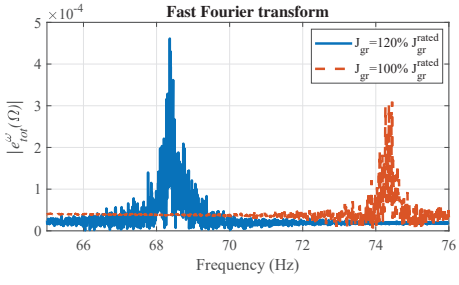
Fast Fourier transform
J_{gr}=120% J_{gr}^{rated}
J_{gr}=100% J_{gr}^{rated}
$|e_{tot}^{\omega}(\Omega)|$
Frequency (Hz)

(h)

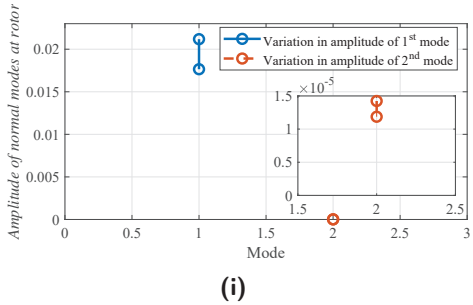

Figure 3: Simulation results based on $10MW$ floating wind turbine model. (a) PSD of τ^{rotor}. (b) PSD of e_{tot}^{vel}. (c) PSD of e_{tot}^{acc}. (d) PSD of e_{tot}^{dis}. (e) Fault in low-speed shaft. (f) Fault in high-speed shaft. (g) Fault in generator. (h) Fault in gearbox. (i) Fault in rotor.

variation in the modal parameters as the fault precursors in the proposed condition monitoring detection algorithm. In order to simulate the shaft crack growth in the low- and high-speed shafts, the torsional stiffness of these two shafts in the Simpack model is reduced in four steps from 5 to 50%. The subsequent changes in the undamped natural frequencies and normal modes are listed and shown in the Tables 6 and 7. As it can be seen from these tables, the simulation results agree with the results obtained from the analytical sensitivity analysis of natural frequencies and normal modes reported in the Table 2. Since the fault detection features are obtained from the variations of the physical model, the threshold for these features is accordingly specified based on the sensitivity analysis employed on a specific drivetrain.

The reduction of the 1^{st} natural frequency due to a crack in low-speed shaft is illustrated in Fig. 3e. In addition, as it can be seen from this figure, for the two operations with the same loading conditions, that one of them is the normal system and the other one is the system with a crack in the low-speed shaft, the amplitude of response at the 1^{st} natural frequency is higher in the system with the cracked shaft compared to the normal system, which agrees with the results of the analytical sensitivity analysis of the amplitude of response as reported in the Table 3. The influence of crack in high-speed shaft and the consequence in drop of the 2^{nd} natural frequency is shown in Fig. 3f. As it can also be seen in this figure, a crack in the high-speed shaft causes an increase in the amplitude of response at the 2^{nd} natural frequency, which agrees with the sensitivity results related to the amplitude of response at the 2^{nd} mode as mentioned in the Table 3. For scaling and demonstration purposes, figures 3e and 3f are normalized with the normal system results.

The detection of inertia changing related faults is also possible by monitoring the consequences of these faults on the drivetrain torsional modes based on the performed sensitivity analysis results. As an example of inertia-related faults, unbalance in the rotor, gearbox or generator shafts results in an increase in the equivalent inertia of the component in the model. Dependent on the severity of unbalance the variation in inertia will be different. A slight unbalance can cause a very slight change in the inertia and subsequently a slight change in the modes which makes the detection challenging by the proposed approach. In here, in order to simulate the severe unbalance faults, the inertia of the associated component is increased in three steps from 5 to 20%. The subsequent changes in the drivetrain modes are listed and shown in the Tables 8- 10. The simulation results agree with the sensitivity analysis results presented in the Table

2.

The reduction of 1^{st} and 2^{nd} natural frequency due to increase of inertia of generator and gearbox as a result of unbalance faults in generator and gearbox are respectively shown in figures 3g and 3h. The influence of increase of rotor inertia, which can model the rotor unbalance fault, on the simultaneous reduction of 1^{st} and 2^{nd} normal modes in rotor position is also shown in Fig. 3i. All these three figures are normalized with the normal system results.

Table 6: Low-speed shaft fault cases.

Fault case	$\frac{k_L}{k_L^n}$	$\frac{\Omega_1^{tor}}{\Omega_1^{tor,n}}$	$\frac{\Omega_2^{tor}}{\Omega_2^{tor,n}}$	$\frac{\Psi_{rot}^{\Omega_1}}{\Psi_{rot}^{\Omega_1,n}}$	$\frac{\Psi_{rot}^{\Omega_2}}{\Psi_{rot}^{\Omega_2,n}}$	$\frac{\Psi_{gear}^{\Omega_1}}{\Psi_{gear}^{\Omega_1,n}}$	$\frac{\Psi_{gear}^{\Omega_2}}{\Psi_{gear}^{\Omega_2,n}}$	$\frac{\Psi_{gen}^{\Omega_1}}{\Psi_{gen}^{\Omega_1,n}}$	$\frac{\Psi_{gen}^{\Omega_2}}{\Psi_{gen}^{\Omega_2,n}}$
$LC0$	1	1	1	1	1	1	1	1	1
$LC1$	0.95	0.975	1.000	1.000	0.950	1.000	1.000	1.000	1.000
$LC2$	0.85	0.923	0.999	1.000	0.851	1.001	1.000	1.000	1.001
$LC3$	0.7	0.838	0.999	1.000	0.000	1.003	1.000	1.000	1.003
$LC4$	0.5	0.709	0.998	1.000	0.000	1.005	1.000	1.000	1.005

Table 7: High-speed shaft fault cases.

Fault case	$\frac{k_H}{k_H^n}$	$\frac{\Omega_1^{tor}}{\Omega_1^{tor,n}}$	$\frac{\Omega_2^{tor}}{\Omega_2^{tor,n}}$	$\frac{\Psi_{rot}^{\Omega_1}}{\Psi_{rot}^{\Omega_1,n}}$	$\frac{\Psi_{rot}^{\Omega_2}}{\Psi_{rot}^{\Omega_2,n}}$	$\frac{\Psi_{gear}^{\Omega_1}}{\Psi_{gear}^{\Omega_1,n}}$	$\frac{\Psi_{gear}^{\Omega_2}}{\Psi_{gear}^{\Omega_2,n}}$	$\frac{\Psi_{gen}^{\Omega_1}}{\Psi_{gen}^{\Omega_1,n}}$	$\frac{\Psi_{gen}^{\Omega_2}}{\Psi_{gen}^{\Omega_2,n}}$
$LC0$	1	1	1	1	1	1	1	1	1
$LC1$	0.95	1.000	0.975	1.000	1.052	1.000	1.000	1.000	1.000
$LC2$	0.85	0.999	0.923	1.000	1.175	0.998	1.000	1.000	0.998
$LC3$	0.7	0.998	0.838	1.000	1.423	0.996	1.000	1.000	0.996
$LC4$	0.5	0.996	0.710	0.993	1.983	0.991	1.000	1.000	0.991

Table 8: Inertia related fault cases (rotor).

Fault case	$\frac{J_r}{J_r^n}$	$\frac{\Omega_1^{tor}}{\Omega_1^{tor,n}}$	$\frac{\Omega_2^{tor}}{\Omega_2^{tor,n}}$	$\frac{\Psi_{rot}^{\Omega_1}}{\Psi_{rot}^{\Omega_1,n}}$	$\frac{\Psi_{rot}^{\Omega_2}}{\Psi_{rot}^{\Omega_2,n}}$	$\frac{\Psi_{gear}^{\Omega_1}}{\Psi_{gear}^{\Omega_1,n}}$	$\frac{\Psi_{gear}^{\Omega_2}}{\Psi_{gear}^{\Omega_2,n}}$	$\frac{\Psi_{gen}^{\Omega_1}}{\Psi_{gen}^{\Omega_1,n}}$	$\frac{\Psi_{gen}^{\Omega_2}}{\Psi_{gen}^{\Omega_2,n}}$
$LC0$	1	1	1	1	1	1	1	1	1
$LC1$	1.05	1.000	1.000	0.952	0.952	1.000	1.000	1.000	1.000
$LC2$	1.10	0.999	1.000	0.909	0.909	1.000	1.000	1.000	1.000
$LC3$	1.20	0.998	1.000	0.833	0.833	1.000	1.000	1.000	1.000

4.3. Experimental validation of proposed modal estimation and condition monitoring approach

The experimental validations are based on the operational data obtained from the drivetrain system of a $1.75MW$ Vestas wind turbine.

4.3.1. Estimation of natural frequencies

The PSD spectrum of angular velocity error function of the Vestas drivetrain operational data for a rated operation is compared with angular displacement and acceleration error functions as shown in figures 4a-4c, which shows the observability of both the drivetrain and blade natural frequencies. The results are validated by comparing with the 1^{st} drivetrain and 1^{st} blade edgewise natural frequencies of another turbine with the same drivetrain technology and a similar power range reported in [35]. The performance of angular velocity error function is compared with angular displacement and acceleration error functions. As it can be seen, angular acceleration shows a slightly higher performance in amplification and extraction of characteristic frequencies of higher values. A comparison between the angular velocity error

Table 9: Inertia related fault cases (gearbox).

Fault case	$\frac{J_{gr}}{J_{gr}^n}$	$\frac{\Omega_1^{tor}}{\Omega_1^{tor,n}}$	$\frac{\Omega_2^{tor}}{\Omega_2^{tor,n}}$	$\frac{\Psi_{rot}^{\Omega_1}}{\Psi_{rot}^{\Omega_1,n}}$	$\frac{\Psi_{rot}^{\Omega_2}}{\Psi_{rot}^{\Omega_2,n}}$	$\frac{\Psi_{gear}^{\Omega_1}}{\Psi_{gear}^{\Omega_1,n}}$	$\frac{\Psi_{gear}^{\Omega_2}}{\Psi_{gear}^{\Omega_2,n}}$	$\frac{\Psi_{gen}^{\Omega_1}}{\Psi_{gen}^{\Omega_1,n}}$	$\frac{\Psi_{gen}^{\Omega_2}}{\Psi_{gen}^{\Omega_2,n}}$
$LC0$	1	1	1	1	1	1	1	1	1
$LC1$	1.05	0.998	0.978	1.004	1.046	1.000	1.000	1.000	1.050
$LC2$	1.10	0.997	0.957	1.007	1.092	1.000	1.000	1.000	1.100
$LC3$	1.20	0.993	0.919	1.015	1.183	1.000	1.000	1.000	1.200

Table 10: Inertia related fault cases (generator).

Fault case	$\frac{J_{gn}}{J_{gn}^n}$	$\frac{\Omega_1^{tor}}{\Omega_1^{tor,n}}$	$\frac{\Omega_2^{tor}}{\Omega_2^{tor,n}}$	$\frac{\Psi_{rot}^{\Omega_1}}{\Psi_{rot}^{\Omega_1,n}}$	$\frac{\Psi_{rot}^{\Omega_2}}{\Psi_{rot}^{\Omega_2,n}}$	$\frac{\Psi_{gear}^{\Omega_1}}{\Psi_{gear}^{\Omega_1,n}}$	$\frac{\Psi_{gear}^{\Omega_2}}{\Psi_{gear}^{\Omega_2,n}}$	$\frac{\Psi_{gen}^{\Omega_1}}{\Psi_{gen}^{\Omega_1,n}}$	$\frac{\Psi_{gen}^{\Omega_2}}{\Psi_{gen}^{\Omega_2,n}}$
$LC0$	1	1	1	1	1	1	1	1	1
$LC1$	1.05	0.978	0.998	1.046	1.003	1.000	1.000	1.000	0.952
$LC2$	1.10	0.958	0.997	1.093	1.007	1.000	1.000	1.000	0.909
$LC3$	1.20	0.920	0.994	1.186	1.012	1.000	1.000	1.000	0.833

function PSD in two different operating speeds is shown in Fig. 4d. As it can be seen, the higher damping coefficient in lower speeds has resulted in a lower damped natural frequency. Furthermore, at the drivetrain natural frequency, the amplitude reacts more significantly to the variation in damping. In other words, the amplitude of response at the natural frequency reduces more compared with other harmonics, for a lower rotor speed which corresponds to a higher damping. The filtered low-speed shaft angular velocity measurement is shown in Fig. 4e. The chosen filter is a first order high-pass butterworth filter with the cutoff frequency $1Hz$. As it can be seen, the filtered signal shows some degree of competence with the angular velocity error function in extracting the torsional properties of the system *i.e.* the drivetrain and the blade in plane natural frequencies.

4.3.2. Diagnosis of the drivetrain fault

Our observation on extensive operational measurements of the drivetrain system of the under consideration turbine shows that for the same turbine rotational speed the natural frequencies do not change under normal operations. The Fig. 4f shows the deviation of 1^{st} natural frequency which is apparently due to a low-speed shaft fatigue crack. Therefore, the method is able to detect the shaft cracks in the early stages of progression. As it can be seen, the reduction of the natural frequency at the same operational speed is observed due to a reduction in the low-speed shaft stiffness as a consequence of fault in the low-speed shaft. The frequency spectra presented in literature for detection of shaft crack are usually unreliable as other types of faults can also generate a similar frequency pattern. More advanced frequency domain approaches call for the coupled analysis of the crack vibrations consequences in all bending, longitudinal and torsion which is both expensive to implement and dependent on the load and excitation frequencies. The cracked shaft can represent a periodic reduction in the shaft stiffness due to nonlinear effects such as breathing of the crack. Dependent on the type of crack the variation of the stiffness of the different directions of lateral, axial and torsional could be different, because the stiffness change is dependent on the direction of bending moment at the crack cross-section. Due to the coupling phenomena that exists in a cracked rotor, *i.e.* bending–torsion, longitudinal–torsion, the variations of longitudinal or bending stiffness parameters, which have relationship with type and depth of crack, also influence the torsional stiffness in later stages. Therefore, the assumptions for modelling of a crack with constant torsional stiffness asymmetry does not seem to be unrealistic. However, the proposed method has a potential to be adjusted based on more

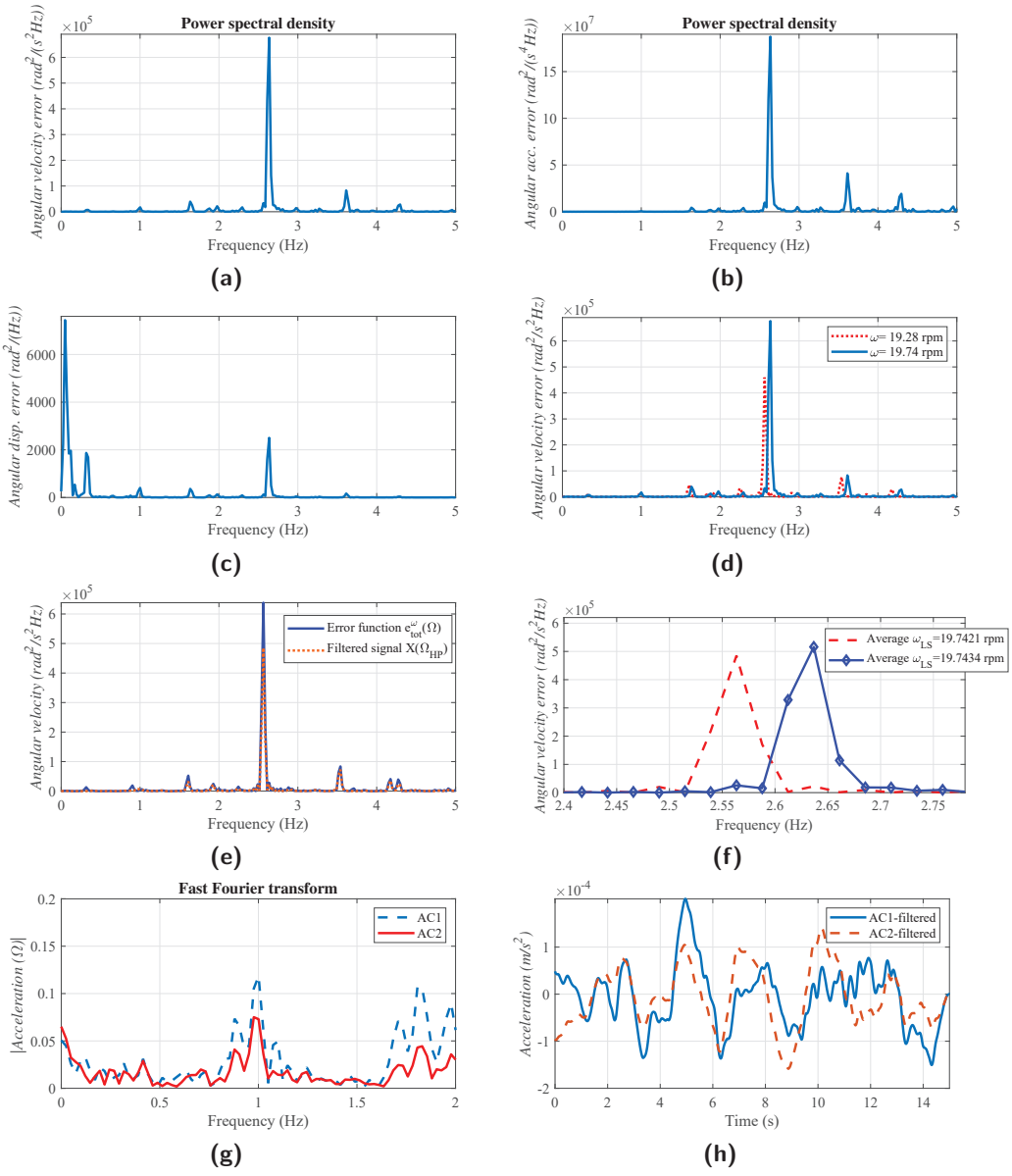

Figure 4: Experimental results based on $1.75MW$ Vestas turbine operational data. (a) PSD of e^{ω}_{tot}. (b) PSD of e^{α}_{tot}. (c) PSD of e^{θ}_{tot}. (d) PSD of e^{ω}_{tot} in two different operations. (e) Comparison of $X(\Omega_{HP})$ and $e^{\omega}_{tot}(\Omega)$ performances. (f) Fault in low-speed shaft: influence on 1^{st} mode. (g) Fault in low-speed shaft: FFT of accelerometers. (h) Fault in low-speed shaft: phase difference.

complex models of stiffness variation in terms of crack properties. The performance of the proposed fault detection feature based on monitoring natural frequency variations from torsional measurements in detection of low-speed shaft faults is compared with three conventional methods in literature based on accelerometers measurements. *First*, the frequency domain indicator based on observing twice the running frequency component and the subharmonic resonance [27; 36]; *second*, the variable phase difference between the time domain measurements of the accelerometers placed on the two sides of shaft at the shaft rotational frequency component; *third*, the r.m.s of time domain acceleration based on standard ISO 10816-21. The frequency spectra of the two accelerometers placed on the two main bearings which support the main shaft are shown in Fig. 4g. In this figure, the under consideration turbine has been working with the nominal rotational speed which is $0.33Hz$ in the low-speed side. As it can be seen, the main revolution frequency, the double frequency and the subharmonics do not show a significant amplitude in the response. The insufficiency of frequency domain analysis in different operating speeds in detecting shaft faults in the general rotor system is also reported in [26]. The other drawback with frequency domain analysis based on our observations is that due to the low frequency content of the low-speed shaft faults, they can be mistaken with a wide range of excitation frequencies due to environmental and structural motions induced vibrations which happen in the low frequency range. The latter is the reason that the second method which is the crack detection criterion based on the analysis of phase difference between the acceleration measurements of the two sides of low-speed shaft is also not helpful. The Fig. 4h shows the synchronized time domain acceleration measurements of AC1 and AC2 which are band-pass filtered around the low-speed shaft rotational frequency. As it can be seen, the figure does not represent any variation in the phase difference between these two signals. Monitoring of the variations of the phase difference of the frequency component $0.33Hz$ is not guaranteed due to the influence of the other frequency components which appear in response in this frequency range. As it can be seen in the Table 11, the described abnormality cannot also be detected by the third method which is the conventional time domain approach based on the evaluation of the r.m.s value of the time series data of the translational vibrations.

Table 11: Acceleration r.m.s compared with the warning limits brought in standard ISO 10816-21.

Comparison \ **Sensor**	$AC1$	$AC2$
$Measured\ r.m.s\ (m/s^2)$	0.01	0.01
$Standard\ r.m.s\ threshold\ (m/s^2)$	0.3	0.3

5. Conclusions

A condition monitoring approach bottomed on the coordination of a data-driven approach for estimation of drivetrain dynamic properties based on signal processing of the torsional measurements, and the analytical/physical model of drivetrain to extract the fault detection features was presented. It was shown that only a reduced order 3-DOF model is enough to detect different categories of drivetrain faults at system level.

The drivetrain modal estimation approach by using torsional measurements was analytically explained and then validated by using both simulation and experimental studies, so that the observability of natural frequencies and the estimation of damping coefficients for the different natural frequencies and operating speeds were demonstrated by different investigated case studies. The estimated modes were later supporting the proposed drivetrain condition monitoring

approach which works based on monitoring the variations of the system dynamic properties and amplitude of response at the drivetrain torsional frequencies. The drivetrain system fault detection features were extracted by sensitivity analysis and were tested by both $10MW$ drivetrain simulated model in Simpack software and $1.75MW$ Vestas operational turbine. The results were showing that the progression state of different categories of drivetrain faults at system level are observable in an early stage by the method developed based on 3-DOF equivalent torsional model of the drivetrain, only by tracking the faults consequent variations in the drivetrain dynamic properties.

The results demonstrate the potentials of torsional measurements for both drivetrain modal estimation and system-level fault detection. The future work will be devoted to the application of higher DOF torsional models as more detailed equivalent models of the drivetrain, which can capture real-time variations in mesh stiffness and inertia of individual gears and intermediate shafts, which can help to detect faults in those subcomponents by taking into account the components internal dynamics.

Acknowledgement

The authors would like to thank Kongsberg Digital AS, Trondheim, Norway, for providing experimental data for this study. The authors also would like to thank John Marius Hegseth of Norwegian University of Science and Technology, Trondheim, Norway, for providing the $10MW$ spar floating wind turbine global analysis simulation data.

Appendix A. 3-DOF equivalent model dynamic properties as a function of model parameters

The two undamped natural frequencies (nonrigid modes) based on 3-DOF lumped-mass-spring model of a geared drivetrain, as functions of model parameters, can be calculated by

$$\Omega_1^{tor} = \sqrt{\frac{k_L}{2J_r} + \frac{k_L + k_H}{2J_{gr}} + \frac{k_H}{2J_{gn}} - \sqrt{(\frac{-k_L}{2J_r} - \frac{k_L - k_H}{2J_{gr}} + \frac{k_H}{2J_{gn}})^2 + \frac{k_L k_H}{J_{gr}^2}}}, \tag{A.1a}$$

$$\Omega_2^{tor} = \sqrt{\frac{k_L}{2J_r} + \frac{k_L + k_H}{2J_{gr}} + \frac{k_H}{2J_{gn}} + \sqrt{(\frac{-k_L}{2J_r} - \frac{k_L - k_H}{2J_{gr}} + \frac{k_H}{2J_{gn}})^2 + \frac{k_L k_H}{J_{gr}^2}}}, \tag{A.1b}$$

where Ω_1^{tor} and Ω_2^{tor} are the 1^{st} and 2^{nd} natural frequencies, k_L and k_H are the torsional stiffness of low- and high-speed shafts, and J_r, J_{gr} and J_{gn} are the moment of inertia of rotor, gearbox and generator, respectively.

The two normal modes related to the two non-rigid modes of the under consideration drivetrain

model, as functions of model parameters, which are scaled to unity length are

$$\Psi_{rot}^{\Omega_1} = \frac{\sqrt{\frac{k_L^2}{\frac{k_H^2}{(k_H - J_{gn}A)^2} + \frac{k_L^2}{(k_L - J_r A)^2} + 1)}}}{k_L - J_r A}, \quad \Psi_{rot}^{\Omega_2} = \frac{\sqrt{\frac{k_L^2}{\frac{k_H^2}{(k_H - J_{gn}B)^2} + \frac{k_L^2}{(k_L - J_r B)^2} + 1}}}{k_L - J_r B}, \tag{A.2a}$$

$$\Psi_{gear}^{\Omega_1} = \sqrt{\frac{1}{\frac{k_H^2}{(k_H - J_{gn}A)^2} + \frac{k_L^2}{(k_L - J_r A)^2} + 1}}, \quad \Psi_{gear}^{\Omega_2} = \sqrt{\frac{1}{\frac{k_H^2}{(k_H - J_{gn}B)^2} + \frac{k_L^2}{(k_L - J_r B)^2} + 1}}, \tag{A.2b}$$

$$\Psi_{gen}^{\Omega_1} = \frac{\sqrt{\frac{k_H^2}{\frac{k_H^2}{(k_H - J_{gn}A)^2} + \frac{k_L^2}{(k_L - J_r A)^2} + 1}}}{k_H - J_{gn}A}, \quad \Psi_{gen}^{\Omega_2} = \frac{\sqrt{\frac{k_H^2}{\frac{k_H^2}{(k_H - J_{gn}B)^2} + \frac{k_L^2}{(k_L - J_r B)^2} + 1}}}{k_H - J_{gn}B}, \tag{A.2c}$$

where

$A = -\sqrt{(\frac{k_H}{2J_{gn}} - \frac{k_L}{2J_r} + \frac{k_H - k_L}{2J_{gr}})^2 + \frac{k_H k_L}{J_{gr}^2}} + \frac{k_H}{2J_{gn}} + \frac{k_L}{2J_r} + \frac{k_H + k_L}{2J_{gr}}$, and

$B = \sqrt{(\frac{k_H}{2J_{gn}} - \frac{k_L}{2J_r} + \frac{k_H - k_L}{2J_{gr}})^2 + \frac{k_H k_L}{J_{gr}^2}} + \frac{k_H}{2J_{gn}} + \frac{k_L}{2J_r} + \frac{k_H + k_L}{2J_{gr}}$.

$\Psi_{rot}^{\Omega_1}$, $\Psi_{gear}^{\Omega_1}$ and $\Psi_{gen}^{\Omega_1}$ are normal modes at rotor, gearbox and generator due to the 1^{st} mode. $\Psi_{rot}^{\Omega_2}$, $\Psi_{gear}^{\Omega_2}$ and $\Psi_{gen}^{\Omega_2}$ are the same parameters for the 2^{nd} mode.

Appendix B. Sensitivity of natural frequencies to the system parameters

The equations describing the sensitivity of natural frequencies to the system parameters are summarized as follows. For this case, there are two natural frequencies and five parameters which results in ten different sensitivity functions.

$$S_{1,1}^{norm} = \frac{k_L}{2} \frac{\frac{(\frac{1}{J_{gr}} + \frac{1}{J_r})(\frac{k_H}{2J_{gn}} - \frac{k_L}{2J_r} + \frac{k_H - k_L}{2J_{gr}}) - \frac{k_H}{J_{gr}^2}}{\sqrt{(\frac{k_H}{J_{gn}} - \frac{k_L}{J_r} + \frac{k_H - k_L}{J_{gr}})^2 + \frac{4k_L k_H}{J_{gr}^2}}} + \frac{1}{2J_{gr}} + \frac{1}{2J_r}}{\frac{k_H}{2J_{gn}} - \sqrt{(\frac{k_H}{2J_{gn}} - \frac{k_L}{2J_r} + \frac{k_H - k_L}{2J_{gr}})^2 + \frac{k_L k_H}{J_{gr}^2}} + \frac{k_L}{2J_r} + \frac{k_H + k_L}{2J_{gr}}}, \tag{B.1}$$

$$S_{2,1}^{norm} = \frac{k_L}{2} \frac{(\frac{1}{2J_{gr}} - \frac{(\frac{1}{J_{gr}} + \frac{1}{J_r})(\frac{k_H}{2J_{gn}} - \frac{k_L}{2J_r} + \frac{k_H - k_L}{2J_{gr}}) - \frac{k_H}{J_{gr}^2}}{\sqrt{(\frac{k_H}{J_{gn}} - \frac{k_L}{J_r} + \frac{k_H - k_L}{J_{gr}})^2 + \frac{4k_L k_H}{J_{gr}^2}}} + \frac{1}{2J_r})}{\sqrt{(\frac{k_H}{2J_{gn}} - \frac{k_L}{2J_r} + \frac{k_H - k_L}{2J_{gr}})^2 + \frac{k_L k_H}{J_{gr}^2}} + \frac{k_H}{2J_{gn}} + \frac{k_L}{2J_r} + \frac{k_H + k_L}{2J_{gr}}}, \tag{B.2}$$

$$S_{1,2}^{norm} = \frac{k_H}{2} \frac{\frac{1}{2J_{gn}} - \frac{(\frac{1}{J_{gr}} + \frac{1}{J_r})(\frac{k_H}{2J_{gn}} - \frac{k_L}{2J_r} + \frac{k_H - k_L}{2J_{gr}}) + \frac{k_L}{J_{gr}^2}}{\sqrt{(\frac{k_H}{J_{gn}} - \frac{k_L}{J_r} + \frac{k_H - k_L}{J_{gr}})^2 + \frac{4k_L k_H}{J_{gr}^2}}} + \frac{1}{2J_{gr}}}{\frac{k_H}{2J_{gn}} - \sqrt{(\frac{k_H}{2J_{gn}} - \frac{k_L}{2J_r} + \frac{k_H - k_L}{2J_{gr}})^2 + \frac{k_L k_H}{J_{gr}^2}} + \frac{k_L}{2J_r} + \frac{k_H + k_L}{2J_{gr}}}, \tag{B.3}$$

$$S_{2,2}^{norm} = \frac{k_H}{2} \frac{\frac{(\frac{1}{J_{gn}}+\frac{1}{J_{gr}})(\frac{k_H}{2J_{gn}}-\frac{k_L}{2J_r}+\frac{k_H-k_L}{2J_{gr}})+\frac{k_L}{J_{gr}^2}}{\sqrt{(\frac{k_H}{J_{gn}}-\frac{k_L}{J_r}+\frac{k_H-k_L}{J_{gr}})^2+\frac{4k_Lk_H}{J_{gr}^2}}} + \frac{1}{2J_{gn}} + \frac{1}{2J_{gr}}}{\sqrt{(\frac{k_H}{2J_{gn}} - \frac{k_L}{2J_r} + \frac{k_H-k_L}{2J_{gr}})^2 + \frac{k_Lk_H}{J_{gr}^2}} + \frac{k_H}{2J_{gn}} + \frac{k_L}{2J_r} + \frac{k_H+k_L}{2J_{gr}}}}, \tag{B.4}$$

$$S_{1,3}^{norm} = -\frac{J_r}{2} \frac{\frac{k_L}{2J_r^2} + \frac{k_L(\frac{k_H}{2J_{gn}}-\frac{k_L}{2J_r}+\frac{k_H-k_L}{2J_{gr}})}{2J_r^2\sqrt{(\frac{k_H}{2J_{gn}}-\frac{k_L}{2J_r}+\frac{k_H-k_L}{2J_{gr}})^2+\frac{k_Lk_H}{J_{gr}^2}}}}{\frac{k_H}{2J_{gn}} - \sqrt{(\frac{k_H}{2J_{gn}} - \frac{k_L}{2J_r} + \frac{k_H-k_L}{2J_{gr}})^2 + \frac{k_Lk_H}{J_{gr}^2}} + \frac{k_L}{2J_r} + \frac{k_H+k_L}{2J_{gr}}}, \tag{B.5}$$

$$S_{2,3}^{norm} = -\frac{J_r}{2} \frac{\frac{k_L}{2J_r^2} - \frac{k_L(\frac{k_H}{2J_{gn}}-\frac{k_L}{2J_r}+\frac{k_H-k_L}{2J_{gr}})}{2J_r^2\sqrt{(\frac{k_H}{2J_{gn}}-\frac{k_L}{2J_r}+\frac{k_H-k_L}{2J_{gr}})^2+\frac{k_Lk_H}{J_{gr}^2}}})}{\sqrt{(\frac{k_H}{2J_{gn}} - \frac{k_L}{2J_r} + \frac{k_H-k_L}{2J_{gr}})^2 + \frac{k_Lk_H}{J_{gr}^2}} + \frac{k_H}{2J_{gn}} + \frac{k_L}{2J_r} + \frac{k_H+k_L}{2J_{gr}}}, \tag{B.6}$$

$$S_{1,4}^{norm} = -\frac{J_{gr}}{2} \frac{\frac{k_H+k_L}{2J_{gr}^2} - \frac{\frac{2k_Lk_H}{J_{gr}^3}+\frac{(k_H-k_L)(\frac{k_H}{2J_{gn}}-\frac{k_L}{2J_r}+\frac{k_H-k_L}{2J_{gr}})}{J_{gr}^2}}{2\sqrt{(\frac{k_H}{2J_{gn}}-\frac{k_L}{2J_r}+\frac{k_H-k_L}{2J_{gr}})^2+\frac{k_Lk_H}{J_{gr}^2}}}}{\frac{k_H}{2J_{gn}} - \sqrt{(\frac{k_H}{2J_{gn}} - \frac{k_L}{2J_r} + \frac{k_H-k_L}{2J_{gr}})^2 + \frac{k_Lk_H}{J_{gr}^2}} + \frac{k_L}{2J_r} + \frac{k_H+k_L}{2J_{gr}}}, \tag{B.7}$$

$$S_{2,4}^{norm} = -\frac{J_{gr}}{2} \frac{\frac{\frac{2k_Lk_H}{J_{gr}^3}+\frac{(k_H-k_L)(\frac{k_H}{2J_{gn}}-\frac{k_L}{2J_r}+\frac{k_H-k_L}{2J_{gr}})}{J_{gr}^2}}{2\sqrt{(\frac{k_H}{2J_{gn}}-\frac{k_L}{2J_r}+\frac{k_H-k_L}{2J_{gr}})^2+\frac{k_Lk_H}{J_{gr}^2}}} + \frac{k_H+k_L}{2J_{gr}^2}}{\sqrt{(\frac{k_H}{2J_{gn}} - \frac{k_L}{2J_r} + \frac{k_H-k_L}{2J_{gr}})^2 + \frac{k_Lk_H}{J_{gr}^2}} + \frac{k_H}{2J_{gn}} + \frac{k_L}{2J_r} + \frac{k_H+k_L}{2J_{gr}}}, \tag{B.8}$$

$$S_{1,5}^{norm} = -\frac{J_{gn}}{2} \frac{\frac{k_H}{2J_{gn}^2} - \frac{k_H(\frac{k_H}{2J_{gn}}-\frac{k_L}{2J_r}+\frac{k_H-k_L}{2J_{gr}})}{2J_{gn}^2\sqrt{(\frac{k_H}{2J_{gn}}-\frac{k_L}{2J_r}+\frac{k_H-k_L}{2J_{gr}})^2+\frac{k_Lk_H}{J_{gr}^2}}}}{\frac{k_H}{2J_{gn}} - \sqrt{(\frac{k_H}{2J_{gn}} - \frac{k_L}{2J_r} + \frac{k_H-k_L}{2J_{gr}})^2 + \frac{k_Lk_H}{J_{gr}^2}} + \frac{k_L}{2J_r} + \frac{k_H+k_L}{2J_{gr}}}, \tag{B.9}$$

$$S_{2,5}^{norm} = -\frac{J_{gn}}{2} \frac{\frac{k_H}{2J_{gn}^2} + \frac{k_H(\frac{k_H}{2J_{gn}}-\frac{k_L}{2J_r}+\frac{k_H-k_L}{2J_{gr}})}{2J_{gn}^2\sqrt{(\frac{k_H}{2J_{gn}}-\frac{k_L}{2J_r}+\frac{k_H-k_L}{2J_{gr}})^2+\frac{k_Lk_H}{J_{gr}^2}}}}{\sqrt{(\frac{k_H}{2J_{gn}} - \frac{k_L}{2J_r} + \frac{k_H-k_L}{2J_{gr}})^2 + \frac{k_Lk_H}{J_{gr}^2}} + \frac{k_H}{2J_{gn}} + \frac{k_L}{2J_r} + \frac{k_H+k_L}{2J_{gr}}}, \tag{B.10}$$

Appendix C. Sensitivity of normal modes to the system parameters

The sensitivity of normal modes to parameters variations can be defined for each element of eigenvector associated to each eigenfrequency. Therefore, for the under consideration 3-DOF model with two nonrigid modes, and five parameters of system, thirty different sensitivity functions are derived. For instance, the sensitivity of the eigenvector element related to gearbox, due to the 1^{st} and 2^{nd} modes, to variations in system parameters are brought as follows:

$$S_{5,1}^{norm} = \frac{-K_L\left(\frac{2K_L(K_L - J_rA + K_L(J_r(\frac{2(\frac{1}{2J_{gr}} + \frac{1}{2J_r})P - \frac{K_H}{J_{gr}^2}}{2Q} + \frac{1}{2J_{gr}} + \frac{1}{2J_r}) - 1))}{(K_L - J_rA)^3} + \frac{2J_{gn}K_H^2\left(\frac{2(\frac{1}{2J_{gr}} + \frac{1}{2J_r})P - \frac{K_H}{J_{gr}^2}}{2Q} + \frac{1}{2J_{gr}} + \frac{1}{2J_r}\right)}{(K_H - J_{gn}A)^3}\right)}{2\left(\frac{K_H^2}{(K_H - J_{gn}A)^2} + \frac{K_L^2}{(K_L - J_rA)^2} + 1\right)} \tag{C.1}$$

$$S_{5,2}^{norm} = \frac{-K_H\left(\frac{2K_H(K_H - J_{gn}A + K_H(J_{gn}(\frac{1}{2J_{gn}} - \frac{2(\frac{1}{2J_{gn}} + \frac{1}{2J_{gr}})P + \frac{K_L}{J_{gr}^2}}{2Q} + \frac{1}{2J_{gr}}) - 1))}{(K_H - J_{gn}A)^3} + \frac{2J_rK_L^2\left(\frac{1}{2J_{gn}} - \frac{2(\frac{1}{2J_{gn}} + \frac{1}{2J_{gr}})P + \frac{K_L}{J_{gr}^2}}{2Q} + \frac{1}{2J_{gr}}\right)}{(K_L - J_rA)^3}\right)}{2\left(\frac{K_H^2}{(K_H - J_{gn}A)^2} + \frac{K_L^2}{(K_L - J_rA)^2} + 1\right)} \tag{C.2}$$

$$S_{5,3}^{norm} = \frac{-J_r\left(\frac{2K_L^2(A - J_r(\frac{K_L}{2J_r^2} + \frac{K_LP}{2J_r^2Q}))}{(K_L - J_rA)^3} - \frac{2J_{gn}K_H^2(\frac{K_L}{2J_r^2} + \frac{K_LP}{2J_r^2Q})}{(K_H - J_{gn}A)^3}\right)}{2\left(\frac{K_H^2}{(K_H - J_{gn}A)^2} + \frac{K_L^2}{(K_L - J_rA)^2} + 1\right)} \tag{C.3}$$

$$S_{5,4}^{norm} = \frac{-J_{gr}\left(\frac{2J_{gn}K_H^2(\frac{\frac{2K_HK_L}{J_{gr}^3} + \frac{(K_H - K_L)P}{J_{gr}^2}}{2Q} - \frac{K_H + K_L}{2J_{gr}^2})}{(K_H - J_{gn}A)^3} + \frac{2J_rK_L^2(\frac{\frac{2K_HK_L}{J_{gr}^3} + \frac{(K_H - K_L)P}{J_{gr}^2}}{2Q} - \frac{K_H + K_L}{2J_{gr}^2})}{(K_L - J_rA)^3}\right)}{2\left(\frac{K_H^2}{(K_H - J_{gn}A)^2} + \frac{K_L^2}{(K_L - J_rA)^2} + 1\right)} \tag{C.4}$$

$$S_{5,5}^{norm} = \frac{-J_{gn}\left(\frac{2K_H^2(A - J_{gn}(\frac{K_H}{2J_{gn}^2} - \frac{K_HP}{2J_{gn}^2Q}))}{(K_H - J_{gn}A)^3} - \frac{2J_rK_L^2(\frac{K_H}{2J_{gn}^2} - \frac{K_HP}{2J_{gn}^2Q})}{(K_L - J_rA)^3}\right)}{2\left(\frac{K_H^2}{(K_H - J_{gn}A)^2} + \frac{K_L^2}{(K_L - J_rA)^2} + 1\right)} \tag{C.5}$$

$$S_{6,1}^{norm} = \frac{-K_L\left(\frac{2K_L(K_L - J_rB + K_L(J_r(\frac{1}{2J_{gr}} - \frac{2(\frac{1}{2J_{gr}} + \frac{1}{2J_r})P - \frac{K_H}{J_{gr}^2}}{2Q} + \frac{1}{2J_r}) - 1))}{(K_L - J_rB)^3} + \frac{2J_{gn}K_H^2(\frac{1}{2J_{gr}} - \frac{2(\frac{1}{2J_{gr}} + \frac{1}{2J_r})P - \frac{K_H}{J_{gr}^2}}{2Q} + \frac{1}{2J_r})}{(K_H - J_{gn}B)^3}\right)}{2\left(\frac{K_H^2}{(K_H - J_{gn}B)^2} + \frac{K_L^2}{(K_L - J_rB)^2} + 1\right)} \tag{C.6}$$

$$S_{6,2}^{norm} = \frac{-K_H\left(\frac{2K_H(K_H - J_{gn}B + (K_H(J_{gn}(\frac{2(\frac{1}{2J_{gn}} + \frac{1}{2J_{gr}})P + \frac{K_L}{J_{gr}^2}}{2Q} + \frac{1}{2J_{gn}} + \frac{1}{2J_{gr}}) - 1)))}{(K_H - J_{gn}B)^3} + \frac{2J_rK_L^2(\frac{2(\frac{1}{2J_{gn}} + \frac{1}{2J_{gr}})P + \frac{K_L}{J_{gr}^2}}{2Q} + \frac{1}{2J_{gn}} + \frac{1}{2J_{gr}})}{(K_L - J_rB)^3}\right)}{2\left(\frac{K_H^2}{(K_H - J_{gn}B)^2} + \frac{K_L^2}{(K_L - J_rB)^2} + 1\right)} \tag{C.7}$$

$$S_{6,3}^{norm} = \frac{-J_r\left(\frac{2K_L^2(B - J_r(\frac{K_L}{2J_r^2} - \frac{K_LP}{2J_r^2Q}))}{(K_L - J_rB)^3} - \frac{2J_{gn}K_H^2(\frac{K_L}{2J_r^2} - \frac{K_LP}{2J_r^2Q})}{(K_H - J_{gn}B)^3}\right)}{2\left(\frac{K_H^2}{(K_H - J_{gn}B)^2} + \frac{K_L^2}{(K_L - J_rB)^2} + 1\right)} \tag{C.8}$$

$$S_{6,4}^{norm} = \frac{J_{gr}\left(\frac{2J_{gn}K_H^2(\frac{\frac{2K_HK_L}{J_{gr}^3} + \frac{(K_H - K_L)P}{J_{gr}^2}}{2Q} + \frac{K_H + K_L}{2J_{gr}^2})}{(K_H - J_{gn}B)^3} + \frac{2J_rK_L^2(\frac{\frac{2K_HK_L}{J_{gr}^3} + \frac{(K_H - K_L)P}{J_{gr}^2}}{2Q} + \frac{K_H + K_L}{2J_{gr}^2})}{(K_L - J_rB)^3}\right)}{2\left(\frac{K_H^2}{(K_H - J_{gn}B)^2} + \frac{K_L^2}{(K_L - J_rB)^2} + 1\right)} \tag{C.9}$$

$$S_{6,5}^{norm} = \frac{-J_{gn}\left(\frac{2K_H^2(B-J_{gn}(\frac{K_H}{2J_{gn}^2}+\frac{K_H P}{2J_{gn}^2 Q}))}{(K_H-J_{gn}B)^3} - \frac{2J_r K_L^2(\frac{K_H}{2J_{gn}^2}+\frac{K_H P}{2J_{gn}^2 Q})}{(K_L-J_r B)^3}\right)}{2(\frac{K_H^2}{(K_H-J_{gn}B)^2}+\frac{K_L^2}{(K_L-J_r B)^2}+1)} \tag{C.10}$$

where

$P = \frac{K_H}{2J_{gn}} - \frac{K_L}{2J_r} + \frac{K_H - K_L}{2J_{gr}}$ and $Q = \sqrt{P^2 + \frac{K_H K_L}{J_{gr}^2}}$.

Appendix D. Sensitivity of amplitude of response at the natural frequencies to the system parameters and loads

The sensitivity of amplitude of response at the natural frequencies to system parameters and loads can be defined for the two natural frequencies with respect to the seven system parameters and the two input/output loads which results in eighteen different cases. In the following, the closed form equations of the sensitivity analysis associated to 1^{st} and 2^{nd} torsional frequencies with respect to both the input and output loads are shown:

$$S_{9,8}^{norm} = \frac{T_r\sqrt{EA+G+J_{gr}^2J_{gn}^2A^2}\sqrt{A}}{2(T_g\sqrt{FA+V+J_r^2J_{gr}^2A^2}\sqrt{A}+T_r\sqrt{EA+G+J_{gr}^2J_{gn}^2A^2}\sqrt{A})} \tag{D.1}$$

$$S_{9,9}^{norm} = \frac{T_g\sqrt{FA+V+J_r^2J_{gr}^2A^2}\sqrt{A}}{2(T_g\sqrt{FA+V+J_r^2J_{gr}^2A^2}\sqrt{A}+T_r\sqrt{EA+G+J_{gr}^2J_{gn}^2A^2}\sqrt{A})} \tag{D.2}$$

$$S_{10,8}^{norm} = \frac{T_r\sqrt{EB+G+J_{gr}^2J_{gn}^2B^2}\sqrt{B}}{2(T_g\sqrt{FB+V+J_r^2J_{gr}^2B^2}\sqrt{B}+T_r\sqrt{EB+G+J_{gr}^2J_{gn}^2B^2}\sqrt{B})} \tag{D.3}$$

$$S_{10,9}^{norm} = \frac{T_g\sqrt{FB+V+J_r^2J_{gr}^2B^2}\sqrt{B}}{2(T_g\sqrt{FB+V+J_r^2J_{gr}^2B^2}\sqrt{B}+T_r\sqrt{EB+G+J_{gr}^2J_{gn}^2B^2}\sqrt{B})} \tag{D.4}$$

References

[1] Ioannou, A., Angus, A. and Brennan, F., 2018. Parametric CAPEX, OPEX, and LCOE expressions for offshore wind farms based on global deployment parameters. Energy Sources, Part B: Economics, Planning, and Policy, 13(5), 281-290.

[2] Pfaffel, S., Faulstich, S. and Rohrig, K., 2017. Performance and reliability of wind turbines: A review. energies, 10(11), 1904.

[3] El-Kafafy, M., Gioia, N., Guillaume, P. and Helsen, J., 2019. Long-term automatic tracking of the modal parameters of an offshore wind turbine drivetrain system in standstill condition. *In Rotating Machinery, Vibro-Acoustics & Laser Vibrometry*, Vol. 7 (pp. 91-99).

[4] Gioia, N., Daems, P.J., Peeters, C., Guillaume, P., Helsen, J., Medico, R., Deschrijver, D. and Dhaene, T., 2019, June. Gaining insight in wind turbine drivetrain dynamics by means of automatic operational modal analysis combined with machine learning algorithms. *In ASME International Conference on Offshore Mechanics and Arctic Engineering* (Vol. 58899, p. V010T09A017).

[5] El-Kafafy, M., Colanero, L., Gioia, N., Devriendt, C., Guillaume, P. and Helsen, J., 2017. Modal parameters estimation of an offshore wind turbine using measured acceleration signals from the drivetrain. *In Struc. Health Monitoring& Damage Detection*, 7, pp.41-48.

[6] Márquez, F. P. G., Tobias, A. M., Pérez, J. M. P. and Papaelias, M., 2012. Condition monitoring of wind turbines: Techniques and methods. Renewable Energy, 46, 169-178.

[7] Artigao, E., Honrubia-Escribano, A. and Gomez-Lazaro, E., 2018. Current signature analysis to monitor DFIG wind turbine generators: A case study. Renewable Energy, 116, 5-14.

[8] Soua, S., Van Lieshout, P., Perera, A., Gan, T. H. and Bridge, B., 2013. Determination of the combined vibrational and acoustic emission signature of a wind turbine gearbox and generator shaft in service as a pre-requisite for effective condition monitoring. Renewable Energy, 51, 175-181.

[9] Yang, W., Tavner, P. J., Crabtree, C. J., Feng, Y. and Qiu, Y., 2014. Wind turbine condition monitoring: technical and commercial challenges. Wind Energy, 17(5), 673-693.

[10] Tonks, O. and Wang, Q., 2017. The detection of wind turbine shaft misalignment using temperature monitoring. CIRP Journal of Manufacturing Science and Technology, 17, 71-79.

[11] Feng, Y., Qiu, Y., Crabtree, C. J., Long, H. and Tavner, P. J., 2013. Monitoring wind turbine gearboxes. Wind Energy, 16(5), 728-740.

[12] Chen, S., Du, M., Peng, Z., Feng, Z. and Zhang, W., 2020. Fault diagnosis of planetary gearbox under variable-speed conditions using an improved adaptive chirp mode decomposition. Journal of Sound and Vibration, 468, 115065.

[13] Qiao, W. and Lu, D., 2015. A survey on wind turbine condition monitoring and fault diagnosis—Part II: Signals and signal processing methods. IEEE Transactions on Industrial Electronics, 62(10), 6546-6557.

[14] Maynard, K. and Trethewey, M., 2001. Blade and shaft crack detection using torsional vibration measurements part 3: field application demonstrations. Noise & Vibration Worldwide, 32(11), 16-23.

[15] Moghadam, F.K., and Nejad, A.R., 2019. Experimental validation of angular velocity measurements for wind turbines drivetrain condition monitoring. *Accepted by Proceedings of* 2^{nd} *International Offshore Wind Technical Conference (IOWTC) 2019.*

[16] Suominen, M., Karhunen, J., Bekker, A., Kujala, P., Elo, M., Enlund, H. and Saarinen, S., 2013. Full-scale measurements on board PSRV SA Agulhas II in the Baltic Sea. In Proceedings of the International Conference on Port and Ocean Engineering Under Arctic Conditions.

[17] Patel, T.H. and Darpe, A.K., 2009. Coupled bending-torsional vibration analysis of rotor with rub and crack. *Journal of Sound and Vibration*, 326(3-5), pp.740-752.

[18] Feng, Z. and Zuo, M.J., 2013. Fault diagnosis of planetary gearboxes via torsional vibration signal analysis. *Mechanical Systems and Signal Processing*, 36(2), pp.401-421.

[19] Lebold, M.S., Maynard, K., Reichard, K., Trethewey, M., Bieryla, D., Lissenden, C. and Dobbins, D., 2004, March. Using torsional vibration analysis as a synergistic method for crack detection in rotating equipment. *IEEE Aerospace Conf. Proc.*, Vol. 6, pp. 3517-3527.

[20] Kia, S.H., Henao, H. and Capolino, G.A., 2009. Torsional vibration assessment using induction machine electromagnetic torque estimation. *IEEE Transactions on Industrial Electronics*, 57(1), pp.209-219.

[21] Lu, B., Li, Y., Wu, X. and Yang, Z., 2009, June. A review of recent advances in wind turbine condition monitoring and fault diagnosis. *In 2009 IEEE Power Electronics and Machines in Wind Applications*, pp. 1-7.

[22] Nejad, A.R., Odgaard, P.F. and Moan, T., 2018. Conceptual study of a gearbox fault detection method applied on a 5-MW spar-type floating wind turbine. *Wind Energy*, 21(11), pp.1064-1075.

[23] Moghadam, F.K., and Nejad, A.R., 2020. Natural frequency estimation by using torsional response, and applications for wind turbine drivetrain fault diagnosis, Torque conference, accepted.

[24] Lebold, M. S., Maynard, K., Reichard, K., Trethewey, M., Bieryla, D., Lissenden, C. and Dobbins, D., 2004, March. Using torsional vibration analysis as a synergistic method for crack detection in rotating equipment. IEEE Aerospace Conference Proceedings, 6, pp. 3517-3527.

[25] Jiang, M., Wu, J., Peng, X. and Li, X., 2017. Nonlinearity measure based assessment method for pedestal looseness of bearing-rotor systems. Journal of Sound and Vibration, 411, 232-246.

[26] Liu, Y., Zhao, Y., Lang, Z. Q., Li, J., Yan, X., Zhao, S. (2019). Weighted contribution rate of nonlinear output frequency response functions and its application to rotor system fault diagnosis. Journal of Sound and Vibration, 460, 114882.

[27] Chatterton, S., Pennacchi, P., Vania, A. and Rubio, P., 2019. Analysis of the periodic breathing of a transverse annular crack propagated in a real rotating machine. Engineering Failure Analysis, 99, pp. 126-140.

[28] Thomson, W., 2018. Theory of vibration with applications. CrC Press.

[29] Lissenden, C.J., Tissot, S.P., Trethewey, M.W. and Maynard, K.P., 2007. Torsion response of a cracked stainless steel shaft. *Fatigue and fracture of engineering materials and structures*, 30(8), pp.734-747.

[30] Morio, J., 2011. Global and local sensitivity analysis methods for a physical system. *European Journal of Physics*. 32. 1577.

[31] Moghadam, F.K., and Nejad, A.R., 2019. Evaluation of PMSG-based drivetrain technologies for 10 MW floating offshore wind turbines: pros and cons in a life-cycle perspective. *Accepted by Wind Energy*.

[32] Saltelli, A., Tarantola, S. and Chan, K.S., 1999. A quantitative model-independent method for global sensitivity analysis of model output. *Technometrics*, 41(1), pp.39-56.

[33] Karimirad, M. MARINTEK Numerical Tools for Coupled Aero-Hydro-Servo-Elastic Simulations of Offshore Wind Turbines. SINTEF. MARINTEK.[Accessed 2019].

[34] Rulka, W. (1990). SIMPACK—A computer program for simulation of large-motion multibody systems. In Multibody systems handbook (pp. 265-284). Springer, Berlin, Heidelberg.

[35] Licari, J., Ugalde-Loo, C.E., Ekanayake, J.B. and Jenkins, N., 2012. Damping of torsional vibrations in a variable-speed wind turbine. *IEEE Transactions on Energy Conversion*, 28(1), pp.172-180.

[36] Darpe, A. K., Gupta, K. and Chawla, A., 2004. Coupled bending, longitudinal and torsional vibrations of a cracked rotor. Journal of sound and vibration, 269(1-2), 33-60.

A.5 Paper 5

Paper 5:
Digital twin modeling for predictive maintenance of floating offshore wind turbine drivetrains.
Authors: Farid Khazaeli Moghadam, Geraldo Francisco de Souza Rebouças, Amir Rasekhi Nejad
Accepted to Springer Journal of Forschung im Ingenieurwesen.

Digital twin modeling for predictive maintenance of gearboxes in floating offshore wind turbine drivetrains

Farid K. Moghadam[1][0000-0002-0795-6887], Geraldo F. de S. Rebouças[1][0000-0001-7112-9512]

and Amir R. Nejad[1][0000-0003-0391-8696]

[1] Norwegian University of Science and Technology, Trondheim, Norway

Abstract. This paper presents a multi-degree of freedom torsional model of drivetrain system as the digital twin model for monitoring the remaining useful lifetime of the drivetrain components. An algorithm is proposed for the model identification, which receives the torsional response and estimated values of rotor and generator torques, and calculates the drivetrain dynamic properties, e.g. eigen values, and torsional model parameters. The applications of this model in prediction of gearbox remaining useful lifetime is discussed. The proposed method is computationally fast, and can be implemented by integrating with the current turbine control and monitoring system without a need for a new system and sensors installation. A test case, using 5 MW reference drivetrain, has been demonstrated.

Keywords: Drivetrain, digital twin model, modal estimation, remaining useful lifetime, torsional response.

1 Introduction

Power train system including rotor, main bearings, gearbox, generator and power converter accounts for *57%* of turbine total failures and *65%* of turbine total downtime [1]. The consequent costs are expected to be higher in floating wind turbines (FWT) due to costly and slow-going marine operations. In FWTs, the power train system is exposed to a wider range of excitations than bottom-fixed turbines due to synergistic impacts of wind, wake, currents and structural motions-induced vibrations [2]. Predictive maintenance is proposed in the literature as a support tool for the time base maintenance to reduce the unexpected shutdowns and the consequent downtimes while it can also help to optimize the inspection intervals. The motivation of this research is increasing the wind turbine (WT) availability by performing predictive maintenance of the drivetrain system through the digital twin models.

Digital twins are highly accurate but computationally fast models of the system which can be run in-line with the real machine. The model should be able to update itself by the online operational measurements, to capture the physical variations in the system over the time [3]. In this paper, digital twin is proposed as a tool for lifetime monitoring of the drivetrain system, and more specifically the gearbox, by using the torsional vibration measurements, which can be included in the farm Supervisory Control and Data Acquisition (SCADA) existing system by using higher resolution encod-

ers. The input data may also be provided by additional installations *e.g.* proximity sensors and angular accelerometers. Correa *et al.* [4] performs a review on the drivetrain components condition monitoring techniques and faults prediction in general and also by using the SCADA data. Digital twin is a proven technology which is used by Siemens Gamesa for prediction of drivetrain loads and subsequently improving the drivetrain design [5]. The application of digital twin for monitoring of the drivetrain lifetime may be looked as an expensive solution. However, in this work, it is shown that by using innovative approaches based on analysis of torsional measurements it is possible to offer computationally-fast solutions for monitoring the lifetime of the drivetrain critical components with a potential to be integrated with the currently available control and monitoring system with minimum additional cost. Digital twin in this context means the combination of model, online measurements and remaining useful lifetime (RUL) model as defined and suggested by [6].

Rebouças *et al*. [7] suggests the 14-DOF torsional model as a fair compromise between complexity and accuracy when the structural integrity of gearbox is taken into consideration. The structural integrity is mainly measured in terms of contact fatigue stresses of the gear pairs, so that this model can be used as the indicator for the gears contact loads. For this purpose, the applicability of a 14-DOF lumped-parameter torsional model of the drivetrain system as the digital twin model for monitoring the degradation in a high-speed drivetrain technology with a three-stages gearbox which consists of two planetary and one parallel stages is investigated. The algorithm for estimation of digital twin model parameters is based on a data-driven approach which operates based on the real-time drivetrain torsional measurements, and the estimated dynamic properties from the torsional response. The algorithm employed for estimation of dynamic properties, namely natural frequencies and damping from the torsional response is according to the modal estimation approach proposed by [8]. In order to estimate the moment of inertia of the components in the equivalent model, an optimization problem is defined based on the least square error between the digital twin model and the online measurements consisting of torsional response and estimated input torque. After all, the stiffness parameters of the model are estimated by using the equations of natural frequencies as a function of equivalent model parameters (stiffness and inertia). It is worth noting that the equivalent lumped parameter model of drivetrain in the proposed digital twin approach is linear. However, the eigenfrequencies of the drivetrain are nonlinear functions of equivalent model parameters. Since the assumption of accessibility of all the system dynamic states is optimistic, the problem is extend to a more general class of problem with a partial knowledge about the system modes. The parameters of the digital twin model are updated by using the real-time operational data. The most prevalent failures of the large gears in WT drivetrain systems are due to gear tooth root bending and pitting fatigue damage [9]. For monitoring the RUL of the gears in this work, the degradation of the gears due to pitting fatigue damage and the gear pairs contact loads are taken into consideration. The contact loads on the gear pairs are estimated by using the load observers designed for the gear pairs based on the real-time estimated digital twin model and torsional measurements. The employed model-based degradation model is based on stress-life method. The online estimated contact stress feeds the time-domain cycle counting approach based on rainflow method for online estimation of fatigue cycles, and then for estimation of fatigue damage for each gear

pair by using the Miner's rule. For all the simulation cases, the floating 5 MW NREL WT with a spar support substructure as a common way of realization of FWT is used. The reason for the latter is the higher motivation in FWT for predictive maintenance.

This paper is the proof of concept for the idea of near real-time estimation of the load and subsequently the residual life in the drivetrain components by using computationally efficient equivalent models estimated from torsional measurements supported by real-time values of torsional response. The proposed algorithm is able to estimate the equivalent model parameters by using only few measurement samples which feed a robust linear regression estimator designed to estimate the equivalent model parameters. On this basis, the main contributions of this work are:

- Proposing the 14-DOF equivalent lumped-parameter model as the digital twin of the drivetrain system for remaining useful lifetime monitoring of the gearbox,
- Proposing an algorithm for the near real-time estimation of the equivalent model parameters by using the torsional measurements,
- Designing computationally inexpensive load observers for the near real-time estimation of the contact load and stress on the gears in planetary and parallel stages of the drivetrain gearbox, by using equivalent model parameters and real-time torsional responses,
- Proposing a physics-based degradation model for near real-time estimation of the residual life of the gears in the drivetrain gearbox by using the online estimated equivalent model, real-time measurements, designed load observers and contact stress estimation approach,
- Simulation studies to evaluate the proposed digital twin approach for estimation of fatigue damage of the gears, and validation of the results by high-fidelity simulation models.

2 Methodology

2.1 Test case

NREL 5 MW reference wind turbine [10] with a spar floating support substructure is selected for this study. The wind turbine specification and the overall characteristics of the floating platform is obtained from [11]. This model is able to capture the global dynamics of spar floating wind turbine from the interaction with the environmental loads. The 5 MW reference drivetrain [12] is employed in this study.

2.2 Global simulation and estimation of drivetrain loads

The decoupled simulation approach is used for the drivetrain studies in this work. The latter means that the turbine global simulation results, namely the rotor aerodynamic load and the bedplate motions are applied to the detailed local drivetrain model in a secondary software. Then the drivetrain local load effects are obtained for further postprocessing aimed at monitoring the drivetrain remaining lifetime. More details on the utilized decoupled approach and the global simulation model is available in [11]. The wind is turbulent based on Kaimal distribution. The turbulence intensity at hub

height *I (-)* is assumed to be *0.14*, for all the wind speeds, according to IEC 61400-1 class B turbines. The wave is modelled stochastic by two parameters, namely significant wave height H_s (m) and peak period T_p (s) in global analysis.

2.3 Drivetrain torsional model as the digital twin model for predictive maintenance

The NREL 5 MW reference drivetrain proposed in [12] is considered in this study, considering only its torsional behavior. Figure 1 contains a schematic representation of the model used in this work. The gearbox is assumed to be clamped to the nacelle's bedplate by rigid torque arm supports, leading to no rotation of the ring gears. This model is based on [13], where the resonant behavior of a single-stage planetary gearbox is discussed. The equations of motion are shown in Eq. (1).

$$\mathbf{J}\ddot{\boldsymbol{\theta}} + \mathbf{D}\dot{\boldsymbol{\theta}} + \mathbf{K}\boldsymbol{\theta} = \mathbf{T}, \tag{1}$$

$$\boldsymbol{\theta} = [\theta_R \quad \boldsymbol{\theta}_1^T \quad \boldsymbol{\theta}_2^T \quad \boldsymbol{\theta}_3^T \quad \theta_G]^T, \qquad \mathbf{T} = [T_R \quad 0 \quad \cdots \quad 0 \quad T_G]^T, \tag{2}$$

In these equations, θ_k and T_k $(k \in \{R, 1, 2, 3, G\})$ represent torsional coordinate and external torques, respectively. The indexes R and G are associated with rotor and generator variables, respectively. The sub-vectors $\boldsymbol{\theta}_i$ $(i \in \{1, 2, 3\})$ refer to the gear stages, see Eqs. (3) and (6). The global inertia and stiffness matrices **J** and **K** are obtained from their local counterparts. The damping is defined using Rayleigh parameters, being proportional to the inertia and stiffness matrices **J** and **K**, *i.e.* $\mathbf{D} = \alpha\mathbf{J} + \beta\mathbf{K}$.

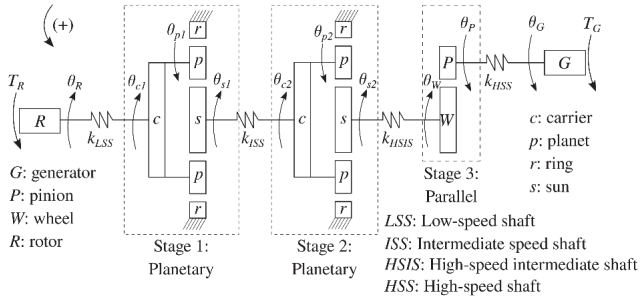

Fig. 1. Representation of the torsional model [7].

The local matrices for the planetary stages can be seen in Eqs. (3) to (5) and are based on the matrices used in [13], while the local matrices for the parallel stage, shown in Eq. (6), were obtained by isolating the sun-planet gear pair of the planetary stage. In these equations, θ, m, k, and r, represent the angular displacement, mass, stiffness and

base radius respectively. The indices c, p, s, P, and W represent the carrier, planet and sun elements of the i^{th} stage, respectively. The mesh stiffness between sun-planet, ring-planet and pinion-wheel gears is represented by k_{sp}, k_{rp}, and k_{PW}, respectively. In this work, the mesh stiffness between different gear pairs is calculated according to ISO 6336-2 [14], which takes a constant value. The center distance for planetary stages is represented by a_w [7]. Shafts are used to connect the adjacent inertia elements, such as the rotor, generator, and gear stages. The shafts were modelled using finite element theory leading to the shaft's inertia and stiffness matrices $\boldsymbol{J}_S$ and $\boldsymbol{K}_S$ in Eq. (7). Assembling the global matrices from the local matrices is illustrated in Fig. 2. In Eq. (7), D, L, and G represent the shaft's diameter, length, and the shear elasticity modulus of its material. The indices a and b on the shaft's displacement vector $\boldsymbol{\theta}_S$ represent DOFs adjacent to the shaft. For the high-speed intermediate shaft (HSIS), shown in Fig. 1, $a = s_2$ and $b = W$.

$$\boldsymbol{\theta}_i = [\theta_{c_i} \quad \theta_{p_{1i}} \quad \theta_{p_{2i}} \quad \theta_{p_{3i}} \quad \theta_{s_i}]^T, \qquad i = 1,2 \tag{3}$$

$$\mathbf{J}_i = \mathrm{diag}\left(\left[m_c a_w^2 \quad m_p r_p^2 \quad m_p r_p^2 \quad m_p r_p^2 \quad m_s r_s^2\right]\right), \tag{4}$$

$$\mathbf{K}_\mathrm{i} = \begin{bmatrix} 3a_w(k_{rp}+k_{sp}) & a_w r_p(k_{rp}-k_{sp}) & a_w r_p(k_{rp}-k_{sp}) & a_w r_p(k_{rp}-k_{sp}) & -3a_w r_s k_{sp} \\ a_w r_p(k_{rp}-k_{sp}) & r_p^2(k_{rp}+k_{sp}) & 0 & 0 & r_p r_s k_{sp} \\ a_w r_p(k_{rp}-k_{sp}) & 0 & r_p^2(k_{rp}+k_{sp}) & 0 & r_p r_s k_{sp} \\ a_w r_p(k_{rp}-k_{sp}) & 0 & 0 & r_p^2(k_{rp}+k_{sp}) & r_p r_s k_{sp} \\ -3a_w r_s k_{sp} & r_p r_s k_{sp} & r_p r_s k_{sp} & r_p r_s k_{sp} & 3r_s^2 k_{sp} \end{bmatrix} \tag{5}$$

$$\boldsymbol{\theta}_3 = [\theta_W \quad \theta_P]^T, \qquad \mathbf{J}_3 = \mathrm{diag}([m_w r_W^2 \quad m_P r_P^2]), \qquad \mathbf{K}_3 = k_{PW}\begin{bmatrix} r_W^2 & r_P r_W \\ r_P r_W & r_P^2 \end{bmatrix} \tag{6}$$

$$\boldsymbol{\theta}_S = [\theta_a \quad \theta_b]^T, \qquad \mathbf{J}_S = \frac{mD^2}{48}\begin{bmatrix} 2 & 1 \\ 1 & 2 \end{bmatrix}, \qquad \mathbf{K}_S = \frac{\pi G D^4}{32L}\begin{bmatrix} 1 & -1 \\ -1 & 1 \end{bmatrix}, \tag{7}$$

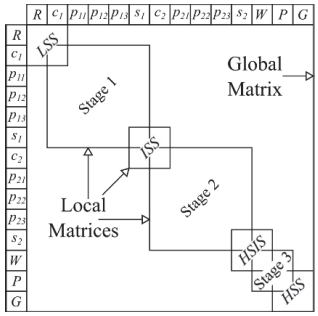

Fig. 2. Assembling the global matrices from their local equivalents [13].

The generator torque is realized by a proportional-integral (PI) speed controller, defined as

$$T_G = K_P \mathrm{e} + K_I \int_0^t e \mathrm{d}\tau\,, \qquad e = \omega_G - \dot{\theta}_G, \tag{8}$$

where the error e is given as the difference between reference and measured generator speedsω_G and $\dot{\theta}_G$, respectively. $K_P = 2200$ is the proportional gain and $K_I = 220$ is the integral gain.

2.4 Estimation of model parameters from torsional response

Drivetrain modal estimation

The torsional response residual function between the inertia $j_m$and j_n from the point m is defined as

$$e^{\alpha}_{m,n} \triangleq \alpha_m - u_{m,n}\alpha_n \text{ ,for } m, n \in \{1, \dots, 14\}, \tag{9}$$

with α is the angular acceleration, and $u_{m,n}$ is the relative gear ratio between $j_m$and j_n to make them in the same coordinate. Gear ratio $u_{m,n}$ as per definition is $\frac{N_m}{N_n}$, where N_m and N_n are the speeds at $m^{th}$and n^{th} inertias. The theoretical explanation of estimation of natural frequencies from the frequency spectrum of $e^{\alpha}_{m,n}$is provided by [8]. The different residual functions can be defined by using the response obtained from the different locations of drivetrain, which present different levels of visibility of the drivetrain torsional modes.

Estimation of moment of inertia matrix

By summing the moments on each of the inertias of the lumped parameter model yields 14 equations of the form

$$j_i\ddot{\theta}_i + D_i\left(\dot{\theta}_i - \dot{\theta}_{i-1}\right) - D_{i+1}\left(\dot{\theta}_{i+1} - \dot{\theta}_i\right) + k_i(\theta_i - \theta_{i-1}) - k_{i+1}(\theta_{i+1} - \theta_i) = 0, \quad \text{for } i = (1, \dots, 14). \tag{10}$$

In the matrix form, these set of equations can be written as

$$\mathbf{J}\ddot{\boldsymbol{\theta}}(t) + \mathbf{D}\dot{\boldsymbol{\theta}}(t) + \mathbf{K}\boldsymbol{\theta}(t) = \mathbf{T}\,. \tag{11}$$

Assuming that the load and response time series are known, the parameter estimation turns to the minimization of the L2 norm of error. The error function is defined by

$$\boldsymbol{E}(t) \triangleq \hat{\mathbf{J}}\ddot{\boldsymbol{\theta}}(t) + \hat{\mathbf{D}}\dot{\boldsymbol{\theta}}(t) + \hat{\mathbf{K}}\boldsymbol{\theta}(t) - \mathbf{T}(\mathrm{t})\,. \tag{12}$$

The least square estimator is defined by

$$\hat{\mathbf{J}}^{\mathbf{LS}}, \hat{\mathbf{K}}^{\mathbf{LS}}, \hat{\mathbf{D}}^{\mathbf{LS}} \in \underset{\mathbf{J},\mathbf{K},\mathbf{D} \geq \mathbf{0}}{\arg\ \min}\{\|\boldsymbol{E}\|^{\mathbf{2}}\}, \tag{13}$$

where **J** is a diagonal matrix. **K** and **D** are nondiagonal but symmetric matrices. The matrices D and K are not full rank. The latter causes some computational difficulty for the above quadratic matrix optimization problem, so that there is no guarantee for the

convergence. In order to remove the coupling between these equations due to the **K** and **D** terms, and to reduce the computational complexity by reduction of the number of variables, the equivalent scalar optimization problem is constructed by the sum of the individual equations of each inertia. The latter leads to the following error function in terms of the variables j_i with rotor as the reference of the rotary coordinate.

$$\boldsymbol{e}(t) = j_1\boldsymbol{\alpha_1}(t) + \cdots + a_{1,i}j_i\boldsymbol{\alpha_i}(t) + \cdots + a_{1,14}j_{14}\boldsymbol{\alpha_{14}}(t) - \boldsymbol{\tau^{Rot}}(t) - a_{1,14}\boldsymbol{\tau^{Gen}}(t), \tag{14}$$

where $\boldsymbol{\alpha_i}$ is the time series of angular acceleration at the i^{th} body. $\boldsymbol{\tau^{Rot}}$ and $\boldsymbol{\tau^{Gen}}$ are the time series of the rotor and generator torques respectively. The sign of $a_{1,i}$ is determined based on the direction of rotation of j_i. The latter leads to the following quadratic scalar optimization problem as

$$\hat{\boldsymbol{j}}^{LS} = \arg \min_{\boldsymbol{j} \geq 0}\{\|\boldsymbol{e}\|^2\}. \tag{15}$$

This estimator is robust to the measurement noises, and can provide a good approximation even with less than 14 input data samples (underdetermined case). For the case of more than 14 samples (overdetermined case), this estimator helps to obtain more accurate estimation than solving the linear equations, when the input measurements are subject to independent identically distributed (i.i.d.) Gaussian noise. In other words, the total LS technique is able to correct the system with minimum perturbation [15]. The above convex optimization problem is numerically solved by Matlab CVX and the global optimizer $\boldsymbol{j}^{LS} = \{j_1, \dots, j_{14}\}$ is estimated.

Estimation of stiffness matrix

The undamped torsional frequencies of the system are the nonlinear function of inertia and stiffness as

$$\boldsymbol{\omega}_i\ (for\ i = 1, \dots, 14) = \sqrt{eig(-\mathbf{J}^{-1}\mathbf{K})}\,. \tag{16}$$

By using the estimated natural frequencies obtained from the modal estimation approach together with the estimated inertia matrix **J** from the LS optimization problem, the stiffness matrix **K** is the root of $\boldsymbol{g}_i$ which is defined by the following nonlinear equation as

$$\boldsymbol{g}_i = \boldsymbol{\omega}_i{}^2 - eig(-\mathbf{J}^{-1}\mathbf{K}),\ (for\ i = 1, \dots, 14)\,. \tag{17}$$

In general, there is not a unique matrix **K** from the above equation for the known set of eigenvalues $\boldsymbol{\lambda_i} = \{\omega_1{}^2, \dots, \omega_{14}{}^2\}$ of the matrix $-\mathbf{J}^{-1}\mathbf{K}$. However, by imposing the sparsity and symmetricity to matrix K from the lumped model, it is possible to calculate the unique matrix **K** numerically by using Matlab fsolve solver. The latter also helps to reduce commutation cost of this matrix algebraic equation by reducing the number of variables from N^2 to N. The matrix $\mathbf{J}^{-1}\mathbf{K}$ is not symmetric in the general case which may give the sense that there are multiple answers for **K** from this equation. However the fact that $-\mathbf{J}^{-1}\mathbf{K}$ always has positive eigenvalues (it is positive definite), brings us

to the believe that this matrix is a small perturbation of a symmetric matrix with positive eigenvalues. Small perturbation keeps the eigenvalues positive [16].
The usual condition for the estimation problem is more restrictive. In other words, it is possible that only some of the eigenfrequencies of the drivetrain system can be estimated by employing the aforedescribed modal estimation approach, especially the higher eigenfrequencies which are excited with a lower energy of the input torque. In this case, the matrix **K** can still be estimated by using the following optimization problem in terms of the first n eigenfrequencies as defined by the following least square error estimator:

$$\hat{\boldsymbol{k}}^{LS} = \arg \min_{\boldsymbol{\Lambda} \in \Lambda} \{\|\boldsymbol{\lambda}_n - eig(\boldsymbol{\Lambda}, n)\|^2\}, \tag{18}$$

with $\boldsymbol{\Lambda}$ is the variable of this problem which is a function of the unknown variable **K** as $\boldsymbol{\Lambda} = -\mathbf{J}^{-1}\mathbf{K}$. Also $\hat{\boldsymbol{k}}^{LS}$ is the set of nonzero elements of matrix **K** which are estimated by the above nonlinear matrix optimization problem. The sign of the elements of $\boldsymbol{k}$ are forced in the optimization problem. $\boldsymbol{\lambda}_n$ is the set of n ($n \in \{1, \dots, 14\}$) smallest magnitude eigenvalues which are known from the modal estimation, $\boldsymbol{\lambda}_n = \{{\omega_1}^2, \dots, {\omega_n}^2\}$. $eig(\boldsymbol{\Lambda}, n)$ is the set of n ($(n \in \{1, \dots, 14\})$) smallest magnitude eigenvalues defined in terms of matrix **J** and the unknown matrix **K**. The feasible set Λ is also defined by

$$\Lambda = \{\boldsymbol{\Lambda}: \boldsymbol{\Lambda} \in \mathbb{R}^{14\times 14},\ \mathbf{K} \geq \mathbf{0},\ \boldsymbol{\Lambda}_{l,m} = 0, \forall\, \boldsymbol{\Lambda}_{l,m} \in \boldsymbol{S}^{\boldsymbol{\Lambda}}\}, \tag{19}$$

where $\boldsymbol{S}^{\boldsymbol{\Lambda}}$ is the sparsity of matrix $\boldsymbol{\Lambda}$. The positive definiteness and sparsity of $\boldsymbol{\Lambda}$ are the nonlinear constraints which are imposed to this problem. For the set of positive semidefinite matrices, this problem is convex and the solution is the global optimizer. However, $\boldsymbol{\Lambda}$ is not symmetric in general so that the definition of the problem is nonconvex for the numerical solvers and convex optimization tools are not able to numerically solve the problem. For this purpose, Matlab fmincon solver as a powerful tool for the general class of nonlinear nonconvex problems is used.

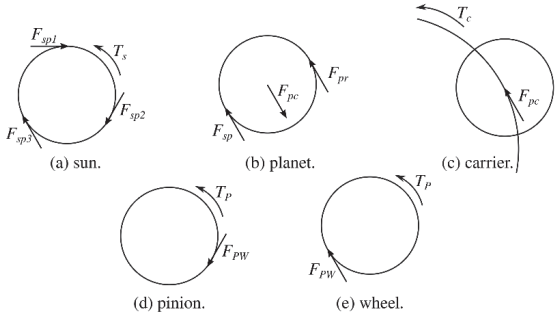

Fig. 3. Free-body diagrams for (a)-(c) planetary and (d)-(e) parallel gear stages.

2.5 Estimation of gearbox loads, and defining degradation model

Estimating contact stresses and loads at each stage

The free-body diagram for the gears in planetary and parallel stages can be seen in Fig. 3. For wind turbine gearboxes, the input and output torques for planetary (parallel) stages are the carrier (pinion) torque T_C (T_P) and the sun (wheel) torque T_s (T_W), respectively. From Fig. 3, one obtains Eqs. (20) and (21) as

Planetary stage:

$$\begin{aligned} J_s\ddot{\theta}_s &= T_S - N_p r_s F_{sp}, \\ J_p\ddot{\theta}_p &= \mathrm{r_p}\left(\mathrm{F_{pr}} - \mathrm{F_{sp}}\right) = -\mathrm{J_p}\frac{\mathrm{r_s}}{\mathrm{r_p}}\ddot{\theta}_s, \\ \mathrm{m_p a_w}\ddot{\theta}_c &= \mathrm{F_{pr}} + \mathrm{F_{sp}} - \mathrm{F_{pc}} = \mathrm{m_p a_w}\frac{\mathrm{r_s}}{\mathrm{r_s}+\mathrm{r_r}}\ddot{\theta}_s, \\ \mathrm{J_c}\ddot{\theta}_c &= \mathrm{T_c} - \mathrm{N_p r_s F_{sp}} = \mathrm{J_c}\frac{\mathrm{r_s}}{\mathrm{r_s}+\mathrm{r_r}}\ddot{\theta}_s, \end{aligned} \tag{20}$$

Parallel stage:

$$\begin{aligned} J_P\ddot{\theta}_P &= T_P - r_P F_{PW} = -J_P\frac{r_P}{r_W}\ddot{\theta}_W, \\ J_W\ddot{\theta}_W &= T_W - r_W F_{PW}, \end{aligned} \tag{21}$$

One can obtain the relationships between the input and output torques by eliminating the internal forces between elements. Speed relations are time differentiated which enables writing the contribution of inertial torques by using a single torsional acceleration and equivalent mass moment of inertia. For the planetary stage, one obtains

$$\begin{aligned} T_s &= J_{EQ}\ddot{\theta}_s - T_c\frac{r_s}{2a_w}, \ \textit{where} \\ J_{EQ} &= J_s + \frac{N_p r_s^2}{2}\left(\frac{J_p}{r_p^2} + m_p\frac{a_w}{r_s+r_r}\right) + J_c\frac{r_s^2}{2a_w(r_s+r_r)}, \end{aligned} \tag{22}$$

with J_{EQ} as the equivalent mass moment of inertia, having contributions from the sun, N_p planet gears and planet carrier. Similarly, for the parallel stage one has

$$\begin{aligned} T_W &= J_{EQ}\ddot{\theta}_W + T_P\frac{r_W}{r_P}, \\ J_{EQ} &= J_W + J_P\left(\frac{r_W}{r_P}\right)^2, \end{aligned} \tag{23}$$

with J_{EQ} having contributions from both pinion and wheel gears. The term multiplying the torque at the pinion is the gear ratio for parallel gears.
Torque transfer between stages is made via shafts, and can be estimated by

$$T_{out} = T_{in} - J_S\ddot{\theta}_S, \tag{24}$$

where $J_S\ddot{\theta}_S$ is the inertial torque from the shaft, [17]. Therefore, for the NREL 5 MW drivetrain, one should have

$$\begin{aligned} T_{in1} = T_{c1} = T_R - J_{LSS}\ddot{\theta}_R, \quad & T_{out1} = T_{s1} = J_{EQ1}\ddot{\theta}_{s1} - T_{in1}\frac{r_{s1}}{2a_{w1}}, \\ T_{in2} = T_{c2} = T_{out1} - J_{ISS}\ddot{\theta}_{s1}, \quad & T_{out2} = T_{s2} = J_{EQ2}\ddot{\theta}_{s2} - T_{in2}\frac{r_{s2}}{2a_{w2}}, \\ T_{in3} = T_P = T_G - J_{HSS}\ddot{\theta}_G, \quad & T_{out3} = T_W = J_{EQ3}\ddot{\theta}_W - T_{in3}\frac{r_W}{r_P}, \end{aligned} \tag{25}$$

The input torques estimated above can be used to estimate the stresses at the different gear stages as described below.

Gear contact stresses are analyzed in this work following ISO 6336-2:2019 [14]. According to this standard, the contact stresses are defined as

$$\sigma_{Hi} = Z_{BD}Z_H Z_E Z_\epsilon Z_\beta \sqrt{K_A K_{\gamma i} K_{vi} K_{H\beta i} K_{H\alpha i}} \sqrt{\frac{2000T_i}{bd_1^2}\frac{u+1}{u}}, \tag{26}$$

where u is the gear ratio of the pair, d_1 and b are reference diameter and face width of the pinion, respectively, T_i is the input torque. The other parameters account for different aspects of the problem, such as contact relations Z_{BD} and ratios Z_ϵ, material properties Z_E, helix angle Z_β, mesh load K_γ, gear speed K_v, load distributions $K_{H\beta i}$ and $K_{H\alpha i}$. These factors are discussed in [15] and references therein. Eq. (26) can be rewritten in a compact form as

$$\sigma_{Hi} = C\sqrt{T_i}, \tag{27}$$

where C represents the K and Z design parameters mentioned above. This parameter, unknown to the maintenance engineer, can be roughly estimated from nominal conditions as $C = \sigma_{HN}/\sqrt{T_{iN}}$, so that Eq. (27)**Error! Reference source not found.** turns to

$$\sigma_{Hi} = \sigma_{HN}\sqrt{\frac{T_i}{T_{iN}}}, \tag{28}$$

where σ_{Hi} is defined in terms of nominal contact stress σ_{HN} and torque T_{iN}, which have a clear physical meaning. Additionally, one can also expand Eq. (28) using Taylor series around the nominal torque T_{iN} as

$$\sigma_{Hi} - \sigma_{HN} = (T_i - T_{iN})\frac{\sigma_{HN}}{2T_{iN}} - (T_i - T_{iN})^2\frac{\sigma_{HN}}{8T_{iN}^2} + O((T_i - T_{iN})^3). \tag{29}$$

This formula gives a polynomial relationship between stress and load deviations. The accuracy of this expression for higher torque deviations can be increased by considering other terms of the Taylor series. The nominal stresses are of order 10^3 and the nominal torques vary between 10^4 and 10^6, thus unitary torque deviations lead to *0.05* to *5%* stress deviations, if only the first term of the series in Eq. (29) is considered. A limitation of this derivation is that C depends on parameters that may change with T_i, but these variations should be negligible.

Remaining useful lifetime estimation

The real-time accumulated damage is estimated as follows. First, the time-varying gear transmitted loads of the gear pairs of three gearbox stages are estimated by using the torque observers designed as explained in the previous part. The latter is based on the real-time aerodynamic and generator torques, and the time-varying digital twin model parameters. Then the gear tooth surface pitting stress is estimated for the differ-

ent gears as explained on above. The number of gear tooth contact stress cycles at different stress levels is counted by using the time-domain rainflow cycle counting approach [18]. The outputs are the amplitude stress level σ_s , and the number of stress cycles at $\sigma_s \; for \; s = (1, \dots, S)$. To consider the influence of nonzero mean stress level, Goodman rule is employed to calculate the effective stress (the equivalent zero mean alternating stress) by [19],

$$\sigma_s^e = \frac{\sigma_s}{1-\frac{\sigma_m}{\sigma_u}}, \forall \, (\mathrm{s} \in \{1, \dots, S\}), \tag{30}$$

where σ_m and σ_u are the mean stress and material yield strength, respectively. The accumulated pitting damage for the data block t with S different stress levels σ_s^e ($s \in \{1, \dots, S\}$) is calculated by using Miner's rule as

$$d^t = \sum_{s=1}^{S} \frac{n_s}{N_s}, \tag{31}$$

where n_s is the number of cycles at the stress level σ_s^e and N_s is the number of cycles to yield at stress level σ_s^e, where $N_s = k(\sigma_s^e)^{-m}$. The total absolute online accumulated damage will then be calculated by

$$D = \sum_{t=1}^{T} d^t, \tag{32}$$

where T stands for the last data block which represents the current time. This method can also be used for estimation of relative damage between different operational periods over the time, to give an insight on variations in degradation between different operational periods.

3 Simulation results

3.1 Aerodynamic and generator torques, and drivetrain torsional response

The input aerodynamic torque obtained from SIMO-RIFLEX-AeroDyn and the performance of the designed controller in controlling the generator torque under variable input torque to set the speed on the shaft is shown in Fig. 3. The drivetrain model responses are the angular displacement, velocity and acceleration in the different bodies in the described 14-DOF model. As an example, the angular velocity responses of the rotor and generator are shown in Fig. 3. For demonstration purposes the torques and response are scaled with the gear ratio. The turbine operation is assumed to be near the rated operation.

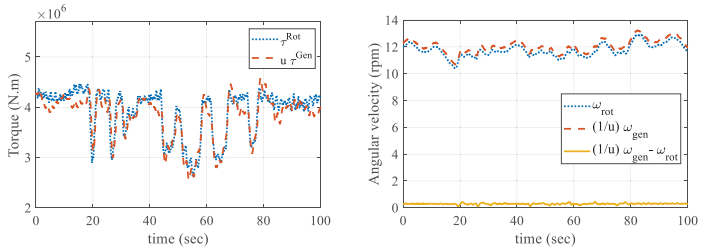

Fig. 4: Drivetrain model loads and responses (a) Rotor and generator torques, (b) Torsional response.

3.2 Estimation of dynamic properties and digital twin model parameters

The undamped frequency modes of the 14-DOF model for the healthy system are listed in the Table 1. The torsional response error function can be defined between different bodies in the drivetrain model. For example, the undamped natural frequencies estimated from the angular acceleration error function for the 2nd gearbox stage is shown in Fig. 5. The main feature of angular acceleration compared to angular velocity and displacement is the amplification of the higher natural frequencies in the response. By defining the angular acceleration error functions in terms of different pairs of bodies in the model, it is possible to estimate the different drivetrain modes. However, the significance of modes is different in the error functions defined between different bodies. As it can be seen in Fig. 5, the 6th and 7th modes are not visible in the error function of the 2nd stage, but they can be observed in the error function defined between rotor and generator bodies. The estimated natural frequencies by using the employed modal estimation approach based on angular acceleration error function are listed in the Table 1. The maximum relative error of estimation is less than *1.5%*. In practice, the torsional response in commercially available turbines is only accessible by the encoders placed on rotor and possibly generator shafts, so that some of the modes may not be observable by only using the error function between rotor and generator.

Table 1. 14-DOF drivetrain model natural frequencies (in Hz).

Mode	**1**	**2**	**3**	**4**	**5**	**6**	**7**	**8**	**9**	**10**	**11**	**12**	**13**	**14**
Healthy^{Actual}	0	2	120	153	208	567	716	716	971	1224	1232	1232	1384	1943
Healthy^{Estimated}	0	2	118	153	208	567	706	706	970	1220	1220	1220	1381	1933

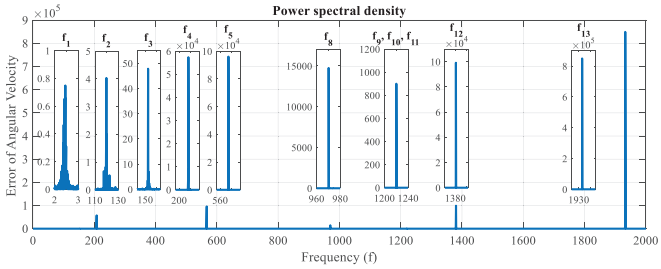

Fig. 5. Estimation of torsional modes from gearbox 2nd stage error function.

The influence of pitting on parameters of drivetrain equivalent model is usually represented by a decrease on the mesh stiffness of the faulty gear pair [20-21]. The NREL 5 MW drivetrain presented in Section 2.3 is used to illustrate this behavior, assuming that the early occurrence of pitting at the sun gear can lead to a 10% decrease in the sun-planet mesh stiffness. The 10% reduction of the faulty gear mesh stiffness assumed for modelling a very early stage fault might be high, but this assumption is made to demonstrate more clearly the influence of the fault on the variations of drivetrain dynamic properties. The results of the mentioned fault in the first and second gear stages can be seen in the second and third rows of Table 2, where one can see that pitting in the first stage sun gear affected mainly the 7th , 8th and 9th resonances, whereas pitting in the second stage sun gear affected mainly the 14th resonances. The results of fault simulation reported in Table 2 show that a 10% reduction in the sun-planet mesh stiffness of the first gear stage, results in around 2.5%, 2.5% and 4.5% reduction of 7th , 8th and 9th drivetrain natural frequencies, respectively, and a 10% reduction in the sun-planet mesh stiffness of the second gear stage, results in about 5% reduction of the highest natural frequency of drivetrain. The influence of pitting fault in the ring of first and second gear stages on the drivetrain natural frequencies are listed respectively in the fourth and fifth rows of Table 2. A 10% reduction in the ring-planet mesh stiffness of the first gear stage, results in around 5%, 3% and 3% reduction of 6th , 7th and 8th natural frequencies, and a 10% reduction in the ring-planet mesh stiffness of the second gear stage, results in the 3.5%, 4% and 5% reduction of 10th , 11th and 13th natural frequencies, respectively. Since the relative error of estimating the natural frequencies can be as high as 1.5%, variations of the natural frequencies which are less than 1.5% cannot be used as the indicator of fault. More detailed models of pitting fault can be engaged to capture more precisely the dynamics of fault [22] and consequent influence on the drivetrain dynamic properties, which is not the scope of this work. The influence of drivetrain faults at system-level on dynamic properties is analytically studied by [23]. Monitoring the variations in the drivetrain system natural frequencies can support the fault detection of the drivetrain at component-level, *e.g.* faults in the gears of the gearbox gear stages, which is also not the main scope of this work.

Table 2. 14-DOF drivetrain model natural frequencies in the different fault cases (in Hz).

Mode	1	2	3	4	5	6	7	8	9	10	11	12	13	14
$Healthy^{Actual}$	0	2	120	153	208	567	716	716	971	1224	1232	1232	1384	1943
$Fault^{sun}_{stage1}$	0	2	120	153	208	565	700	700	929	1224	1232	1232	1384	1943
$Fault^{sun}_{stage2}$	0	2	119	153	208	567	716	716	971	1220	1220	1224	1383	1850
$Fault^{ring}_{stage1}$	0	2	120	153	208	541	696	696	968	1224	1232	1232	1384	1943
$Fault^{ring}_{stage2}$	0	2	120	153	208	567	716	716	971	1181	1181	1224	1314	1941

The actual values of moment of inertia of the different bodies in the 14-DOF model and the performance of the designed LS estimator in estimation of those parameters from the torsional measurements based on the theory elaborated in Section 2 can be seen in the Table 3. The accuracy increases as the number of input samples increases while the data outliers are filtered to improve the estimation. The number of input samples can be selected to reach a good tradeoff between the accuracy and computational speed. The actual values of the diagonal elements of stiffness matrix as the main stiffness parameters are listed in the Table 3. In the case that the exact values of eigenfrequencies and inertia parameters are accessed, the solution of Eq. (16) gives the exact values of stiffness parameters. The estimated values of stiffness parameters of the main diagonal of the matrix, by considering both the natural frequencies and inertia parameters estimation errors, are listed in the Table 3. $Estimated^{M1}$ is the designation used to indicate that the first proposed stiffness estimation method which denotes the case that all the eigenfrequencies are accessed. $Estimated^{M2}$ indicates that the second method of stiffness estimation is used, which is associated to the case that some of the frequency modes are not observable. In order to calculate $Estimated^{M2}$, two different cases in which only the first ten and eleven estimated modes are available are simulated, and the optimization problem defined by the LS estimator in Eq. (18) is solved. The results are listed in the Table 4. The estimation error of the associated underdetermined LS estimator reduces as more frequency modes are known. It is worth noting that our extensive simulations show that high values of error in the input data of stiffness estimation problem, namely the estimated eigenfrequencies and inertia parameters, may cause instability of the nonlinear numerical solver in Eq. (16). From the stability perspective, the LS estimator outperforms the first method which is based on solving the nonlinear Eq. (16), because the eigenfrequencies of $\mathbf{\Lambda}$ in the LS estimator are forced to be positive, which ensures the convergence of the solver. In other words, $Estimated^{M2}$ is more robust to the input data, and is recommended also when all the frequency modes are available.

Table 3. Estimation of the digital twin model parameters by using the proposed approach.

Digital twin model parameters							
	Inertia				Stiffness		
	Actual	Estimated	Error (%)		Actual	Estimated^{M1}	Error (%)
j_1	57231658	57233035	0.0	$k_{R\text{-}R}$	933804433	930722878	0.3
j_2	11378	11406	0.2	$k_{c1\text{-}c1}$	68281102095	68267445875	0.0
j_3	218	218	0.2	$k_{p11\text{-}p11}$	4410016425	4402960399	0.2
j_4	218	218	0.2	$k_{p12\text{-}p12}$	4410016425	4402960399	0.2
j_5	218	218	0.2	$k_{p13\text{-}p13}$	4410016425	4402960399	0.2
j_6	351	352	0.2	$k_{s1\text{-}s1}$	8654576740	8643325790	0.1
j_7	2654	2658	0.1	$k_{c2\text{-}c2}$	93292722671	93115466498	0.2
j_8	214	215	0.1	$k_{p21\text{-}p21}$	12852864792	12820732630	0.3
j_9	214	215	0.1	$k_{p22\text{-}p22}$	12852864792	12820732630	0.3
j_{10}	214	215	0.1	$k_{p23\text{-}p23}$	12852864792	12820732630	0.3
j_{11}	15	15	0.2	$k_{s2\text{-}s2}$	1975494815	1971938924	0.2
j_{12}	1624	1625	0.0	$k_{W\text{-}W}$	6005991606	5992778424	0.2
j_{13}	8	8	0.0	$k_{P\text{-}P}$	469799716	468390317	0.3
j_{14}	537	537	0.0	$k_{G\text{-}G}$	95646856	95321657	0.3

Table 4. Estimated stiffness by Estimated^{M2}.

Error (%) by using Estimated^{M2}														
Parameter	$k_{R\text{-}R}$	$k_{c1\text{-}c1}$	$k_{p11\text{-}p11}$	$k_{p12\text{-}p12}$	$k_{p12\text{-}p12}$	$k_{p13\text{-}p13}$	$k_{s1\text{-}s1}$	$k_{c2\text{-}c2}$	$k_{p21\text{-}p21}$	$k_{p23\text{-}p23}$	$k_{s2\text{-}s2}$	$k_{W\text{-}W}$	$k_{P\text{-}P}$	$k_{G\text{-}G}$
10 modes	0.9	27.4	26.8	26.8	26.8	27.1	2.1	1.7	1.7	1.7	1.8	1.9	1.9	.9
11 modes	1.9	17.3	16.8	16.8	16.8	17.1	2.0	1.9	1.9	1.9	2.1	0.8	1.9	0.8

3.3 Loads, contact stress and accumulated damage

Contact load and stress validation on the three different gear stages

The input and output torques derived in Section 2.5 and shown in Eq. (25) can be seen in Fig. 6. There one can see that all torques present similar oscillating pattern around their nominal values, and that there is little difference between the output and input torques at adjacent stages, see Fig. 6 (d)-(b) and (e)-(c).

One can estimate the stresses at a sun-planet gear pair by inserting the input torques shown in Fig. 3 at the first order approximation using Taylor series, based on Eq. (12). The results for such operation can be seen in Fig. 6, together with results from high-fidelity Simpack multi-body simulation model of NREL 5 MW drivetrain reported in [12]. The results show reasonable agreement between the results for the simplified torsional model and the high-fidelity multi-body simulation platform.

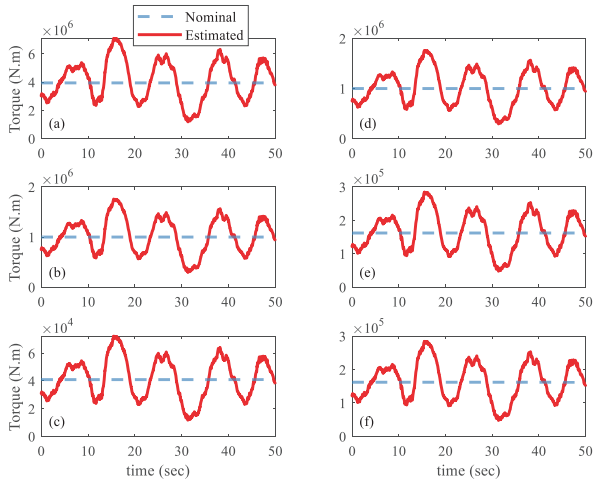

Fig. 6. Comparison between nominal and estimated torques. (a)-(c) input torques and (d)-(f) output torques at the 1st, 2nd, and 3rd stages respectively.

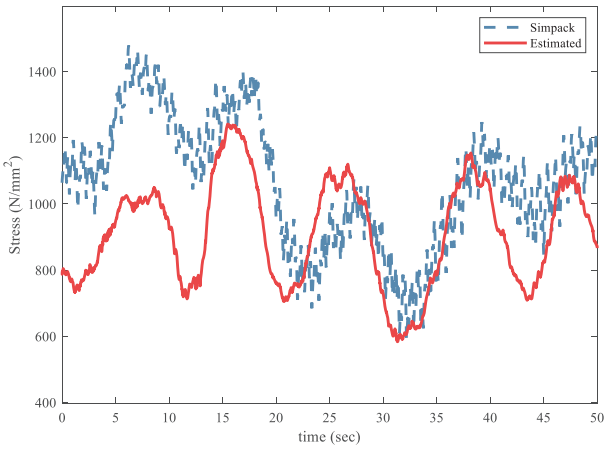

Fig. 7. Sun-planet contact stress comparison at second stage: results using estimated input torque and 1st order Taylor series (see Sec. 2.5) against Simpack simulation.

Calculation of average accumulated damage

The SN curve parameters for pitting fatigue damage calculations depend on material, load and gear geometry. These two parameters for the pitting fatigue damage estimated in this paper are obtained based on ISO 6336-2:2019 [14]. Only one region is assumed for the SN curve. For instance, k is 3.051×10^{44}, and m is 12 for the sun gear of the 2nd stage. The numbers of stress cycles of sun gear is multiplied by 3, because it meshes with 3 gears simultaneously at each revolution. The accumulated damage of 1st stage sun, 2nd stage sun and 3rd stage pinion gears due to contact fatigue for one hour of operation by using the proposed digital twin-based remaining useful lifetime monitoring approach is listed in the Table 4. The online accumulated damage D of the 2nd stage sun gear is shown in the Fig. 8.

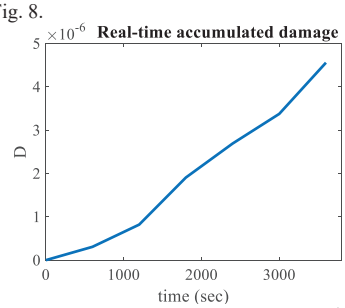

Fig. 8. Accumulated damage of the sun gear of the gearbox 2nd stage over one hour of operation.

Table 4. Accumulated damage for 3600 seconds of operation.

Gear	Damage
1st stage sun	0.00000482
2nd stage sun	0.00000456
3rd stage pinion	0.00000759

3.4 Practical implementation challenges and real-time performance

Challenges to overcome for practical implementation

In practical turbines, uncertainties are an important issue. The different sources of uncertainties and their influences on the digital twin-based degradation estimation approach grounded on drivetrain torsional equivalent models for estimation of residual life of *the drivetrain shafts* are investigated by Moghadam and Nejad in [24]. The latter is performed by using stochastic models and statistical approaches, where uncertainties in both the model estimation and real-time measurements are addressed to mitigate their influence and improve the efficacy of the digital twin approach in presence of uncertainties. The statistical uncertainties in fatigue calculation due to material uncertainties can be accounted for by stochastic modelling of damage as explained by [24]. It is also

worth noting that the employed least-square estimator is robust to the measurement noises, so that it can mitigate the influence of measurement noise in general, and cancel the influence of Gaussian noise [25]. The other issue in practical turbines is a call for computationally fast and inexpensive health monitoring techniques. The proposed algorithm is based on inexpensive linear equivalent models of the drivetrain, and the computational time depends on the sampling frequency and the number of input measurement samples. The algorithm can be managed to be executed only in order of a second. The method relies on a linear regression-based estimator and a few measurement samples, linear torque observers, and the real-time cycle counting of the estimated stress. The selected linear 14-DOF model of drivetrain is a compromise between simplicity and accuracy, which demonstrates similar results to results of high fidelity models for estimation of load aimed at estimating the degradation of the gears. The practical implementation of the algorithm integrated with turbine fully automated control and monitoring systems means the automated pre-processing of the turbine measurements to continuously feed updated input data into the proposed system identification approach to estimate real-time equivalent model of drivetrain in the digital twin framework. This task aims at the optimization of data streaming and continuous processing architectures to deal with the experimental data aspect of the digital twin framework. Within the pre-processing stage, a significant step will be on time signal correlation methods to verify and ensure time synchronicity when the data comes from different sources by mapping them on common spaces and dealing with the effect of different samples rates. Another practical issue with the realization of this idea is the possible need for new sensor installations to access additional torsional measurements, communication links with the main operation control unit, and the processing power for the execution of algorithm in near real-time.

Real-time performance metrics

As discussed in detail in Section 2, the digital twin algorithm consists of three main components, namely drivetrain equivalent model identification, load estimation and damage calculation. Therefore, for the simulation-based studies of this paper, the runtime of algorithm can be estimated by the summation of data recording time, time for estimation of equivalent model parameters, time for estimation of load and time for calculation of damage.

The model identification computation time, t^{model}, is mainly influenced by the linear regression estimator operation, which its computational time depends on the degree of model complexity and the number of input samples. For the case of 14-DOF model, the model identification algorithm can estimate the model parameters by less than 5% error only by using 14 data samples, where the estimation error can be reduced by increasing the number of input samples. By assuming 30 data samples, with the sampling frequency 300 Hz, the time length of recorded data block will be 0.1 sec. The processing time depends on the processing power, but can be managed to be only a fraction of a second. The estimation of load and stress computation time, t^{load}, is determined by the operation of designed torque observers which are simple arithmetic functions of estimated model parameters and measured real-time response, with the computational time very close to zero. The damage calculation computation time, t^{damage}, is reliant on

real-time cycle counting operation on the data blocks of stress time series, which can be executed quite fast in fraction of a second.

Two real-time metrics are employed to evaluate the algorithm run-time, namely real-time factor (RTF) and run time (TR), as they can be estimated by [26]

$$\begin{aligned} TF &= \frac{t^{process}}{t^{input}}, \\ TR &= t^{input} + t^{process}, \\ t^{process} &= t^{model} + t^{load} + t^{damage}. \end{aligned} \tag{33}$$

These equations can be used to provide a rough estimation of the real-time performance of the algorithm, based on testing it with a system with 1.9 GHz Intel Core i7 CPU and 16 GB memory, which leads to

$$\text{RTF} = \frac{0.8\,s + 0.1\,s + 0.2\,s}{0.1\,s} = 11, \qquad TR = 0.1\,s + 0.8\,s + 0.1\,s + 0.2\,s = 1.2\,s.$$

Generally speaking, for a system to be considered real-time, RTF should be ≤ 1 [27]. The run-time of the algorithm can be compensated in the proposed digital twin approach by repeating the results of data processing phase for all the data blocks captured during the processing time. The latter is expected to provide fair enough results for the drivetrain components' fatigue damage estimation, since degradation usually happens during longer periods of time than *one* second. Hardware-in-the-loop (HIL) simulation of the algorithm to study the possibility of executing the algorithm in real-time in practice is considered as the future work.

Conclusion

The possibility of using 14-DOF lumped parameter model as the drivetrain digital twin model for monitoring the remaining useful lifetime of the gears in the different gearbox gear stages due to contact fatigue stress was investigated. An algorithm for near real-time estimation of the parameters of drivetrain equivalent model by using the torsional measurements was proposed and tested by simulation studies. The estimated contact load and stress obtained by using the designed load observers in the proposed digital twin approach were validated by the results obtained from a Simpack high-fidelity simulation model, which showed a fair agreement between the results, whereas the proposed digital twin approach based on a linear torsional model is computationally fast and can be implemented integrated with turbine fully automated control and monitoring systems for online monitoring of gearbox components. The estimated stress was later used for near real-time estimation of the fatigue damage of the gears by using a physics-based degradation model. The influence of pitting faults on the system's resonances was demonstrated by simulation studies, which can support the fault diagnosis of the gearbox.

Hardware-in-the-loop (HIL) simulation of the algorithm to check the possibility of executing it in real-time for the fault prognosis purpose, tackling with the described practicality issues and implementation of the algorithm in an operational wind turbine

drivetrain system are considered as the next steps that will be investigated in the future work.

References

[1] Pfaffel, S., Faulstich, S. and Rohrig, K., 2017. Performance and reliability of wind turbines: A review. energies, 10(11), 1904.

[2] Moghadam, F.K., and Nejad, A.R., 2019. Evaluation of PMSG-based drivetrain technologies for 10 MW floating offshore wind turbines: pros and cons in a life-cycle perspective. Wind Energy.

[3] Goossens, P. (2017). Industry 4.0 and the Power of the Digital Twin. Retrieved, 5(3), 2017.

[4] Maldonado-Correa, J., Martín-Martínez, S., Artigao, E., and Gómez-Lázaro, E. (2020). Using SCADA Data for Wind Turbine Condition Monitoring: A Systematic Literature Review. Energies, 13(12), 3132.

[5] Snieckus, D., 2019. https://www.rechargenews.com/wind/siemens-gamesa-unveils-digitally-souped-up-11mw-offshore-turbine/2-1-711795.

[6] Johansen, S. S., and Nejad, A. R. (2019, June). On Digital Twin Condition Monitoring Approach for Drivetrains in Marine Applications. In International Conference on Offshore Mechanics and Arctic Engineering (Vol. 58899, p. V010T09A013). American Society of Mechanical Engineers.

[7] Rebouças, G. F. S., and Nejad, A. R. (2020, September). On Down-Scaled Modelling of Wind Turbine Drivetrains. In Journal of Physics: Conference Series (Vol. 1618, No. 5, p. 052008). IOP Publishing.

[8] Khazaeli Moghadam, F., and Nejad, A. R. (2020). Natural frequency estimation by using torsional response, and applications for wind turbine drivetrain fault diagnosis.

[9] Gorla, C., Rosa, F., Conrado, E., and Albertini, H. (2014). Bending and contact fatigue strength of innovative steels for large gears. Proceedings of the Institution of Mechanical Engineers, Part C: Journal of Mechanical Engineering Science, 228(14), 2469-2482.

[10] Jonkman, J., Butterfield, S., Musial, W., and Scott, G., 2009, "Definition of a 5- MW Reference Wind Turbine for Offshore System Development," U.S. National Renewable Energy Laboratory, Golden, CO, Technical Report No. NREL/TP-500-38060.

[11] Nejad, A. R., Bachynski, E. E., and Moan, T. (2019). Effect of axial acceleration on drivetrain responses in a spar-type floating wind turbine. Journal of Offshore Mechanics and Arctic Engineering, 141(3).

[12] Nejad, A. R., Guo, Y., Gao, Z., and Moan, T., 2016, "Development of a 5 MW Reference Gearbox for Offshore Wind Turbines," Wind Energy, 19(6), pp. 1089–1106.

[13] Kahraman, A.: Natural Modes of Planetary Gear Trains. Journal of Sound and Vibration 173(1), 125-130 (1994).

[14] ISO6336-2. Calculation of load capacity of spur and helical gears, part 2: calculation of surface durability (pitting). International Organization for Standardization: Geneva, Switzerland; 2006

[15] Pilanci, M., Arikan, O., and Pinar, M. C. (2010). Structured least squares problems and robust estimators. IEEE transactions on signal processing, 58(5), 2453-2465.

[16] Golub, G. H., and Van Loan, C. (1979). Unsymmetric positive definite linear systems. Linear Algebra and its Applications, 28, 85-97.

[17] Nejad, A. R., Gao, Z., Moan, T. (2014). On long-term fatigue damage and reliability analysis of gears under wind loads in offshore wind turbine drivetrains. International Journal of Fatigue, 61, 116-128.

[18] Downing, S. D., and Socie, D. F. (1982). Simple rainflow counting algorithms. International journal of fatigue, 4(1), 31-40.
[19] Manwell, J. F., McGowan, J. G., and Rogers, A. L. (2010). Wind energy explained: theory, design and application. John Wiley & Sons.
[20] Liang, X., Zhang, H., Liu, L., & Zuo, M. J. (2016). The influence of tooth pitting on the mesh stiffness of a pair of external spur gears. Mechanism and Machine Theory, 106, 1-15.
[21] Lei, Y., Liu, Z., Wang, D., Yang, X., Liu, H., & Lin, J. (2018). A probability distribution model of tooth pits for evaluating time-varying mesh stiffness of pitting gears. Mechanical Systems and Signal Processing, 106, 355-366.
[22] Liu, J., Wang, C., & Wu, W. (2020). Research on meshing stiffness and vibration response of pitting fault gears with different degrees. International Journal of Rotating Machinery, 2020.
[23] Moghadam, F.K., and Nejad, A.R. (2020), Theoretical and experimental study of wind turbine drivetrain fault diagnosis by using torsional vibrations and modal estimation, Under review by Journal of Sound and Vibration.
[24] Moghadam, F. K., and Nejad, A. R. (2020). Online condition monitoring of floating wind turbines drivetrain by using digital twin modeling approach. Under review by Elsevier Journal of Mechanical Systems and Signal Processing.
[25] Xu, W., Chen, W., and Liang, Y. (2018). Feasibility study on the least square method for fitting non-Gaussian noise data. Physica A: Statistical Mechanics and its Applications, 492, 1917-1930.
[26] Duda, K. R., Prasov, Z., York, S. P., West, J. J., Robinson, S. K., and Handley, P. M. (2015, March). Development of an integrated simulation platform for real-time task performance assessment. In 2015 IEEE Aerospace Conference (pp. 1-9). IEEE.
[27] Pratap, V., Xu, Q., Kahn, J., Avidov, G., Likhomanenko, T., Hannun, A., ... and Collobert, R. (2020). Scaling up online speech recognition using convnets. arXiv preprint arXiv:2001.09727.

A.6 Paper 6

Paper 6:
Online condition monitoring of floating wind turbines drivetrain by using digital twin modeling approach.
Authors: Farid Khazaeli Moghadam, Amir Rasekhi Nejad
Under review at Elsevier Journal of Mechanical Systems and Signal Processing.

Online condition monitoring of floating wind turbines drivetrain by means of digital twin

Farid K. Moghadam[a,*], Amir R. Nejad[a]

[a]Department of Marine Technology, Norwegian University of Science and Technology, Trondheim, Norway

ARTICLE INFO

Keywords:

Digital twin model

Modal estimation

System identification

Torsional measurements

Remaining useful life

ABSTRACT

This paper presents a digital twin (DT) condition monitoring approach for drivetrains on floating offshore wind turbines. digital twin in this context consists of torsional dynamic model, online measurements and fatigue damage estimation which is used for remaining useful life (RUL) estimation. At first methods for system parameter estimation are presented. The digital twin model provides sufficient inputs for the load observers designed in specific points of the drivetrain to estimate the online load and subsequently stress in the different components. The estimated real-time stress values feed the degradation model of the components. The stochastic degradation model proposed for estimation of real-time fatigue damage in the components is based on a proven model-base approach which is tested under different drivetrain operations, namely normal, faulty and overload conditions. The uncertainties in model, measurements and material properties are addressed, and confidence interval for the estimations is provided by a detailed analysis on the signal behavior and using Monte Carlo simulations. A test case, using $10MW$ drivetrain, has been demonstrated.

1. Introduction

In order to realize EU's goal of climate neutrality by 2050, the EU strategy is that 22% of electricity demand in Europe ($300GW/1361GW = 0.22$) should be generated by offshore wind by 2050, [1] and [2]. A recent report confirms the feasibility of this plan by showing that the levelized cost of energy (LCOE) of both onshore and offshore wind power has dropped considerably in 2019, so that they along with solar photovoltaic (PV) power have been the cheapest form of power generation in Europe, where yet there is a big gap between offshore and onshore [3] wind LCOE. The results of an investigation performed by Beiter *et al.* [4] emphasizes on the operating expenditures (OPEX) as the main contributor to this gap, so that OPEX in bottom-fixed offshore wind turbines is based on another study [5] in average twice higher than the land-based turbines. There are yet very limited experiences with floating wind turbines (FWT) to estimate the actual OPEX. The motivation of this research is increasing the wind turbine availability by performing predictive maintenance of the drivetrain system and the subsequent reduction of unexpected maintenance and expensive offshore transport/operation cost through digital twin (DT) monitoring and subsequent dynamic optimization of the turbine overhaul plan and scheduled maintenance intervals. Predictive maintenance accounts for the components of the system with the highest risk of loss of turbine availability. Power train system including rotor, main bearings, gearbox, generator and power converter accounts for 57% of turbine total failures and 65% of turbine total downtime [6]. The drivetrain system in this study comprises rotor, gearbox, generator, main and high-speed shafts, and main bearings, which together cause the majority of the total turbine downtime. The overall consequences are expected to be higher in offshore and more specifically FWT which apply to higher power ranges, contain larger components and are encountered with wider range of excitation sources. The real-time lifetime monitoring of the critical drivetrain component for large FWT is expected to happen in near future [7].

According to the classification provided by Rausand *et al.* [8], predictive maintenance is a subcategory of condition-base maintenance, which is based on assessment of remaining useful lifetime (RUL). The latter can be implemented for the turbine critical components to set alarms based on the severity and deviation from the nominal lifetime to inform the operator to take proper actions. The action can be integrated with the scheduled clock-base maintenance for further investigations. The other possibility is to integrate the predictive maintenance outcomes to the farm-level decision making support to set the operating point of units based on the turbines condition. Dependent on the risk, the action can also be integrated to the protection system. DT models are proposed in the recent literature for both predictive and condition-base maintenance in different application domains, *e.g.* in aerospace and aviation, oil& gas structures and marine transports industries. The computationally fast equivalent models of the system components which update themselves based on the operational data

*Corresponding author

ORCID(s): 0000-0002-0795-6887 (F.K. Moghadam); 0000-0003-0391-8696 (A.R. Nejad)

facilitate the real-time inexpensive and even automated lifetime monitoring of the critical system components. These models are expected to be able to properly capture the physical variations in system.

As discussed earlier, the nominal capacity of wind turbines and subsequently the rating and size of drivetrain components is growing rapidly. The largest operational offshore wind turbine is currently $14MW$. FWT drivetrains are exposed to the synergistic impacts of wind, wave, currents, structural motions-induced forces, power grid and their interactions with the drivetrain internal dynamics. In order to deal with those complexities and for making offshore wind power a more cost-effective solution by improving the turbine availability, utilization of DT models for monitoring the lifetime of the drivetrain critical components which cause the highest risk in loss of turbine is emphasized. DT is a proven technology used by Siemens Gamesa for prediction of drivetrain loads and subsequently improving the drivetrain design in $11MW$ offshore wind turbine technology manufactured by this company [9]. DT modelling is proposed in the industrial revolution Industry 4.0 [10] as the core of development process which can offer unlimited possibilities beyond the design process. The possibility of online estimation of loads enables another potential application domain for DT models which is for monitoring of the drivetrain components residual life, where DT is proposed for real-time estimation of the stress in different components of the drivetrain, which can provide sufficient input for probabilistic physic-based/data-driven approaches for estimation of RUL or probability of failure (PoF) of the individual components and system.

The focus of this research is proposing a drivetrain RUL prediction solution by the estimation of drivetrain equivalent real-time DT model parameters and a subsequent monitoring of variations of stress concentration in different components of the drivetrain, and employing the estimated stress values in probabilistic degradation models which can indicate the fatigue damage in the components. DT in the predictive maintenance context means the combination of model, online measurements and RUL model as defined and suggested by [11]. A starting point in realization of DT modelling for fault prognosis/diagnosis purposes is to specify the critical failure modes of the drivetrain system components and then to identify the related failure criteria/feature by analyzing one or a combination of different categories of measurements, namely vibration analysis, electrical signature (current and power signals), acoustic emissions analysis, thermography and temperature analysis, and analysis of oil particles. Those measurements can also be used for indirect estimation of the loads from the load effects (vibration, temperature, pressure, etc.) which can later be used by failure functions and degradation models. Nejad *et al.* [12] discloses a vulnerability map for the drivetrain gearbox which sorts the drivetrain components from the highest to lowest PoF, and discusses about the critical failure modes of each component. Sethuraman *et al.* [13] reports the critical failure modes of the main bearings, whereas Liu *et al.* [14] investigates the critical failure modes of the generator.

In general, degradation models comprise two components, namely failure parameter estimation and RUL units. The failure parameter can be directly measured by physical sensors or estimated by employment of either data-driven or physic-based observers. Data-driven approaches depend on analysis of historical data and application of artificial intelligence in different operational and environmental condition and estimation of a parameter which is directly related to the components lifetime heuristically and by analysis of the patterns observed based on the available data. More specifically, the artificial intelligence techniques preform regression or correlation analysis with respect to the data of a sensor network and look out for similarities, variations and deviations from a pattern in the dataset over the time. It is usually difficult to rely on the results obtained from analyzing limited datasets, and not easy to extend the results to different operating conditions and applications. However, physic-based approaches are based on the system physical rules of flow of energy in the components and the resulted vibrations and temperature as the responses. Finding an efficient way to address complex dynamics and transients, and various sources of uncertainties of the real problems by physical models is sometimes challenging. However, owe to advances in analytical models and stochastic modelling techniques, improved and reliable physical models are the preferred choice for engineering applications. Adjustability and adaptability of model complexity based on the application, independency of results of historical data and confortability in defining meaningful thresholds are the other motivations for sticking to physical models.

There are different approaches to realize DT models:

In the *first* approach, high fidelity physical models which are able to represent the full dynamics with respect to the under consideration failure mode are created. Then the order of model is reduced to maintain the same results while the computational speed is improved. The reduced models are preferred to be implementable in microcontrollers and integrated with turbine fully automated control and monitoring systems, where the operational measurements are also available. This model is then supported by the operational measurements aimed to estimate the equivalent real-time load which degrades the component with respect to the under consideration failure mode. The latter then plays the role as the input for failure functions which can be a function of different failure modes of different components, and then model-based reliability analysis which is able to capture the degradation and predict the RUL of a component or system by comparing the estimated stress and the resistance of the components material due to the specified failure modes. Pedersen *et al.* [15] applies a similar approach to predict RUL in offshore platform structures, where DT is a finite element model (FEM) which is updated by the online estimation of modal parameters obtained by operational modal analysis (OMA). FEMs are computationally expensive mod-

els. The latter makes these models not to be considered as a feasible solution for drivetrain condition monitoring which is a complex system with a wide range of components. On the other side, drivetrain is a rotational system with a wide range of components and defects and excitation frequencies, which cause OMA not to be the most efficient tool for estimation of drivetrain dynamic properties. In this work, DT is considered as an analytical model which its complexity can be adjusted based on the objectives of the model. The latter can reduce the computational complexity of DT model and facilitate the implementation in real-time. For the modal estimation, the approach based on analysis of the torsional response proposed by Moghadam *et al.* [16] is employed.

In the *second* approach, signal processing approaches including machine learning techniques (*e.g.* neural networks and statistical learning approaches) are leveraged to extract the features which are able to capture the dynamics of various failures. In this category, which is pointed with signal denoising and feature selection, RUL models are more based on empirical models and mostly limited to historical data and based on the available observations of the system operation, so that for a new system with limited observations in different operational conditions these methods might be impractical. As an instance of this category, Herp *et al.* [17] uses a date-driven approach based on artificial neural networks (ANN) to estimate response (in this case, bearing temperature form the turbine operational measurements). The residual life monitoring is based on estimation and monitoring the variations of the statistical properties of the distribution fitting the PoF based on the defined empirical hazard function. RUL is then empirically estimated based on the specified feature space and the defined failure function supported by different categories of machine learning approaches, namely statistical learning and recurrent neural networks. Statistical models are used for defining the RUL function and optimization problem, and neural networks are employed for solving the optimization problem.

All these approaches are based on linking computation models with stochastic models. The resultant is able to relate the variations in the computation model to the expected value of degradation and fatigue damage, and the PoF of the system components [18]. If the stress time series is available, physic-base reliability approaches can be engaged to estimate RUL, where stochastic models and signal processing techniques (mainly based on statistical learning and neural networks) can be engaged to address uncertainties in the degradation model [19]. For the case of RUL estimation based on the feature space and penalization of the deviation from the distribution of the feature space defined for the normal operation, for instance, statistical learning approaches based on Bayesian method [20], particle filtering [21] and likelihood function [17] are used in the literature for estimation of RUL of the wind turbine drivetrain components. Different classes of neural networks are also proposed in the literature to support both the feature extraction and the probabilistic models proposed for RUL estimation, [17] and [22].

This paper is based on a proven physic-base approach for degradation estimation, which is supported by statistical approaches and stochastic models to address uncertainties to improve the accuracy. This method which relies on real-time measurements, is computationally fast and can apply to different dirvetrain components and is not restricted by the operational conditions.

The main purpose of this work is the proof of concept for the proposed DT model for residual life monitoring of the drivetrain components. The input measurements come from the high fidelity models. The validation of the estimated model parameters is performed by comparing the estimated parameters with the actual values. The RUL model is based on the proven physical rules of stress concentration and degradation of the components material. As discussed earlier, DT models rely on real-time operational measurements to update themselves. Due to the limited historical data of FWTs and the test facilities for high power applications, the validation is limited to simulation studies, so that experimental validation of the proposed DT model is looked as future work. In here, decoupled simulation technique is engaged. Where the turbine data is obtained from $10MW$ spar global simulation model. The offline measurements then feed the drivetrain multi-body simulation (MBS) model in simpack software, and the real-time response time series are used for estimation of DT parameters. The input torque is applied to the model once from the global simulation outcome. Since in a real case, the input torque is not among the accessible measurements, In another simulation, applied input torque is estimated from the accessible turbine and blade parameters. The error in estimation of DT parameters by using the exact torque and estimated torque will be calculated. The proposed method combines high fidelity models to generate the torsional response, reduced order models (ROM) to represent as the DT of the system, signal processing approaches to estimate ROM parameters, and stochastic frameworks to address uncertainties in the proposed DT model. High fidelity models are use to estimate the drivetrain loads from the global simulations, and then to calculate the drivetrain response in the different bodies. The degradation model works based on the updated DT parameters and online response measurements. The sources of uncertainty in the proposed DT model mainly arise from the load estimation approach, and the estimation of fatigue damage by relying on the material properties obtained from the S-N curve, which are sufficiently addressed by using statistical approaches and stochastic models based on Kalman filtering and Monte Carlo simulations, respectively.

Johansen *et al.* [11] performs a preliminary study about the capacity of different simulation models with different levels of complexity to play the role as drivetrain DT model for condition monitoring purposes. The criterion emphasized in

that study is to achieve the same dynamic response by the equivalent model compared to the response from actual system. The literature of drivetrain fault diagnosis is based on monitoring the performance of the individual components by using the variations in physical parameters *e.g.* temperature and pressure. The latter is supported by the condition monitoring systems based on three-axial measurements of acceleration in the different positions of the drivetrain to support the earlier stage component-level fault detection in the drivetrain [23]. However, drivetrain is a rotary system with torsional responses. In order to monitor the operation of drivetrain in system level, *e.g.* for detecting the faults in the drive line in early stage, the possibility of using drivetrain torsional response is discussed in the recent literature, [16] and [24]. A drivetrain torsional ROM identified based on the operational torsional measurements, can support fault diagnosis in the drivetrain, since the drivetrain faults in the system-level show themselves by variations in ROM parameters (stiffness and moment of inertia) and dynamic properties (torsional natural frequencies and normal modes), so that the threshold can be defined based on the deviation from the reference values of these parameter estimated based on the system normal operations.

This paper is aimed at estimation of the drivetrain ROM parameters by using the torsional measurements. The model will then be integrated with the real-time drivetrain measurements in a DT platform for updating the ROM parameters and dynamic properties. The drivetrain real-time ROM estimated/identified from the torsional measurements can be used for *two purposes*: *First*, for fault diagnosis and condition-base maintenance based on torsional response (see *e.g.* [16] and [24]). In a direct way, by having access to the real-time values of system parameters, it is possible to define different fault states of the different classes of progressive faults in terms of variations in the ROM parameters. Since these parameters are directly representing the physical nature of the system and components, defining the threshold for different fault states is straightforward. In an indirect way, the proposed algorithm helps to access a full knowledge on the real-time values of drivetrain dynamic properties. The deviation from the dynamic properties can be used by the method proposed by [37] to detect the drivetrain faults. The parameters of ROM are gradually updated based on the new data blocks, which help to attain the updated values of dynamic properties. *Second*, for monitoring the drivetrain components residual life and predictive maintenance, which is emphasized in this work. The uncertainties in the torsional response, load and DT model parameters are taken into account, and the states/unnoisy response are estimated by using Kalman filter, where the output provides the sufficient inputs for the designed load observers. As the following step, the load in different parts of this system can be estimated by using the updated DT model parameters and designed load observers. The load observers are designed by using the analytical model of the system and the ROM parameters fed by the operational measurements. The required input for the proposed method are the torsional measurements including response and drivetrain applied loads. The torsional response can be provided by encoders or strain gauges. It is assumed that the different types of torsional response can be interchangeably used by performing derivation and integration operations. The main loads applied on the drivetrain are the aerodynamic and generator torques. A good estimation of the generator torque is available due to the generator control purposes. However, the measurement of aerodynamic torque is conventionally unavailable, but a good estimation can be attained by using the available measurements. The error in estimation of ROM parameters in both cases of using the actual value and the estimated value of aerodynamic torques as the input for the system identification approach is reported.

Based on the theoretical study in [16] and [37], a 3-DOF torsional model of the drivetrain is sufficient for detection of the drivetrain system level faults. System-level faults are categorized into the faults which change the torsional stiffness the most (*e.g.* crack in the shafts and bearing wear specially in gearbox), and faults which influence mostly the inertia of the drivetrain bodies (changes in mass balance/distribution which can be due to *e.g.* loss of mass, wear and unbalance; and also change in the axis of rotation which can be due to *e.g.* misalignment and looseness), which all can be observed by using 3-DOF ROM. This model is also the reference model for the degradation studies in the system-level as will be discussed further. This model is used in this work for estimation of degradation in the drivetrain components. As the test case for the proposed algorithm in this work, the estimated system parameters along with the angular velocity measurements are used to design two observers for estimation of load in main- and high-speed shafts. The estimated torques will be then applied as inputs to the shaft degradation models which are able to estimate the accumulated damage in the drivetrain shafts. The shafts are the components that can directly contribute in the turbine downtime. They can also indirectly contribute by causing the expedited degradation of the other drivetrain components [25]. Motivations for detection of shaft faults for different applications *e.g.* ship propulsion and wind turbine drivetrain is discussed in the literature, (see *e.g.* [26] and [27]), which is possible to arise from various conditions such as inappropriate use, stress concentration and unanticipated loading conditions, improper prior fabrication, improper or inadequate design, inadequate maintenance or a combination of them, all of which reduce the fatigue strength of the shaft [28]. Shaft carries all the load and is a core mechanical component in the drivetrain, especially for FWTs which are encountered with high turbulent wind and larger variations of drivetrain loads. In direct-drive technologies the main shaft is considered as a more critical component. A detailed investigation on the wind turbine main shaft failure modes, failure rate, consequences, and economic justifications for monitoring the main shaft lifetime are discussed in [26]. The consequences of shaft failures are usually high. Damaged shafts can also cause excessive vibrations in the other turbine-generator components, so that monitoring of their operation is important. In the literature, shaft fatigue damage due to different failure modes is discussed. Rauert *et al.* [30] focuses on fretting-fatigue-damage which is described by the product of the frictional shear stress and tangential tensile stress. Zhang *et al.* [29]

presents the fracture analysis of the wind turbine main shaft. That study considers torsion, transverse moment and axial force, and estimates equivalent stress. All these studies agree on shear stress as the main role player in the shaft degradation while the bending stress can exacerbate the damage. Based on those studies, the critical step for the shaft fatigue damage estimation is monitoring the shear stress concentration. The main shaft is generally supported by two main bearings in high power drivetrain technologies. The main shaft is designed to meet the requirements of deflections and rigidity [31]. In the detailed design, the main shaft model includes a rotational shaft transmitting the torsional torque due to the rotor main torque component and a fixed shaft supporting the bending moment due to the shaft weight [32]. The equivalent stress can then be estimated by applying the von Mises theory. Safety factors are selected and applied according to the specific material type in EN10083 standard [33]. The same procedure is followed, so that the fatigue damage due to cyclic torsional-bending load is focused in estimations of shaft residual life in this study.

An innovative drivetrain health monitoring approach based on estimation of residual life of the components is proposed by using the torsional measurements and digital twin modeling. Drivetrain model identification by using torsional measurements, and application of the real-time estimated DT model for estimation of load and residual life of the components is the main goal of this work. The method is designed in the general form for n-DOF torsional model of the drivetrain, and then developed by using 3-DOF torsional model as the drivetrain DT for monitoring the residual life of main and high-speed shafts. An algorithm is proposed for the model identification, which receives the torsional response and the estimated rotor and generator torques, and estimates the drivetrain ROM parameters and dynamic properties. The proposed method is computationally fast, and can be implemented in the farm level. The method can be adjusted based on higher DOF models to monitor the lifetime of different drivetrain components. For demonstration purposes, the algorithm is designed and tested for monitoring the lifetime of shafts in the drivetrain system. This approach is in particular useful for operators with limited knowledge of the drivetrain dynamic parameters, as we propose a method for model estimation first - in other words the approach is not limited to have all the drivetrain design data. On this basis, the main contributions of this work are:

1. Proposing a computationally fast digital twin model of the drivetrain system based on the torsional measurements, aimed at monitoring the residual life of the components, and defining the estimation error margin by using stochastic models,
2. Proposing a robust estimator for online estimation of digital twin model parameters,
3. Proposing a stochastic physic-base degradation model for estimation of RUL in the drivetrain main shaft by using the online estimated ROM, real-time operational measurements, designed load observer and equivalent stress estimation approach, and taking into consideration the various sources of uncertainty by using statistical approaches and a stochastic modelling.

The rest of paper is organized as follows: In Section II, the drivetrain DT model and the online estimation of ROM parameters by using the torsional response and aerodynamic torque observer is discussed. Then, in the rest of this Section, the design of real-time load observers for the drivetrain components by using DT model and operational measurements, the estimation of equivalent stress and then the degradation model is explained. The proposed DT model estimation approach and its application for monitoring of drivetrain components residual life is evaluated by the simulation studies in Section III. The work is closed with the final remarks in Section IV.

2. Methodology

2.1. Global simulation and drivetrain loads

DTU $10MW$ reference wind turbine [34] with a spar floating support substructure is selected for this study. The wind turbine specification and the overall characteristics of the floating platform is obtained from [34] and [35]. This model is able to capture the global dynamics of spar FWT from the interactions with the environmental loads. The drivetrain system is a medium-speed permanent magnet synchronous generator technology based on the gearbox and generator design specifications reported by Moghadam *et al.* [36]. The decoupled simulation approach is used for the drivetrain studies in this work, which consists of two steps. In the first step, global simulation analysis for different environmental conditions is performed. In the global simulation, the blades and hub assembly, the structural module including the flexible multi-body systems for tower and platform including the floating support substructure and the nacelle are modelled. This model is coping with combined aerodynamic and hydrodynamic loading by using numerical and probabilistic models of wind, waves and current in the global simulation software to capture the integrated effect of the loads and the wind turbine control system on the turbine components. The results of the global simulation are the load effects on different parts of turbine, which contain the information about the interactions between the turbine subsystems. The latter includes the loads transmitted to the drivetrain by the rotor and structure specified by the time series of the resultant moments and forces on the rotor, tower top accelerations and other responses of interest. The second step of the decoupled analysis is that the calculated rotor aerodynamic torque and other responses of interest estimated from global simulation are applied as the input to an offline

drivetrain model in mechanical/electrical machinery simulation software to calculate and analyse the drivetrain components local dynamic responses. Then the drivetrain local load effects are obtained for further post processing aimed at health monitoring of the drivetrain system based on monitoring the critical components residual life. The wind model in the global simulations is turbulent based on Kaimal distribution. The turbulence intensity at hub height I $(-)$ is assumed to be 0.14. The wave is modelled stochastic by two parameters, namely significant wave height H_s (m) and peak period T_p (s) in global analysis.

2.2. Estimation of the drivetrain model parameters and dynamic properties

The proposed algorithm for estimation of the drivetrain equivalent ROM and dynamic properties is summarized by the flowchart illustrated in Fig. 1. In the following, the different components of the algorithm are described.

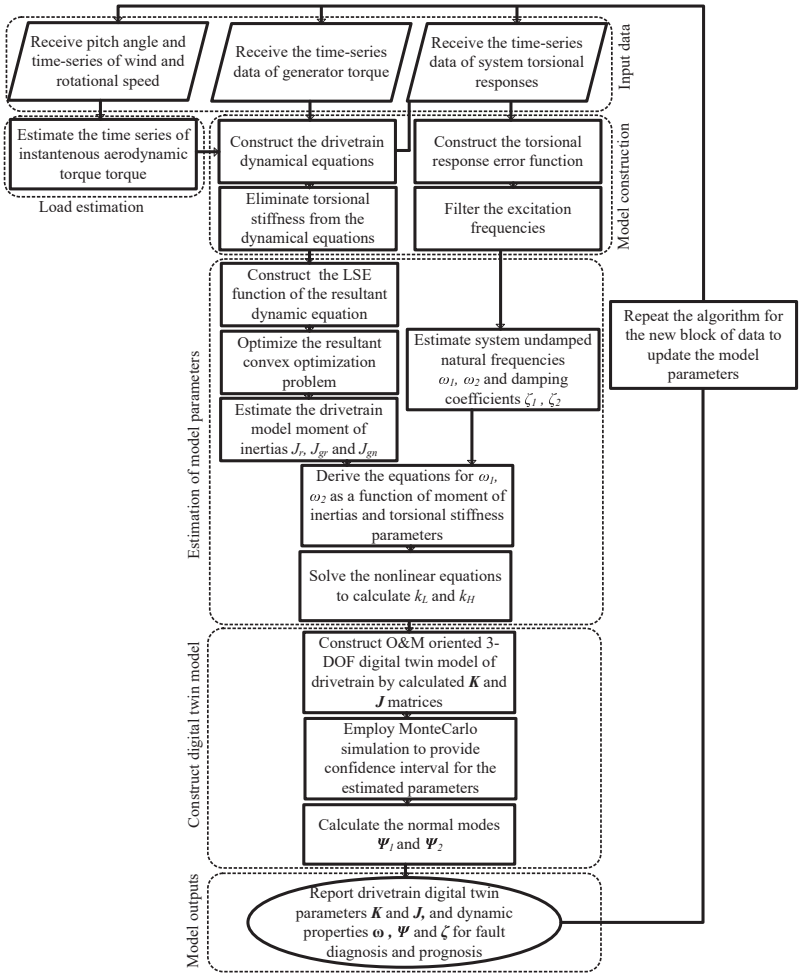

Figure 1: Proposed algorithm for estimation of drivetrain equivalent model parameters.

2.2.1. Drivetrain modal estimation

The free vibration time-domain torsional response of n-DOF damped rotational system in terms of the system dynamic properties can be represented by

$$\boldsymbol{\theta}(t) = \sum_{i=1}^{n} \boldsymbol{a}^i e^{-\boldsymbol{\zeta}^i \boldsymbol{\omega}^i t} \boldsymbol{\Psi}^i \sin(\boldsymbol{\omega_d}^i t + \boldsymbol{\phi}^i), \tag{1}$$

where $\boldsymbol{\theta}$ is a vector representing response in different DOFs. The amplitude coefficients $\boldsymbol{a}^i$ and phase shifts $\boldsymbol{\phi}^i$ are determined by the initial conditions of angular displacements and velocities. The complex mode shape vectors $\boldsymbol{\Psi}^i$, the undamped natural frequencies $\boldsymbol{\omega}^i$, and the damping coefficients $\boldsymbol{\zeta}^i$ are all representing the dynamic properties of the system which all are functions of physical parameters of the system and not the loading or initial conditions. The damped natural frequencies $\boldsymbol{\omega_d}^i$ can also be related to the undamped frequencies by using the damping coefficients as

$$\boldsymbol{\omega_d}^i = \boldsymbol{\omega}^i \sqrt{1 - (\boldsymbol{\zeta}^i)^2}. \tag{2}$$

As mentioned earlier, the drivetrain dynamic properties can each be represented as a function of system parameters. In [37], the closed form equations of the reference 3-DOF model dynamic properties as a function of model parameters are derived. By this method, it is possible to achieve a full dynamic characterization of the drivetrain system by specification of natural frequencies, mode shapes and damping in the system. By estimation of the model parameters by using the torsional measurements and the theory developed in the continued parts of this section, it is possible to access a full knowledge on the system dynamic properties, which can be used as input for the drivetrain system fault detection method proposed by [16] and [37]. Among the dynamic properties, the natural frequencies can also be directly estimated by using the torsional response [16], which are later used as inputs for the proposed system identification approach.

The torsional response residual function between the inertias j_l and j_m from the point l is defined as [37]

$$e^{\boldsymbol{\Omega}}_{\boldsymbol{l,m}}(t) \triangleq \boldsymbol{\Omega_l}(t) - u_{l,m}\boldsymbol{\Omega_m}(t), \quad for\ l\ and\ m\ \in \{1, \dots, n\}, \tag{3}$$

with $\boldsymbol{\Omega}$ as the time series of angular velocity, and $u_{l,m}$ as the relative gear ratio between j_l and j_m to make them in the same coordinate. Gear ratio $u_{l,m}$ as per definition is $\frac{N_l}{N_m}$, where N_l and N_m are the speeds at l^{th} and m^{th} inertias. The analytical proof of estimation of natural frequencies from the frequency spectrum of $e^{\Omega}_{l,m}$ is provided by [37].

2.2.2. Estimation of moment of inertia matrix

As the first step, the general damped n-DOF torsional dynamical model of drivetrain is constructed. The summation of the moments on each inertia in the lumped parameter model yields n equations of the form

$$j_i\ddot{\theta}_i(t) + C_i\left(\dot{\theta}_i(t) - \dot{\theta}_{i-1}(t)\right) - C_{i+1}\left(\dot{\theta}_{i+1}(t) - \dot{\theta}_i(t)\right) + k_i(\theta_i(t) - \theta_{i-1}(t)) - k_{i+1}(\theta_{i+1}(t) - \theta_i(t)) = T_i(t)\ \ for\ \ i = (1, \dots, n) \tag{4}$$

where θ_i is the angular displacement at i^{th} body. j_i is the inertia of i^{th} body. k_i is the equivalent stiffness between $(i-1)^{th}$ and i^{th} bodies. k_{i+1} is the equivalent stiffness between i^{th} and $(i+1)^{th}$ bodies. T_i is the external excitation applied to the i^{th} body. In the matrix form, these set of equations can be written as

$$\mathbf{J}\ddot{\boldsymbol{\Theta}}\ (t) + \mathbf{C}\dot{\boldsymbol{\Theta}}\ (t) + \mathbf{K}\boldsymbol{\Theta}\ (t) = \mathbf{T}(t). \tag{5}$$

where $\mathbf{J}$, $\mathbf{C}$ and $\mathbf{K}$ are the moment of inertia, damping and stiffness matrices with the size $n \times n$. $\boldsymbol{\Theta}$ and $\boldsymbol{T}$ are the response and load vectors with the size $n \times 1$, where each element of these two vectors represents a time series data. This model alongside the torsional measurements provide the inputs for the drivetrain model parameter estimation approach. The optimization variables are $\mathbf{J}$, $\mathbf{C}$ and $\mathbf{K}$ matrices which are the drivetrain equivalent lumped model parameters. The sparsity of the matrix variables $\mathbf{J}$, $\mathbf{C}$ and $\mathbf{K}$ are specified based on the drivetrain topology and is imposed to the optimization problem. Assuming that the load and response time series are known, the parameter estimation turns to the minimization of the $L2$-norm of error. The error function is defined by

$$\boldsymbol{E}\ (t) \triangleq\ \widehat{\mathbf{J}}\ddot{\boldsymbol{\Theta}}\ \ (t) + \widehat{\mathbf{C}}\dot{\boldsymbol{\Theta}}\ (t) + \widehat{\mathbf{K}}\boldsymbol{\Theta}\ (t) - \mathbf{T}(\mathrm{t}). \tag{6}$$

The least square estimator is defined by

$$\begin{aligned} \widehat{\mathbf{J}}^{\mathbf{LS}}, \widehat{\mathbf{K}}^{\mathbf{LS}}, \widehat{\mathbf{C}}^{\mathbf{LS}} \in\ & \arg\ \min\{\|\boldsymbol{E}\|_2\} \\ & \mathbf{J}, \mathbf{K}, \mathbf{C} \geq \mathbf{0} \\ & \mathbf{J}_{l,m} \in \boldsymbol{S}^{\mathbf{J}} \\ & \mathbf{K}_{l,m} \in \boldsymbol{S}^{\mathbf{K}} \\ & \mathbf{C}_{l,m} \in \boldsymbol{S}^{\mathbf{C}} \end{aligned}, \tag{7}$$

where $\boldsymbol{S}^{\mathbf{J}}$, $\boldsymbol{S}^{\mathbf{K}}$ and $\boldsymbol{S}^{\mathbf{C}}$ are the sparsity sets of matrices **J**, **K** and **C**. The matrix **J** is diagonal. **K** and **C** are non-diagonal symmetric matrices, but are not full rank. The latter causes computational difficulty for the above quadratic matrix optimization problem, so that it may result in the divergence of the numerical solver. To be more specific, these terms can introduce larger perturbations into the calculations than its numerically stable counterpart; this can lead to larger errors in the final computed solution. In order to remove the coupling between the equations due to the **K** and **C** terms, to cope with the round-off error which arises from the ill-condition terms of model, and to reduce the computational complexity by reduction of the number of variables, the equivalent scalar optimization problem is constructed by the sum of the dynamic equations (4) of each inertia, which leads to the elimination of stiffness and damping from the resultant scalar equation. The latter leads to the following error function in terms of the inertia variables j_i as the model scalar variables and torsional measurements time-series as input, with rotor as the reference of the rotary coordinate.

$$\boldsymbol{e}(t) = j_1 \dot{\boldsymbol{\Omega}}_1(t) + \cdots + u_{1,i} j_i \dot{\boldsymbol{\Omega}}_i(t) + \cdots + u_{1,n} j_n \dot{\boldsymbol{\Omega}}_n(t) - T_r(t) - u_{1,n} T_{gn}(t), \tag{8}$$

where $\dot{\boldsymbol{\Omega}}_i$ is the time series of angular acceleration and j_i is the moment of inertia of the i^{th} DOF. $\boldsymbol{T_r}$ and $\boldsymbol{T_{gn}}$ are the time series of the rotor and generator torques, respectively. The response used in this equation is the angular acceleration which can be obtained by applying a derivation operation on the angular velocity measurements, or the second derivation on the angular displacement measurements. The sign of $u_{1,i}$ is determined based on the direction of rotation of j_i. Since the real-time values of response is known, the inertia parameters can be estimated by minimizing the square error between the model and measurements. The average of the squares of the errors — that is, the average squared difference between the estimated values as the model outputs and the actual value as the sensor measurements is defined as least squares produces best linear unbiased estimators of the coefficients in a linear regression model. Therefore, a least-square-error (LSE) function is defined to minimize the error between the dual optimization problem and input operational measurements. The latter leads to the following quadratic scalar optimization problem as

$$\hat{\mathbf{j}}^{\mathrm{LS}} = \arg \min_{\boldsymbol{j} \geq 0} \{\|\boldsymbol{e}\|_2\} \quad . \tag{9}$$

This estimator is robust to the measurement noises, and can provide a good approximation even with less than n input data samples (underdetermined case). For the case of more than n samples (overdetermined case), this estimator helps to obtain more accurate estimation than solving the linear equations, when the input measurements are subject to independent and identically distributed (IID) Gaussian noise. In other words, the total LS technique is able to correct the system with minimum perturbation [38]. The above convex multi-variate scalar optimization problem is numerically solved by Matlab CVX and the global optimizer $\boldsymbol{j}^{LS} = \{j_1, \ldots, j_n\}$ is estimated. Since this $L2$-norm regression optimization problem is in a quadratic convex form, the results which are the estimated values of the drivetrain ROM inertia parameters are the global optimizers of the problem.

The maximum likelihood estimator (MLE) defined by the following maximization problem can also be used, which is mathematically equivalent to the LSE problem defined by eq. (9), for the special case of Gaussian noise.

$$\hat{\boldsymbol{j}}^{ML} = L(\boldsymbol{e}(1), ..., \boldsymbol{e}(t); j_1, ..., j_n, \sigma^2) = \arg \max\{\frac{1}{(2\pi)^{t/2}\sigma^t} exp(\frac{-1}{2\sigma^2}\|\boldsymbol{e}\|_2)\} \equiv \arg \min\{\|\boldsymbol{e}\|_2\} \tag{10}$$

where σ is the standard deviation of the Gaussian distribution fitting the noise. To use MLE to estimate those parameters, the method is restricted to the assumption that the form of the distribution of the random noise defined by the error function $\mathbf{e}(t)$ is known, so that the likelihood function can be obtained. Based on the extensive simulations, the error calculated from the torsional measurements in the under consideration application shows a near Gaussian distribution. Therefore, both LSE and MLE estimators lead to the similar set of results.

2.2.3. Estimation of stiffness matrix

Afterwards, the stiffness parameters of the model are estimated by using the estimated inertias and the drivetrain resonance frequencies estimated from the torsional measurements in the previous steps. The undamped torsional frequencies of the system are the nonlinear function of inertia and stiffness as

$$\boldsymbol{\omega}_i \ (for\ i = 1, \ldots, n) = \sqrt{eig(-\mathbf{J}^{-1}\mathbf{K})}. \tag{11}$$

By using the estimated natural frequencies obtained from the modal estimation approach together with the estimated inertia matrix **J** from the LSE optimization problem, the stiffness matrix **K** is the root of $\boldsymbol{g}_i$ which is defined by the following nonlinear equation as

$$\boldsymbol{g}_i = {\boldsymbol{\omega}_i}^2 - eig(-\mathbf{J}^{-1}\mathbf{K}), \quad (for\ i = 1, \ldots, n). \tag{12}$$

In general, there is not a unique matrix $\mathbf{K}$ from the above equation for the known set of eigenvalues $\lambda_i = \{{\omega_1}^2, \dots, {\omega_n}^2\}$ of the matrix $-\mathbf{J}^{-1}\mathbf{K}$. However, by imposing the sparsity and symmetricity to matrix $\mathbf{K}$ from the lumped model, it is possible to calculate the unique matrix $\mathbf{K}$ numerically by using Matlab fsolve solver. The latter also helps to reduce commutation cost of this matrix algebraic equation by reducing the number of variables from n^2 to n. The matrix $\mathbf{J}^{-1}\mathbf{K}$ is not symmetric in the general case which may give the sense that there are multiple answers for $\mathbf{K}$ from this equation. However the fact that $-\mathbf{J}^{-1}\mathbf{K}$ always has positive eigenvalues (it is positive definite), brings us to the believe that this matrix is a small perturbation of a symmetric matrix with positive eigenvalues. Small perturbation keeps the eigenvalues positive [39].

The usual condition for the estimation problem is more restrictive. In other words, it is possible that only some of the eigenfrequencies of the drivetrain system can be estimated by employing the aforedescribed modal estimation approach, especially the higher eigenfrequencies which are excited with a lower energy of the input torque. In this case, the matrix $\mathbf{K}$ can still be estimated by using the following optimization problem in terms of the first i eigenfrequencies as defined by the following least square error estimator:

$$\hat{\mathbf{k}}^{\mathrm{LS}} = \arg \min_{\mathbf{\Lambda} \in \Lambda} \{ \left\| \lambda_i - eig(\mathbf{\Lambda},\ i) \right\|^{\mathbf{2}} \}\ , \tag{13}$$

with $\mathbf{\Lambda}$ is the variable of this problem which is a function of the unknown variable $\mathbf{K}$ as $\mathbf{\Lambda} = -\mathbf{J}^{-1}\mathbf{K}$. Also $\hat{\boldsymbol{k}}^{LS}$ is the set of nonzero elements of matrix $\mathbf{K}$ which are estimated by the above nonlinear matrix optimization problem. The sign of the elements of $\boldsymbol{k}$ are forced in the optimization problem. λ_i is the set of i ($\mathrm{i} \in \{1, \dots, \mathrm{n}\}$) smallest magnitude eigenvalues which are known from the modal estimation, $\lambda_i = \{{\omega_1}^2, \dots, {\omega_i}^2\}$. $eig(\mathbf{\Lambda},\ i)$ is the set of i ($\mathrm{i} \in \{1, \dots, \mathrm{n}\}$) smallest magnitude eigenvalues defined in terms of matrix $\mathbf{J}$ and the unknown matrix $\mathbf{K}$. The feasible set Λ is also defined by

$$\Lambda = \{\mathbf{\Lambda} : \mathbf{\Lambda} \in \mathbb{R}^{n\times \mathrm{n}},\ \mathbf{K} \geq \mathbf{0},\ \mathbf{\Lambda}_{l,m} = 0,\ \forall\, \mathbf{\Lambda}_{l,m} \in \boldsymbol{S}^{\mathbf{\Lambda}}\}, \tag{14}$$

where $\boldsymbol{S}^{\mathbf{\Lambda}}$ is the sparsity set of matrix $\mathbf{\Lambda}$. The positive definiteness and sparsity of $\mathbf{\Lambda}$ are the nonlinear constraints which are imposed to this problem. For the set of positive semidefinite matrices, this problem is convex and the solution is the global optimizer. However, $\mathbf{\Lambda}$ is not symmetric in general so that the definition of the problem is nonconvex for the numerical solvers and convex optimization tools are not able to numerically solve the problem. For this purpose, Matlab fmincon solver as a powerful tool for the general class of nonlinear nonconvex problems is used.

The estimation of undamped natural frequencies and damping coefficients from the torsional measurements is discussed in the algorithm proposed by [16]. For the system with n-DOF, the system has $n-1$ nonrigid torsional modes. The latter leads to $n-1$ nonlinear equations which are the undamped natural frequencies as nonlinear functions of equivalent model inertia and stiffness links. These set of nonlinear equations are numerically solved, and n equivalent stiffness seen by each body are estimated. The estimated values of stiffness parameters of the main diagonal of the matrix, by considering both the natural frequencies and inertia parameters estimation errors. When the degree of the model increases, it is not easy to access the closed form of these n nonlinear equations, so that one may decide to solve the equations numerically in matrix form. The increase of the degree of model increases the algorithm computationally more expensive but can provide more detailed DT model for condition monitoring of the different drivetrain subcomponents. As discussed earlier, 3-DOF model can be used for the drivetrain system-level faults. This model can also be used for lifetime monitoring of the drivetrain main and high-speed shafts. The estimation of 3-DOF model parameters and dynamic properties by this approach needs an additional torsional measurement installed on the gearbox input or output shafts. fault prognosis *e.g.* for shaft crack may be performed by using more detailed models (*e.g.* finite element models) able to better model the stress concentration in the crack side in the nonuniform shape of shafts. In order to compromise between the complexity and accuracy in this application and for providing a rough estimation of RUL by using a method implementable by turbine on-board automation system, 3-DOF model is proposed. The summary of the proposed algorithm adjusted for estimation of 3-DOF model parameters and dynamic properties from the torsional measurements is presented by Fig. 1. In this case, the nonlinear matrix equation represented by eq. (13) is reduced to the two nonlinear scalar equations for the two nonrigid modes as [37]

$$F1(\mathrm{k_L}, \mathrm{k_H}) = \omega_1 - \sqrt{\frac{\mathrm{k_L}}{2\mathrm{J_r}} + \frac{\mathrm{k_L}+\mathrm{k_H}}{2\mathrm{J_{gr}}} + \frac{\mathrm{k_H}}{2\mathrm{J_{gn}}} - \sqrt{(\frac{-\mathrm{k_L}}{2\mathrm{J_r}} - \frac{\mathrm{k_L}-\mathrm{k_H}}{2\mathrm{J_{gr}}} + \frac{\mathrm{k_H}}{2\mathrm{J_{gn}}})^2 + \frac{\mathrm{k_L k_H}}{\mathrm{J_{gr}^2}}}}, \tag{15a}$$

$$F2(\mathrm{k_L}, \mathrm{k_H}) = \omega_2 - \sqrt{\frac{\mathrm{k_L}}{2\mathrm{J_r}} + \frac{\mathrm{k_L}+\mathrm{k_H}}{2\mathrm{J_{gr}}} + \frac{\mathrm{k_H}}{2\mathrm{J_{gn}}} + \sqrt{(\frac{-\mathrm{k_L}}{2\mathrm{J_r}} - \frac{\mathrm{k_L}-\mathrm{k_H}}{2\mathrm{J_{gr}}} + \frac{\mathrm{k_H}}{2\mathrm{J_{gn}}})^2 + \frac{\mathrm{k_L k_H}}{\mathrm{J_{gr}^2}}}}. \tag{15b}$$

By solving these two nonlinear equations, the values of k_L and k_H which are respectively the stiffness of main and high-speed shafts are estimated. For all $k_L, k_H \in R^+$, there is a unique solution for the above set of nonlinear equations which

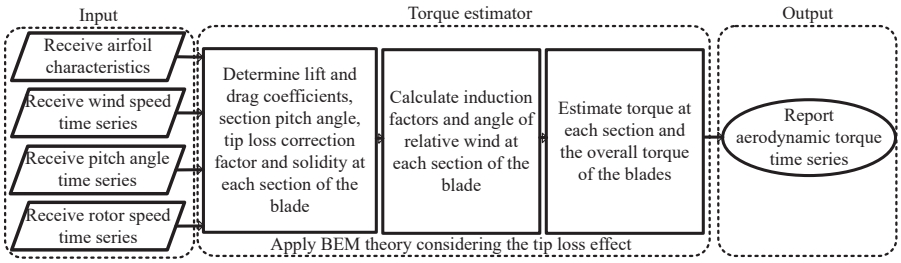

Figure 2: Estimation of aerodynamic torque from the turbine measurements and airfoil characteristics.

make it easy to numerically solve the equations. In case of access to the preliminary values of the parameters, these two equations can be approximated with the affine functions by using the two first Taylor series terms

$$F1(\mathrm{k_L},\mathrm{k_H}) \approx F1(\mathrm{k_L}^*,\mathrm{k_H}^*) + (\mathrm{k_L}-\mathrm{k_L}^*)F1_{\mathrm{k_L}}(\mathrm{k_L}^*,\mathrm{k_H}^*) + (\mathrm{k_H}-\mathrm{k_H}^*)F1_{\mathrm{k_H}}(\mathrm{k_L}^*,\mathrm{k_H}^*), \tag{16a}$$

$$F2(\mathrm{k_L},\mathrm{k_H}) \approx F2(\mathrm{k_L}^*,\mathrm{k_H}^*) + (\mathrm{k_L}-\mathrm{k_L}^*)F2_{\mathrm{k_L}}(\mathrm{k_L}^*,\mathrm{k_H}^*) + (\mathrm{k_H}-\mathrm{k_H}^*)F2_{\mathrm{k_H}}(\mathrm{k_L}^*,\mathrm{k_H}^*). \tag{16b}$$

Note that $F_{\mathrm{k_L}}$ and $F_{\mathrm{k_H}}$ are the partial derivatives of F with respect to k_L and k_H, which their values should be updated based on the new values of natural frequencies and inertia parameters.

2.2.4. Inputs of the proposed parameter estimation approach

The input data can be classified into two categories: first, the torsional response time series of the bodies, which are obtained from the drivetrain MBS model in Simpack. Second, the drivetrain loads consisting of the generator and rotor torques time series. The generator torque is a measurement available in the turbine for the generator control purposes. The generator torque is estimated from the generator electrical measurements, and available in turbine main control unit. The generator reference torque is calculated from the following equation

$$T_{gn}^* = \frac{P^*}{\Omega_{gn}}, \tag{17}$$

where P^* is the reference power and Ω_{gn} is the generator speed. T_{gn}^* is then used for the design of generator internal current control loop by using the equation

$$i_q{}^* = \frac{2T_{gn}^*}{3\Omega_{gn}p\phi_f}. \tag{18}$$

where $i_q{}^*$ is the reference q-axis current in rotating dq frame, used for the generator current control loop. p is the number of poles pairs, and ϕ_f is the flux linkage. The resulted electromagnetic torque on the shaft is calculated by using the measured current i_q as

$$T_{gn} = \frac{3}{2}p\phi_f i_q. \tag{19}$$

The aerodynamic torque applied to the drivetrain MBS model in Simpack is obtained from the global simulations. This torque is considered as the the applied torque on the drivetrain model. However, in the real case the real value of applied aerodynamic torque is not available, but a estimation can be available by using the turbine operational measurements and general information of the airfoil. The estimated torque is applied as the input to the drivetrain model identification approach. The algorithm for aerodynamic torque estimation approach is illustrated by flowchart shown in Fig. 2.

About the practicality issues of implementing this idea in current turbines, Supervisory Control and Data Acquisition (SCADA) existing system contains the encoder measurements, but implementation of the method needs higher resolution angular velocity measurements than what is available today from SCADA. SCADA data contains generator torque that is calculated from voltage and electric current. A good estimation of the rotor torque can also be available by using the available turbine measurements from SCADA.

2.2.5. Estimation error and confidence interval

The computational complexity of the proposed approach is proportional to the length t of the data block. In order to check the estimation accuracy versus the number of samples, the relative estimation error of each estimated parameter should be monitored versus different lengths of input data. To mitigate the influence of uncertainty in the input measurements in the estimated error, the crude Monte Carlo simulation is employed. The concept behind this is to make the calculated estimation error independent of the uncertainty in the input data. The model estimated parameter y is a random variable. Zero overlapping is allowed for the input data blocks which help to be able to assume that the estimated parameters are statistically independent. For the case that the data is captured during the similar operational conditions with respect to the operational speed, the response and subsequently the estimated parameters can be assumed to be identically distributed. Therefore, such rules in setting the test condition, will help to make the realistic assumption that y is IID. These conditions help to attain the confidence interval for the estimation error by using the results of IID central limit theorem (CLT). If $\varepsilon_1, ..., \varepsilon_r \in R$ are the errors in estimation of y based on r different blocks of input data each with the length t, with $\beta\%$ confidence, the estimation error locates in the interval [40]

$$\{\overline{\varepsilon}_r^t\}_y \in [\hat{\mu}_l - \phi^{-1}(1-\beta/2)\frac{s}{\sqrt{r}} \quad \hat{\mu}_l + \phi^{-1}(1-\beta/2)\frac{s}{\sqrt{r}}], \tag{20}$$

where $\{\overline{\varepsilon}_r^t\}_y$ is the average error associated with parameter y calculated based on t samples of data and r blocks of data. μ and s are the average and standard deviation of ε_i, $for\ i = (1, ..., r)$. Therefore to achieve a specific level of estimation error $\overline{\varepsilon}_r^t$ with a specific confidence $\beta\%$, the number of data blocks can be analytically acquired. The size of each block can also influence on the covariance, so that the larger the block of data, the easier to attain a specific accuracy.

Finally by using the estimated parameters, the eigenvectors associated to each natural frequency can be estimated. The results are the drivetrain ROM parameters and dynamic properties. The DT model parameters and the drivetrain dynamic properties are updated over the time by using the online measurements, to be used for fault diagnosis and prognosis purposes. The estimated drivetrain dynamic properties supported with the model parameters can be used for drivetrain fault diagnosis algorithm as discussed in [37], where the estimated DT model is used first to suuport modal estimation, and then to establish analytical features and threshold for fault detection by establishing the relationship between the dynamic properties and physical variations/faults in system. *In this paper*, the estimated DT model is used to provide inputs for the proposed drivetrain lifetime monitoring approach. Therefore, the estimated model feeds the load observers designed for estimation of load in main and high-speed shafts as elaborated in the following.

2.3. Drivetrain remaining useful lifetime monitoring

The possibility of estimation of load in the different drivetrain components depends of the model complexity and its capacity in representing the internal dynamics. By using the 3-DOF model it is possible to estimate the real-time loading and equivalent stress on the drivetrain main and high-speed shafts, which helps to estimate the residual life of these shafts by physic-base estimation of fatigue damage. Stiffness-related faults and more specifically shaft cracks are among the prevalent and influential system-level faults (see [19]) which are selected in this study, and predictive maintenance algorithm is developed accordingly. The procedure used for online estimation of stress and the shafts degradation by using the model estimated in Section 2.2 is summarized in Fig. 3, which is described in the following.

2.3.1. Estimation of load and stress

The estimation of load and stress in the drivetrain components is based on real-time operational data and the online estimated ROM model to design the load observers. Then the load observers are used to calculate stress and subsequently damage. Dependent on the degree of the DT model, the algorithm can be adjusted for lifetime monitoring of different components of the drivetrain. The algorithm shown is based on 3-DOF DT model and is able to estimate the online load in the main and high-speed shafts and measures RUL based on the loading on the shafts. As can be seen, two torque observers are designed to estimate the main and high-speed shafts torques by using the torsional measurements and updated values of torsional stiffness parameters from the DT model. By using the estimated loads by the observers, the maximum equivalent stress throughout the two shafts is calculated. The latter provides sufficient inputs for estimation of the fatigue damage and residual life of the two shafts.

In order to account for the statistical uncertainties due to both the measurements noise and estimation error of model parameters, the torsional measurements as the inputs of the load observers are estimated by using Kalman filtering. This technique is used to preprocess the input torsional response applied to the degradation model, by cancellation of background noises and the model uncertainties. The assumed linear state-space model as the input numerical model applied to the Kalman filter is obtained by applying the generalized coordinate approach as

$$\dot{\mathbf{x}} = \mathbf{A}\mathbf{x} + \mathbf{B}\mathbf{u} + \mathbf{w}, \quad (State\ equation) \tag{21a}$$

$$\mathbf{z} = \mathbf{H}\mathbf{x} + \mathbf{v}, \quad (Measurement\ equation) \tag{21b}$$

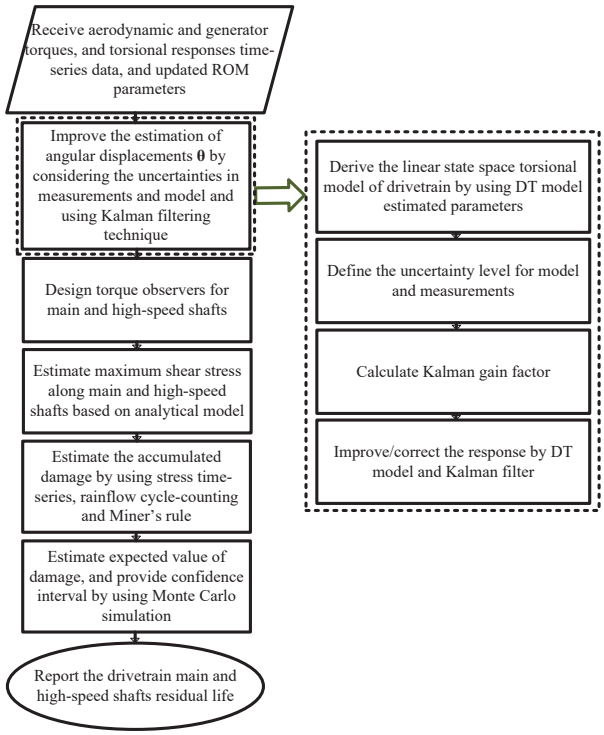

Figure 3: Estimation of drivetrain components RUL by using DT model, torsional measurements and stress-life method.

$$\mathbf{x} = \begin{bmatrix} \dot{\theta} \\ \theta \end{bmatrix}, \quad \mathbf{A} = \begin{bmatrix} \mathbf{0} & \mathbf{I} \\ -\mathbf{J}^{-1}\mathbf{K} & -\mathbf{J}^{-1}\mathbf{C} \end{bmatrix} \begin{bmatrix} \dot{\theta} \\ \theta \end{bmatrix}, \quad \mathbf{B} = \begin{bmatrix} \mathbf{0} \\ \mathbf{J}^{-1} \end{bmatrix}, \tag{21c}$$

where $\mathbf{x}$ and $\mathbf{z}$ represent states and measurements, respectively. $\mathbf{A}$, $\mathbf{B}$ and $\mathbf{H}$ are describing the expected relation between the measurements, states, and inputs. $\mathbf{H}$ is the identity matrix. $\mathbf{w}$ and $\mathbf{v}$ are Gaussian, uncorrelated noise sources, which correspond to the uncertainty on the model and measurements, respectively. The desired result is an improved estimate of the system state vector $\mathbf{x}$ by realization of discrete Kalman filter. At each discretized time step k, the following procedure is performed to estimate the torsional response by considering the uncertainties in the model and input measurements.

$$\mathbf{x}(k) = \mathbf{A}\mathbf{x}(k-1) + \mathbf{B}\mathbf{u}(k-1), \quad \mathbf{P}(k) = \mathbf{A}\mathbf{P}(k-1)\mathbf{A}' + \mathbf{Q} \tag{22}$$

where $\mathbf{x}(k)$ and $\mathbf{P}(k)$ are the state vector and its covariance matrix at k, respectively. $\mathbf{A}'$ is the transpose of matrix $\mathbf{A}$. Then the Kalman gain is calculated, and subsequently, the estimated states are corrected by the following equations and the calculated Kalman gain factors $\mathbf{G}$ as

$$\mathbf{G} = \mathbf{P}\mathbf{H}'(\mathbf{H}\mathbf{P}\mathbf{H}' + \mathbf{R})^{-1}, \quad \mathbf{x} = \mathbf{x} + \mathbf{G}(\mathbf{z} - \mathbf{H}\mathbf{x}), \quad \mathbf{P} = \mathbf{P} - \mathbf{G}\mathbf{H}\mathbf{P}. \tag{23}$$

In the above equations, $\mathbf{Q}$ is the covariance of process noise, and $\mathbf{R}$ is the covariance of measurements noise. The Kalman filtering operation is summarized in Fig. 3. The measurement and process noises are both modeled by Gaussian distributions. The eq. 23 is used to calculate the proper value of Kalman filter gain which is then used to attain the improved estimation of the angular displacements by considering the system uncertainties.

The next step is the design of load observers for the main and high-speed shafts. The torsional moment on the low- and high-speed shafts is estimated based on the following equations

$$\mathrm{T_{LSS}} = \mathrm{k_{LS}}(\theta_\mathrm{r} - \theta_\mathrm{gr}) + \mathrm{c_{LS}}(\Omega_\mathrm{r} - \Omega_\mathrm{gr}), \tag{24a}$$

$$T_{HSS} = k_{HS}(\theta_{gr} - \theta_{gn}) + c_{HS}(\Omega_{gr} - \Omega_{gn}), \tag{24b}$$

where T_{LSS} and T_{HSS} are the equivalent torque on the low- and high-speed shafts, respectively. θ_r, Ω_r, θ_{gr}, Ω_{gr}, θ_{gn} and Ω_{gn} are the angular displacement and velocity on rotor, gearbox and generator, respectively. Therefore, the implementation of the above torque observers need an additional torsional measurement installed on the drivetrain system. However, the approximated values can be provided by approximating the torsional response of gear in eq. 24a and eq. 24b respectively with the scaled torsional response of generator and scaled torsional response of rotor. The estimated loads are used as the input to estimate the stress on the shafts. The employed stochastic model-base approach for online estimation of the expected value of the residual life is based on estimation of fatigue damage due to shear/torsional stress which plays the main role in the fatigue failure of the shafts in wind turbines and bending stress due to the shaft weight. In other words, deformation and fracture from simultaneous influence of shear and bending stress is emphasized, which is based on crack blunting and crack propagation on a plane of maximum shear stress on the shaft [28]. The shear stress of the shaft can be calculated by

$$\tau = \frac{Tc}{J}, \tag{25}$$

where T is the torsional moment which is estimated in real-time by eq. 24, c is the radial distance from the shaft center line, and J is the polar moment of inertia around the shaft axis defined by

$$J = \frac{\pi}{2}(d_o^4 - d_i^4), \tag{26}$$

where d_i and d_o are respectively the inner and outer radius of the shaft. Therefore, the maximum shear stress happens on the outer surface of the shaft. Due to the large mass of main shaft especially in high-power applications, the bending stress can also take a significant value which can be calculated by

$$\sigma = \frac{Mc}{J}, \tag{27}$$

where M is the bending moment of the shaft due to the shaft weight. By using a distributed mass model, the maximum bending moment happens in the center point of the shaft on the surface area, as can be calculated by

$$M^{max} = \frac{WL^2}{8}, \tag{28}$$

where W is the mass per unit length of the shaft, and L is the length of the shaft. Therefore, the maximum bending and shear stresses happen simultaneously on the surface in the middle of the shaft as

$$\tau_{LSS}^{max} = \frac{2}{\pi}\frac{d_o^{LSS}(k_{LS}(\theta_r - \theta_{gr}) + c_{LS}(\Omega_r - \Omega_{gr}))}{(d_o^{LSS})^4 - (d_i^{LSS})^4}, \tag{29a}$$

$$\tau_{HSS}^{max} = \frac{2}{\pi}\frac{d_o^{HSS}(k_{HS}(\theta_{gr} - \theta_{gn}) + c_{HS}(\Omega_{gr} - \Omega_{gn}))}{(d_o^{HSS})^4 - (d_i^{HSS})^4}, \tag{29b}$$

$$\sigma^{max} = \frac{WL^2 d_o}{4\pi(d_o^4 - d_i^4)}. \tag{29c}$$

The equivalent stress is calculated by applying von Mises theory. The equivalent stress due to the combined bending and torsion is maximum in the middle of the shaft on the surface. Von Mises stress under combined bending and torsion loading is calculated by [43]

$$\sigma_d = \sqrt{\sigma_{max}^2 + 3\tau_{max}^2}, \tag{30}$$

where σ_d is von Mises stress, and τ_{max} and σ_{max} are the maximum torsional and bending stresses, respectively.

2.3.2. Classification of stress signal for estimation of average damage

Statistical analysis of damage consists of two main steps: First, classification of the sources of uncertainty and a proper way of modelling to address them in the degradation model. Second, analyzing the stress signal type and the specific properties of that type of signal, which helps to determine confidence interval for average and variance of damage. Based on eq. (29), for determining the stress signal properties, one should look into the torsional response signal. In order to evaluate the type

of torsional response signal, the spectral moments of the signal and the bandwidth parameters are evaluated. The spectral moments λ_m of the autospectral density function S both in discrete-frequency horizon are defined as

$$\lambda_{\mathrm{m}} = \sum_{\mathrm{j}=0}^{\mathrm{N}/2} (\mathrm{j}^{\mathrm{m}} \mathrm{S(j)}, \tag{31a}$$

$$\mathrm{S(j)} = \frac{2(\sigma_{\mathrm{d}}(\mathrm{j})\sigma_{\mathrm{d}}(\mathrm{j})^*}{\mathrm{N}}, \quad \mathrm{j} = (0, ..., \frac{\mathrm{N}}{2}), \tag{31b}$$

where S is the power spectral density of stress signal σ_d. The bandwidth parameters α_1 and α_2 have a critical role to specify the type of signal σ_d, which are defined by

$$\alpha_1 = \frac{\lambda_1}{\sqrt{\lambda_0 \lambda_2}}, \quad \alpha_2 = \frac{\lambda_2}{\sqrt{\lambda_0 \lambda_4}}. \tag{32}$$

For a strictly narrow-band/harmonic signal, these two metrics tend to 1. However, for a strictly broad-band/independent signal, they tend to 0. Even though the drivetrain torsional response may seem as a narrow-band signal with the rotor revolution frequency as the characteristic frequency, our extensive observations on both simulation and operational data show that the two metrics tend to zero under different turbine operating conditions.

In the literature, the drivetain vibration responses are considered as both stationary and non-stationary signals [44]. The possibility of fitting different distributions to the drivetrain response is investigated by researchers. Ghane *et al.*[45] proposes t-distribution as the best fit for the transnational vibration measurements captured from drivetrain. It is a common practice to model the drivetrain loads and responses as Rayleigh, Weibull and the generalized gamma distributions with reference to the distribution of mean wind speed. For data-driven fault detection of wind turbine drivetrain system, it is common to assume the operational vibration measurements as a stationary Gaussian process at each mean wind speed, which means each sensor measurement follows a Gaussian distribution [46]. Our observations on the drivetrain system torsional response show that the data at each operating condition follows a Gaussian distribution or in other words is identically distributed. The parameters of the distribution tend to vary as the operational speed changes. Therefore, in different operating zones/ranges of input wind speed, it can be assumed that the response follows a Gaussian distribution which its parameters vary in transition between different zones. The method can use an additional input from the operational speed to accordingly select the relevant parameters of the associated distribution. Based on this explanation, the torsional response is assumed to be IID. The metric α_2 is more commonly used. From mathematical perspectives, this metric for a stationary signal is equal to the cross correlation between the signal and its second derivative, which is 1 for a narrow-band and 0 for a broad-band signal. As discussed earlier, torsional response for each operating speed shows a stationary Gaussian behavior. Stress as a linear function of response shows the same pattern as expected. For a particular case of stationary-Gaussian process (our case), the metric α_2 is equivalent to the irregularity factor, IF, defined as

$$IF = \frac{s^2_{\dot{\sigma_d}}}{s_{\sigma_d} s_{\ddot{\sigma_d}}}, \tag{33}$$

where s_X, $s_{\dot{X}}$ and $s_{\ddot{X}}$ are the standard deviations of the signal and its first and second derivatives.

The response is IID and so does the stress signal as a linear function of torsional response. For such a signal, it is possible to apply crude Monte Carlo to obtain CLT-based approximate confidence interval [40] for the fatigue damage as is discussed in the next part. For some applications which the stress signal demonstrates narrow-band properties, the expected value and variance of damage can be estimated by using the theory explained by [19].

2.3.3. Degradation model for residual life estimation

The estimation of fatigue damage and residual life of the shaft is performed by using stress-life method. Even though the stress life method is not the most accurate approach, this method is able to represent high-cycle applications adequately. The criterion for high-cycle fatigue is $N > 10^3$ over the component lifetime, which is the case for a wide range of applications *e.g.* wind turbines and ship propulsion systems. The estimated online time series of maximum stress feeds the time-domain cycle counting approach based on rainflow approach. Therefore, the rainflow cycle counting and Goodman rule are used to calculate the effective stress and the number of cycles at each stress level. Then damage is estimated in real-time and the shaft RUL is calculated. For this purpose, Miner's rule is used to calculate the accumulated damage and subsequently residual life of the drivetrain components.

The degradation model for the main shaft is elaborated in the following. The number of stress cycles at different stress levels is counted by using the time-domain rainflow cycle counting approach [48]. Cycle counting is especially important for the

broad-band stress signal to distinguish small cycles which are interruptions of larger ones. Rainflow method has shown proven performance in time domain analysis of stress signal to count the stress cycles. The outputs are the amplitude stress levels σ_s , and the number of stress cycles at $\sigma_s \ for \ s = (1, \dots, S)$. In order to consider the influence of nonzero mean stress level, Goodman rule is employed to calculate the effective stress (the equivalent zero mean alternating stress) by the equation [49]

$$\sigma_s^e = \frac{\sigma_s}{1 - \frac{\sigma_m}{\sigma_u}}, \ \forall \ s \in \{1, \dots, S\}, \tag{34}$$

where σ_m and σ_u are the mean stress and material yield strength, respectively. The accumulated damage for the data block t with S different stress levels σ_s^e ($s \in \{1, \dots, S\}$) is calculated by using Miner's rule as

$$d^t = \sum_{s=1}^{S} \frac{n_s}{N_s}, \tag{35}$$

where n_s is the number of cycles at the stress level σ_s^e and N_s is the number of cycles to yield at stress level σ_s^e, where the relationship is defined by S-N curve characteristic as

$$\sigma_s^e = a(2N_s)^b. \tag{36}$$

The absolute total online accumulated damage can then be calculated by

$$D = \sum_{t=1}^{Time} d^t, \tag{37}$$

where $Time$ stands for the last data block which represents the current time. Note that d^t represents the "short-term" damage, since is related to only a specific environmental condition. However, damage D characterizes the long-term damage provided having measurements form all possible environmental conditions [41]. The described method can also be used for estimation of relative damage between different operational periods over the time, to give an insight on variations in degradation between different operational periods. It can also be used to estimate the relative damage between the different drivetrain components at the time, to give the operator a sense about the most vulnerable parts of the system at different operational periods.

The described deterministic approach does not necessarily provide precise results. Stochastic models which can adequately address the uncertainties in the aforedescribed stress-life degradation estimation approach can be used in conjunction with the above described deterministic model-base approach to improve the accuracy. According to eq. (35), the two sources of uncertainty are evolved out of the stress calculation and the material property captured by S-N curve. To address the stress calculation uncertainty, a significant part of uncertainty arises from the estimation of load. In order to account for uncertainties in load estimation approach, the influence of measurement noise and uncertainties in estimated model parameters were mitigated by employing Kalman filtering. However, the other significant source of uncertainty arises from stress life method and the procedure employed to obtain S-N curve parameters a and b which represent the best-fitting estimates of experimental fatigue data [42]. In this work, the statistical uncertainty in fatigue calculation due to material uncertainties accounted for by assuming the damage at each stress level as a random variable. In other words, in order to estimate damage for the t^{th} data block of the stress timeseries, d^t, the damage is calculated by assuming the S-N curve parameters a and b as random variables, so that for each stress level σ_i, the number of cycles to failure are estimated by randomly selecting a and b in the intervals $\pm 5\%$ of their nominal values.

Benasciutti *et al.* [50] suggests closed form approximations for the expected value of damage for both Gaussian narrow-band and broad-band processes. In this research, for the case that stress time series are IID, which is a practical assumption based on the observations and measurements of the under consideration test case and the analysis of stress signal spectral moments in Section 2.3.2, in order to obtain confidence interval for average damage, Monte Carlo simulation is employed and the results of IID CLT are applied, [47] and [40]. The above procedure for stochastic estimation of fatigue damage is repeated k different times with the same data block to realize k different cases of $d_i^t \in \{d_1^t, ..., d_k^t\}$ to attain the confidence interval for the average damage. As a result, with the confidence 95%, the average damage is placed in the following interval

$$[\widehat{\mu}_{\mathrm{d^t}} - 1.96\mathrm{s}_{\mathrm{d^t}}/\sqrt{(\mathrm{k})} \quad \widehat{\mu}_{\mathrm{d^t}} + 1.96\mathrm{s}_{\mathrm{d^t}}/\sqrt{(\mathrm{k})}], \tag{38a}$$

$$\widehat{\mu}_{\mathrm{d^t}} = \frac{1}{\mathrm{k}} \sum_{\mathrm{i}=1}^{\mathrm{k}} \mathrm{d}_{\mathrm{i}}^{\mathrm{t}}, \tag{38b}$$

Table 1
Environmental conditions for drivetrain analysis

Environmental condition	EC1	EC2	EC3
$U_w\ (m/s)$	7	9	11
$H_s\ (m)$	2.5	3.5	3.5
$T_p\ (s)$	6.5	7.5	7.5

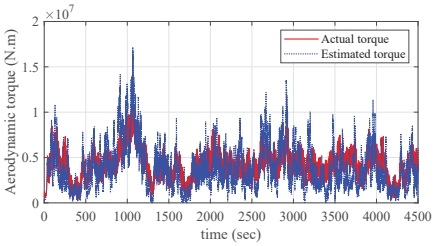

(a) T_a vs. time

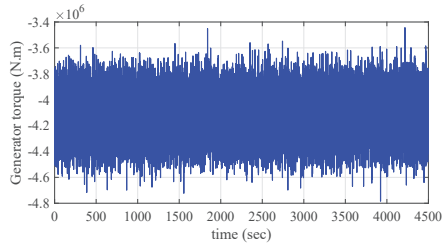

(b) T_g vs. time

Figure 4: Drivetrain model input loads. (a) Aerodynamic torque. (b) Generator torque.

$$s_{d^t} = \sqrt{\frac{1}{k-1}\sum_{i=1}^{k}(d_i^t - \hat{\mu}_{d^t})^2}, \tag{38c}$$

where the value of k is selected to realize an interval $\pm 5\%$ around the mean value of d_i^t. $\hat{\mu}_{d^t}$ and s_{d^t} are the average and variance estimates.

3. Simulation studies

3.1. Test case

In this Section, the methodology developed for lifetime monitoring of the drivetrain components is simulated and tested for the main shaft of the drivetrain system of DTU 10MW turbine. The shafts dimensions and weight are taken based on the work performed by Wang *et al.* [51]. The shafts material properties are obtained from [32]. Environmental conditions for the global simulations are summarized in the Table 1. The system identification algorithm is tested for different operational conditions, namely below rated, rated and over rated conditions.

3.2. DT model estimation

3.2.1. Estimation of the drivetrain model loads

The loads applied to the model are the aerodynamic and generator torques. A comparison between the actual and estimated aerodynamic torque is shown in Fig. 4a. The actual torque is assumed to be the torque obtained from the global simulations, and the estimated torque is the value estimated by using the turbine online measurements as explained in Section 2.2.4. The applied generator torque is also shown in Fig. 4b. For demonstration purposes, the generator torque is up-scaled by applying the gear ratio.

3.2.2. Parameter estimation by using torsional measurements

Here, the possibility of using the proposed algorithm for identifying the model parameters of 3-DOF torsional DT by using the real-time torsional measurements is investigated. This model will then be used for monitoring the variations in stiffness and subsequently feed the load observers designed in the drivetrain shafts. The actual values of the drivetrain 3-DOF model parameters and the estimated nonrigid natural frequencies by using the angular velocity error function are reported in [16]. The validation criterion for the estimated model parameters is the relative error percentage to be less than 5%.

In order to identify this model, five parameters, namely J_r, J_{gr}, J_{gn}, k_L and k_H which are respectively the equivalent rotor inertia, gearbox inertia, generator inertia, main shaft stiffness and high-speed shaft stiffness should be specified. The error of these parameters estimation versus the number of response samples (2, 3, 5, 7, 10, 100, 1000) for the three different drivetrain operational conditions (EC1, EC2 and EC3) by using both the actual input torque and the estimated torque is investigated in here. The procedure explained in Section 2.2.5 is followed to provide an analytical criterion/margin of the

error for the proposed parameter estimation approach. With respect to the fact that the error time series at each test case meets the conditions of IID CLT, in order to attain a reliable value of error in each test case, the number of data blocks for each test case is selected to ensure that with the confidence 99%, the error places in the interval $\hat{\mu}_l \pm 2.58\frac{s}{\sqrt{l}}$. Therefore, the reported estimated parameters and the associated errors are the most expected values with the specified confidence interval. For the case of fewer number of samples, the variance of errors is higher, which need higher number of data blocks to realize the specified confidence level. In order to realize the confidence 99% at the interval ±5% around the average estimate of error, the minimum required number of data blocks at each test can be calculated by $l > 2662.56(\frac{s}{\hat{\mu}})^2$.

The Fig. 5 shows the estimated parameters versus the estimation error. As it can be seen, the error is less than 1% when the number of algorithm input samples are more than 5. By increase of the number of samples, the error tends to zero. In addition, the method is not sensitive to the turbine operational conditions, and demonstrates a similar performance under different environmental conditions. By reduction of the number of input measurements samples from 1000 to 10, the computational time reduces by about 70%. When the number of variables (the order of ROM) increases, the improvements in the computation time by reduction of the number of samples will be more significant. The use of 10 samples with the sampling frequency $300Hz$, leads to the estimation of parameters in only fraction of a second, which shows that the algorithm can be executed in real-time.

The Fig. 6 illustrates more realistic values for estimation error vs. number of samples, by using the estimated torque instead of the actual torque as the input of parameters estimation approach. The latter is to address the uncertainty in the input torque for the proposed system identification algorithm. The estimated torque is calculated in real-time by an aerodynamic torque observer based on the turbine and blades online information by using the theory explained in Section 2. The values of error shown in Fig. 6 are again the expected values of error. As it can be seen, for the case of using the estimated torque, the method needs more input data to maintain the 5% threshold set for the estimation error. The reason is that in case of few samples, the LS estimator is more sensitive to the error of torque estimation of the individual samples. The error tends mostly to reduce by increase of the input samples.

The Fig. 7 estimation of drivetrain parameters in monitoring the variations of the model parameters which can model five different categories of faults, namely main shaft stiffness, high-speed shaft stiffness, rotor inertia, gear inertia and generator inertia sensitive faults. In Fig. 7a, the main shaft stiffness is reduced by 20%, in Fig. 7c, the generator shaft stiffness is reduced by 20%, in Fig. 7e, the rotor inertia is increased by 10%, in Fig. 7g, the gearbox inertia is increased by 10%, and in Fig. 7i, the generator inertia is increased by 10%. These simulation cases are designed to evaluate the capability of the proposed algorithm in tracking the variations of the system parameters which are representing different system-level fault cases. Variations in each equivalent model parameter can represent a specific class of the drivetrain faults. It shows that the proposed DT model parameter estimation algorithm can track/measure the variations in system perfectly. Our observations also show that the algorithm is also not sensitive to the sampling frequency. However, the sufficient sampling frequency will ensure the observability of higher frequency modes as the input of model estimation approach to be able to realize higher DOF models.

3.3. Estimation of stress and damage

3.3.1. Shaft material S-N curve

According to EN10083 [33], the S-N curve of 42CrMo4 which is commonly used as the main shaft material, with the specified finite-life region consisting of low-cycle and high-cycle fatigue regions, is shown in Fig. 8. The infinite-life region of the shaft is characterized by 10^{11} number of cycles [28].

3.3.2. Estimation of main shaft load and stress in normal operations

The time series of the estimated main shaft load and the equivalent von Mises stress by using the proposed algorithm, for 200 seconds of normal operations, are shown in the figures 9 and 10. Figures 9a and 10a are the actual values of load and stress on the main shaft. Figures 9b and 10b are the load and stress when the actual value of aerodynamic torque is applied as input to the DT algorithm. Figures 9d and 10d are the errors calculated for this case. As it can be seen, the estimation error is negligible when the exact value of aerodynamic torque is available.

Figures 9c and 10c are for when the aerodynamic torque applied as input to the DT algorithm is not available, but the estimated value of real-time aerodynamic torque is calculated and applied to DT model. Figures 9e and 10e are the errors calculated for this case. As it can be seen, even though the error increases, it is still less than the 5% threshold considered for the relative error for the DT model estimations in the work.

3.3.3. Estimation of load and stress in overload condition

The overload is modeled with 20% increase in the drivetrain torque. The time series of the estimated main shaft load and the equivalent stress by using the proposed algorithm, are shown in the figures 9 and 10.

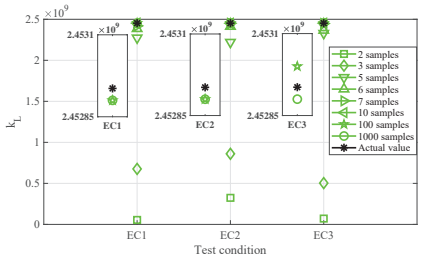

(a) Estimated main shaft stiffness vs. EC_i

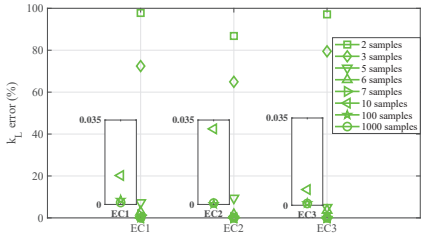

(b) Error in estimated main shaft stiffness vs. EC_i

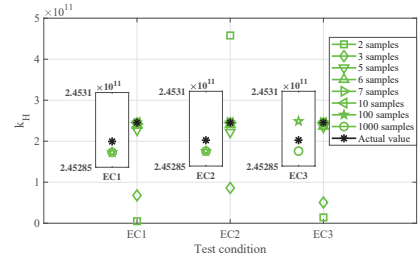

(c) Estimated high-speed shaft stiffness vs. EC_i

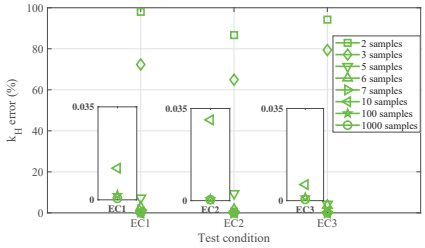

(d) Error in estimated high-speed shaft stiffness vs. EC_i

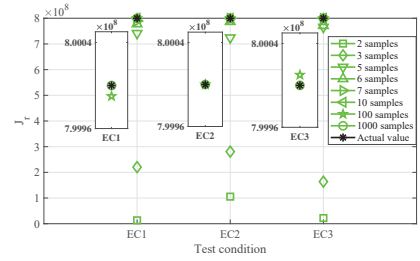

(e) Estimated rotor inertia vs. EC_i

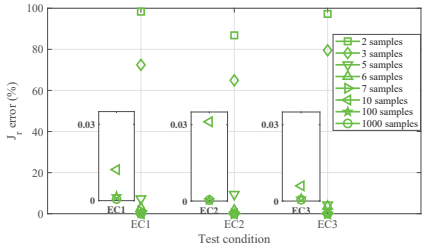

(f) Error in estimated rotor inertia vs. EC_i

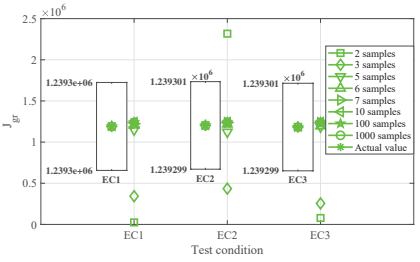

(g) Estimated gearbox inertia vs. EC_i

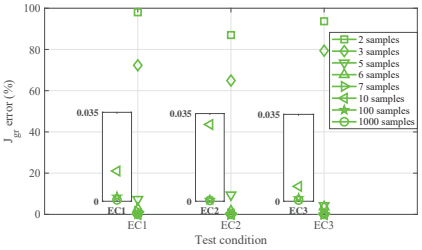

(h) Error in estimated gearbox inertia vs. EC_i

Figures 9a and 10a are the actual values of load and stress on the main shaft. Figures 9b and 10b are the load and stress when the actual value of aerodynamic torque is applied as input to the DT algorithm. Figures 9d and 10d are the errors calculated for this case. As it can be seen, the estimation error is negligible when the exact value of aerodynamic torque is available. Figures 9c and 10c are the aerodynamic torque applied as input to the DT algorithm is not available, but the estimated value of real-time aerodynamic torque is calculated and applied to DT model. Figures 9e and 10e are the errors calculated for this case. As it can be seen, the proposed DT error in estimation of both load and stress in overload conditions is lower than normal and faulty operations.

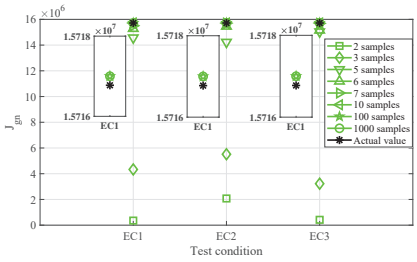

(i) Estimated generator inertia vs. EC_i

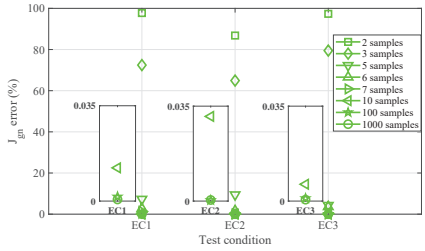

(j) Error in estimated generator inertia vs. EC_i

Figure 5: Estimated ROM model parameters, by using the actual aerodynamic torque. (a) k_L . (b) k_L relative error. (c) k_H. (d) k_H relative error. (e) J_r. (f) J_r relative error. (g) J_{gr}. (h) J_{gr} relative error. (i) J_{gn}. (j) J_{gn} relative error.

Table 2
Expected value of main shaft accumulated damage for different test scenarios for $3600sec$ of operation.

Test scenario	Actual damage	Estimated damage$_1$	Estimated damage$_2$
Normal operation	$1.8e^{-7}$	$1.8e^{-7}$	$1.8e^{-7}$
Overload (20%)	$1.1e^{-5}$	$1.1e^{-5}$	$1.1e^{-5}$
Fault (10%)	$8.3e^{-7}$	$8.3e^{-7}$	$8.3e^{-7}$
Overload and fault	$3.4e^{-5}$	$3.4e^{-5}$	$3.3e^{-5}$

3.3.4. Estimation of load and stress in main shaft fault condition

The early stage fault in the main shaft is modeled with 10% reduction in the shaft stiffness. The time series of the estimated main shaft load and the equivalent stress by using the proposed algorithm, are shown in the figures 9 and 10.

Figures 9a and 10a are the actual values of load and stress on the main shaft. Figures 9b and 10b are the load and stress when the actual value of aerodynamic torque is applied as input to the DT algorithm. Figures 9d and 10d are the errors calculated for this case. As it can be seen, the estimation error is negligible when the exact value of aerodynamic torque is available. Figures 9c and 10c are the aerodynamic torque applied as input to the DT algorithm is not available, but the estimated value of real-time aerodynamic torque is calculated and applied to DT model. Figures 9e and 10e are the errors calculated for this case. The estimation error in case of main shaft fault shows a higher value compared to both the normal operation and overload condition.

3.3.5. Estimation of damage in different operational conditions

In order to address the material uncertainty in damage calculations, for each stress data block, k different pairs of the two coefficients of S-N curve are randomly generated in an interval $\pm 5\%$ around their nominal values. Then the confidence interval for the damage d^t can be provided by assuming that the k different cases of d^t are IID. These k cases are generated from k independent cases, and our observations show a Gaussian pattern as the number of samples increases, which shows the consistency of the results of IID central limit theorem for $d_i^t,\ for\ i \in (1, ..., k)$. The average real-time accumulated damage by using the proposed DT approach for different operating conditions, namely normal operation, overload, main shaft fault and the combination of overload and shaft fault is listed in the Table 2. The early stage fault in the main shaft is modeled by 10% reduction of the main shaft stiffness. The overload is modeled by 20% increase of the drivetrain torque. *Actual damage* is the accumulated damage when the actual value of drivetrain parameters and input loads are accessed. *Estimated damage*$_1$ is the damage estimated by using the proposed DT model and the actual value of drivetrain input loads. *Estimated damage*$_2$ is the damage estimated when the DT model and estimated values of drivetrain input loads are used. As it can be seen, the estimated damage by the proposed approach in all the different test scenarios matches with the actual damage, with an exception for the test case which represents a combination of fault and overload, where the proposed approach slightly underestimates the damage. The real-time estimation of the accumulated damage D of the main shaft for one hour operation during the drivetrain overload is shown in the Fig. 11.

It should be noted that this work does not mean that the faults in the main shaft are the most prevalent faults in the wind turbine drivetrain systems, though it can contribute to a wide range of other secondary faults. The main purpose of focusing on the main shaft in the simulation studies is the proof of concept for the possibility of using an innovative RUL monitoring approach based on torsional vibration measurements for monitoring the residual life of the drivetrain components by using

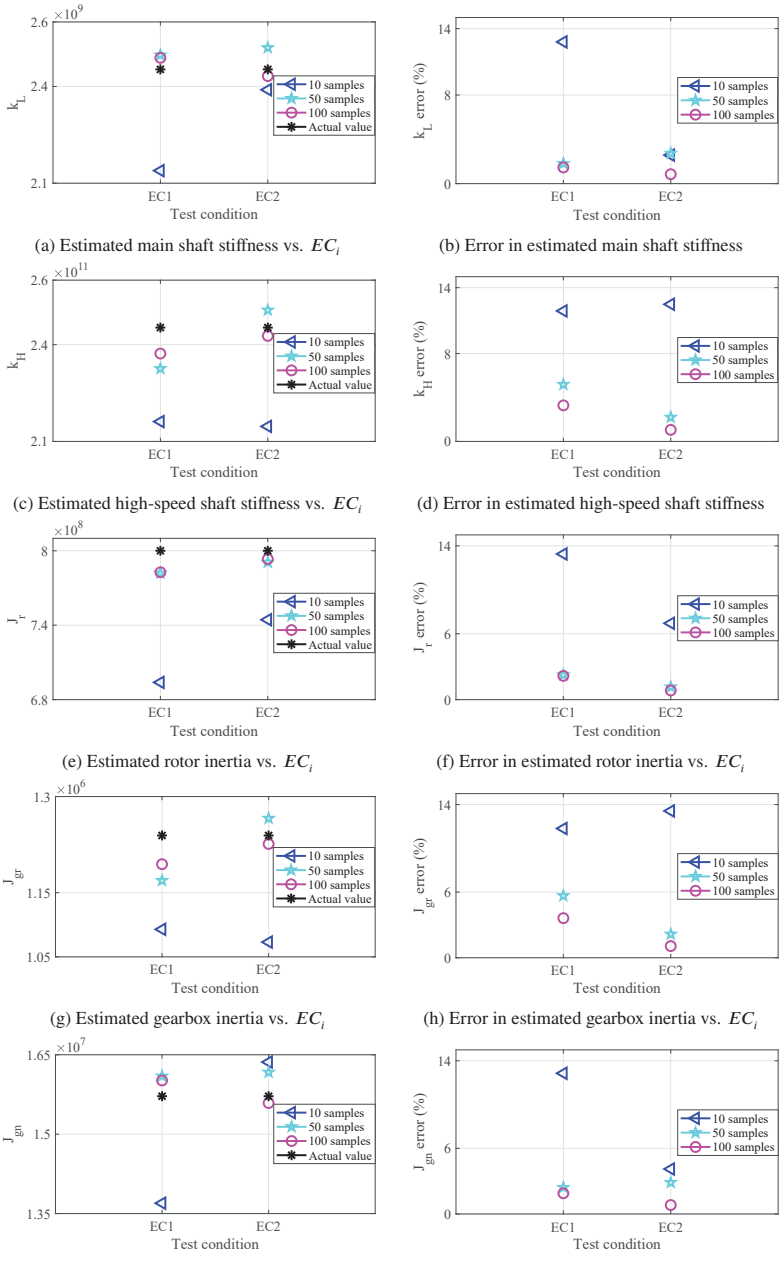

(a) Estimated main shaft stiffness vs. EC_i (b) Error in estimated main shaft stiffness

(c) Estimated high-speed shaft stiffness vs. EC_i (d) Error in estimated high-speed shaft stiffness

(e) Estimated rotor inertia vs. EC_i (f) Error in estimated rotor inertia vs. EC_i

(g) Estimated gearbox inertia vs. EC_i (h) Error in estimated gearbox inertia vs. EC_i

(i) Estimated generator inertia vs. EC_i (j) Error in estimated generator inertia vs. EC_i

Figure 6: Estimated ROM parameters, by using the estimated aerodynamic torque. (a) k_L . (b) k_L relative error. (c) k_H. (d) k_H relative error. (e) J_r. (f) J_r relative error. (g) J_{gr}. (h) J_{gr} relative error. (i) J_{gn}. (j) J_{gn} relative error.

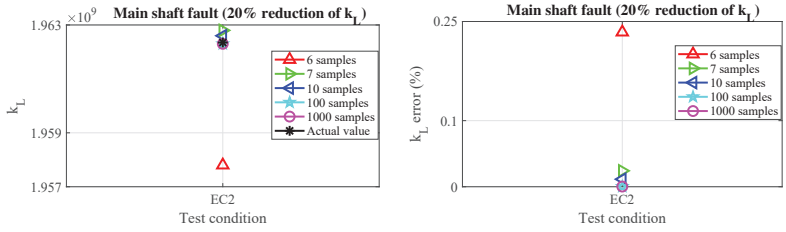

(a) Tracking main shaft stiffness variation

(b) Error in tracking main shaft stiffness variation

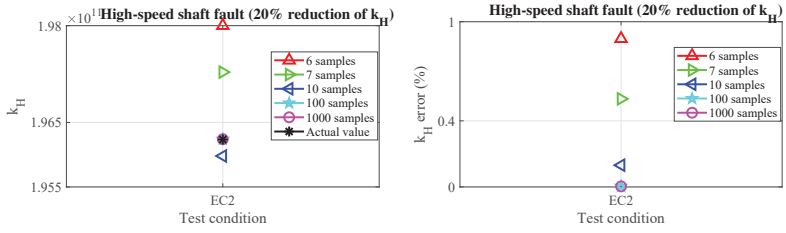

(c) Tracking HS shaft stiffness variation

(d) Error in tracking HS shaft stiffness variation

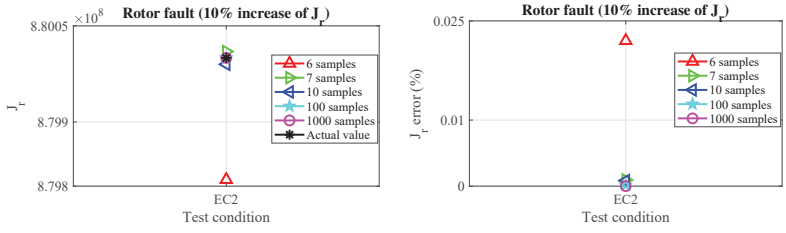

(e) Tracking rotor inertia variation

(f) Error in tracking rotor inertia variation

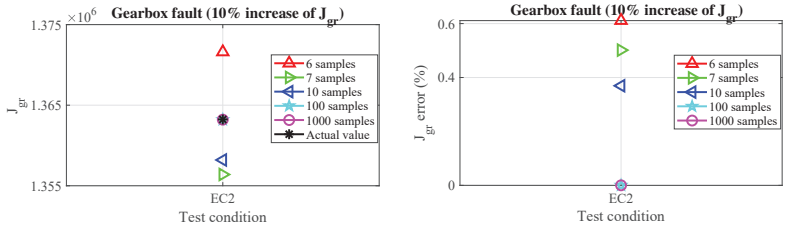

(g) Tracking gearbox inertia variation

(h) Error in tracking gearbox inertia variation

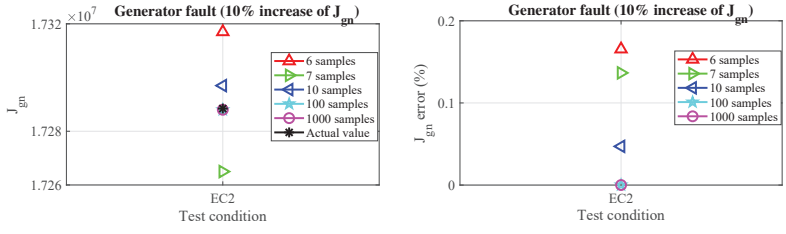

(i) Tracking generator inertia variation

(j) Error in tracking generator inertia variation

Figure 7: Estimated ROM model parameters in different fault scenarios (Test condition: EC_2). (a) k_L . (b) k_L relative error. (c) k_H. (d) k_H relative error. (e) J_r. (f) J_r relative error. (g) J_{gr}. (h) J_{gr} relative error. (i) J_{gn}. (j) J_{gn} relative error.

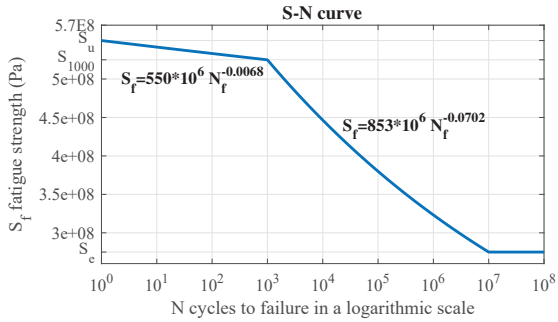

Figure 8: Main shaft steel S-N curve.

a simple model. For other components, *e.g.* the gears and bearings of the gearbox, it is still possible to use the proposed approach but by using more detailed torsional models, and probably a combination of torsional and translational models which is considered as the future work.

4. Conclusion

This work provided a basis for the development of preventive maintenance in FWT drivetrain systems based on monitoring the residual life of the components, by means of digital twin and employment of a stochastic physic-base model for determining the drivetrain components RUL. As a critical part of DT, a toolbox was proposed which receives the drivetrain torsional response and estimated input loads, and calculates the system dynamic properties (torsional natural frequencies, damping and mode shapes) and the equivalent torsional dynamic model parameters (torsional stiffnesses and moment of inertias). The application of this model in estimation of the drivetrain components residual life in real-time, and more specifically the RUL of the drivetrain main shaft was demonstrated. In order to evaluate the proposed DT approach, it was shown that by using only more than 10 data samples with the sampling frequency $300 Hz$ for the real-time measurements, the estimation error of DT model parameters and the estimated values of load and stress in the drivetrain components in all simulation cases, namely normal operations, fault on the main shaft and overload is always less than 5 percent.

The application of higher DOF torsional models as more detailed DT models which can capture real-time variations in mesh stiffness and inertia of individual gears and intermediate shafts, which can help to estimate the real-time load of the individual subcomponents by taking into account the components internal dynamics, and subsequently to calculate stress and fatigue damage due to different failure modes for a wide range of drivetrain subcomponents is looked as the future work.

Acknowledgement

The authors would like to thank John Marius Hegseth of Norwegian University of Science and Technology, Trondheim, Norway, for providing the $10 MW$ spar FWT global analysis simulation data, and for his support in estimation of aerodynamic torque in general.

References

[1] European Commission - Press release. Boosting Offshore Renewable Energy for a Climate Neutral Europe, https://ec.europa.eu/commission/presscorner/detail/en/IP_20_2096, Online; accessed 19 November 2020.
[2] Feldhaus, P., and Vahlenkamp, T. (2010). Transformation of Europe's Power System until 2050 Including Specific Considerations for Germany Electric Power and Natural Gas Practice.
[3] IEA (2020), World Energy Outlook 2020, IEA, Paris https://www.iea.org/reports/world-energy-outlook-2020
[4] Beiter, Philipp, Musial, Walter, Duffy, Patrick, Cooperman, Aubryn, Shields, Matthew, Heimiller, Donna, Optis, Michael. The Cost of Floating Offshore Wind Energy in California Between 2019 and 2032. Technical report, NREL, United States, 2020.
[5] Ioannou, A., Angus, A., Brennan, F. (2018). Parametric CAPEX, OPEX, and LCOE expressions for offshore wind farms based on global deployment parameters. Energy Sources, Part B: Economics, Planning, and Policy, 13(5), 281-290.
[6] Pfaffel, S., Faulstich, S. and Rohrig, K., 2017. Performance and reliability of wind turbines: A review. energies, 10(11), 1904.
[7] Beiter, P., Musial, W., Duffy, P., Cooperman, A., Shields, M., Heimiller, D., Optis, M. (2020). The Cost of Floating Offshore Wind Energy in California Between 2019 and 2032 (No. NREL/TP-5000-77384; BOEM-2020-48). National Renewable Energy Lab.(NREL), Golden, CO (United States).

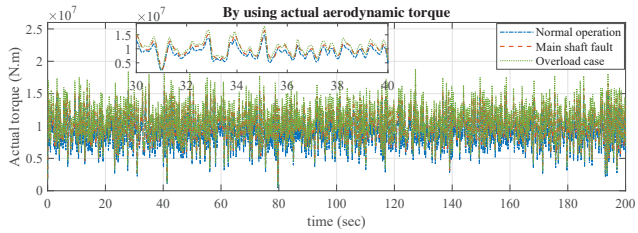

(a) Main shaft actual torque

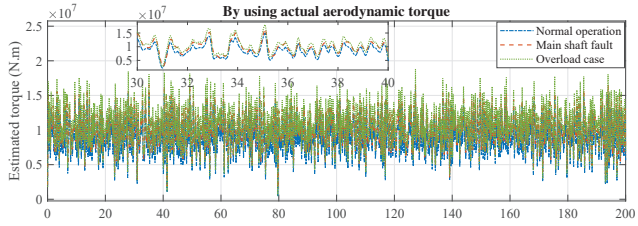

(b) Main shaft estimated torque

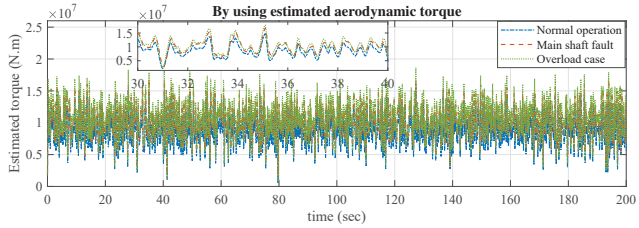

(c) Main shaft estimated torque

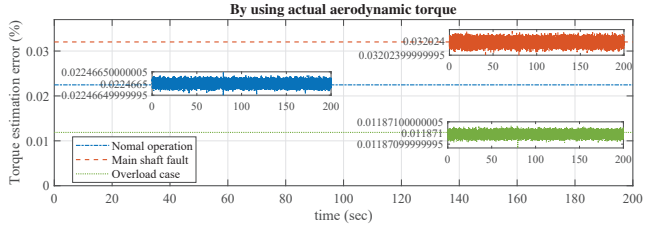

(d) Main shaft estimated torque error

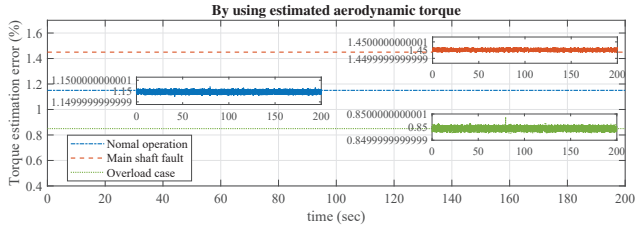

(e) Main shaft estimated torque error

Figure 9: Real-time torque on the main shaft. (a) Actual torque, (b) Estimated torque in case of using actual aerodynamic torque, (c) Estimated torque in case of using estimated aerodynamic torque, (d) Torque estimation relative error in case of using actual aerodynamic torque, (e) Torque estimation relative error in case of using estimated aerodynamic torque.

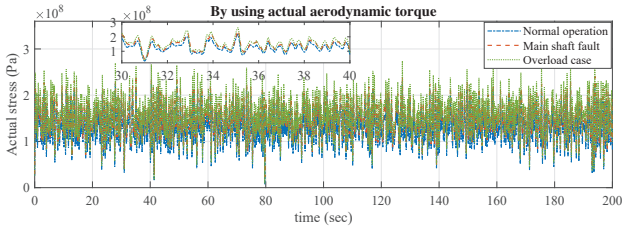

(a) Main shaft actual maximum stress

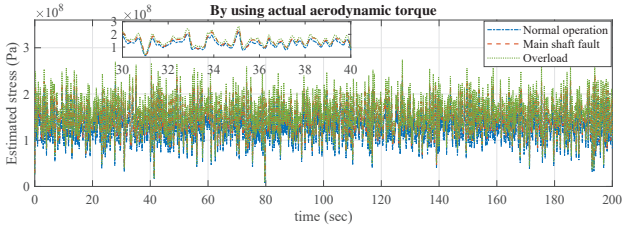

(b) Main shaft estimated maximum stress

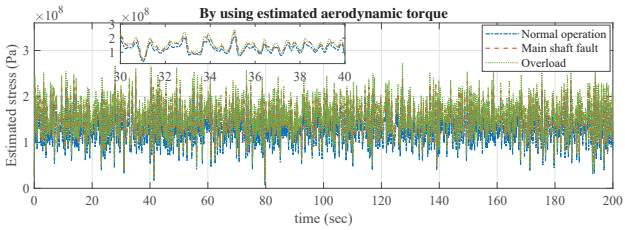

(c) Main shaft estimated maximum stress

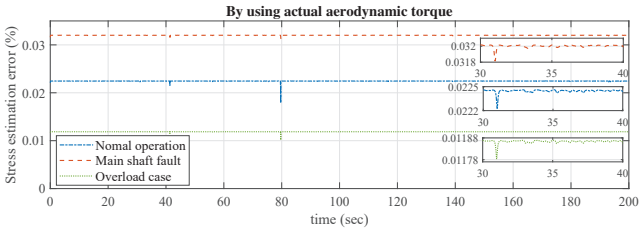

(d) Main shaft estimated stress error

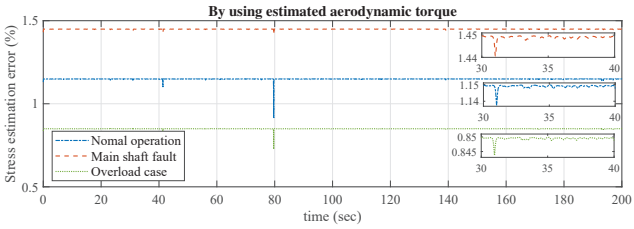

(e) Main shaft estimated stress error

Figure 10: Real-time equivalent equivalent von Mises stress on the main shaft. (a) Actual stress, (b) Estimated stress in case of using actual aerodynamic torque, (c) Estimated stress in case of using estimated aerodynamic torque, (d) Stress estimation relative error in case of using actual aerodynamic torque, (e) Stress estimation relative error in case of using estimated aerodynamic torque.

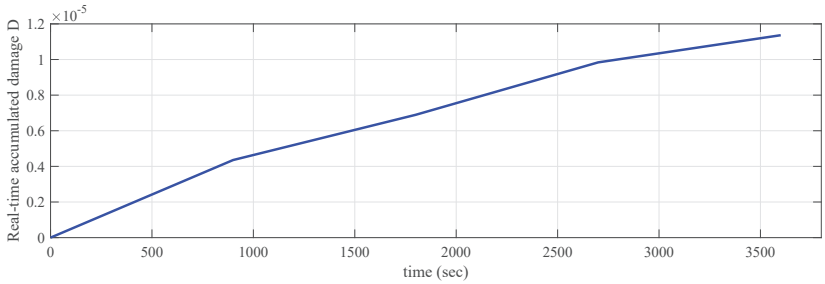

Figure 11: Expected accumulated damage of the main shaft over one hour of operation (overload condition: 20%).

[8] Rausand, M., Barros, A., and Hoyland, A. (2020). System reliability theory: models, statistical methods, and applications. John Wiley & Sons.

[9] Snieckus, D., 2019. https://www.rechargenews.com/wind/siemens-gamesa-unveils-digitally-souped-up-11mw-offshore-turbine/2-1-711795

[10] Goossens, P. (2017). Industry 4.0 and the Power of the Digital Twin. Retrieved, 5(3), 2017.

[11] Johansen, S. S., and Nejad, A. R. (2019, June). On Digital Twin Condition Monitoring Approach for Drivetrains in Marine Applications. In International Conference on Offshore Mechanics and Arctic Engineering (Vol. 58899, p. V010T09A013). American Society of Mechanical Engineers.

[12] Nejad, A. R., Gao, Z., and Moan, T. (2014). Fatigue reliability-based inspection and maintenance planning of gearbox components in wind turbine drivetrains. Energy Procedia, 53, 248-257.

[13] Sethuraman, L., Guo, Y., and Sheng, S. (2015). Mitigation of Micropitting in Wind Turbine Main Shaft Bearings (No. NREL/JA-5000-65026). National Renewable Energy Lab.(NREL), Golden, CO (United States).

[14] Liu, Z., and Zhang, L. (2020). A review of failure modes, condition monitoring and fault diagnosis methods for large-scale wind turbine bearings. Measurement, 149, 107002.

[15] Pedersen, E. B., Jørgensen, D., Riber, H. J., Ballani, J., Vallaghé, S., and Paccaud, B. (2019, July). True Fatigue Life Calculation Using Digital Twin Concept and Operational Modal Analysis. In The 29^{th} International Ocean and Polar Engineering Conference. International Society of Offshore and Polar Engineers.

[16] Moghadam, F. K., and Nejad, A. R. (2020, September). Natural frequency estimation by using torsional response, and applications for wind turbine drivetrain fault diagnosis. In Journal of Physics: Conference Series (Vol. 1618, No. 2, p. 022019). IOP Publishing.

[17] Herp, J., Pedersen, N. L., and Nadimi, E. S. (2020). Assessment of Early Stopping through Statistical Health Prognostic Models for Empirical RUL Estimation in Wind Turbine Main Bearing Failure Monitoring. Energies, 13(1), 83.

[18] Liu, H., Song, W., Niu, Y., Zio, E. A generalized cauchy method for remaining useful life prediction of wind turbine gearboxes. Mechanical Systems and Signal Processing, 153, 107471.

[19] Marques, J. M. E., Benasciutti, D., and Tovo, R. (2020). Variability of the fatigue damage due to the randomness of a stationary vibration load. International Journal of Fatigue, 141, 105891.

[20] Rezamand, M., Kordestani, M., Carriveau, R., Ting, D. S. K., and Saif, M. (2020). An integrated feature-based failure prognosis method for wind turbine bearings. IEEE/ASME Transactions on Mechatronics.

[21] Cheng, F., Qu, L., Qiao, W., and Hao, L. (2018). Enhanced particle filtering for bearing remaining useful life prediction of wind turbine drivetrain gearboxes. IEEE Transactions on Industrial Electronics, 66(6), 4738-4748.

[22] Kordestani, M., Samadi, M. F., and Saif, M. (2020). A New Hybrid Fault Prognosis Method for MFS Systems Based on Distributed Neural Networks and Recursive Bayesian Algorithm. IEEE Systems Journal.

[23] Wang, T., Han, Q., Chu, F., Feng, Z. (2019). Vibration based condition monitoring and fault diagnosis of wind turbine planetary gearbox: A review. Mechanical Systems and Signal Processing, 126, 662-685.

[24] Moghadam, F. K., and R. Nejad, A. (2019, November). Experimental Validation of Angular Velocity Measurements for Wind Turbines Drivetrain Condition Monitoring. In International Conference on Offshore Mechanics and Arctic Engineering (Vol. 59353, p. V001T01A035). American Society of Mechanical Engineers.

[25] Sheng, S., Link, H., LaCava, W., van Dam, J., McNiff, B., Veers, P., ... and Oyague, F. (2011). Wind turbine drivetrain condition monitoring during GRC phase 1 and phase 2 testing (No. NREL/TP-5000-52748). National Renewable Energy Lab.(NREL), Golden, CO (United States).

[26] Andrawus, J. A. (2008). Maintenance optimisation for wind turbines (Doctoral dissertation).

[27] Vizentin, G., Vukelić, G., and Srok, M. (2017). Common failures of ship propulsion shafts. Pomorstvo, 31(2), 85-90.

[28] Becker, W. T., and Lampman, S. (2002). Fracture appearance and mechanisms of deformation and fracture. Materials Park, OH: ASM International, 2002., 559-586.

[29] Zhang, Z., Yin, Z., Han, T., and Tan, A. C. (2013). Fracture analysis of wind turbine main shaft. Engineering Failure Analysis, 34, 129-139.

[30] Rauert, T., Herrmann, J., Dalhoff, P., and Sander, M. (2016). Fretting fatigue induced surface cracks under shrink fitted main bearings in wind turbine rotor shafts. Procedia Structural Integrity, 2, 3601-3609.

[31] Bortolotti, P., Canet Tarrés, H., Dykes, K., Merz, K., Sethuraman, L., Verelst, D., and Zahle, F. (2019). Systems engineering in wind energy-WP2. 1 reference wind turbines. Technical Report No. NREL/TP-5000-73492, National Renewable Energy Laboratory (NREL).

[32] Kang, J. H., and Lee, H. (2017). Structural Safety Analysis of Main Shaft for Wind Power Generators Considering Mass Effect. International Journal of Applied Engineering Research, 12(17), 6862-6869.

[33] DIN EN 10083-3: 2007-01. (2007). Steels for Quenching and Tempering—Part 3: Technical Delivery Conditions for Alloy Steels, German Version EN 10083-3: 2006.

[34] Bak C, Zahle F, Bitsche R, Kim T, Yde A, Henriksen LC, Natarajan A, Hansen MH. Description of the DTU 10 MW reference wind turbine. *DTU Wind Energy Report-I-0092* 2013;5.

[35] Hegseth JM, Bachynski EE. A semi-analytical frequency domain model for efficient design evaluation of spar floating wind turbines. *Marine Struc-*

tures 2019;**64**:186-210.

[36] Moghadam, F. K., and Nejad, A. R. (2020). Evaluation of PMSG-based drivetrain technologies for 10-MW floating offshore wind turbines: Pros and cons in a life cycle perspective. Wind Energy.

[37] Moghadam, F.K., and Nejad, A.R., Theoretical and experimental study of wind turbine drivetrain fault diagnosis by using torsional vibrations and modal estimation, Under review by Journal of Sound and Vibration.

[38] Pilanci, M., Arikan, O., and Pinar, M. C. (2010). Structured least squares problems and robust estimators. IEEE transactions on signal processing, 58(5), 2453-2465.

[39] Golub, G. H., and Van Loan, C. (1979). Unsymmetric positive definite linear systems. Linear Algebra and its Applications, 28, 85-97.

[40] Owen, A. B. (2013). Monte Carlo theory, methods and examples. Monte Carlo Theory, Methods and Examples. Art Owen.

[41] Nejad, A. R., Gao, Z., Moan, T. (2014). On long-term fatigue damage and reliability analysis of gears under wind loads in offshore wind turbine drivetrains. International Journal of Fatigue, 61, 116-128.

[42] Sudret, B., Guédé, Z., Hornet, P., Stéphan, J. M., and Lemaire, M. (2003, August). Probabilistic assessment of fatigue life including statistical uncertainties in the SN curve. In Proceedings of the 17^{th} International Conference on Structural Mechanics in Reactor Technology.

[43] Engel, B., and Al-Maeeni, S. S. H. (2017). Failure analysis and fatigue life estimation of a shaft of a rotary draw bending machine. constraints, 3, 1785-1790.

[44] Maheswari, R. U., and Umamaheswari, R. (2017). Trends in non-stationary signal processing techniques applied to vibration analysis of wind turbine drive train–A contemporary survey. Mechanical Systems and Signal Processing, 85, 296-311.

[45] Ghane, M., Rasekhi Nejad, A., Blanke, M., Gao, Z., and Moan, T. (2018). Condition monitoring of spar-type floating wind turbine drivetrain using statistical fault diagnosis. Wind Energy, 21(7), 575-589.

[46] Toft, H. S., Sørensen, J. D., and Veldkamp, D. (2011). Assessment of load extrapolation methods for wind turbines. Journal of solar energy engineering, 133(2).

[47] Montgomery DC, Runger GC. Applied statistics and probability for engineers. sixth ed. Hoboken, NJ, USA: John Wiley & Sons; 2014.

[48] Downing, S. D., and Socie, D. F. (1982). Simple rainflow counting algorithms. International journal of fatigue, 4(1), 31-40.

[49] Manwell, J. F., McGowan, J. G., and Rogers, A. L. (2010). Wind energy explained: theory, design and application. John Wiley & Sons.

[50] Benasciutti, D. E. N. I. S., and Tovo, R. O. B. E. R. T. O. (2004). Rainflow cycle distribution and fatigue damage in Gaussian random loadings. Internal Report No. 129, Department of Engineering, University of Ferrara, Italy.

[51] Wang, S., Nejad, A. R., and Moan, T. (2020). On design, modelling, and analysis of a 10-MW medium-speed drivetrain for offshore wind turbines. Wind Energy, 23(4), 1099-1117.

Appendix B

List of previous PhD theses at Dept. of Marine Tech.

Previous PhD theses published at the Department of Marine Technology (earlier: Faculty of Marine Technology)
NORWEGIAN UNIVERSITY OF SCIENCE AND TECHNOLOGY

Report No.	Author	Title
	Kavlie, Dag	Optimization of Plane Elastic Grillages, 1967
	Hansen, Hans R.	Man-Machine Communication and Data-Storage Methods in Ship Structural Design, 1971
	Gisvold, Kaare M.	A Method for non-linear mixed -integer programming and its Application to Design Problems, 1971
	Lund, Sverre	Tanker Frame Optimalization by means of SUMT-Transformation and Behaviour Models, 1971
	Vinje, Tor	On Vibration of Spherical Shells Interacting with Fluid, 1972
	Lorentz, Jan D.	Tank Arrangement for Crude Oil Carriers in Accordance with the new Anti-Pollution Regulations, 1975
	Carlsen, Carl A.	Computer-Aided Design of Tanker Structures, 1975
	Larsen, Carl M.	Static and Dynamic Analysis of Offshore Pipelines during Installation, 1976
UR-79-01	Brigt Hatlestad, MK	The finite element method used in a fatigue evaluation of fixed offshore platforms. (Dr.Ing. Thesis)
UR-79-02	Erik Pettersen, MK	Analysis and design of cellular structures. (Dr.Ing. Thesis)
UR-79-03	Sverre Valsgård, MK	Finite difference and finite element methods applied to nonlinear analysis of plated structures. (Dr.Ing. Thesis)
UR-79-04	Nils T. Nordsve, MK	Finite element collapse analysis of structural members considering imperfections and stresses due to fabrication. (Dr.Ing. Thesis)
UR-79-05	Ivar J. Fylling, MK	Analysis of towline forces in ocean towing systems. (Dr.Ing. Thesis)
UR-80-06	Nils Sandsmark, MM	Analysis of Stationary and Transient Heat Conduction by the Use of the Finite Element Method. (Dr.Ing. Thesis)
UR-80-09	Sverre Haver, MK	Analysis of uncertainties related to the stochastic modeling of ocean waves. (Dr.Ing. Thesis)
UR-81-15	Odland, Jonas	On the Strength of welded Ring stiffened cylindrical Shells primarily subjected to axial Compression
UR-82-17	Engesvik, Knut	Analysis of Uncertainties in the fatigue Capacity of

		Welded Joints
UR-82-18	Rye, Henrik	Ocean wave groups
UR-83-30	Eide, Oddvar Inge	On Cumulative Fatigue Damage in Steel Welded Joints
UR-83-33	Mo, Olav	Stochastic Time Domain Analysis of Slender Offshore Structures
UR-83-34	Amdahl, Jørgen	Energy absorption in Ship-platform impacts
UR-84-37	Mørch, Morten	Motions and mooring forces of semi submersibles as determined by full-scale measurements and theoretical analysis
UR-84-38	Soares, C. Guedes	Probabilistic models for load effects in ship structures
UR-84-39	Aarsnes, Jan V.	Current forces on ships
UR-84-40	Czujko, Jerzy	Collapse Analysis of Plates subjected to Biaxial Compression and Lateral Load
UR-85-46	Alf G. Engseth, MK	Finite element collapse analysis of tubular steel offshore structures. (Dr.Ing. Thesis)
UR-86-47	Dengody Sheshappa, MP	A Computer Design Model for Optimizing Fishing Vessel Designs Based on Techno-Economic Analysis. (Dr.Ing. Thesis)
UR-86-48	Vidar Aanesland, MH	A Theoretical and Numerical Study of Ship Wave Resistance. (Dr.Ing. Thesis)
UR-86-49	Heinz-Joachim Wessel, MK	Fracture Mechanics Analysis of Crack Growth in Plate Girders. (Dr.Ing. Thesis)
UR-86-50	Jon Taby, MK	Ultimate and Post-ultimate Strength of Dented Tubular Members. (Dr.Ing. Thesis)
UR-86-51	Walter Lian, MH	A Numerical Study of Two-Dimensional Separated Flow Past Bluff Bodies at Moderate KC-Numbers. (Dr.Ing. Thesis)
UR-86-52	Bjørn Sortland, MH	Force Measurements in Oscillating Flow on Ship Sections and Circular Cylinders in a U-Tube Water Tank. (Dr.Ing. Thesis)
UR-86-53	Kurt Strand, MM	A System Dynamic Approach to One-dimensional Fluid Flow. (Dr.Ing. Thesis)
UR-86-54	Arne Edvin Løken, MH	Three Dimensional Second Order Hydrodynamic Effects on Ocean Structures in Waves. (Dr.Ing. Thesis)
UR-86-55	Sigurd Falch, MH	A Numerical Study of Slamming of Two-Dimensional Bodies. (Dr.Ing. Thesis)
UR-87-56	Arne Braathen, MH	Application of a Vortex Tracking Method to the Prediction of Roll Damping of a Two-Dimension Floating Body. (Dr.Ing. Thesis)

UR-87-57	Bernt Leira, MK	Gaussian Vector Processes for Reliability Analysis involving Wave-Induced Load Effects. (Dr.Ing. Thesis)
UR-87-58	Magnus Småvik, MM	Thermal Load and Process Characteristics in a Two-Stroke Diesel Engine with Thermal Barriers (in Norwegian). (Dr.Ing. Thesis)
MTA-88-59	Bernt Arild Bremdal, MP	An Investigation of Marine Installation Processes – A Knowledge - Based Planning Approach. (Dr.Ing. Thesis)
MTA-88-60	Xu Jun, MK	Non-linear Dynamic Analysis of Space-framed Offshore Structures. (Dr.Ing. Thesis)
MTA-89-61	Gang Miao, MH	Hydrodynamic Forces and Dynamic Responses of Circular Cylinders in Wave Zones. (Dr.Ing. Thesis)
MTA-89-62	Martin Greenhow, MH	Linear and Non-Linear Studies of Waves and Floating Bodies. Part I and Part II. (Dr.Techn. Thesis)
MTA-89-63	Chang Li, MH	Force Coefficients of Spheres and Cubes in Oscillatory Flow with and without Current. (Dr.Ing. Thesis
MTA-89-64	Hu Ying, MP	A Study of Marketing and Design in Development of Marine Transport Systems. (Dr.Ing. Thesis)
MTA-89-65	Arild Jæger, MH	Seakeeping, Dynamic Stability and Performance of a Wedge Shaped Planing Hull. (Dr.Ing. Thesis)
MTA-89-66	Chan Siu Hung, MM	The dynamic characteristics of tilting-pad bearings
MTA-89-67	Kim Wikstrøm, MP	Analysis av projekteringen for ett offshore projekt. (Licenciat-avhandling)
MTA-89-68	Jiao Guoyang, MK	Reliability Analysis of Crack Growth under Random Loading, considering Model Updating. (Dr.Ing. Thesis)
MTA-89-69	Arnt Olufsen, MK	Uncertainty and Reliability Analysis of Fixed Offshore Structures. (Dr.Ing. Thesis)
MTA-89-70	Wu Yu-Lin, MR	System Reliability Analyses of Offshore Structures using improved Truss and Beam Models. (Dr.Ing. Thesis)
MTA-90-71	Jan Roger Hoff, MH	Three-dimensional Green function of a vessel with forward speed in waves. (Dr.Ing. Thesis)
MTA-90-72	Rong Zhao, MH	Slow-Drift Motions of a Moored Two-Dimensional Body in Irregular Waves. (Dr.Ing. Thesis)
MTA-90-73	Atle Minsaas, MP	Economical Risk Analysis. (Dr.Ing. Thesis)
MTA-90-74	Knut-Aril Farnes, MK	Long-term Statistics of Response in Non-linear Marine Structures. (Dr.Ing. Thesis)
MTA-90-75	Torbjørn Sotberg, MK	Application of Reliability Methods for Safety Assessment of Submarine Pipelines. (Dr.Ing.

		Thesis)
MTA-90-76	Zeuthen, Steffen, MP	SEAMAID. A computational model of the design process in a constraint-based logic programming environment. An example from the offshore domain. (Dr.Ing. Thesis)
MTA-91-77	Haagensen, Sven, MM	Fuel Dependant Cyclic Variability in a Spark Ignition Engine - An Optical Approach. (Dr.Ing. Thesis)
MTA-91-78	Løland, Geir, MH	Current forces on and flow through fish farms. (Dr.Ing. Thesis)
MTA-91-79	Hoen, Christopher, MK	System Identification of Structures Excited by Stochastic Load Processes. (Dr.Ing. Thesis)
MTA-91-80	Haugen, Stein, MK	Probabilistic Evaluation of Frequency of Collision between Ships and Offshore Platforms. (Dr.Ing. Thesis)
MTA-91-81	Sødahl, Nils, MK	Methods for Design and Analysis of Flexible Risers. (Dr.Ing. Thesis)
MTA-91-82	Ormberg, Harald, MK	Non-linear Response Analysis of Floating Fish Farm Systems. (Dr.Ing. Thesis)
MTA-91-83	Marley, Mark J., MK	Time Variant Reliability under Fatigue Degradation. (Dr.Ing. Thesis)
MTA-91-84	Krokstad, Jørgen R., MH	Second-order Loads in Multidirectional Seas. (Dr.Ing. Thesis)
MTA-91-85	Molteberg, Gunnar A., MM	The Application of System Identification Techniques to Performance Monitoring of Four Stroke Turbocharged Diesel Engines. (Dr.Ing. Thesis)
MTA-92-86	Mørch, Hans Jørgen Bjelke, MH	Aspects of Hydrofoil Design: with Emphasis on Hydrofoil Interaction in Calm Water. (Dr.Ing. Thesis)
MTA-92-87	Chan Siu Hung, MM	Nonlinear Analysis of Rotordynamic Instabilities in Highspeed Turbomachinery. (Dr.Ing. Thesis)
MTA-92-88	Bessason, Bjarni, MK	Assessment of Earthquake Loading and Response of Seismically Isolated Bridges. (Dr.Ing. Thesis)
MTA-92-89	Langli, Geir, MP	Improving Operational Safety through exploitation of Design Knowledge - an investigation of offshore platform safety. (Dr.Ing. Thesis)
MTA-92-90	Sævik, Svein, MK	On Stresses and Fatigue in Flexible Pipes. (Dr.Ing. Thesis)
MTA-92-91	Ask, Tor Ø., MM	Ignition and Flame Growth in Lean Gas-Air Mixtures. An Experimental Study with a Schlieren System. (Dr.Ing. Thesis)
MTA-86-92	Hessen, Gunnar, MK	Fracture Mechanics Analysis of Stiffened Tubular Members. (Dr.Ing. Thesis)

MTA-93-93	Steinebach, Christian, MM	Knowledge Based Systems for Diagnosis of Rotating Machinery. (Dr.Ing. Thesis)
MTA-93-94	Dalane, Jan Inge, MK	System Reliability in Design and Maintenance of Fixed Offshore Structures. (Dr.Ing. Thesis)
MTA-93-95	Steen, Sverre, MH	Cobblestone Effect on SES. (Dr.Ing. Thesis)
MTA-93-96	Karunakaran, Daniel, MK	Nonlinear Dynamic Response and Reliability Analysis of Drag-dominated Offshore Platforms. (Dr.Ing. Thesis)
MTA-93-97	Hagen, Arnulf, MP	The Framework of a Design Process Language. (Dr.Ing. Thesis)
MTA-93-98	Nordrik, Rune, MM	Investigation of Spark Ignition and Autoignition in Methane and Air Using Computational Fluid Dynamics and Chemical Reaction Kinetics. A Numerical Study of Ignition Processes in Internal Combustion Engines. (Dr.Ing. Thesis)
MTA-94-99	Passano, Elizabeth, MK	Efficient Analysis of Nonlinear Slender Marine Structures. (Dr.Ing. Thesis)
MTA-94-100	Kvålsvold, Jan, MH	Hydroelastic Modelling of Wetdeck Slamming on Multihull Vessels. (Dr.Ing. Thesis)
MTA-94-102	Bech, Sidsel M., MK	Experimental and Numerical Determination of Stiffness and Strength of GRP/PVC Sandwich Structures. (Dr.Ing. Thesis)
MTA-95-103	Paulsen, Hallvard, MM	A Study of Transient Jet and Spray using a Schlieren Method and Digital Image Processing. (Dr.Ing. Thesis)
MTA-95-104	Hovde, Geir Olav, MK	Fatigue and Overload Reliability of Offshore Structural Systems, Considering the Effect of Inspection and Repair. (Dr.Ing. Thesis)
MTA-95-105	Wang, Xiaozhi, MK	Reliability Analysis of Production Ships with Emphasis on Load Combination and Ultimate Strength. (Dr.Ing. Thesis)
MTA-95-106	Ulstein, Tore, MH	Nonlinear Effects of a Flexible Stern Seal Bag on Cobblestone Oscillations of an SES. (Dr.Ing. Thesis)
MTA-95-107	Solaas, Frøydis, MH	Analytical and Numerical Studies of Sloshing in Tanks. (Dr.Ing. Thesis)
MTA-95-108	Hellan, Øyvind, MK	Nonlinear Pushover and Cyclic Analyses in Ultimate Limit State Design and Reassessment of Tubular Steel Offshore Structures. (Dr.Ing. Thesis)
MTA-95-109	Hermundstad, Ole A., MK	Theoretical and Experimental Hydroelastic Analysis of High Speed Vessels. (Dr.Ing. Thesis)
MTA-96-110	Bratland, Anne K., MH	Wave-Current Interaction Effects on Large-Volume Bodies in Water of Finite Depth. (Dr.Ing. Thesis)
MTA-96-111	Herfjord, Kjell, MH	A Study of Two-dimensional Separated Flow by a Combination of the Finite Element Method and

		Navier-Stokes Equations. (Dr.Ing. Thesis)
MTA-96-112	Æsøy, Vilmar, MM	Hot Surface Assisted Compression Ignition in a Direct Injection Natural Gas Engine. (Dr.Ing. Thesis)
MTA-96-113	Eknes, Monika L., MK	Escalation Scenarios Initiated by Gas Explosions on Offshore Installations. (Dr.Ing. Thesis)
MTA-96-114	Erikstad, Stein O., MP	A Decision Support Model for Preliminary Ship Design. (Dr.Ing. Thesis)
MTA-96-115	Pedersen, Egil, MH	A Nautical Study of Towed Marine Seismic Streamer Cable Configurations. (Dr.Ing. Thesis)
MTA-97-116	Moksnes, Paul O., MM	Modelling Two-Phase Thermo-Fluid Systems Using Bond Graphs. (Dr.Ing. Thesis)
MTA-97-117	Halse, Karl H., MK	On Vortex Shedding and Prediction of Vortex-Induced Vibrations of Circular Cylinders. (Dr.Ing. Thesis)
MTA-97-118	Igland, Ragnar T., MK	Reliability Analysis of Pipelines during Laying, considering Ultimate Strength under Combined Loads. (Dr.Ing. Thesis)
MTA-97-119	Pedersen, Hans-P., MP	Levendefiskteknologi for fiskefartøy. (Dr.Ing. Thesis)
MTA-98-120	Vikestad, Kyrre, MK	Multi-Frequency Response of a Cylinder Subjected to Vortex Shedding and Support Motions. (Dr.Ing. Thesis)
MTA-98-121	Azadi, Mohammad R. E., MK	Analysis of Static and Dynamic Pile-Soil-Jacket Behaviour. (Dr.Ing. Thesis)
MTA-98-122	Ulltang, Terje, MP	A Communication Model for Product Information. (Dr.Ing. Thesis)
MTA-98-123	Torbergsen, Erik, MM	Impeller/Diffuser Interaction Forces in Centrifugal Pumps. (Dr.Ing. Thesis)
MTA-98-124	Hansen, Edmond, MH	A Discrete Element Model to Study Marginal Ice Zone Dynamics and the Behaviour of Vessels Moored in Broken Ice. (Dr.Ing. Thesis)
MTA-98-125	Videiro, Paulo M., MK	Reliability Based Design of Marine Structures. (Dr.Ing. Thesis)
MTA-99-126	Mainçon, Philippe, MK	Fatigue Reliability of Long Welds Application to Titanium Risers. (Dr.Ing. Thesis)
MTA-99-127	Haugen, Elin M., MH	Hydroelastic Analysis of Slamming on Stiffened Plates with Application to Catamaran Wetdecks. (Dr.Ing. Thesis)
MTA-99-128	Langhelle, Nina K., MK	Experimental Validation and Calibration of Nonlinear Finite Element Models for Use in Design of Aluminium Structures Exposed to Fire. (Dr.Ing. Thesis)
MTA-99-	Berstad, Are J., MK	Calculation of Fatigue Damage in Ship Structures.

129		(Dr.Ing. Thesis)
MTA-99-130	Andersen, Trond M., MM	Short Term Maintenance Planning. (Dr.Ing. Thesis)
MTA-99-131	Tveiten, Bård Wathne, MK	Fatigue Assessment of Welded Aluminium Ship Details. (Dr.Ing. Thesis)
MTA-99-132	Søreide, Fredrik, MP	Applications of underwater technology in deep water archaeology. Principles and practice. (Dr.Ing. Thesis)
MTA-99-133	Tønnessen, Rune, MH	A Finite Element Method Applied to Unsteady Viscous Flow Around 2D Blunt Bodies With Sharp Corners. (Dr.Ing. Thesis)
MTA-99-134	Elvekrok, Dag R., MP	Engineering Integration in Field Development Projects in the Norwegian Oil and Gas Industry. The Supplier Management of Norne. (Dr.Ing. Thesis)
MTA-99-135	Fagerholt, Kjetil, MP	Optimeringsbaserte Metoder for Ruteplanlegging innen skipsfart. (Dr.Ing. Thesis)
MTA-99-136	Bysveen, Marie, MM	Visualization in Two Directions on a Dynamic Combustion Rig for Studies of Fuel Quality. (Dr.Ing. Thesis)
MTA-2000-137	Storteig, Eskild, MM	Dynamic characteristics and leakage performance of liquid annular seals in centrifugal pumps. (Dr.Ing. Thesis)
MTA-2000-138	Sagli, Gro, MK	Model uncertainty and simplified estimates of long term extremes of hull girder loads in ships. (Dr.Ing. Thesis)
MTA-2000-139	Tronstad, Harald, MK	Nonlinear analysis and design of cable net structures like fishing gear based on the finite element method. (Dr.Ing. Thesis)
MTA-2000-140	Kroneberg, André, MP	Innovation in shipping by using scenarios. (Dr.Ing. Thesis)
MTA-2000-141	Haslum, Herbjørn Alf, MH	Simplified methods applied to nonlinear motion of spar platforms. (Dr.Ing. Thesis)
MTA-2001-142	Samdal, Ole Johan, MM	Modelling of Degradation Mechanisms and Stressor Interaction on Static Mechanical Equipment Residual Lifetime. (Dr.Ing. Thesis)
MTA-2001-143	Baarholm, Rolf Jarle, MH	Theoretical and experimental studies of wave impact underneath decks of offshore platforms. (Dr.Ing. Thesis)
MTA-2001-144	Wang, Lihua, MK	Probabilistic Analysis of Nonlinear Wave-induced Loads on Ships. (Dr.Ing. Thesis)
MTA-2001-145	Kristensen, Odd H. Holt, MK	Ultimate Capacity of Aluminium Plates under Multiple Loads, Considering HAZ Properties. (Dr.Ing. Thesis)
MTA-2001-146	Greco, Marilena, MH	A Two-Dimensional Study of Green-Water

		Loading. (Dr.Ing. Thesis)
MTA-2001-147	Heggelund, Svein E., MK	Calculation of Global Design Loads and Load Effects in Large High Speed Catamarans. (Dr.Ing. Thesis)
MTA-2001-148	Babalola, Olusegun T., MK	Fatigue Strength of Titanium Risers – Defect Sensitivity. (Dr.Ing. Thesis)
MTA-2001-149	Mohammed, Abuu K., MK	Nonlinear Shell Finite Elements for Ultimate Strength and Collapse Analysis of Ship Structures. (Dr.Ing. Thesis)
MTA-2002-150	Holmedal, Lars E., MH	Wave-current interactions in the vicinity of the sea bed. (Dr.Ing. Thesis)
MTA-2002-151	Rognebakke, Olav F., MH	Sloshing in rectangular tanks and interaction with ship motions. (Dr.Ing. Thesis)
MTA-2002-152	Lader, Pål Furset, MH	Geometry and Kinematics of Breaking Waves. (Dr.Ing. Thesis)
MTA-2002-153	Yang, Qinzheng, MH	Wash and wave resistance of ships in finite water depth. (Dr.Ing. Thesis)
MTA-2002-154	Melhus, Øyvin, MM	Utilization of VOC in Diesel Engines. Ignition and combustion of VOC released by crude oil tankers. (Dr.Ing. Thesis)
MTA-2002-155	Ronæss, Marit, MH	Wave Induced Motions of Two Ships Advancing on Parallel Course. (Dr.Ing. Thesis)
MTA-2002-156	Økland, Ole D., MK	Numerical and experimental investigation of whipping in twin hull vessels exposed to severe wet deck slamming. (Dr.Ing. Thesis)
MTA-2002-157	Ge, Chunhua, MK	Global Hydroelastic Response of Catamarans due to Wet Deck Slamming. (Dr.Ing. Thesis)
MTA-2002-158	Byklum, Eirik, MK	Nonlinear Shell Finite Elements for Ultimate Strength and Collapse Analysis of Ship Structures. (Dr.Ing. Thesis)
IMT-2003-1	Chen, Haibo, MK	Probabilistic Evaluation of FPSO-Tanker Collision in Tandem Offloading Operation. (Dr.Ing. Thesis)
IMT-2003-2	Skaugset, Kjetil Bjørn, MK	On the Suppression of Vortex Induced Vibrations of Circular Cylinders by Radial Water Jets. (Dr.Ing. Thesis)
IMT-2003-3	Chezhian, Muthu	Three-Dimensional Analysis of Slamming. (Dr.Ing. Thesis)
IMT-2003-4	Buhaug, Øyvind	Deposit Formation on Cylinder Liner Surfaces in Medium Speed Engines. (Dr.Ing. Thesis)
IMT-2003-5	Tregde, Vidar	Aspects of Ship Design: Optimization of Aft Hull with Inverse Geometry Design. (Dr.Ing. Thesis)
IMT-	Wist, Hanne Therese	Statistical Properties of Successive Ocean Wave

2003-6		Parameters. (Dr.Ing. Thesis)
IMT-2004-7	Ransau, Samuel	Numerical Methods for Flows with Evolving Interfaces. (Dr.Ing. Thesis)
IMT-2004-8	Soma, Torkel	Blue-Chip or Sub-Standard. A data interrogation approach of identity safety characteristics of shipping organization. (Dr.Ing. Thesis)
IMT-2004-9	Ersdal, Svein	An experimental study of hydrodynamic forces on cylinders and cables in near axial flow. (Dr.Ing. Thesis)
IMT-2005-10	Brodtkorb, Per Andreas	The Probability of Occurrence of Dangerous Wave Situations at Sea. (Dr.Ing. Thesis)
IMT-2005-11	Yttervik, Rune	Ocean current variability in relation to offshore engineering. (Dr.Ing. Thesis)
IMT-2005-12	Fredheim, Arne	Current Forces on Net-Structures. (Dr.Ing. Thesis)
IMT-2005-13	Heggernes, Kjetil	Flow around marine structures. (Dr.Ing. Thesis
IMT-2005-14	Fouques, Sebastien	Lagrangian Modelling of Ocean Surface Waves and Synthetic Aperture Radar Wave Measurements. (Dr.Ing. Thesis)
IMT-2006-15	Holm, Håvard	Numerical calculation of viscous free surface flow around marine structures. (Dr.Ing. Thesis)
IMT-2006-16	Bjørheim, Lars G.	Failure Assessment of Long Through Thickness Fatigue Cracks in Ship Hulls. (Dr.Ing. Thesis)
IMT-2006-17	Hansson, Lisbeth	Safety Management for Prevention of Occupational Accidents. (Dr.Ing. Thesis)
IMT-2006-18	Zhu, Xinying	Application of the CIP Method to Strongly Nonlinear Wave-Body Interaction Problems. (Dr.Ing. Thesis)
IMT-2006-19	Reite, Karl Johan	Modelling and Control of Trawl Systems. (Dr.Ing. Thesis)
IMT-2006-20	Smogeli, Øyvind Notland	Control of Marine Propellers. From Normal to Extreme Conditions. (Dr.Ing. Thesis)
IMT-2007-21	Storhaug, Gaute	Experimental Investigation of Wave Induced Vibrations and Their Effect on the Fatigue Loading of Ships. (Dr.Ing. Thesis)
IMT-2007-22	Sun, Hui	A Boundary Element Method Applied to Strongly Nonlinear Wave-Body Interaction Problems. (PhD Thesis, CeSOS)
IMT-2007-23	Rustad, Anne Marthine	Modelling and Control of Top Tensioned Risers. (PhD Thesis, CeSOS)
IMT-2007-24	Johansen, Vegar	Modelling flexible slender system for real-time simulations and control applications
IMT-2007-25	Wroldsen, Anders Sunde	Modelling and control of tensegrity structures.

		(PhD Thesis, CeSOS)
IMT-2007-26	Aronsen, Kristoffer Høye	An experimental investigation of in-line and combined inline and cross flow vortex induced vibrations. (Dr. avhandling, IMT)
IMT-2007-27	Gao, Zhen	Stochastic Response Analysis of Mooring Systems with Emphasis on Frequency-domain Analysis of Fatigue due to Wide-band Response Processes (PhD Thesis, CeSOS)
IMT-2007-28	Thorstensen, Tom Anders	Lifetime Profit Modelling of Ageing Systems Utilizing Information about Technical Condition. (Dr.ing. thesis, IMT)
IMT-2008-29	Refsnes, Jon Erling Gorset	Nonlinear Model-Based Control of Slender Body AUVs (PhD Thesis, IMT)
IMT-2008-30	Berntsen, Per Ivar B.	Structural Reliability Based Position Mooring. (PhD-Thesis, IMT)
IMT-2008-31	Ye, Naiquan	Fatigue Assessment of Aluminium Welded Box-stiffener Joints in Ships (Dr.ing. thesis, IMT)
IMT-2008-32	Radan, Damir	Integrated Control of Marine Electrical Power Systems. (PhD-Thesis, IMT)
IMT-2008-33	Thomassen, Paul	Methods for Dynamic Response Analysis and Fatigue Life Estimation of Floating Fish Cages. (Dr.ing. thesis, IMT)
IMT-2008-34	Pákozdi, Csaba	A Smoothed Particle Hydrodynamics Study of Two-dimensional Nonlinear Sloshing in Rectangular Tanks. (Dr.ing.thesis, IMT/ CeSOS)
IMT-2007-35	Grytøyr, Guttorm	A Higher-Order Boundary Element Method and Applications to Marine Hydrodynamics. (Dr.ing.thesis, IMT)
IMT-2008-36	Drummen, Ingo	Experimental and Numerical Investigation of Nonlinear Wave-Induced Load Effects in Containerships considering Hydroelasticity. (PhD thesis, CeSOS)
IMT-2008-37	Skejic, Renato	Maneuvering and Seakeeping of a Singel Ship and of Two Ships in Interaction. (PhD-Thesis, CeSOS)
IMT-2008-38	Harlem, Alf	An Age-Based Replacement Model for Repairable Systems with Attention to High-Speed Marine Diesel Engines. (PhD-Thesis, IMT)
IMT-2008-39	Alsos, Hagbart S.	Ship Grounding. Analysis of Ductile Fracture, Bottom Damage and Hull Girder Response. (PhD-thesis, IMT)
IMT-2008-40	Graczyk, Mateusz	Experimental Investigation of Sloshing Loading and Load Effects in Membrane LNG Tanks Subjected to Random Excitation. (PhD-thesis, CeSOS)
IMT-2008-41	Taghipour, Reza	Efficient Prediction of Dynamic Response for Flexible amd Multi-body Marine Structures. (PhD-

		thesis, CeSOS)
IMT-2008-42	Ruth, Eivind	Propulsion control and thrust allocation on marine vessels. (PhD thesis, CeSOS)
IMT-2008-43	Nystad, Bent Helge	Technical Condition Indexes and Remaining Useful Life of Aggregated Systems. PhD thesis, IMT
IMT-2008-44	Soni, Prashant Kumar	Hydrodynamic Coefficients for Vortex Induced Vibrations of Flexible Beams, PhD thesis, CeSOS
IMT-2009-45	Amlashi, Hadi K.K.	Ultimate Strength and Reliability-based Design of Ship Hulls with Emphasis on Combined Global and Local Loads. PhD Thesis, IMT
IMT-2009-46	Pedersen, Tom Arne	Bond Graph Modelling of Marine Power Systems. PhD Thesis, IMT
IMT-2009-47	Kristiansen, Trygve	Two-Dimensional Numerical and Experimental Studies of Piston-Mode Resonance. PhD-Thesis, CeSOS
IMT-2009-48	Ong, Muk Chen	Applications of a Standard High Reynolds Number Model and a Stochastic Scour Prediction Model for Marine Structures. PhD-thesis, IMT
IMT-2009-49	Hong, Lin	Simplified Analysis and Design of Ships subjected to Collision and Grounding. PhD-thesis, IMT
IMT-2009-50	Koushan, Kamran	Vortex Induced Vibrations of Free Span Pipelines, PhD thesis, IMT
IMT-2009-51	Korsvik, Jarl Eirik	Heuristic Methods for Ship Routing and Scheduling. PhD-thesis, IMT
IMT-2009-52	Lee, Jihoon	Experimental Investigation and Numerical in Analyzing the Ocean Current Displacement of Longlines. Ph.d.-Thesis, IMT.
IMT-2009-53	Vestbøstad, Tone Gran	A Numerical Study of Wave-in-Deck Impact usin a Two-Dimensional Constrained Interpolation Profile Method, Ph.d.thesis, CeSOS.
IMT-2009-54	Bruun, Kristine	Bond Graph Modelling of Fuel Cells for Marine Power Plants. Ph.d.-thesis, IMT
IMT 2009-55	Holstad, Anders	Numerical Investigation of Turbulence in a Sekwed Three-Dimensional Channel Flow, Ph.d.-thesis, IMT.
IMT 2009-56	Ayala-Uraga, Efren	Reliability-Based Assessment of Deteriorating Ship-shaped Offshore Structures, Ph.d.-thesis, IMT
IMT 2009-57	Kong, Xiangjun	A Numerical Study of a Damaged Ship in Beam Sea Waves. Ph.d.-thesis, IMT/CeSOS.
IMT 2010-58	Kristiansen, David	Wave Induced Effects on Floaters of Aquaculture Plants, Ph.d.-thesis, CeSOS.

IMT 2010-59	Ludvigsen, Martin	An ROV-Toolbox for Optical and Acoustic Scientific Seabed Investigation. Ph.d.-thesis IMT.
IMT 2010-60	Hals, Jørgen	Modelling and Phase Control of Wave-Energy Converters. Ph.d.thesis, CeSOS.
IMT 2010- 61	Shu, Zhi	Uncertainty Assessment of Wave Loads and Ultimate Strength of Tankers and Bulk Carriers in a Reliability Framework. Ph.d. Thesis, IMT/ CeSOS
IMT 2010-62	Shao, Yanlin	Numerical Potential-Flow Studies on Weakly-Nonlinear Wave-Body Interactions with/without Small Forward Speed, Ph.d.thesis,CeSOS.
IMT 2010-63	Califano, Andrea	Dynamic Loads on Marine Propellers due to Intermittent Ventilation. Ph.d.thesis, IMT.
IMT 2010-64	El Khoury, George	Numerical Simulations of Massively Separated Turbulent Flows, Ph.d.-thesis, IMT
IMT 2010-65	Seim, Knut Sponheim	Mixing Process in Dense Overflows with Emphasis on the Faroe Bank Channel Overflow. Ph.d.thesis, IMT
IMT 2010-66	Jia, Huirong	Structural Analysis of Intect and Damaged Ships in a Collission Risk Analysis Perspective. Ph.d.thesis CeSoS.
IMT 2010-67	Jiao, Linlin	Wave-Induced Effects on a Pontoon-type Very Large Floating Structures (VLFS). Ph.D.-thesis, CeSOS.
IMT 2010-68	Abrahamsen, Bjørn Christian	Sloshing Induced Tank Roof with Entrapped Air Pocket. Ph.d.thesis, CeSOS.
IMT 2011-69	Karimirad, Madjid	Stochastic Dynamic Response Analysis of Spar-Type Wind Turbines with Catenary or Taut Mooring Systems. Ph.d.-thesis, CeSOS.
IMT - 2011-70	Erlend Meland	Condition Monitoring of Safety Critical Valves. Ph.d.-thesis, IMT.
IMT – 2011-71	Yang, Limin	Stochastic Dynamic System Analysis of Wave Energy Converter with Hydraulic Power Take-Off, with Particular Reference to Wear Damage Analysis, Ph.d. Thesis, CeSOS.
IMT – 2011-72	Visscher, Jan	Application of Particla Image Velocimetry on Turbulent Marine Flows, Ph.d.Thesis, IMT.
IMT – 2011-73	Su, Biao	Numerical Predictions of Global and Local Ice Loads on Ships. Ph.d.Thesis, CeSOS.
IMT – 2011-74	Liu, Zhenhui	Analytical and Numerical Analysis of Iceberg Collision with Ship Structures. Ph.d.Thesis, IMT.
IMT – 2011-75	Aarsæther, Karl Gunnar	Modeling and Analysis of Ship Traffic by Observation and Numerical Simulation. Ph.d.Thesis, IMT.

Imt – 2011-76	Wu, Jie	Hydrodynamic Force Identification from Stochastic Vortex Induced Vibration Experiments with Slender Beams. Ph.d.Thesis, IMT.
Imt – 2011-77	Amini, Hamid	Azimuth Propulsors in Off-design Conditions. Ph.d.Thesis, IMT.
IMT – 2011-78	Nguyen, Tan-Hoi	Toward a System of Real-Time Prediction and Monitoring of Bottom Damage Conditions During Ship Grounding. Ph.d.thesis, IMT.
IMT- 2011-79	Tavakoli, Mohammad T.	Assessment of Oil Spill in Ship Collision and Grounding, Ph.d.thesis, IMT.
IMT- 2011-80	Guo, Bingjie	Numerical and Experimental Investigation of Added Resistance in Waves. Ph.d.Thesis, IMT.
IMT- 2011-81	Chen, Qiaofeng	Ultimate Strength of Aluminium Panels, considering HAZ Effects, IMT
IMT- 2012-82	Kota, Ravikiran S.	Wave Loads on Decks of Offshore Structures in Random Seas, CeSOS.
IMT- 2012-83	Sten, Ronny	Dynamic Simulation of Deep Water Drilling Risers with Heave Compensating System, IMT.
IMT- 2012-84	Berle, Øyvind	Risk and resilience in global maritime supply chains, IMT.
IMT- 2012-85	Fang, Shaoji	Fault Tolerant Position Mooring Control Based on Structural Reliability, CeSOS.
IMT- 2012-86	You, Jikun	Numerical studies on wave forces and moored ship motions in intermediate and shallow water, CeSOS.
IMT- 2012-87	Xiang ,Xu	Maneuvering of two interacting ships in waves, CeSOS
IMT- 2012-88	Dong, Wenbin	Time-domain fatigue response and reliability analysis of offshore wind turbines with emphasis on welded tubular joints and gear components, CeSOS
IMT- 2012-89	Zhu, Suji	Investigation of Wave-Induced Nonlinear Load Effects in Open Ships considering Hull Girder Vibrations in Bending and Torsion, CeSOS
IMT- 2012-90	Zhou, Li	Numerical and Experimental Investigation of Station-keeping in Level Ice, CeSOS
IMT- 2012-91	Ushakov, Sergey	Particulate matter emission characteristics from diesel enignes operating on conventional and alternative marine fuels, IMT
IMT- 2013-1	Yin, Decao	Experimental and Numerical Analysis of Combined In-line and Cross-flow Vortex Induced Vibrations, CeSOS

IMT-2013-2	Kurniawan, Adi	Modelling and geometry optimisation of wave energy converters, CeSOS
IMT-2013-3	Al Ryati, Nabil	Technical condition indexes doe auxiliary marine diesel engines, IMT
IMT-2013-4	Firoozkoohi, Reza	Experimental, numerical and analytical investigation of the effect of screens on sloshing, CeSOS
IMT-2013-5	Ommani, Babak	Potential-Flow Predictions of a Semi-Displacement Vessel Including Applications to Calm Water Broaching, CeSOS
IMT-2013-6	Xing, Yihan	Modelling and analysis of the gearbox in a floating spar-type wind turbine, CeSOS
IMT-7-2013	Balland, Océane	Optimization models for reducing air emissions from ships, IMT
IMT-8-2013	Yang, Dan	Transitional wake flow behind an inclined flat plate-----Computation and analysis, IMT
IMT-9-2013	Abdillah, Suyuthi	Prediction of Extreme Loads and Fatigue Damage for a Ship Hull due to Ice Action, IMT
IMT-10-2013	Ramirez, Pedro Agustin Pèrez	Ageing management and life extension of technical systems- Concepts and methods applied to oil and gas facilities, IMT
IMT-11-2013	Chuang, Zhenju	Experimental and Numerical Investigation of Speed Loss due to Seakeeping and Maneuvering. IMT
IMT-12-2013	Etemaddar, Mahmoud	Load and Response Analysis of Wind Turbines under Atmospheric Icing and Controller System Faults with Emphasis on Spar Type Floating Wind Turbines, IMT
IMT-13-2013	Lindstad, Haakon	Strategies and measures for reducing maritime CO2 emissons, IMT
IMT-14-2013	Haris, Sabril	Damage interaction analysis of ship collisions, IMT
IMT-15-2013	Shainee, Mohamed	Conceptual Design, Numerical and Experimental Investigation of a SPM Cage Concept for Offshore Mariculture, IMT
IMT-16-2013	Gansel, Lars	Flow past porous cylinders and effects of biofouling and fish behavior on the flow in and around Atlantic salmon net cages, IMT
IMT-17-2013	Gaspar, Henrique	Handling Aspects of Complexity in Conceptual Ship Design, IMT
IMT-18-2013	Thys, Maxime	Theoretical and Experimental Investigation of a Free Running Fishing Vessel at Small Frequency of Encounter, CeSOS
IMT-19-2013	Aglen, Ida	VIV in Free Spanning Pipelines, CeSOS

IMT-1-2014	Song, An	Theoretical and experimental studies of wave diffraction and radiation loads on a horizontally submerged perforated plate, CeSOS
IMT-2-2014	Rogne, Øyvind Ygre	Numerical and Experimental Investigation of a Hinged 5-body Wave Energy Converter, CeSOS
IMT-3-2014	Dai, Lijuan	Safe and efficient operation and maintenance of offshore wind farms ,IMT
IMT-4-2014	Bachynski, Erin Elizabeth	Design and Dynamic Analysis of Tension Leg Platform Wind Turbines, CeSOS
IMT-5-2014	Wang, Jingbo	Water Entry of Freefall Wedged – Wedge motions and Cavity Dynamics, CeSOS
IMT-6-2014	Kim, Ekaterina	Experimental and numerical studies related to the coupled behavior of ice mass and steel structures during accidental collisions, IMT
IMT-7-2014	Tan, Xiang	Numerical investigation of ship's continuous- mode icebreaking in leverl ice, CeSOS
IMT-8-2014	Muliawan, Made Jaya	Design and Analysis of Combined Floating Wave and Wind Power Facilities, with Emphasis on Extreme Load Effects of the Mooring System, CeSOS
IMT-9-2014	Jiang, Zhiyu	Long-term response analysis of wind turbines with an emphasis on fault and shutdown conditions, IMT
IMT-10-2014	Dukan, Fredrik	ROV Motion Control Systems, IMT
IMT-11-2014	Grimsmo, Nils I.	Dynamic simulations of hydraulic cylinder for heave compensation of deep water drilling risers, IMT
IMT-12-2014	Kvittem, Marit I.	Modelling and response analysis for fatigue design of a semisubmersible wind turbine, CeSOS
IMT-13-2014	Akhtar, Juned	The Effects of Human Fatigue on Risk at Sea, IMT
IMT-14-2014	Syahroni, Nur	Fatigue Assessment of Welded Joints Taking into Account Effects of Residual Stress, IMT
IMT-1-2015	Bøckmann, Eirik	Wave Propulsion of ships, IMT
IMT-2-2015	Wang, Kai	Modelling and dynamic analysis of a semi-submersible floating vertical axis wind turbine, CeSOS
IMT-3-2015	Fredriksen, Arnt Gunvald	A numerical and experimental study of a two-dimensional body with moonpool in waves and current, CeSOS
IMT-4-2015	Jose Patricio Gallardo Canabes	Numerical studies of viscous flow around bluff bodies, IMT

IMT-5-2015	Vegard Longva	Formulation and application of finite element techniques for slender marine structures subjected to contact interactions, IMT
IMT-6-2015	Jacobus De Vaal	Aerodynamic modelling of floating wind turbines, CeSOS
IMT-7-2015	Fachri Nasution	Fatigue Performance of Copper Power Conductors, IMT
IMT-8-2015	Oleh I Karpa	Development of bivariate extreme value distributions for applications in marine technology,CeSOS
IMT-9-2015	Daniel de Almeida Fernandes	An output feedback motion control system for ROVs, AMOS
IMT-10-2015	Bo Zhao	Particle Filter for Fault Diagnosis: Application to Dynamic Positioning Vessel and Underwater Robotics, CeSOS
IMT-11-2015	Wenting Zhu	Impact of emission allocation in maritime transportation, IMT
IMT-12-2015	Amir Rasekhi Nejad	Dynamic Analysis and Design of Gearboxes in Offshore Wind Turbines in a Structural Reliability Perspective, CeSOS
IMT-13-2015	Arturo Jesùs Ortega Malca	Dynamic Response of Flexibles Risers due to Unsteady Slug Flow, CeSOS
IMT-14-2015	Dagfinn Husjord	Guidance and decision-support system for safe navigation of ships operating in close proximity, IMT
IMT-15-2015	Anirban Bhattacharyya	Ducted Propellers: Behaviour in Waves and Scale Effects, IMT
IMT-16-2015	Qin Zhang	Image Processing for Ice Parameter Identification in Ice Management, IMT
IMT-1-2016	Vincentius Rumawas	Human Factors in Ship Design and Operation: An Experiential Learning, IMT
IMT-2-2016	Martin Storheim	Structural response in ship-platform and ship-ice collisions, IMT
IMT-3-2016	Mia Abrahamsen Prsic	Numerical Simulations of the Flow around single and Tandem Circular Cylinders Close to a Plane Wall, IMT
IMT-4-2016	Tufan Arslan	Large-eddy simulations of cross-flow around ship sections, IMT

IMT-5-2016	Pierre Yves-Henry	Parametrisation of aquatic vegetation in hydraulic and coastal research,IMT
IMT-6-2016	Lin Li	Dynamic Analysis of the Instalation of Monopiles for Offshore Wind Turbines, CeSOS
IMT-7-2016	Øivind Kåre Kjerstad	Dynamic Positioning of Marine Vessels in Ice, IMT
IMT-8-2016	Xiaopeng Wu	Numerical Analysis of Anchor Handling and Fish Trawling Operations in a Safety Perspective, CeSOS
IMT-9-2016	Zhengshun Cheng	Integrated Dynamic Analysis of Floating Vertical Axis Wind Turbines, CeSOS
IMT-10-2016	Ling Wan	Experimental and Numerical Study of a Combined Offshore Wind and Wave Energy Converter Concept
IMT-11-2016	Wei Chai	Stochastic dynamic analysis and reliability evaluation of the roll motion for ships in random seas, CeSOS
IMT-12-2016	Øyvind Selnes Patricksson	Decision support for conceptual ship design with focus on a changing life cycle and future uncertainty, IMT
IMT-13-2016	Mats Jørgen Thorsen	Time domain analysis of vortex-induced vibrations, IMT
IMT-14-2016	Edgar McGuinness	Safety in the Norwegian Fishing Fleet – Analysis and measures for improvement, IMT
IMT-15-2016	Sepideh Jafarzadeh	Energy effiency and emission abatement in the fishing fleet, IMT
IMT-16-2016	Wilson Ivan Guachamin Acero	Assessment of marine operations for offshore wind turbine installation with emphasis on response-based operational limits, IMT
IMT-17-2016	Mauro Candeloro	Tools and Methods for Autonomous Operations on Seabed and Water Coumn using Underwater Vehicles, IMT
IMT-18-2016	Valentin Chabaud	Real-Time Hybrid Model Testing of Floating Wind Tubines, IMT
IMT-1-2017	Mohammad Saud Afzal	Three-dimensional streaming in a sea bed boundary layer
IMT-2-2017	Peng Li	A Theoretical and Experimental Study of Wave-induced Hydroelastic Response of a Circular Floating Collar
IMT-3-2017	Martin Bergström	A simulation-based design method for arctic maritime transport systems

IMT-4-2017	Bhushan Taskar	The effect of waves on marine propellers and propulsion
IMT-5-2017	Mohsen Bardestani	A two-dimensional numerical and experimental study of a floater with net and sinker tube in waves and current
IMT-6-2017	Fatemeh Hoseini Dadmarzi	Direct Numerical Simualtion of turbulent wakes behind different plate configurations
IMT-7-2017	Michel R. Miyazaki	Modeling and control of hybrid marine power plants
IMT-8-2017	Giri Rajasekhar Gunnu	Safety and effiency enhancement of anchor handling operations with particular emphasis on the stability of anchor handling vessels
IMT-9-2017	Kevin Koosup Yum	Transient Performance and Emissions of a Turbocharged Diesel Engine for Marine Power Plants
IMT-10-2017	Zhaolong Yu	Hydrodynamic and structural aspects of ship collisions
IMT-11-2017	Martin Hassel	Risk Analysis and Modelling of Allisions between Passing Vessels and Offshore Installations
IMT-12-2017	Astrid H. Brodtkorb	Hybrid Control of Marine Vessels – Dynamic Positioning in Varying Conditions
IMT-13-2017	Kjersti Bruserud	Simultaneous stochastic model of waves and current for prediction of structural design loads
IMT-14-2017	Finn-Idar Grøtta Giske	Long-Term Extreme Response Analysis of Marine Structures Using Inverse Reliability Methods
IMT-15-2017	Stian Skjong	Modeling and Simulation of Maritime Systems and Operations for Virtual Prototyping using co-Simulations
IMT-1-2018	Yingguang Chu	Virtual Prototyping for Marine Crane Design and Operations
IMT-2-2018	Sergey Gavrilin	Validation of ship manoeuvring simulation models
IMT-3-2018	Jeevith Hegde	Tools and methods to manage risk in autonomous subsea inspection,maintenance and repair operations
IMT-4-2018	Ida M. Strand	Sea Loads on Closed Flexible Fish Cages
IMT-5-2018	Erlend Kvinge Jørgensen	Navigation and Control of Underwater Robotic Vehicles

IMT-6-2018	Bård Stovner	Aided Intertial Navigation of Underwater Vehicles
IMT-7-2018	Erlend Liavåg Grotle	Thermodynamic Response Enhanced by Sloshing in Marine LNG Fuel Tanks
IMT-8-2018	Børge Rokseth	Safety and Verification of Advanced Maritime Vessels
IMT-9-2018	Jan Vidar Ulveseter	Advances in Semi-Empirical Time Domain Modelling of Vortex-Induced Vibrations
IMT-10-2018	Chenyu Luan	Design and analysis for a steel braceless semi-submersible hull for supporting a 5-MW horizontal axis wind turbine
IMT-11-2018	Carl Fredrik Rehn	Ship Design under Uncertainty
IMT-12-2018	Øyvind Ødegård	Towards Autonomous Operations and Systems in Marine Archaeology
IMT-13-2018	Stein Melvær Nornes	Guidance and Control of Marine Robotics for Ocean Mapping and Monitoring
IMT-14-2018	Petter Norgren	Autonomous Underwater Vehicles in Arctic Marine Operations: Arctic marine research and ice monitoring
IMT-15-2018	Minjoo Choi	Modular Adaptable Ship Design for Handling Uncertainty in the Future Operating Context
MT-16-2018	Ole Alexander Eidsvik	Dynamics of Remotely Operated Underwater Vehicle Systems
IMT-17-2018	Mahdi Ghane	Fault Diagnosis of Floating Wind Turbine Drivetrain- Methodologies and Applications
IMT-18-2018	Christoph Alexander Thieme	Risk Analysis and Modelling of Autonomous Marine Systems
IMT-19-2018	Yugao Shen	Operational limits for floating-collar fish farms in waves and current, without and with well-boat presence
IMT-20-2018	Tianjiao Dai	Investigations of Shear Interaction and Stresses in Flexible Pipes and Umbilicals
IMT-21-2018	Sigurd Solheim Pettersen	Resilience by Latent Capabilities in Marine Systems
IMT-22-2018	Thomas Sauder	Fidelity of Cyber-physical Empirical Methods. Application to the Active Truncation of Slender Marine Structures
IMT-23-2018	Jan-Tore Horn	Statistical and Modelling Uncertainties in the Design of Offshore Wind Turbines

IMT-24-2018	Anna Swider	Data Mining Methods for the Analysis of Power Systems of Vessels
IMT-1-2019	Zhao He	Hydrodynamic study of a moored fish farming cage with fish influence
IMT-2-2019	Isar Ghamari	Numerical and Experimental Study on the Ship Parametric Roll Resonance and the Effect of Anti-Roll Tank
IMT-3-2019	Håkon Strandenes	Turbulent Flow Simulations at Higher Reynolds Numbers
IMT-4-2019	Siri Mariane Holen	Safety in Norwegian Fish Farming – Concepts and Methods for Improvement
IMT-5-2019	Ping Fu	Reliability Analysis of Wake-Induced Riser Collision
IMT-6-2019	Vladimir Krivopolianskii	Experimental Investigation of Injection and Combustion Processes in Marine Gas Engines using Constant Volume Rig
IMT-7-2019	Anna Maria Kozlowska	Hydrodynamic Loads on Marine Propellers Subject to Ventilation and out of Water Condition.
IMT-8-2019	Hans-Martin Heyn	Motion Sensing on Vessels Operating in Sea Ice: A Local Ice Monitoring System for Transit and Stationkeeping Operations under the Influence of Sea Ice
IMT-9-2019|	Stefan Vilsen	Method for Real-Time Hybrid Model Testing of Ocean Structures – Case on Slender Marine Systems
IMT-10-2019	Finn-Christian W. Hanssen	Non-Linear Wave-Body Interaction in Severe Waves
IMT-11-2019	Trygve Olav Fossum	Adaptive Sampling for Marine Robotics
IMT-12-2019	Jørgen Bremnes Nielsen	Modeling and Simulation for Design Evaluation
IMT-13-2019	Yuna Zhao	Numerical modelling and dyncamic analysis of offshore wind turbine blade installation
IMT-14-2019	Daniela Myland	Experimental and Theoretical Investigations on the Ship Resistance in Level Ice
IMT-15-2019	Zhengru Ren	Advanced control algorithms to support automated offshore wind turbine installation
IMT-16-2019	Drazen Polic	Ice-propeller impact analysis using an inverse propulsion machinery simulation approach
IMT-17-2019	Endre Sandvik	Sea passage scenario simulation for ship system performance evaluation

IMT-18-2019	Loup Suja-Thauvin	Response of Monopile Wind Turbines to Higher Order Wave Loads
IMT-19-2019	Emil Smilden	Structural control of offshore wind turbines – Increasing the role of control design in offshore wind farm development
IMT-20-2019	Aleksandar-Sasa Milakovic	On equivalent ice thickness and machine learning in ship ice transit simulations
IMT-1-2020	Amrit Shankar Verma	Modelling, Analysis and Response-based Operability Assessment of Offshore Wind Turbine Blade Installation with Emphasis on Impact Damages
IMT-2-2020	Bent Oddvar Arnesen Haugaløkken	Autonomous Technology for Inspection, Maintenance and Repair Operations in the Norwegian Aquaculture
IMT-3-2020	Seongpil Cho	Model-based fault detection and diagnosis of a blade pitch system in floating wind turbines
IMT-4-2020	Jose Jorge Garcia Agis	Effectiveness in Decision-Making in Ship Design under Uncertainty
IMT-5-2020	Thomas H. Viuff	Uncertainty Assessment of Wave-and Current-induced Global Response of Floating Bridges
IMT-6-2020	Fredrik Mentzoni	Hydrodynamic Loads on Complex Structures in the Wave Zone
IMT-7-2020	Senthuran Ravinthrakumar	Numerical and Experimental Studies of Resonant Flow in Moonpools in Operational Conditions
IMT-8-2020	Stian Skaalvik Sandøy	Acoustic-based Probabilistic Localization and Mapping using Unmanned Underwater Vehicles for Aquaculture Operations
IMT-9-2020	Kun Xu	Design and Analysis of Mooring System for Semi-submersible Floating Wind Turbine in Shallow Water
IMT-10-2020	Jianxun Zhu	Cavity Flows and Wake Behind an Elliptic Cylinder Translating Above the Wall
IMT-11-2020	Sandra Hogenboom	Decision-making within Dynamic Positioning Operations in the Offshore Industry – A Human Factors based Approach
IMT-12-2020	Woongshik Nam	Structural Resistance of Ship and Offshore Structures Exposed to the Risk of Brittle Failure
IMT-13-2020	Svenn Are Tutturen Værnø	Transient Performance in Dynamic Positioning of Ships: Investigation of Residual Load Models and Control Methods for Effective Compensation
IMT-14-2020	Mohd Atif Siddiqui	Experimental and Numerical Hydrodynamic Analysis of a Damaged Ship in Waves
IMT-15-2020	John Marius Hegseth	Efficient Modelling and Design Optimization of Large Floating Wind Turbines

IMT-16-2020	Asle Natskår	Reliability-based Assessment of Marine Operations with Emphasis on Sea Transport on Barges
IMT-17-2020	Shi Deng	Experimental and Numerical Study of Hydrodynamic Responses of a Twin-Tube Submerged Floating Tunnel Considering Vortex-Induced Vibration
IMT-18-2020	Jone Torsvik	Dynamic Analysis in Design and Operation of Large Floating Offshore Wind Turbine Drivetrains
IMT-1-2021	Ali Ebrahimi	Handling Complexity to Improve Ship Design Competitiveness
IMT-2-2021	Davide Proserpio	Isogeometric Phase-Field Methods for Modeling Fracture in Shell Structures
IMT-3-2021	Cai Tian	Numerical Studies of Viscous Flow Around Step Cylinders
IMT-4-2021	Farid Khazaeli Moghadam	Vibration-Based Condition Monitoring of Drivetrains in Large Offshore Wind Turbines in a Digital Twin Perspective